
Quantum Frequency Conversion of Indistinguishable Photons from Independent Solid State Emitters

Dissertation

zur Erlangung des Grades
des Doktors der Naturwissenschaften
der Naturwissenschaftlich-Technischen Fakultät
der Universität des Saarlandes

von

Benjamin Kambs



Saarbrücken

2019

Tag des Kolloquiums: 04.02.2020

Dekan: Univ.-Prof. Dr. rer. nat. Guido Kickelbick

Berichterstatter: Univ.-Prof. Dr. rer. nat. Christoph Becher
J.-Prof. Dr. rer. nat. Tim Bartley

Vorsitz: Univ.-Prof. Dr. rer. nat. Rolf Pelster

Akad. Mitarbeiter: Dr. rer. nat. Stephan Kucera

Don't Panic.

— Douglas Adams,
“The Hitchhiker’s Guide to the Galaxy”

Abstract

Indistinguishable single photons are an indispensable resource for various quantum technological applications. In order to exploit the lowest possible losses in fiber-based long-haul networks, these photons are required to be at telecom wavelengths around $1.55\ \mu\text{m}$. Available sources of indistinguishable telecom photons, however, are premature as of yet. The present thesis attends to this need using efficient quantum frequency conversion (QFC, device efficiency $> 30\%$) to transduce single photons as emitted by InAs semiconductor quantum dots (QD) from $904\ \text{nm}$ to $1557\ \text{nm}$. The indistinguishability is assessed with quantum interference experiments after Hong-Ou-Mandel in two major settings: first, with photons consecutively emitted by the same QD, and second, with photons stemming from two independent sources. All indistinguishabilities observed prior and subsequent to the QFC are in the order of $30\text{-}50\%$ and consistently explained using available emitter and device parameters. To that end we derive and use a theoretical model, which predicts indistinguishabilities assuming homogeneously and inhomogeneously broadened emission lines as typically encountered for solid state single photon sources. Based on our results, we conclude that QFC conserves photon indistinguishabilities and that the present scheme provides an efficient tool to aid the realization of quantum networks.

Zusammenfassung

Ununterscheidbare einzelne Photonen sind eine unverzichtbare Ressource für diverse quantentechnologische Anwendungen. Um Verluste in faserbasierten Langstreckennetzwerken zu minimieren, müssen diese Photonen außerdem Wellenlängen im Telekommunikationsbereich um $1.55\ \mu\text{m}$ aufweisen. Verfügbare Quellen ununterscheidbarer Telekomphotonen sind jedoch bisher wenig ausgereift. Die vorliegende Arbeit widmet sich diesem Mangel mit Hilfe effizienter Quanten-Frequenzkonversion (QFC, Geräteeffizienz $> 30\%$), um einzelne Photonen, die von InAs Halbleiterquantenpunkten (QD) emittiert wurden, von $904\ \text{nm}$ nach $1557\ \text{nm}$ zu konvertieren. Die Ununterscheidbarkeit wird mit Hilfe von Quanteninterferenzexperimenten nach Hong-Ou-Mandel in zwei verschiedenen Szenarien bewertet: mit konsekutiv emittierten Photonen aus einem QD und mit Photonen aus zwei unabhängigen Quellen. Alle Ununterscheidbarkeiten, die vor und nach der Konversion beobachtet wurden, liegen im Bereich $30\text{-}50\%$ und werden konsistent mit Hilfe verfügbarer Emitter- und Geräteparameter erklärt. Zu diesem Zweck entwickeln und benutzen wir ein theoretisches Modell, welches Ununterscheidbarkeiten anhand homogen und inhomogen verbreiteter Emissionslinien, wie sie oft bei festkörperbasierten Einzelphotonenquellen angetroffen werden, vorhersagt. Aufgrund unserer Ergebnisse schließen wir, dass QFC die Ununterscheidbarkeit von Photonen erhält und das präsentierte Schema ein überzeugendes Hilfsmittel zur Realisierung von Quantennetzwerken darstellt.

Contents

1	Introduction	1
2	Fundamentals	9
2.1	Semiconductor Quantum Dots	9
2.1.1	Fabrication	10
2.1.2	Level Structure and Optical Transitions	12
2.1.3	Excitation Schemes	15
2.2	Mechanisms of Spectral Line Broadening	16
2.2.1	Timescales of Frequency Fluctuations	17
2.2.2	Emission from a Perturbed Two-Level System	20
2.2.3	Fluctuator Model	22
2.3	Nonlinear Optics	25
2.3.1	Three Wave Mixing	25
2.3.2	Difference Frequency Generation in Waveguides	29
2.4	Two-Photon Quantum Interference	32
2.4.1	Photon Coalescence	33
2.4.2	Time-Resolved Two-Photon Interference	35
2.4.3	Quantum Beats and Hong-Ou-Mandel Dip	37
3	Quantum Interference of Independent Photons	41
3.1	Derivation	41
3.1.1	Joint Detection Probability for Linear Optical Gates	42
3.1.2	Cross-Correlation Function	44
3.1.3	Overall Coincidence Probability	47
3.2	Experiments after Hong-Ou-Mandel	48
3.2.1	Comparison to Literature	49
3.2.2	Remote HOM Visibility and Coherence Time	52
3.2.3	Quantum Interference of Consecutively Emitted Photons	53
3.3	Summary	56

4	Frequency Conversion Setup	59
4.1	Overview	59
4.1.1	Nonlinear Waveguide Chip	61
4.1.2	Pump Laser System	62
4.2	Temperature Tuning	64
4.3	Dichroic Waveguide Coupling	66
4.4	Stimulated Down-Conversion	69
4.5	Converter Noise	71
4.6	Summary	74
5	Quantum Interference with Photons from a Single Quantum Dot	77
5.1	Single Photon Generation	78
5.1.1	Confocal Microscope and Quantum Dot Selection	78
5.1.2	Frequency Converter Performance	81
5.2	Spectral and Temporal Properties	83
5.2.1	Radiative Lifetime	83
5.2.2	Coherence Time	85
5.2.3	Spectral Background Analysis	87
5.2.4	Antibunching	89
5.3	Preservation of Indistinguishability during Quantum Frequency Conversion	93
5.3.1	Experimental Concept	93
5.3.2	Mach-Zehnder Interferometers	96
5.3.3	Correlation Measurements	98
5.4	Summary	101
6	Quantum Interference with Photons from Remote Quantum Dots	105
6.1	Experimental Overview	106
6.2	Single Photon Generation	108
6.2.1	Confocal Microscope for Resonant Excitation of Trions	108
6.2.2	Frequency Converter Performance	114
6.3	Spectral and Temporal Properties	118
6.3.1	Radiative Lifetime	119
6.3.2	High Resolution Emission Spectra	120
6.3.3	Antibunching	121
6.3.4	Indistinguishability of Consecutively Emitted Photons	123
6.4	Recovering Spectral Indistinguishability via Quantum Frequency Conversion	125
6.4.1	Correlation Measurements	125
6.4.2	Relative Spectral Tuning of Converted Telecom Photons	131
6.5	Summary	133

7 Entanglement Generation Based on Quantum Interference	137
7.1 Entanglement via a Controlled NOT Operation	138
7.2 Attenuation and Dispersion in Fiber-Based Quantum Repeater Networks	143
7.2.1 Two-Photon Interference with Dispersed Photons	148
7.2.2 Entanglement Efficiencies in Optical Fiber Networks . .	152
7.3 Summary	157
8 Summary and Conclusion	159
Appendices	165
A Eigenvalue Equations for Rectangular Waveguide Modes	165
B Adapted Sellmeier Coefficients for Lithium Niobate	166
C Continuous Noise Floor in Intensity Correlations	166
D Monte Carlo Simulations	168
E Fitting Model for HOM Measurements	176
References	181
Publications	207

Introduction

In order to define the field of quantum technologies, researchers frequently speak of the *second quantum revolution* [1], which is motivated by a historic comparison: The establishment of quantum mechanical theories in the early 20th century paved the way for a deep understanding of physical processes at the level of single or few atoms, led to the notion of photons, and eventually triggered numerous technological developments including lasers, transistors, and microwave atomic clocks throughout the following decades. Considering the worldwide impact these inventions entailed, this period is referred to as the *first quantum revolution*. By now quantum mechanics is a mature discipline. Despite its many predictions that apparently contradict the physical laws governing our everyday life, it is often quoted as the most successful physical theory. Technological progress does not only enable us to test these predictions with increasing precision, but also to engineer coherent and entangled quantum states of matter and light, which do not naturally occur. The unique properties of such states can be employed for various novel applications, which would be impossible to realize based on non-quantum systems. It is these applications that are summarized as quantum technologies and that currently bring us to the verge of a second quantum revolution.

Placing quantum technologies on the same level with the progress achieved through fundamental quantum theories is certainly an ambitious comparison at the current stage. The prospects of quantum technologies, on the other hand, are indeed profound. An operational universal quantum computer, for instance, could tackle various numerical problems, which are considered intractable on classical machines [2], such as the quantum chemical simulation of molecules [3–5]. One possible application, which illustrates the large scale industrial impact, is the modeling of nitrogenase [6] - an enzyme, which is capable of fixing atmospheric nitrogen on a small energy budget. Understanding and controlling the underlying mechanism might lead to a procedure which supersedes the Haber-Bosch process, whose contribution to the global CO₂ emission is currently more than 2% [7]. An early but very important exam-

ple of the supremacy of quantum over classical computers is the fast integer factorization using Shor's algorithm [8]. Its implementation would pose a considerable threat to the security of public-key cryptosystems, which rely on the assumption that no such algorithm exists [9, 10]. Ironically enough, quantum technologies do not only cause this dilemma, but also suggest a solution: quantum key distribution (QKD) is a sub-discipline of quantum communication investigating possible protocols on how to share encryption keys encoded in the state of single or few photons between two distant parties [11]. Ideally, these protocols offer absolute security against eavesdropping based on fundamental physical laws, which make it impossible for a spy to go unnoticed [12–14]. Moreover, both quantum computers and communication are often associated with the more general concept of a quantum internet [15], being a system of numerous stationary quantum nodes, which are linked via quantum channels within a decentralized long-haul network. The resources and capabilities of a quantum internet exponentially scale with the number of nodes and channels and quickly overcome size restrictions of local systems. Such a network is therefore the ideal platform not only to implement secure communication, but also to approach extremely complex computational tasks.

In view of these and other exciting applications, there are growing efforts across countries worldwide to push forward the development of quantum technologies. In particular, several industrial as well as public initiatives aim at first real-world quantum networks that make use of QKD [16]. Arguably the most astonishing project is the quantum backbone connecting the four Chinese cities Beijing, Jinan, Hefei, and Shanghai [17, 18]. The overall network spans more than 2,000 km of optical fiber with each city hosting an additional metropolitan network of its own. As of now, the backbone is partially operational and total costs in the order of USD 100 million have been estimated [16]. However, despite its pioneering work, China is certainly not the sole driving force. In 2015, for instance, the UK established a quantum technology hub equipped with overall GBP 270 million in order to promote quantum communication technologies and set up a British backbone connecting Bristol and Cambridge during a period of 5 years [19]. The US government, on the other hand, reports annual investments of around USD 200 million in the field [20] and recently passed the *National Quantum Initiative Act* releasing another USD 1.2 billion [21]. It is against this background that the European Commission reacted to a call of its own research community and initiated the quantum technology flagship programme in 2018, which provides funding in the order of EUR 1 billion over 10 years [22]. It intends to support fundamental research in the fields of quantum communication, computation, simulation, as well as sensing and metrology, but also strongly emphasizes the necessary technology transfer from academia to commercializable applications.

In a draft of its research agenda [23], the flagship highlights the demonstration of fiber-based QKD schemes over distances of more than 500 km as one of its major objectives. Considering that distances of 400 km have already

been exceeded [24,25], the progress of this proposal might seem incremental at best. However, the achieved secure key rates reported in both publications are severely limited by transmission losses of the employed optical fibers. In [25], for instance, the key rate is merely 6.5 bits per second, although the experiment is driven at a repetition rate as high as 2.5 GHz. This discrepancy is shocking, but the result is close to the limit of what is technically feasible: the experiment has been performed at a wavelength of 1.55 μm , i.e. within the telecom C-band where losses of optical fibers are minimized. More specifically, the employed ultralow-loss fiber has an attenuation of 0.17 dB/km [26], which is the lowest value commercially available as of now. Yet, the overall loss amounts to 69 dB corresponding to a fiber length of 405 km, which explains the low rate for the better part. These losses are well known and their impact on various QKD schemes has been intensely studied [27–29]. As it turns out, the attainable secure key rates of most point-to-point protocols become too small for practical applications after no more than a few 100 km. Unfortunately, this issue cannot be encountered with signal amplification using classical repeaters, as those destroy the quantum state of the corresponding photons, which is one of the many consequences of the *no-cloning* theorem [30]. A possible solution is offered by quantum repeaters (QR) [31–33]. Simply put, a QR creates a joint entangled state between two local quantum systems at the site of sender and receiver without any direct interaction. Once the entanglement is established, it can be used as a resource, e.g. in order to generate an encryption key between the two parties. The advantage is that no photon ever has to travel the entire distance between sender and receiver, but only up to the QR station located somewhere in between. Consequently, a quantum communication channel including QRs is not as much affected by optical losses and holds out the prospect of higher key rates [29]. It is for this reason that the quantum flagship intends to incorporate at least three QRs in their network. As no full QR has been demonstrated so far, let alone its integration into a complete QKD scheme, this plan constitutes the actual challenge of the flagship’s proposal.

The concept of a QR network is based on the distribution of entanglement across a chain of elementary segments using an operation termed entanglement swapping [34]. In the original proposal of a QR [31] each segment contains an EPR-pair (after Einstein, Podolsky, and Rosen [35]), being a set of two entangled two-level systems, whose physical nature is not further specified. The most common protocols, however, employ entangled quantum memories (QM) as EPR-pairs [32,36,37]. A QM is a stationary node, which is capable of storing a quantum state with long lifetime, coherence time as well as high fidelity and provides suitable read and write mechanisms. They are often implemented based on ensembles of neutral atoms [38–40] or rare earth ions in solids [41–43], but also single quantum emitters such as trapped neutral atoms [44,45] and ions [46–48] as well as solid state emitters are considered [49–51]. In order to establish the elementary entanglement link between both

QMs of one segment, various possibilities exist, which are for instance well summarized in [33]. All approaches are typically classified as either *one* or *two photon detection* techniques, of which the following two are arguably the most prominent ones:

- (i) According to the protocols described in [32, 36], both memories emit a photon, each of which heralds an excited state of its source. The photons are overlapped on a beam splitter and subsequently detected. If the probability that both memories are simultaneously excited is negligible, the detection of a single photon projects the system into an entangled state of a single excitation delocalized between both memories.
- (ii) Another approach after [37, 52] starts with the two memories emitting each one photon entangled with their internal quantum states. Both QMs are then projected to an entangled state via two-photon coincidence detection in a Bell-state measurement [53]. The necessary matter-photon entanglement has been shown for the entire range of emitter platforms mentioned above [54–57].

There are numerous variations of both methods. Often considered are for instance protocols based on single photons [58] or entangled photon-pairs [59] with QMs being integrated via absorption processes. All strategies moreover only work, if the origin of the detected photons cannot be determined, which implies that the photons of both sources must be mutually indistinguishable. The indistinguishability can be separately assessed via destructive two-photon interference (TPI) in an experiment after *Hong-Ou-Mandel* (HOM) [60]. In particular TPI between photons from independent sources, as required for QRs, has been observed in a vast number of experiments for all kinds of potential QMs [61–68]. Using these methods, the entanglement of distant stationary nodes has been realized in a number of very successful experiments based on trapped atomic [69–72] as well as solid state systems [73, 74]. Furthermore, we like to mention the quantum relay, which is a memoryless modification of the QR [75–77]. Instead of a QM it employs entangled photon-pairs as obtained from SPDC sources (abbr. for *spontaneous parametric down-conversion*) [78] or via radiative cascades in atomic systems [79, 80]. While a fundamental entanglement swapping operation between photons from two independent SPDC-sources has been shown as early as 1998 [81], a very recent experiment demonstrated the functionality of a complex relay network consisting of six independent SPDC-sources and four Bell-state measurement stations generating entangled states of four photons [82].

Although these experiments demonstrate some of the most essential functionalities of a QR, one realizes that none of the investigated QMs provides photons at telecom wavelengths. Instead, most systems emit in the visible or near infrared range, entailing the anticipated high losses in optical fibers. As a consequence, the established entanglement-links are typically limited to

distances of no more than a few 100 m with a maximum of 1.3 km reported in [83]. In light of this issue, a number of encouraging experiments have been performed with ensembles of Erbium ions in glass fibers [84] or nanophotonic structures [85] serving as direct memories for telecom photons. However, these memories still suffer from low efficiencies and low coherence times as of now. Moreover, carefully tailored semiconductor quantum dots have been investigated as sources of telecom photons [86, 87], but the corresponding emitters usually lack the performance of their near infrared emitting counterparts in terms of brightness, purity, and indistinguishability [88, 89]. A very different approach bypasses the intricate search for suitable telecom emitters and memories altogether: the field of quantum frequency conversion (QFC) [90, 91] deals with various nonlinear optical processes typically based on $\chi^{(2)}$ and $\chi^{(3)}$ media [92, 93], which are used to manipulate the spectral properties of single photons. In particular, they provide the means to shift the carrier frequency of photons from their short emission wavelength to the telecommunication bands and vice versa. This allows to combine the best available emitter platforms with the lowest possible losses in optical fibers. Soon after the initial proposal, QFC was demonstrated in a first proof-of-principle experiment in 1992 [94], but for the converters to become a tool of quantum technologies substantial performance improvements were required. Around two decades later, device efficiencies in the order of 30 % became accessible [95, 96] owing to state-of-the-art materials such as periodically poled lithium niobate structured into waveguides [97–99]. Moreover, Raman scattering [100, 101] and parametric fluorescence [102] of the optical pump were found to be the sources of severe noise pollution at the target wavelength, which was minimized by careful process design and rigorous spectral filtering thereafter. Equipped with such high-efficiency, low-noise devices it became possible to address experiments investigating the quantum nature of the converted photons. So far, the conservation of coherence [95], photon-statistics [95, 103, 104], nonclassical light-matter correlations [105, 106], as well as photon-photon [107–110] and matter-photon entanglement [96, 111–114] have been successfully demonstrated. We like to single out an experiment recently reported in [115]. The authors employ two independent frequency converters to interface two remote atomic ensembles to the telecom O-band and perform entanglement swapping after transmitting the converted photons of both memories over several 10 km of optical fiber. The experiment demonstrates for the first time a complete QR segment in a long-haul fiber network made possible owing to QFC. By now these promising results have led researchers to accept QFC as an indispensable enabling technology for quantum networks [23].

Quantum frequency conversion is not restricted to a specific emitter platform. Solely the experiments mentioned above cover photons obtained from an ensemble of cold Rb atoms, nitrogen-vacancy centers in diamond, trapped Ca-ions, and others. In the present work we pursue the frequency conversion of single photons as emitted from semiconductor quantum dots (QD). Among

all available quantum emitters, QDs are a compelling option mostly owing to advanced fabrication techniques that allow to integrate them into various nanophotonic structures [116]. In particular QDs embedded into microcavities [117–119] or waveguides [120, 121] enable directed light emission leading to highly efficient light-matter interfaces. Combined with the enhanced fluorescence decay rate of emitters coupled to high finesse cavities [122–124], QDs became single photon sources that are extraordinarily bright and can be operated at high system clock rates [125]. A major issue for QDs, as for all solid-state systems for that matter, is the coupling to a fluctuating environment leading to line broadening due to pure dephasing [126, 127] and spectral diffusion [128, 129]. These effects severely limit coherence as well as indistinguishability of the emitted photons. However, operating QDs at low temperatures and under strictly resonant excitation conditions [130] as well as the use of other passive or active mitigation techniques [131–133] helped to achieve nearly Fourier-limited photon emission in recent years [125, 134]. In order to exploit QDs as a component in quantum networks, different approaches are being pursued. First of all single electron or hole spins in QDs are considered as possible QMs. On that account, basic requirements such as spin-photon interfaces [135, 136] and spin-photon [57, 137, 138] as well as remote spin-spin entanglement [74] have been demonstrated. However, the storage capabilities of QDs are currently limited by spin-coherence times of no more than a few microseconds [139]. Another possibility relies on QDs being sources of polarization-entangled photons [80]: doubly excited QDs decay in a radiative cascade emitting two spectrally separate and orthogonally polarized photons. The polarization states of the photons correspond to the fine-structure components of both transitions, which in turn depend on the in-plane ellipticity of the QD. In case of a perfectly spherical shape the fine-structure components are degenerate and the emitted photons polarization-entangled. Accordingly, it is possible to use these QDs as an EPR-pair source for the aforementioned quantum relay. The emission of polarization-entangled photon-pairs from QDs has been observed in a number of experiments [140–144], and a quantum relay scheme based on an electrically driven InAs QD was demonstrated in [145].

The main focus of the QFC experiments in this work is to study the indistinguishability of converted single photons. As mentioned before, indistinguishable photons are one of the main requirements of a functional QR, but also optical quantum computing [146, 147] and sensing schemes [148, 149] profit from them. Therefore, understanding whether and how indistinguishability is affected by QFC is a question relevant to a variety of applications. Prior to this work, photons from two spectrally distinct transitions around 980 nm of one quantum dot were up-converted to a common wavelength at 600 nm and TPI between both photons could be observed in a subsequent HOM experiment [104]. A different experiment reported on TPI between photons emitted by a quantum dot and an independent laser down-converted from around 910 nm to the telecom C-band [150]. Here, we consider a similar

down-conversion scheme interfacing the spectral regions around 905 nm and 1557 nm. It will be employed, however, to convert photons from two remote QDs to a common telecom wavelength. In a subsequent HOM experiment the indistinguishability of both independently converted telecom photons will be demonstrated. In view of an entanglement swapping operation, these results suggest that QFC can be readily used to extend the range of a single entanglement-link from only a few kilometers to a realistic quantum network scale of several 10 to 100 km. Another benefit in this scheme stems from the convenient tunability of the telecom photons during the QFC process. Like all solid-state sources the emission of QDs exhibits strong inhomogeneous broadening caused by processing uncertainties and interactions between the emitter and its host matrix. As a consequence, HOM experiments usually require an additional tuning mechanism to overcome the spectral distinguishability of distinct emitters, usually realized via a control parameter such as temperature [151–153], strain [154–156], as well as static electric [64–67] or magnetic fields [157, 158]. Shifting this task to the QFC step, tuning methods directly acting on the emitter become unnecessary, which not only avoids a potential degradation of its spectral properties but also decreases the complexity of the experiment.

The contents of this thesis is presented in topical order: in Chap. 2 we first address a selection of fundamentals, which are essential to understand both theoretical and experimental results of this work. These include information on semiconductor quantum dots as single photon sources, spectral line broadening mechanisms, nonlinear optics with a focus on difference frequency generation in waveguides, as well as the time-dependent description of two-photon interference in HOM-type experiments. In Chap. 3 we develop a theory to describe HOM-experiments, whose photons are subject to homogeneous and inhomogeneous line broadening mechanisms. The resulting formalism is used throughout the thesis to consistently explain the non-ideal TPI contrasts observed in experiment. Moreover, the formalism is extended to predict the performance of partially indistinguishable photons in general linear optical gates. As QFC is a key component to all experiments of this thesis, Chap. 4 is dedicated to the relevant design and performance aspects of the converter. Besides a basic description of its integral components, we offer information on tunability, efficiency, as well as noise characteristics. In Chap. 5 we turn to HOM experiments with down-converted photons. In this first set of experiments we test the indistinguishability of photons consecutively emitted by the same quantum dot. The results suggest that QFC conserves photon indistinguishabilities and therefore open the way for the experiments presented in Chap. 6. Here, two identical but independent converters are used to transduce the single photon emitted by two remote quantum dots to the same center wavelength at the telecom C-band. In a final HOM experiment we show their mutual indistinguishability and how the conversion step can be used to tune the independent photons in and out of resonance. In Chap. 7 we theoreti-

cally address the impact of limited TPI contrasts in different entanglement generation schemes. More specifically, we investigate how homogeneous and inhomogeneous line broadening mechanisms affect the entanglement fidelity of independent photons via a controlled-NOT gate, and the extent to which chromatic dispersion in optical fibers degrades possible entanglement rates in entanglement swapping schemes. Eventually, all results of the present thesis are reviewed and discussed in Chap. 8.

Fundamentals

In this chapter we address a number of fundamentals necessary to understand the results obtained in the scope of this work as well as their interpretation. Fig. 2.1 illustrates a segment of the two-photon interference experiment performed on single photons from remote quantum emitters: single photons emitted by a semiconductor quantum dot (QD) are transferred from the near infrared regime (red photons) to the telecom C-band (blue photons) via quantum frequency down-conversion (QFDC) and subsequently overlapped on a beam splitter with converted photons from a second QD. This arrangement constitutes a Hong-Ou-Mandel (HOM) experiment and is meant to test the mutual indistinguishability of both photons.

In the course of our considerations we will discuss pivotal elements of the shown experiment including spectroscopic features of QDs (Sect. 2.1), single photon spectra homogeneously and inhomogeneously broadened beyond their Fourier limit (Sect. 2.2), nonlinear optics with focus on difference frequency generation in ridge waveguides (Sect. 2.3), as well as the description of HOM experiments in the time-domain (Sect. 2.4). Note that these fundamentals do not only cover the experiment with photons from remote QDs as shown in Fig. 2.1 (Chap. 6), but also with consecutively emitted photons from a single QD (Chap. 5).

2.1 Semiconductor Quantum Dots

In the presented experiments we use self-assembled semiconductor quantum dots as sources of single indistinguishable photons. A QD is a small cluster containing 10^3 to 10^5 atoms of a semiconductor material embedded in a host crystal with wider bandgap. As their size ($\approx 10 - 100$ nm) is comparable to the matter wavelength of electrons, QDs give rise to a three-dimensional confining potential for charge carriers with several localized states and are therefore often referred to as *artificial atoms*.

The material platform of the quantum dot samples employed in our work

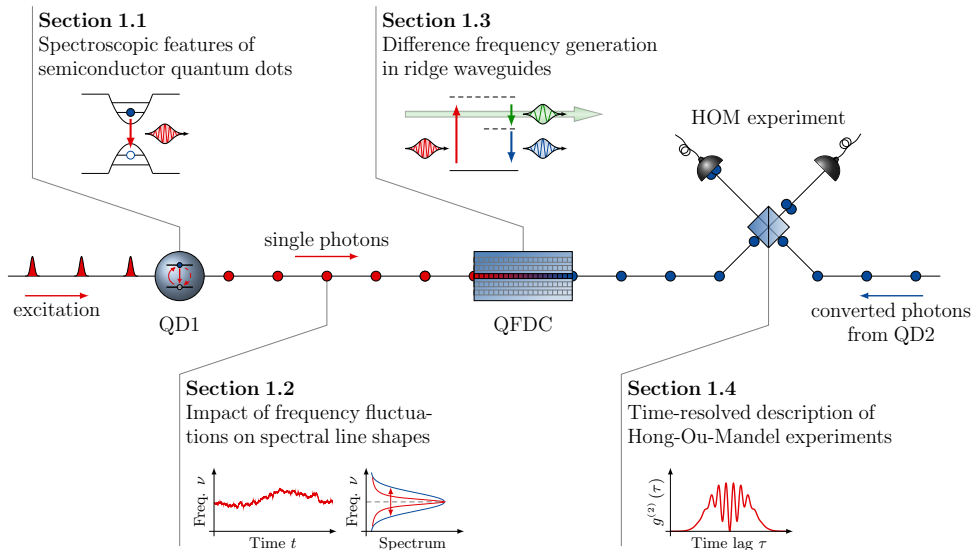


Figure 2.1. Covered fundamentals in the context of the performed experiments. A sketch of a Hong-Ou-Mandel (HOM) experiment is shown, including emission of single photons from a quantum dot (QD), their quantum frequency down-conversion (QFDC) to telecom wavelengths and the final coalescence with converted photons from a second QD on a beam splitter. The fundamentals provide details on QD physics, spectral line broadening mechanisms, nonlinear optics, and time-resolved measurements of HOM experiments.

is one of the most common, being indium arsenide (InAs) QDs in a gallium arsenide (GaAs) matrix [159,160]. InAs QDs typically emit in a range of 850-1000 nm, exhibit radiative lifetimes of around 1 ns and have to be operated at cryogenic temperatures due to a shallow charge carrier confinement [161].

In the following we describe the most vital basics of semiconductor QD physics necessary to understand the spectroscopic features encountered in the scope of this work. In particular, we focus on fabrication, level structure, optically active transitions, and excitation schemes of QDs. The outline of this section mostly follows [162] and compiles additional information found in the comprehensive reviews [161,163,164].

2.1.1 Fabrication

As opposed to colloidal QDs, which are produced in solution [165], *self-assembled* QDs are grown by epitaxial methods in bulk, i.e. by consecutive deposition of two or more different crystalline materials on a solid substrate. The main parameters defining the mode of growth are the lattice constants of the involved materials, as a large mismatch leads to significant strain at their interface. Generally, three different regimes are distinguished, correspond-

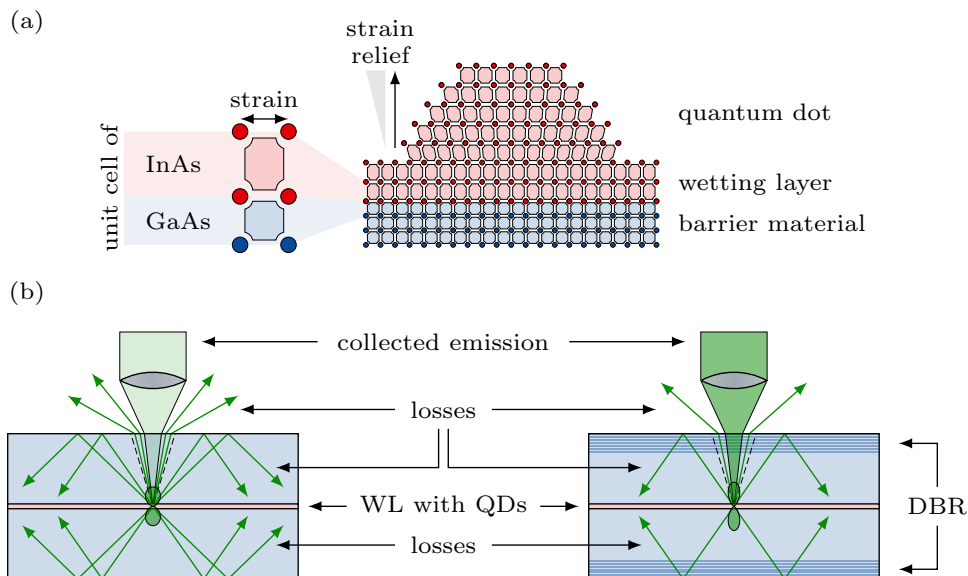


Figure 2.2. Fabrication of self-assembled quantum dots. (a) Growing InAs on GaAs corresponds to the Stranski-Krastanov regime: after the growth of a few layers of InAs (wetting layer, WL), the strain due to lattice mismatch leads to the formation of small nano-islands - the quantum dots. (b) The high refractive index of GaAs causes significant losses (green arrows) due to total internal reflection and the limited NA of the collection system (finite width of gray lens). The dashed line represents Snell's window. Distributed Bragg reflectors (DBR) on both sides of the sample (right side) form a planar cavity around the emitter, which enhances emission towards the objective and improves the collection efficiency (illustrated by darker green color).

ing to **(i)** a small mismatch, which hardly induces strain and allows smooth 2D-layers to grow (*Frank-van der Merwe* [166]), **(ii)** a large mismatch, in which the deposited material forms small droplets to minimize the contact area (*Volmer-Weber* [167]), and **(iii)** an intermediate regime (*Stranski-Krastanov* [168]). With a lattice-mismatch of $\approx 7\%$ InAs QDs are grown on GaAs in Stranski-Krastanov mode [169]. A resulting QD is schematically depicted in Fig. 2.2 (a). Deposition of the low-bandgap material (here InAs, red) on the barrier material (BM, here GaAs, blue) first leads to a few strained monolayers, commonly known as wetting-layer (WL). At a critical thickness the energy penalty stemming from strain predominates the surface energy and small nano-islands start to emerge, in which the strain is relieved. These nano-islands constitute the actual QD. Prior to the deposition of more BM, the QDs are often terminated by a capping layer.

Fig. 2.2 (b) illustrates a common problem encountered with solid state emitter systems: due to the high refractive index of the host crystal, only photons emitted within a small solid angle-range can be extracted (green cone).

The rest is lost due to total internal reflection at the surface and the limited numerical aperture (NA) of the collecting microscope objective. In case of GaAs, which exhibits $n \approx 3.6$ at 900 nm [170], these losses are severe, as they can exceed 99 % of the overall emission [171]. It is possible, however, to tailor the direction of light emission towards the objective and thus increase the extraction efficiency by structuring the QD environment. The QD sample employed in the present work was embedded between two distributed Bragg reflectors (DBR, compare Fig. 2.2 (b) right side) made of multiple alternating layers of GaAs and AlAs, which improves the extracted photon flux by an order of magnitude to around 10 % [171]. Note that even higher extraction efficiencies have been achieved using more sophisticated structures, such as QDs embedded into micropillars [117–119] or waveguides [120, 121], or with the sample surface shaped into a solid immersion lens [153, 172].

Two techniques are employed for the growth of QDs, namely molecular beam epitaxy (MBE) and metal-organic vapor-phase epitaxy (MOVPE). MBE vaporizes and deposits material at high to ultra-high vacuum and therefore achieves high purity at the cost of low rates. In contrast MOVPE employs a carrier gas slightly below atmospheric pressure to transport metal-organic compounds to the substrate. Accordingly, MOVPE is a suitable method, if high deposition rates are necessary, e.g. for the growth of DBRs. On the downside, MOVPE typically causes a defect density high compared to MBE grown samples.

2.1.2 Level Structure and Optical Transitions

Light emission from QDs stems from a recombination process of bound electron-hole pairs, the so-called excitons. Accordingly, the spectrum of emitted light is determined by the spectrum of available exciton states, which are typically modeled as eigenstates of a 3D confining potential [173]. Fig. 2.3 (a) and (b) outline one of the most common QD geometries, referred to as *lens-shape*. It corresponds to an oblate semi-ellipsoid of thickness a in growth direction with lateral principal axes b_x and b_y , sitting on top of a WL of thickness d . As the thickness of the QD varies only slowly within the xy -plane, the charge carrier movements along the z -direction and perpendicular to it can be adiabatically decoupled. On that note it is convenient to first consider the conduction band structure as function of z for a fixed lateral position as illustrated in Fig. 2.3 (c). At any position the InAs layer constitutes a simple 1D quantum well with finite walls (red) within the GaAs continuum (blue). With a thickness of merely a few nm, WL and QD accommodate only the ground state at energy E_0 . Due to the varying InAs thickness, the energy becomes a function of the lateral position, where its minimum can be found at the QD center (x_0, y_0) [bottom diagram in (c)]. With the Schrödinger equation solved with respect to z , we obtain a function $E_0(x, y)$ defining the in-plane movement, which approximately resembles a 2D-harmonic potential (1D cut

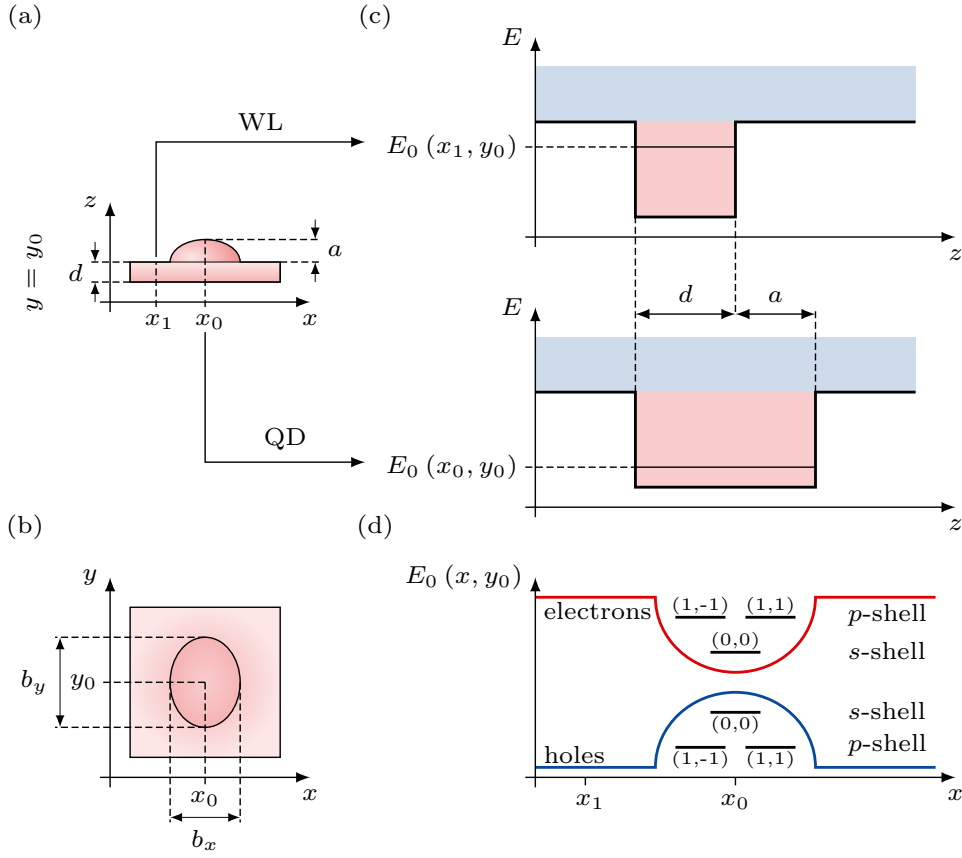


Figure 2.3. Level structure of self-assembled quantum dots.

Side view (a) and top view (b) of a lens-shaped quantum dot (QD) and the surrounding wetting layer (WL). Its geometry is defined by height a , diameters b_x and b_y , as well as WL thickness d . (c) Conduction band edge along the z -axis. The low-band gap QD material (red) inside the wide-bandgap barrier material (blue) constitutes a quantum well for the charge carrier movement in z -direction. In the WL [top diagram, thickness d at position (x_1, y_0)] and QD [bottom diagram, $d + a$ at (x_0, y_0)] only the fundamental modes are allowed with energies $E_0(x_1, y_0)$ and $E_0(x_0, y_0)$, respectively. (d) The energy E_0 for the z -movement as a function of the radial position approximately resembles a 2D-harmonic potential for the in-plane movement (here the potential is illustrated in 1D for $y = y_0$). The bound states are characterized by a set of quantum numbers (N, l) .

illustrated in Fig. 2.3 (d) as red curve). In the simple case of a rotationally symmetric QD ($b_x = b_y$), the eigenenergies can therefore be written as

$$E(n_x, n_y) = \hbar\omega(n_x + n_y + 1) = \hbar\omega(N + 1), \quad (2.1)$$

where $\hbar\omega$ is the ground state energy and n_x, n_y are non-negative integers. The eigenstates of a QD are typically identified by the tuple (N, l) with the principal and angular momentum quantum numbers $N = n_x + n_y$ and $l = n_x - n_y$, respectively. Sets of eigenstates of constant N are degenerate with respect to l and commonly referred to as s -, p -, d -shell for $N = 0, 1, 2$, as N is related to the number of azimuthal nodes. Up to this point, we implicitly bypassed the description of holes and only considered electrons moving within the conduction band. Localized states of holes are obtained in the same manner taking the inverted structure of the valance band as confining potential [blue curve, Fig. 2.3 (d)].

As electrons and holes are fermions, each shell can be occupied by up to two excitons, although for moderate excitation powers the only relevant states exhibit a single exciton (spectroscopic notation X) or two excitons (XX or X₂). The latter is typically referred to as biexciton. Furthermore, it is possible that an exciton coexists with a single electron or hole in the s -shell. These states are called negative trion (X⁻) and positive trion (X⁺), respectively. In the present work, we only encounter emission from the recombination of excitons and trions in the ground state, as the relaxation of excitons from higher shells to the s -shell is fast (1 - 100 ps) compared to the recombination dynamics (100 ps - 1 ns).

To establish selection rules governing the relevant optically active transitions in QDs, it is necessary to understand the angular momentum of excitons, which we briefly review in the following: due to spin-orbit coupling, electron and hole states are best described by a total angular momentum quantum number j . As the conduction band accommodates electrons in s -like states, they are associated with an angular momentum projection of $j_z = \pm 1/2$, where z refers to an arbitrary preferential direction. The valence band, on the other hand, exhibits p -like states, of which holes occupy the subset with a total angular momentum of $3/2$. Their projections $j_z = \pm 1/2$ and $\pm 3/2$ are accompanied with differing effective masses, resulting in the distinction of light and heavy holes, respectively. Both are degenerate for vanishing crystal momentum. The degeneracy is lifted, however, due to material strain inherent to InAs QDs, which causes the holes to be predominantly heavy with $j_z = \pm 3/2$. Considering the angular momentum of both electrons and holes, we find that excitons can have overall angular momentum projections of ± 1 and ± 2 , where the latter is optically inactive and accordingly called a dark exciton. Bright excitons with a projection of ± 1 , on the other hand, emit circularly polarized photons. However, this only holds for rotationally symmetric QDs with $b_x = b_y$ [compare Fig. 2.3 (b)]. For the more general case of $b_x \neq b_y$, both projections with ± 1 mix due to exchange-interaction between electron and hole leading to a fine-structure splitting of the emission line with each component emitting linearly polarized light [174, 175]. For InAs QDs the fine-structure splitting is around 10-100 μeV , which is approximately 2 orders of magnitude smaller than the separation between the respective exciton

and biexciton transitions (a few meV) [162, 163]. Furthermore, the individual fine-structure components possess orthogonal linear polarization along the principal axes of the QD. Note that the fine-structure splitting vanishes for trions, as the single electron or hole spin prohibits the necessary superposition state of the exciton following the Pauli exclusion principle (also refer to the more detailed discussion in Sect. 6.2.1).

2.1.3 Excitation Schemes

Although excitons can be generated electronically by applying DC voltages across the QD, optical excitation schemes are often preferable, in particular when Fourier-limited single photons are required. Depending on the energy of the excitation light three regimes are distinguished, namely non-resonant, quasi-resonant, and resonant excitation. In the first case the excitation photon energy is sufficient to lift an electron from the valence to the conduction band of the barrier material leaving a hole behind, as illustrated in Fig. 2.4. In subsequent phonon-assisted processes, the charge carriers relax to the band-edge, are captured by the QD into an excited bound state, and relax to the s -shell. In a final recombination step, a single photon is released with an energy below the excitation light. Non-resonant excitation is convenient, as excitation and emission light are easily separated by spectral filtering and the excitation wavelength does not need to be tuned to specific transitions of the QD. It is detrimental, however, for the coherence properties of the emitted photons, as the additional relaxation steps add a jitter to the emission time and induce dephasing. Moreover, the non-resonant excitation creates an excess of free

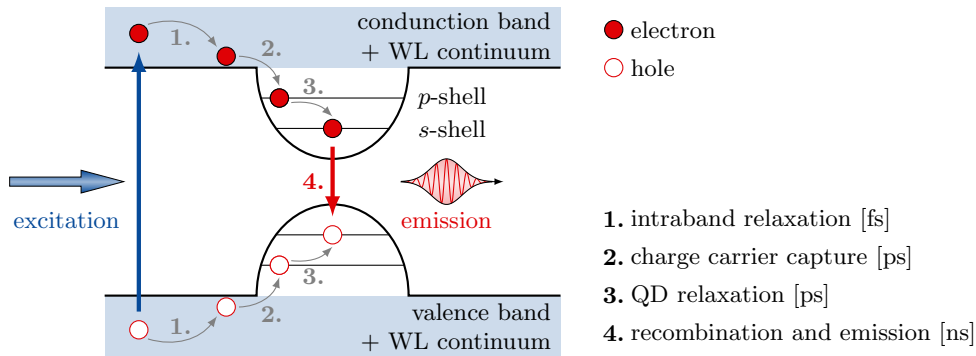


Figure 2.4. Non-resonant optical excitation and emission from a quantum dot. The excitation laser lifts an electron from the valence band to the conduction band in vicinity of the quantum dot and leaves a hole behind. Electron and hole subsequently relax to the band edge (1. step, fs-timescale) and are captured by the quantum dot (2. step, ps-timescale). The exciton now relaxes to the ground-state (3. step, ps-timescale) and eventually recombines emitting a single photon (4. step, ns-timescale).

charge carriers. As a consequence, the QD typically captures more than a single exciton at a time, whose mutual interactions significantly complicate temporal and spectral properties of the emitted light. Additionally, the electrostatic environment of the QD is destabilized by the excess charges, which leads to spectral line broadening and further deteriorates the coherence of the emitted photons (cf. Sect. 2.2). Both time-jitter and line broadening can be reduced using resonant excitation schemes. Although resonant generation of excitons in the s -shell leads to the best achievable coherence properties, it is inconvenient in practice as spectral separation of excitation and emission is impossible. Instead techniques that rely on polarization suppression or spatial separation of excitation light must be employed [130, 176, 177] (see also Sect. 6.2.1). Quasi-resonant excitation constitutes a valuable trade-off: Resonantly addressing excitons in the p -shell prevents charge-carriers from being generated close to the QD, significantly decreasing unwanted line-broadening. Although the time-jitter is not completely removed, spectral separation of excitation and emission is still possible, making quasi-resonant excitation a compelling and often employed method, e.g. in the scope of Sect. 5.1.1. Eventually, we like to mention a scheme, in which the excitation laser is tuned to an energy of $(E_X + E_{XX})/2$ with E_X and E_{XX} being the binding energies of exciton and biexciton, respectively. The laser is in resonance with neither of them, but the absorption of two photons simultaneously creates two excitons, lifting the QD directly into a biexciton state [178]. This method is particularly interesting for the coherent generation of polarization-entangled photon pairs from the radiative cascade of a decaying biexciton [141, 143].

Furthermore, the excitation laser can be operated in continuous wave (cw) or pulsed mode. The latter is of central importance for the *on-demand* generation of single-photons [159], or more specifically their emission at a well-defined time. As the experiments presented here require the synchronization of two independently emitted photons, all experiments are performed under pulsed excitation.

2.2 Mechanisms of Spectral Line Broadening

Solid state emitters in general and semiconductor QDs in particular are not closed systems, but subject to various interactions with their environment. Some of those effects can be exploited in the operation of QDs, such as the aforementioned phonon assisted carrier capture and transitions between excitonic states. More often than not, however, they are associated with declining optical properties of the emitter. For instance, the coupling to optical phonons leads to distinct phonon sidebands, while acoustic phonons add a broad band around the zero phonon line (ZPL) [179, 180]. Furthermore, an elastic Raman-scattering process involving two acoustic phonons broadens the ZPL itself [126, 127]. An often encountered noise source is the coupling between

a QD and charges trapped nearby via fluctuating electrical fields [128, 129]. This noise typically occurs at low frequencies, but with a large amplitude, and therefore leads to significant inhomogeneous broadening of the ZPL. Similarly, random spin flips of nuclei in the vicinity of the QD appear as fluctuating magnetic fields, which potentially depolarize single electron spins [129, 181] and thereby impair the application of QDs as spin qubits.

As we will see in the upcoming sections, the contrast of two-photon interference (TPI) crucially depends on the spectral properties of the emitted photons and approaches unity only in the Fourier limit. Assessing the outcome of a TPI experiment therefore requires a profound understanding of spectral line shapes and the closely related optical coherence. On that note, we here offer an approach to the formal description of homogeneously and inhomogeneously broadened ZPLs. Despite their relevance in terms of indistinguishability, we do not cover the influence of phonon sidebands [182, 183], as they have been mostly removed by spectral filtering throughout all experiments presented in this work.

2.2.1 Timescales of Frequency Fluctuations

To get a first insight into the impact of frequency fluctuations on emission spectra, we outline a few results of the stochastic theory of line shapes, also known as *Kubo model* [184, 185], guided by the reviews presented in [186, 187]. Therein, the momentary frequency $\nu(t)$ of an arbitrary light emitting system is resolved in its mean frequency $\nu_0 = \langle \nu(t) \rangle$ and a fluctuating term $\delta\nu(t)$ according to

$$\nu(t) = \nu_0 + \delta\nu(t) \quad \text{with} \quad \langle \delta\nu(t) \rangle = 0. \quad (2.2)$$

Here $\langle \cdot \rangle$ denotes the time average. As $\delta\nu(t)$ stems from *random* fluctuations, its time dependency is not explicitly known. Most underlying processes, however, can be modeled by an interaction of the emitter with a large number of random fluctuators, as we will discuss in some more detail in Sect. 2.2.3. In this case $\nu(t)$ explores a normally distributed frequency region centered around ν_0 , which is a direct consequence of the central limit theorem [188, 189]. It follows that the frequency correlation function $C_{\delta\nu}(\tau) = \langle \delta\nu(t) \delta\nu(t + \tau) \rangle$ exponentially decays according to

$$C_{\delta\nu}(\tau) = \sigma^2 \cdot \exp(-|\tau|/\tau_c), \quad (2.3)$$

where σ is the standard deviation of the underlying normal distribution and τ_c the correlation time of the fluctuations. The correlation function $C_{\delta\nu}(\tau)$ yields information on how long the system can memorize its history, i.e. for $\tau \gg \tau_c$ the momentary frequency is not anymore correlated with the initial frequency. Although we are interested in photons spontaneously emitted from

an excited two-level system, it is instructive to first consider a continuously emitting light source, described by the wave function

$$\zeta(t) = \zeta_0 \cdot \exp[i 2\pi\nu(t) t]. \quad (2.4)$$

In this case, Eq. (2.3) can be used to compute the auto-correlation of $\zeta(t)$, often referred to as optical coherence function, which reads

$$\begin{aligned} g^{(1)}(\tau) &= \frac{\langle \zeta(t) \cdot \zeta^*(t + \tau) \rangle}{\langle \zeta(t) \cdot \zeta^*(t) \rangle} \\ &= \exp\{i 2\pi\nu_0 \tau - \sigma^2 \tau_c^2 [\exp(-|\tau|/\tau_c) + |\tau|/\tau_c - 1]\}. \end{aligned} \quad (2.5)$$

Following the Wiener-Khinchin theorem, the coherence function is linked to the power spectral density $S(\nu)$ (PSD, or short *spectrum*) via a Fourier transformation according to

$$S(\nu) = \mathcal{F}[g^{(1)}(\tau)](\nu) = \frac{1}{\sqrt{2\pi}} \cdot \int_{-\infty}^{+\infty} g^{(1)}(\tau) \cdot e^{-i 2\pi\nu\tau} d\tau. \quad (2.6)$$

As illustrated in Fig. 2.5, the resulting optical coherence and PSD are best categorized comparing the amplitude of frequency fluctuations σ to their decay rate τ_c^{-1} . Here, we find three different regimes:

(i) For short correlation times, i.e. $\tau_c \ll \sigma^{-1}$, the frequency rapidly fluctuates [Fig. 2.5 (b)] causing a fast collapse of the frequency correlation [Fig. 2.5 (a)]. In this limit the optical coherence goes over to an exponential decay

$$g^{(1)}(\tau) = \exp(i 2\pi\nu_0 t - \Gamma^* |\tau|) \quad \text{with} \quad \Gamma^* = 4\pi^2 \sigma^2 \tau_c. \quad (2.7)$$

Via Fourier transformation (2.6), we find that the spectrum is given by a Lorentzian peak according to [Fig. 2.5 (c), red]

$$S(\nu) = \sqrt{\frac{2}{\pi}} \cdot \frac{\Gamma^*}{4\pi^2 (\nu - \nu_0)^2 + \Gamma^{*2}}. \quad (2.8)$$

Note that the spectrum is narrower than the available frequency range. This is a consequence of the fast relaxation after any perturbation and commonly known as *motional narrowing*, first observed in nuclear magnetic resonance experiments with hydrogen gas [190], but also relevant for QD emission [191]. As these rapid fluctuations affect every photon in a uniform manner, the Lorentzian line shape is typically called homogeneously broadened.

(ii) In the intermediate regime $\tau_c \approx \sigma^{-1}$, the frequency noticeably fluctuates, but too slow to adopt every available value of the distribution during σ^{-1} [Fig. 2.5 (e)]. As a result, the spectrum is broadened compared to (c), yet narrower than the overall distribution [Fig. 2.5 (f)]. This will be discussed in more detail in Sect. 2.2.3.

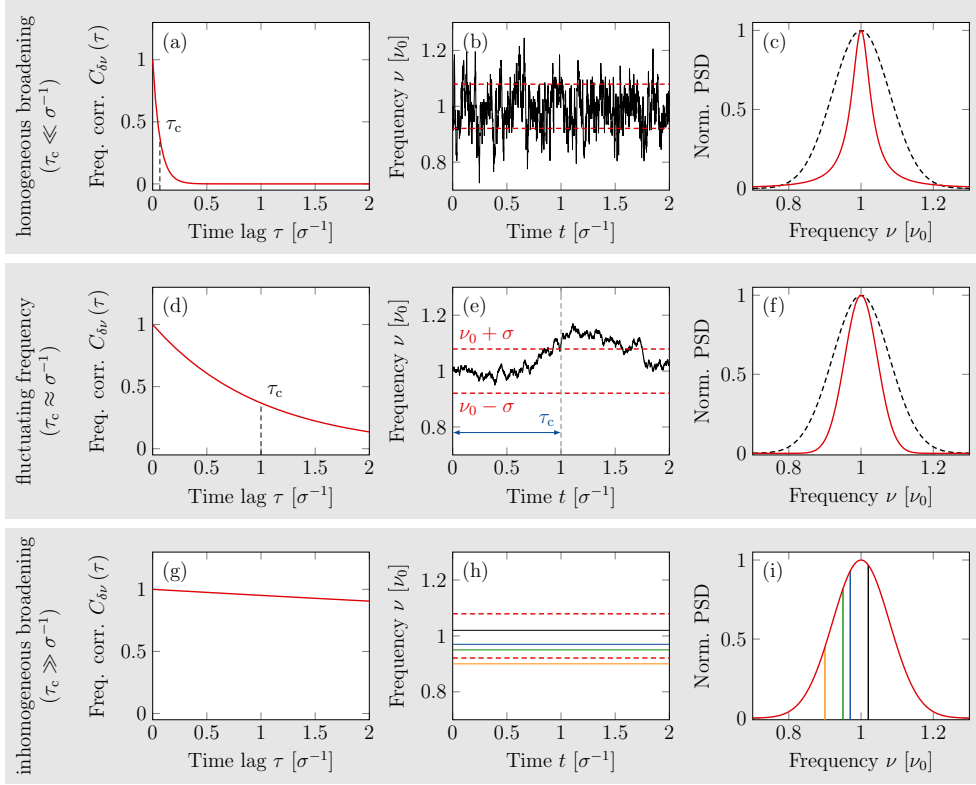


Figure 2.5. Impact of frequency fluctuations on emission spectra. The emitter explores a normally distributed frequency space [black dashed line in (c) and (f)]. Its standard deviation σ is illustrated as red dashed line in (b), (e), and (h). Three cases are considered comparing the frequency correlation time τ_c to σ^{-1} leading to different frequency correlations [(a), (d), and (g)] and emission lines [red in (c), (f), and (i)]. For details cf. main text. Adapted with permission from [186].

(iii) The last case corresponds to $\tau_c \gg \sigma^{-1}$, in which the optical coherence takes on a Gaussian shape reading

$$g^{(1)}(\tau) = \exp(i2\pi\nu_0 t - 2\pi^2\sigma^2 t^2). \quad (2.9)$$

This regime stands out due to a highly inert relaxation of a perturbed emitter. As a result its emission frequency remains quasi-stationary over a long time [Fig. 2.5 (h)]. For ensembles of many emitters, this implies that at any time the probability to find an emitter at frequency ν equals the PSD [Fig. 2.5 (i)]

$$S(\nu) = \frac{1}{\sqrt{2\pi}\sigma^2} \cdot \exp\left[-\frac{(\nu - \nu_0)^2}{2\sigma^2}\right]. \quad (2.10)$$

As the overall line shape is a consequence of every emitter being in a differently perturbed state, it is said to be inhomogeneously broadened. Under

the assumption of our single QD being an ergodic system, the inhomogeneous broadening (2.10) describes the frequency distribution of a large number of consecutively emitted photons, where each individual photon exhibits a constant frequency throughout its lifetime.

We like to conclude with some notes on the nomenclature: All three discussed cases are limits of the same phenomenon, called spectral diffusion (SD). In the research field of quantum emitters it became a custom, however, to associate SD with slowly varying emission frequencies, i.e. the latter two cases. The opposite limit of homogeneous broadening, on the other hand, is referred to as pure dephasing (PD) instead. Despite not being accurate in its original sense, we conform with this standard in the scope of the present work.

2.2.2 Emission from a Perturbed Two-Level System

The considerations of the preceding section have two shortcomings regarding our requirements. First, realistic single photons have a finite lifetime in contrast to Eq. (2.4), leading to a finite spectral linewidth even in absence of perturbations. Furthermore, the notion of a single correlation time τ_c separating homogeneous from inhomogeneous broadening suggests that both limits cannot simultaneously affect the emitted photons. It is common, however, that the underlying noise spectrum is broadband [129, 133] and covers both regimes [192–195]. Most measurements performed in this thesis are integrated over a time which is (presumably) long compared to any τ_c governing the emitter dynamics. Accordingly, each single photon is homogeneously broadened while the overall measurement averages over the inhomogeneous ensemble distribution, i.e. we must incorporate both limiting cases into our considerations. On that account, we now use the wave-function

$$\zeta(t) = \frac{1}{\sqrt{\tau_r}} H(t) \cdot \exp\{-t/2\tau_r - i[2\pi\nu t + \varphi(t)]\}, \quad (2.11)$$

which models single photons as emitted by a radiative decay from a two-level system with lifetime τ_r and at a constant carrier frequency ν . The Heaviside-function $H(t)$ ensures that the emission process only starts after an initial excitation step at time $t = 0$. The phase term $\varphi(t)$ is introduced to account for phase fluctuations corresponding to homogeneous broadening. The optical coherence is obtained by evaluating

$$g^{(1)}(\tau) = \frac{\int_{-\infty}^{+\infty} \langle\langle \zeta(t) \cdot \zeta^*(t+\tau) \rangle\rangle_{\text{PD}} \rangle_{\text{SD}} dt}{\int_{-\infty}^{+\infty} \langle\langle \zeta(t) \cdot \zeta^*(t) \rangle\rangle_{\text{PD}} \rangle_{\text{SD}} dt}, \quad (2.12)$$

where the necessary averaging over the entire time trace in Eq. (2.5) was substituted by a time-integral covering only a single photon and two ensemble averages corresponding to PD and SD. The PD average exploits the expression

$$\langle \exp[i\varphi(t+\tau) - i\varphi(t)] \rangle = \exp(-\Gamma^*|\tau|) \quad (2.13)$$

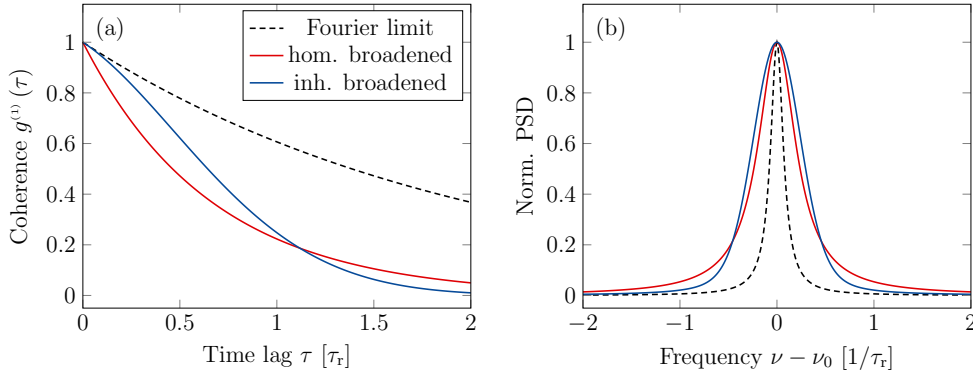


Figure 2.6. Simultaneous impact of homogeneous and inhomogeneous broadening. (a) Optical coherence function and (b) spectra of photons under the influence of pure dephasing and spectral diffusion. Shown is the Fourier limited case (dashed) as well as predominantly homogeneously and inhomogeneously broadened photons (red and blue, resp.). The parameters Γ^* and σ' are chosen such that the overall broadening is $\approx \tau_r^{-1}$. The spectra are evaluated using the Faddeeva function.

found in [196] with Γ^* being the pure dephasing rate. To account for SD the static carrier frequency ν is weighted based on the distribution Eq. (2.10). The evaluation of Eq. (2.12) is detailed in the supplement of [197] and yields

$$g^{(1)}(\tau) = \exp [i 2\pi\nu_0 t - 2\pi^2\sigma^2\tau^2 - |\tau|(1/2\tau_r + \Gamma^*)]. \quad (2.14)$$

Besides an oscillation at the central frequency ν_0 , the first order coherence function is determined by two contributions. The term linear in τ corresponds to homogeneous broadening and now includes the natural linewidth $1/2\tau_r$ besides the pure dephasing rate. The quadratic term on the other hand stems from SD and contains the inhomogeneous linewidth σ . To assess the optical coherence of the emitted photons, it is common to state the coherence time τ_{coh} , which is defined as half the $1/e$ -width of $|g^{(1)}(\tau)|$ and reads

$$\tau_{\text{coh}} = -\frac{2 \ln 2}{\pi^2} \cdot \frac{\Gamma_h}{\sigma'^2} + \sqrt{\left(\frac{2 \ln 2}{\pi^2} \cdot \frac{\Gamma_h}{\sigma'^2}\right)^2 + \frac{4 \ln 2}{\pi^2 \cdot \sigma'^2}}. \quad (2.15)$$

Here, we introduced the full width at half maximum (FWHM) of the inhomogeneous linewidth distribution $\sigma' = 2\sqrt{2 \ln 2} \sigma$ as well as the homogeneous linewidth $\Gamma_h = 1/2\tau_r + \Gamma^*$. Note that the FWHM of the homogeneous contribution is given by Γ_h/π . In order to obtain the PSD, the Fourier transformation (2.6) needs to be solved. Using the substitutions $a(\tau) = \exp(-\Gamma_h|\tau|)$ and $b(\tau) = \exp(-2\pi^2\sigma^2\tau^2)$ as well as the Fourier-convolution theorem we find

$$\begin{aligned}
S(\nu) &= \mathcal{F}[a(\tau) \cdot b(\tau)] [2\pi(\nu - \nu_0)] \\
&= \frac{1}{\sqrt{2\pi}} \cdot \mathcal{F}[a(\tau)] [2\pi\nu] * \mathcal{F}[b(\tau)] [2\pi(\nu - \nu_0)] \\
&= \frac{1}{\sqrt{2\pi}} \cdot \left\{ \sqrt{\frac{2}{\pi}} \cdot \frac{\Gamma_h}{4\pi^2\nu^2 + \Gamma_h^2} \right\} * \left\{ \frac{\exp[-(\nu - \nu_0)^2/2\sigma^2]}{2\pi\sigma} \right\} \\
&= \sqrt{\frac{2\ln 2}{\pi^2}} \cdot \frac{\text{Re}[w(z)]}{\sigma'} \quad \text{with} \quad z = \sqrt{\frac{\ln 2}{\pi^2}} \cdot \frac{2\pi(\nu - \nu_0) + i\Gamma_h}{\sigma'}, \quad (2.16)
\end{aligned}$$

where $*$ denotes the convolution operator. Furthermore, we used the aforementioned Fourier-transformations of $a(\tau)$ and $b(\tau)$ leading to a Lorentzian and Gaussian peak, respectively. The convolution of both yields a Voigt-function, which does not have any analytical solution. It can be expressed, however, in terms of the real part of the Faddeeva function $w(z)$ [198, Chapter 7], which can be evaluated fast and accurately using the algorithms [199, 200]. In Fig. 2.6 (a) the optical coherence function and (b) the emission spectra are illustrated for an arbitrary lifetime τ_r . Shown are the Fourier-limited case (dashed) along with predominantly homogeneously (red) and inhomogeneously (blue) broadened photons. Both model parameters Γ^* and σ' are chosen such that the overall broadening is approximately τ_r^{-1} .

2.2.3 Fluctuator Model

In the course of our TPI experiments using consecutively emitted single photons we will find that the measured indistinguishability is superior compared to what can be expected from the corresponding spectral line width (cf. Sect. 5.3.3). As it turns out, the time lag passing between the respective emission events is below the correlation time of SD. Therefore, the measurement is sensitive to slow fluctuations that did not yet fully unfold, which is incompatible with the corresponding assumption made in Sect. 2.2.2. Put another way, the experiment was performed at the intermediate regime **(ii)** of fluctuating frequencies mentioned in Sect. 2.2.1, which we are treating in the following.

An often used model considers the emitter to be amidst a lattice of $2N$ fluctuators, where each fluctuator i can take on two different states $\xi_i(t) = \pm 1/2$ randomly varying in time t [129, 189, 191, 201]. The state $\xi_i(t)$ can refer to a nuclear spin or also an empty or full charge trapping site (see also Fig. 2.7). Assuming a coupling strength κ_i between the fluctuator and a corresponding degree of freedom σ of the emitter leads to a shift of the emission frequency

$$\Delta\nu = \frac{1}{2\pi\hbar} \cdot \chi(t) \sigma \quad \text{with} \quad \chi(t) = \sum_i \kappa_i \xi_i(t), \quad (2.17)$$

where $\chi(t)$ can be interpreted as a fluctuating (electric or magnetic) field. In what follows, we consider fluctuating trapped charges as an example and

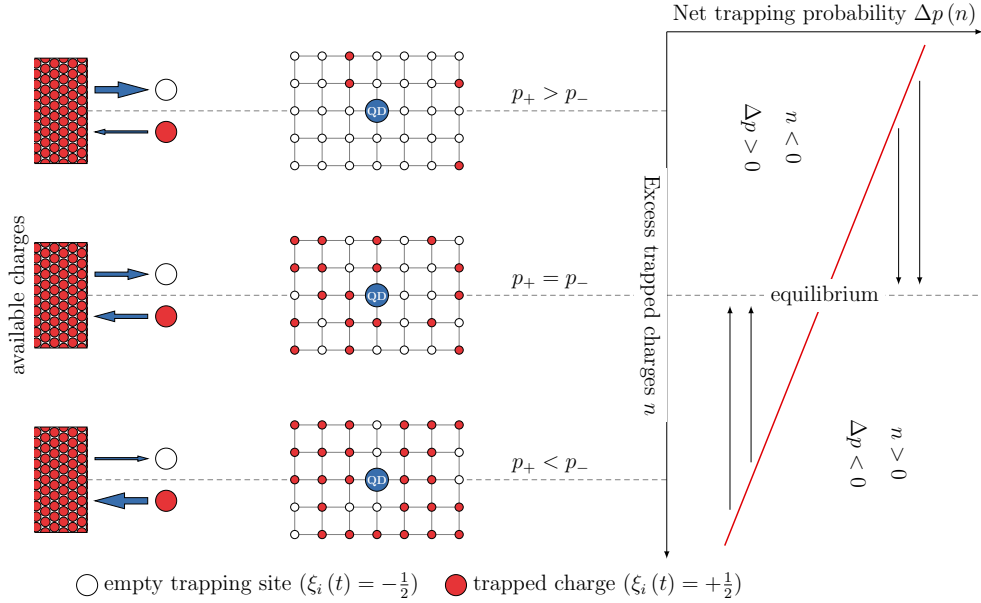


Figure 2.7. Illustration of the fluctuator model. The emitter is within a lattice of fluctuators (red, here exemplary trapped charges) shifting the emission frequency. At each time step τ one fluctuator changes its state. The probabilities of a charge being released and becoming trapped are p_- and p_+ . The net trapping probability $\Delta p = p_+ - p_- = -n/N$ is linear in the number of excess trapped charges n , which follows from simple combinatorial considerations. As a result, the system is always driven towards an equilibrium at $p_+ = p_- = 1/2$.

simplify the problem by **(i)** using a uniform coupling strength $\kappa_i = \kappa$ for all fluctuators and **(ii)** assuming equal capture and escape rates for each charge. In this case, the fluctuations in $\chi(t)$ are merely determined by the number of trapped charges and each charge induces the same frequency shift $\delta\nu = \kappa\sigma/2\pi\hbar$. Consider a time step τ , in which exactly one trapping site changes its state. If there are initially $N + n$ filled and $N - n$ empty trapping sites, we find the probabilities

$$p_{\pm} = \frac{N \mp n}{2N} = \frac{1}{2} \left(1 \mp \frac{n}{N} \right) \quad (2.18)$$

of a charge being captured ('+') or released ('-'). The difference between both $\Delta p = p_+ - p_- = -n/N$ can be understood as a net restoring force that is linear in n and drives the system towards a state, in which exactly half of the trapping sites are filled (compare Fig. 2.7 right side)¹. These dynamics do not only remind of Hook's law, but it was indeed shown that the continuous limit

¹Note that this only holds for equal capture and escape rates. The more realistic case of unequal rates leads to a shifted equilibrium, but does not alter our conclusions.

2. FUNDAMENTALS

of the problem ($N \rightarrow \infty$, $\delta\nu \rightarrow 0$, $\tau \rightarrow 0$) corresponds to the Brownian motion of a particle in a harmonic potential, also known as an Ornstein-Uhlenbeck process [202, 203]. Accordingly, the time evolution of the probability density $S_n(n, t)$ to find an excess of n filled trapping sites at time t is obtained by solving the corresponding Fokker-Planck equation. Mapping the problem back from the number of trapped charges to a frequency shift using Eq. (2.17), this equation reads

$$\frac{\partial S}{\partial t} = -\beta \frac{\partial}{\partial \nu} [(\nu - \nu_0) S] + D \frac{\partial^2 S}{\partial \nu^2}. \quad (2.19)$$

Here, the diffusion constant $D = \delta\nu^2/2\tau$ corresponds to the stochastic force and $\beta = 1/N\tau \ll 1/\tau$ indicates strongly overdamped dynamics. The solution of Eq. (2.19) equals our desired PSD and is given by

$$S(\nu, t) = \frac{1}{\sqrt{2\pi\sigma^2(t)}} \cdot \exp\left\{-\frac{[\nu - \nu_c(t)]^2}{2\sigma^2(t)}\right\} \quad \text{with} \quad (2.20)$$

$$\sigma^2(t) = \sigma_0^2 \cdot [1 - \exp(-2\beta t)] \quad \text{and}$$

$$\nu_c(t) = \nu_0 + (\nu' - \nu_0) \cdot \exp(-\beta t).$$

The spectrum is identical to the inhomogeneous SD case given by Eq. (2.10) with the only difference that standard deviation $\sigma(t)$ and central frequency

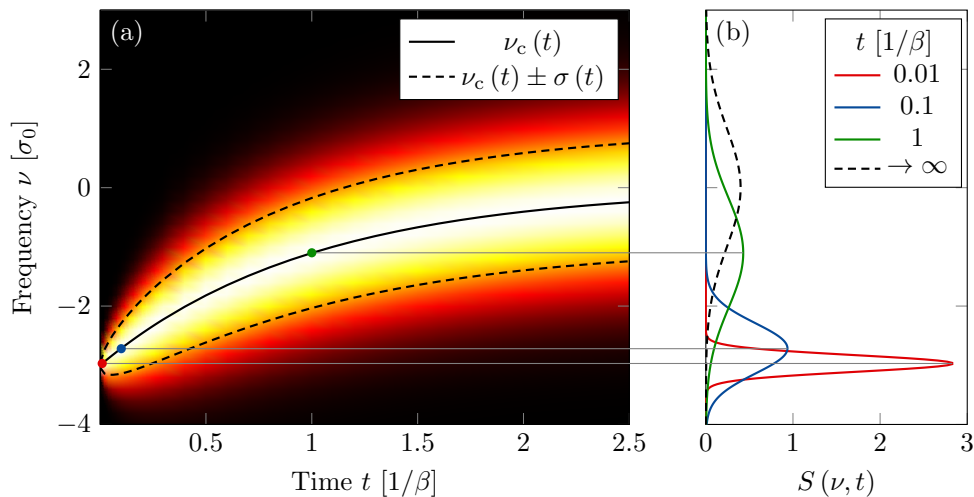


Figure 2.8. Emission spectrum of a perturbed emitter during relaxation towards equilibrium. (a) Time evolution of Power spectral density $S(\nu, t)$, if the system was at an initial emission frequency of $\nu' = -3\sigma_0$. The central frequency slowly converges towards the equilibrium value ν_0 (black solid), while the emission line rapidly broadens (black dashed). (b) Different spectra at discrete times t . The equilibrium is depicted as black dashed line.

$\nu_c(t)$ now exhibit explicit time-dependencies. Thereby it is possible to describe the relaxation dynamics of the emitter via rate β , if it was found at a frequency ν' at time $t = 0$. The time evolution for $\nu' = -3\sigma_0$ is illustrated in Fig. 2.8. It can be seen that the central frequency $\nu_c(t)$ only slowly creeps towards its equilibrium value ν_0 (black solid), while the emission line quickly reaches its full width σ_0 (black dashed).

We here only discussed the shape of the inhomogeneous contribution to the overall emission line. The result can be used, however, to describe an emitter, which is homogeneously broadened at the same time. To that end, it is only necessary to evaluate Eq. (2.16) using $\sigma(t)$ and $\nu_c(t)$. It is also noteworthy that the fluctuator model directly results in a Gaussian frequency distribution and thereby justifies the corresponding initial assumption made in Sect. 2.2.1.

2.3 Nonlinear Optics

A central intention of the presented experiments is to establish an interface between near-infrared wavelengths and the telecom C-band in order to take advantage of both the favorable optical properties of single photons emitted by QDs and the lowest possible transmission losses in optical fibers. To that end the wavelength of the photons is altered via quantum frequency down-conversion (QFDC), being the analogue of a difference frequency generation (DFG) process at the single photon level. In the following, we provide basic information on second-order nonlinear optical processes in general as well as DFG and parametric fluorescence in particular. As all conversion experiments were performed in ridge waveguides (WG) to obtain high conversion efficiencies, we briefly address the computation of fundamental WG modes and the impact of WG dispersion. All remarks concerning general nonlinear optics are based on [92], while information specific to DFG in waveguides are taken from [204].

2.3.1 Three Wave Mixing

The response of matter to external electromagnetic fields is typically described using its susceptibility χ , which connects a time-dependent incident electrical field $\vec{E}(t)$ to the induced polarization $\vec{P}(t)$. In the limit of small intensities the relationship of both quantities is governed by terms linear in the electrical field, which are sufficient to explain phenomena such as dispersion and absorption. For increasing intensities, also higher order terms come into play, giving rise to the regime of nonlinear optics. In case of materials with a lack of inversion symmetry, the leading nonlinear term describes matter polarization

quadratically depending on the electrical field according to

$$P_i^{(2)}(t) = \varepsilon_0 \sum_{jk} \chi_{ijk}^{(2)} E_j(t) E_k(t), \quad (2.21)$$

where (2) refers to the second-order and the indices i , j , and k denote the Cartesian components of the respective fields. Note that the second-order susceptibility connects three components of three different fields and therefore consists of $3^3 = 27$ elements. However, with help of various symmetry considerations regarding the underlying process and material this number can be drastically reduced. In fact, we are only interested in second-order processes mediated by lithium niobate (LN), which exhibits the highest susceptibility for $i = j = k = 3$ [205–208]. In this case all incident fields as well as the generated polarization are directed along the z -axis of the crystal and a single scalar nonlinear coefficient $d_{33} = \chi_{333}^{(2)}/2$ is sufficient to describe the process. Note that d_{33} refers to a commonly used contracted notation of nonlinear coefficients, which can be found in [209]. As we only consider the z -component in the following, we omit the indices of all fields and obtain the expression

$$P^{(2)}(t) = 2\varepsilon_0 d_{33} E^2(t). \quad (2.22)$$

The next step is to specify the electrical input field, which, for the sake of simplicity, is assumed to be only dichromatic according to

$$E(t) = E_1 e^{i\omega_1 t} + E_2 e^{i\omega_2 t} + c.c. \quad (2.23)$$

Plugging Eq. (2.23) into the polarization response (2.22), we find a plethora of different terms, which oscillate at new frequencies ω_3 , namely $\omega_3 = 2\omega_{1,2}$ and $\omega_3 = \omega_1 \pm \omega_2$, as well as a static polarization contribution. According to Maxwell's equations the time-dependent polarization acts as a source of electromagnetic fields, which oscillate at ω_3 as well. As can be seen, a second-order nonlinear susceptibility $\chi^{(2)}$ couples up to three different frequency components of an electrical field, motivating the often used expression *three wave mixing* (TWM). At this point it is worthwhile to visualize the energy exchange between the participating fields using fundamental photon creation and annihilation processes in an energy diagram as depicted in Fig. 2.9. Three processes can occur being second harmonic generation [SHG, (a)], sum frequency generation [SFG, (b)], as well as difference frequency generation [DFG, (c)], corresponding to the aforementioned frequency combinations ω_3 of the output photon. Furthermore, this picture emphasizes that all processes obey energy conservation. In the present work, we exploit the DFG scheme for the desired QFDC: a single input photon at high energy $\hbar\omega_1$ decays into two new photons at lower energies $\hbar\omega_{2,3}$ stimulated by the presence of another photon at $\hbar\omega_2$. Accordingly, we will focus on DFG in the remainder of this section. Also, we will comply with the commonly used nomenclature

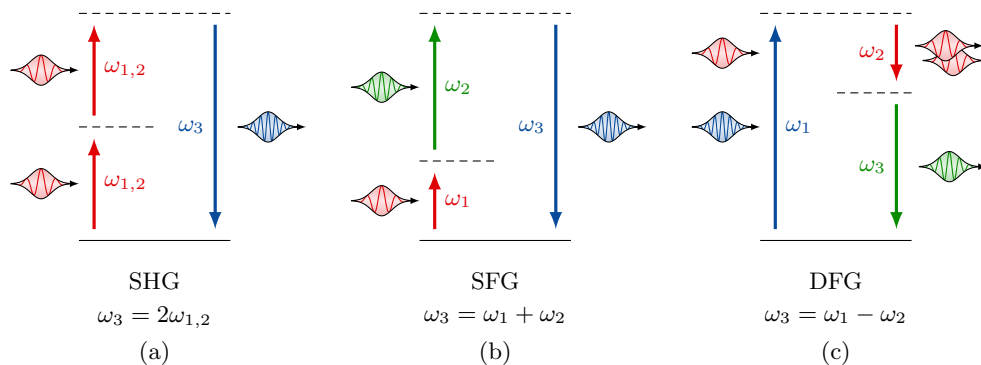


Figure 2.9. Basic three wave mixing processes in the single photon picture.

Depicted are (a) the second harmonic generation (SHG), (b) sum frequency generation (SFG), and (c) difference frequency generation (DFG). In a SHG process 2 photons of equal frequency $\omega_{1,2}$ are annihilated, creating a new photon at double frequency $\omega_3 = 2\omega_{1,2}$. In SFG both input photons exhibit different frequencies $\omega_1 \neq \omega_2$ and the output photon oscillates at the sum frequency $\omega_3 = \omega_1 + \omega_2$. A DFG process on the other hand yields a new photon at the difference frequency $\omega_3 = \omega_1 - \omega_2$ and second photon at ω_2 . Note that for DFG it is always $\omega_1 > \omega_2$.

denoting the fields corresponding to ω_1 , ω_2 , and ω_3 as signal, pump, and idler, respectively.

To obtain quantitative results the ansatz (2.23) is insufficient, as it does not cover the propagation of each wave within the nonlinear material as well as their spatially varying amplitudes due to conversion. To that end, the field can be synthesized by three scalar frequency components $E_i(z, t)$ with $i = 1, 2, 3$, which read

$$E_i(z, t) = A_i(z) \cdot e^{i(k_i z - \omega_i t)} + c.c., \quad (2.24)$$

where the amplitude of each component A_i now explicitly depends on the position along the propagation direction z ². The wavenumbers k_i are connected to the respective frequencies via the dispersion relation $ck_i = n_i \omega_i$ with c the speed of light and n_i the refractive index of the medium at frequency ω_i . Furthermore, according to a DFG process the idler frequency is given by $\omega_3 = \omega_1 - \omega_2$. Using Eq. (2.24) in Maxwell's equation including the

²Note that the propagation direction z does not coincide with the aforementioned crystal's z -axis. Instead, both are perpendicular with respect to each other.

second-order polarization yields the coupled mode equations

$$\begin{aligned}\frac{\partial A_1(z)}{\partial z} &= -i \kappa_1 A_2(z) A_3(z) e^{+i \Delta k' z}, \\ \frac{\partial A_2(z)}{\partial z} &= -i \kappa_2 A_1(z) A_3^*(z) e^{-i \Delta k' z}, \quad \text{and} \\ \frac{\partial A_3(z)}{\partial z} &= -i \kappa_3 A_1(z) A_2^*(z) e^{-i \Delta k' z},\end{aligned}\tag{2.25}$$

whose solution describes the evolution of all field components along the propagation direction. Here we introduced the coupling constants $\kappa_i = 2\omega_i d_{\text{eff}} / (n_i c)$, where d_{eff} is the effective nonlinear coefficient ($d_{\text{eff}} = d_{33}$ in our case). An important quantity is the phase mismatch

$$\Delta k' = k_1 - k_2 - k_3,\tag{2.26}$$

which indicates how close a given DFG process is to momentum conservation. Only in case of $\Delta k' = 0$ the secondary wavelets generated at each position within the nonlinear material interfere in phase, thereby leading to a significant converted output field. To illustrate that, consider a DFG process in a nonlinear material of length L . If the signal and pump input intensities $I_{1,2}^0$ are strong compared to the output intensity of the idler field $I_3(L)$, we can approximate $I_{1,2}(z) \approx I_{1,2}^0$ and obtain via integration of Eq. (2.25)

$$I_3(L) \propto \kappa_3^2 \cdot I_1^0 I_2^0 \cdot L^2 \text{sinc}^2\left(\frac{\Delta k' L}{2}\right),\tag{2.27}$$

which is shown as red curve in Fig. 2.10 (a). Consider first case 1: $\Delta k' = 0$ implies that the momentum is conserved [compare vector diagram in (c)] and we obtain the highest possible output intensity of the idler field. However, due to dispersion, energy and momentum are in general not simultaneously conserved. Instead, for a given process, we typically find a remaining net momentum $\Delta k' \neq 0$ and end up with an inefficient conversion (case 2).

An established way to encounter this issue is known as quasi-phasematching (QPM). Considering the given case of LN as material platform, the second-order susceptibility can be connected to a permanent polarization \vec{p}_{LN} of the crystal, which defines an anisotropy axis and thereby a directionality of the nonlinear coefficient d_{33} [see white arrows in Fig. 2.10 (b)]. If the sign of the polarization \vec{p}_{LN} and accordingly d_{33} is periodically flipped with a grating period Λ ³, the crystal will absorb an additional momentum given by $K = 2\pi/\Lambda$. The output intensity now follows the modified phase mismatch relation

$$I_3(L) \propto L^2 \text{sinc}^2\left(\frac{\Delta k L}{2}\right) \quad \text{with} \quad \Delta k = \Delta k' - K\tag{2.28}$$

³Remarks on the practical implementation of periodic poling of LN crystals will be provided in Sect. 4.1.1.

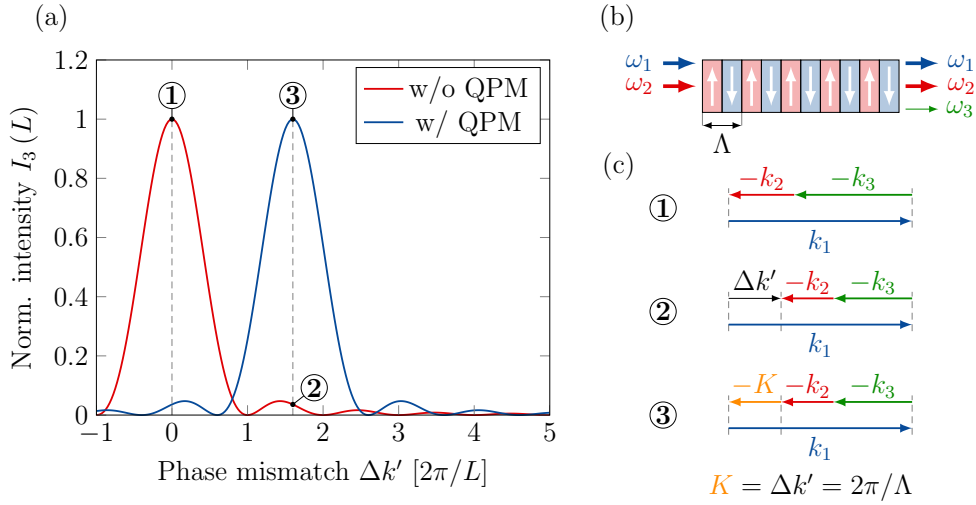


Figure 2.10. Conversion efficiency depending on the phase mismatch. An efficient conversion is generally only possible if the phase mismatch $\Delta k' = k_1 - k_2 - k_3$ vanishes as in case 1 [see red curve in (a) and momentum diagram in (c)]. If $\Delta k' \neq 0$ (case 2), the underlying process does not fulfill momentum conservation and is therefore inefficient. With help of quasi-phasing (QPM), the anisotropy axis of the crystal is periodically flipped with a grating period $\Lambda = \Delta k'/2\pi$ [see (b)]. The crystal then compensates the net momentum, leading to a shifted phase mismatch curve (blue) and thereby enabling efficient conversion (case 3).

shown as blue curve in Fig. 2.10 (a). Case 3 illustrates that even conversion processes with $\Delta k' \neq 0$ can meet the phase matching condition $\Delta k = 0$ with help of QPM, provided an appropriately chosen Λ .

2.3.2 Difference Frequency Generation in Waveguides

Maximizing the photon-to-photon conversion efficiency is naturally a central objective in the converter design. Although our previous discussion assumes no depletion of the signal field and therefore corresponds to the limit of small efficiencies, it is possible to identify available tuning knobs from Eq. (2.27). On one hand the output intensity I_3 scales with L^2 , but besides being unpractical, an increasing crystal length limits the attainable efficiency due to transmission losses. Another option is to increase the pump intensity I_2^0 , which is typically accomplished by minimizing the cross section of the participating light fields, more specifically by performing the conversion in optical WGs.

The WGs employed in the present work are of rectangular cross section. Although there is no exact analytical solution of the guided modes, an analytical approximation can be obtained following the method described in [210,211]. Therein, the WG and its environment is segmented into 5 differ-

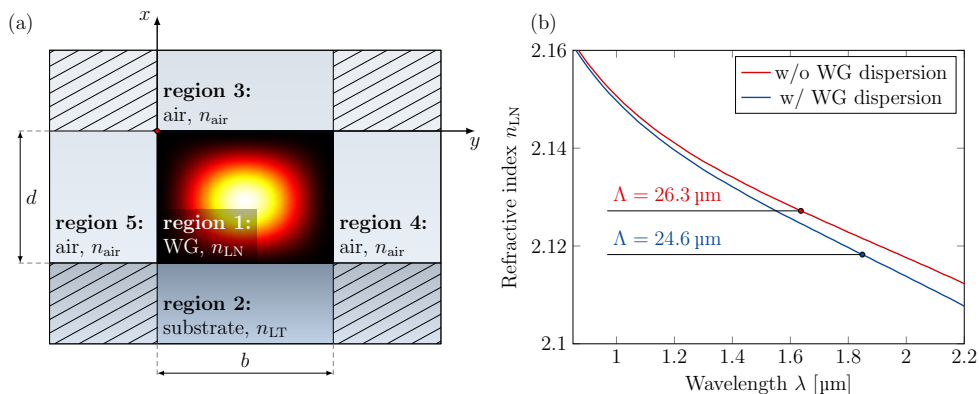


Figure 2.11. Fundamental mode of a waveguide with rectangular cross section. (a) Geometry used for an approximate solution according to the method presented in [210, 211]. The cross section is divided into 5 regions: region 1 is the waveguide (WG) with width b and height d , here made of lithium niobate (LN). Region 2 corresponds to the substrate [here lithium tantalate (LT)] and region 3-5 describe the surrounding air. (b) Comparison of the refractive index of LN without (red) and with WG dispersion (blue). The indicated quasi-phases-matching periods Λ correspond to the DFG process defined by $1/905 \text{ nm} - 1/2175 \text{ nm} = 1/1550 \text{ nm}$.

ent regions as shown in Fig. 2.11 (a). We are only interested in the solution describing the mode in region 1, which corresponds to the core of the WG with width b and height d . Furthermore, for DFG in LN we can restrict the solution to its vertically polarized contribution defined by the field components

$$\begin{aligned}
 E_x &= \frac{i A}{\kappa_x \beta} (n_1^2 k^2 - \kappa_x^2) \sin[\kappa_x (x + \xi)] \cos[\kappa_y (y + \eta)] \quad \text{and} \\
 H_y &= i A \sqrt{\frac{\varepsilon_0}{\mu_0}} n_1^2 \frac{k}{\kappa_x} \sin[\kappa_x (x + \xi)] \cos[\kappa_y (y + \eta)], \quad (2.29)
 \end{aligned}$$

where n_1 is the refractive index of the material in region 1 and k the vacuum wavenumber of the field, whose eigenmodes we intend to find. While A is a free scaling parameter, the transversal wavenumbers κ_x and κ_y as well as the mode's displacement defined by ξ and η must be determined considering the materials and dimensions of the WG and its environment, which is detailed in Appx. A. For our purpose it is important to realize that the confinement of the field entails finite κ_x and κ_y even for the fundamental mode. The propagation constant

$$\beta = \sqrt{n_1^2 k^2 - \kappa_x^2 - \kappa_y^2} \quad (2.30)$$

can then be used to obtain an effective refractive index $n_{\text{eff}} = \beta/k$, which accounts for WG dispersion besides material dispersion. Consequently, the

phase mismatch relation given in Eq. (2.28) must be replaced according to

$$\Delta k \rightarrow \Delta\beta = \beta_1 - \beta_2 - \beta_3 - \frac{2\pi}{\Lambda}. \quad (2.31)$$

To illustrate that WG dispersion has a tremendous impact on the design of QPM poling periods, we calculate the fundamental mode for the WG employed in the present work, i.e. we assume $d = 10 \mu\text{m}$ and $b = 10.8 \mu\text{m}$ (cf. Sect. 4.1.1 for WG dimensions) as well as the refractive indices of LN as WG material [212], lithium tantalate (LT) as substrate [213] and air for regions 3-5 [214] at a temperature of 25°C . The intensity of the fundamental mode is given by the z -component of the Poynting vector reading

$$S_z = \frac{1}{2} \text{Re} [E_x H_y^* - E_y H_x^*] = \frac{1}{2} E_x H_y^*, \quad (2.32)$$

which is depicted for a wavelength of 905 nm in region 1 of Fig. 2.11 (a). The refractive index of LN based on [212] is plotted in Fig. 2.11 (b) (red curve) and compared to the effective index including WG dispersion (blue curve) in a range from 850 nm to 2200 nm . In the present work, we are concerned with a DFG process converting light at 905 nm to the telecom C-band at 1550 nm , which requires a pump field at 2175 nm . Considering only material dispersion results in a QPM period of $\Lambda = 26.3 \mu\text{m}$. On the contrary, taking WG dispersion into account yields $\Lambda = 24.6 \mu\text{m}$. In Sect. 4.2 we will see that this is indeed a vast deviation, as even an offset of as few as 100 nm in the poling period can hardly be compensated by temperature tuning of the LN crystal.

The second major modification of the coupled mode equations (2.25) in the regime of DFG in waveguides affects the coupling constants κ_i . In contrast to plane waves, the amplitude of guided modes changes within the transversal plane. This can be accounted for by substituting the coupling constants with a spatial average according

$$\begin{aligned} \kappa_1 &= \frac{\omega_1 \varepsilon_0 d_{\text{eff}}}{2} \int_0^b \int_{-d}^0 \mathcal{E}_{x1}^*(x, y) \mathcal{E}_{x2}(x, y) \mathcal{E}_{x3}(x, y) dx dy \\ \text{and } \kappa_1/\omega_1 &= \kappa_2^*/\omega_2 = \kappa_3^*/\omega_3, \end{aligned} \quad (2.33)$$

where $\mathcal{E}_{xi}(x, y)$ refers to the field (2.29) of frequency component i normalized to unit power.

Due to the spatial confinement, the field amplitudes $A_i(z)$ in Eq. (2.25) are significantly enhanced, enabling to achieve high conversion efficiencies even for moderate pump intensities I_2^0 . For the conversion of single photons, we certainly have $I_2^0 \gg I_3(z)$ as well as $I_2^0 \gg I_1(z)$, i.e. we can still assume $I_2^0 \approx \text{const}$. However, we must allow the signal field to deplete by considering an explicit dependency on z according to $I_1(z)$. The coupled mode equations can

now be solved to obtain the output power P_3 of the idler field, which reads

$$P_3(P_2) = P_1 P_2 \kappa_3^2 L^2 \cdot \text{sinc}^2 \left(\sqrt{\frac{\omega_1}{\omega_2} \kappa_3^2 P_2 + \Delta\beta^2/4} \cdot L \right), \quad (2.34)$$

where P_1 and P_2 are the optical input powers of signal and pump, respectively. Using the photon flux $\Phi_i = P_i/(\hbar\omega_i)$, we are able to define the photon-to-photon conversion efficiency η for a quasi-phasematched process ($\Delta\beta = 0$) as

$$\eta(P_2) = \frac{\Phi_3(P_2)}{\Phi_1} = \sin^2 \left(\sqrt{\frac{\omega_1}{\omega_2} \kappa_3^2 P_2} \cdot L \right). \quad (2.35)$$

In experiment, the ideal conversion efficiencies of $\eta(P_2) = 1$ cannot be achieved due inevitable transmission losses or fabrication errors of the QPM poling period. Furthermore, the coupling constant κ_3 is not accurately known. Therefore, measurements of the conversion efficiency are typically fitted using the model function

$$\eta(P_2) = \eta_{\max} \sin^2 \left(\sqrt{\kappa_{\text{norm}} P_2} \cdot L \right) \quad (2.36)$$

instead, where the fitting parameters η_{\max} and κ_{norm} correspond to the maximum attainable efficiency and a normalized coupling constant, respectively.

We like to conclude with remarks on parametric fluorescence. The coupled mode equations (2.25) suggest that nonlinear optical processes of second order only work with at least two input fields. However, as we will investigate in Sect. 4.2, a spectrally broad optical output can be observed at the idler wavelength, even if the nonlinear crystal was only fed with a signal field at input power P_1 . This so-called parametric fluorescence, also known as spontaneous parametric down-conversion (SPDC), corresponds to a decay of the signal field and originates from vacuum fluctuations creating virtual photons that are subsequently amplified via DFG. The spectral distribution of the optical output is therefore given by the gain of the virtual photons due to parametric amplification in the limit of no signal depletion, which reads [204]

$$D(\Gamma, \Delta\beta) = \Gamma^2 L^2 \left| \frac{\sinh \left(\sqrt{\Gamma^2 - \Delta\beta^2/4} \cdot L \right)}{\sqrt{\Gamma^2 - \Delta\beta^2/4} \cdot L} \right|^2 \quad (2.37)$$

with $\Gamma^2 = (\omega_2 \omega_3 / \omega_1^2) |\kappa_1|^2 P_1$.

2.4 Two-Photon Quantum Interference

All experiments presented within this thesis revolve around the coalescence of two indistinguishable photons at a beam splitter (BS), being derivations of

the famous Hong-Ou-Mandel (HOM) experiment [60]. The coalescence relies on phase-insensitive destructive interference between both photons and can therefore not be explained in a purely classical framework. Accordingly, it is often referred to as *quantum* interference. In this section, we first revisit a standard introductory approach to TPI emphasizing its two-photon nature [215, 216]. Thereafter, a formal description of HOM experiments in the time-domain is established based on [217, 218], which is then used to shed light on the concept of indistinguishability as well as the frequently encountered HOM-dip and quantum beats.

2.4.1 Photon Coalescence

The basic situation of a HOM experiment is depicted in Fig. 2.12. Considered is a symmetric BS with input ports a and b , where symmetric refers to equal reflectivity R and transmittance T , i.e. $R = T = 1/2$. Each input port is fed with a single photon, here shown in red and blue. The photons are labeled with the numbers i and j , which might refer to a certain degree of freedom or even their entire quantum state. Using the respective creation operators \hat{a}_i^\dagger and \hat{b}_j^\dagger it is possible to write the input Fock state as

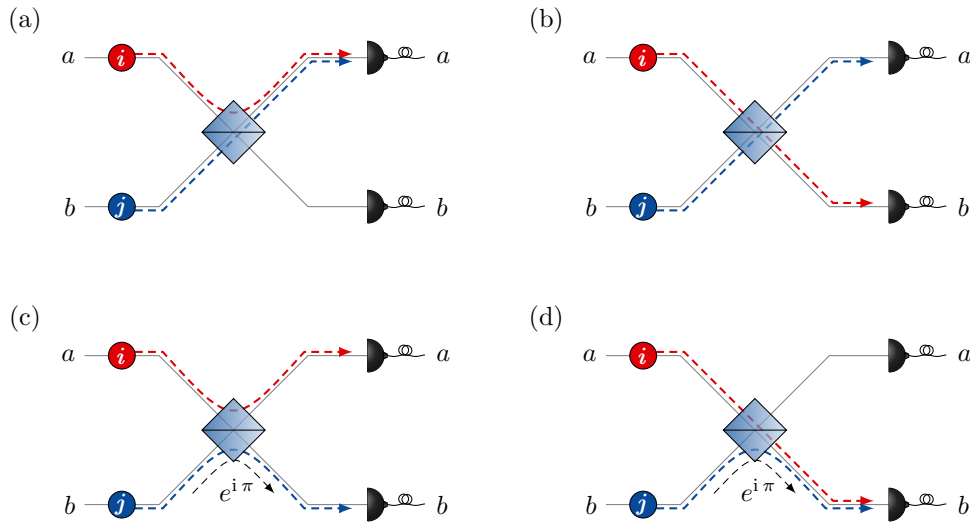


Figure 2.12. Illustration of the initial situation of a Hong-Ou-Mandel experiment. Two photons in quantum states i and j impinge via two different input ports a and b on a symmetric beam splitter. Depending on reflection and transmission of the photons four outcomes are possible, shown from (a) through (d). Due to the phase shift of π upon reflection in port b , cases (b) and (c) have opposite signs and cancel each other, if the photons are indistinguishable, i.e. if $i = j$. As a result the photons coalesce and no correlations can be measured between both output ports.

$$|\Psi_{\text{in}}\rangle = |1_i\rangle_a |1_j\rangle_b = \hat{a}_i^\dagger \hat{b}_j^\dagger |0\rangle. \quad (2.38)$$

At the beam splitter each photon is either reflected or transmitted. However, prior to a respective measurement, the photons are mapped to a superposition state according to

$$\begin{aligned} \hat{a}_i^\dagger &\xrightarrow{\hat{U}_{\text{BS}}} \frac{1}{\sqrt{2}} (\hat{a}_i^\dagger + \hat{b}_i^\dagger) \\ \hat{b}_j^\dagger &\xrightarrow{\hat{U}_{\text{BS}}} \frac{1}{\sqrt{2}} (\hat{a}_j^\dagger - \hat{b}_j^\dagger), \end{aligned} \quad (2.39)$$

where \hat{U}_{BS} represents the unitary BS transformation. Note that the action of a BS requires a relative phase shift of π between both reflected modes, which we here introduced upon reflection from input mode b to output mode b . Using the transformations (2.39), the overall output state can be written as

$$\begin{aligned} |\Psi_{\text{out}}\rangle &= \hat{U}_{\text{BS}} |\Psi_{\text{in}}\rangle \\ &= \frac{1}{2} (\hat{a}_i^\dagger + \hat{b}_i^\dagger) \cdot (\hat{a}_j^\dagger - \hat{b}_j^\dagger) |0\rangle \\ &= \frac{1}{2} (\hat{a}_i^\dagger \hat{a}_j^\dagger + \hat{a}_j^\dagger \hat{b}_i^\dagger - \hat{a}_i^\dagger \hat{b}_j^\dagger - \hat{b}_i^\dagger \hat{b}_j^\dagger) |0\rangle \\ &= \frac{1}{2} \left(\underbrace{|1_i 1_j\rangle_a |0_i 0_j\rangle_b}_{(a)} + \underbrace{|0_i 1_j\rangle_a |1_i 0_j\rangle_b}_{(b)} \right. \\ &\quad \left. - \underbrace{|1_i 0_j\rangle_a |0_i 1_j\rangle_b}_{(c)} - \underbrace{|0_i 0_j\rangle_a |1_i 1_j\rangle_b}_{(d)} \right), \end{aligned} \quad (2.40)$$

where all contributions to the output state are denoted (a) to (d) according to the four cases illustrated in Fig. 2.12. The negative sign due to reflection of the photon in mode b appears in (c) and (d). Furthermore, we realize that both cases (b) and (c) exhibit an opposite sign and contain exactly one photon in each output channel. However, both terms differ by the quantum state the photons are in, which we are elaborating on in the following.

First, assume that i and j refer to two orthogonal quantum states, e.g. the photons might exhibit horizontal and vertical polarization, but are identical otherwise. A respective state measurement enables us to determine, whether a photon detected in either of the two output modes originates from input mode a or b . Therefore, both photons are said to be distinguishable. The opposite case of indistinguishable photons occurs, if $i = j$, i.e. both photons are identical in all degrees of freedom. Now (b) and (c) exactly cancel out, leading to the notion of destructive interference between two photons. Accordingly, Eq. (2.40) simplifies to

$$|\Psi_{\text{out}}\rangle = (|2\rangle_a |0\rangle_b - |0\rangle_a |2\rangle_b) / \sqrt{2}, \quad (2.41)$$

where $(\hat{a}^\dagger)^2 |0\rangle = \sqrt{2} |2\rangle$ was used. The most important experimental tool to test indistinguishability is a coincidence measurement of detection events between both output ports. As the BS is symmetric, all cases (a) through (d) equally contribute to the output state, but only (b) and (c) yield coincidences. Therefore, we simply find a coincidence probability of $p_{\text{coinc}} = 1/2$ for distinguishable photons. In case of indistinguishable photons, however, we directly read from Eq. (2.41) that coincidences are impossible, thus it is $p_{\text{coinc}} = 0$. Hence, the absence of coincidences implies that the input photons were indistinguishable.

Although the present approach is hardly useful in order to describe realistic photons propagating in complex field modes, it reveals a couple of important properties intrinsic to TPI:

- (i) **TPI is phase-insensitive:** From Eq. (2.40) we see that arbitrary phases of both input photons only change the global phase of $|\Psi_{\text{out}}\rangle$, but do not alter the destructive interference of (b) and (c).
- (ii) **The output state is entangled:** the output state (2.41) is non-separable, i.e. there are no complex coefficients α_i and β_j so that

$$|\Psi_{\text{out}}\rangle = \left(\sum_i \alpha_i |i\rangle_a \right) \otimes \left(\sum_j \beta_j |j\rangle_b \right). \quad (2.42)$$

In other words, detecting a photon in mode a allows the conclusion that there is no photon in mode b and vice versa. Therefore $|\Psi_{\text{out}}\rangle$ is referred to as a path-entangled number state [219].

- (iii) **TPI leads to effective photon-photon interaction:** From the transformation Eq. (2.39) we see that reflected and transmitted part of a photon fed into mode a have a relative phase of zero. In presence of an indistinguishable photon in mode b , however, the output state (2.41) reveals that this phase changed to π . This conditional phase flip is commonly interpreted as photon-photon interaction and plays a key role in various linear optical quantum computing schemes (LOQC) [146, 220], such as the controlled-NOT gate [147].

2.4.2 Time-Resolved Two-Photon Interference

Indistinguishability is not a binary feature, but photons can be only partially indistinguishable as well. Already the original HOM experiment [60] demonstrated that the coincidence probability can be tuned between its classical and quantum limits by varying the temporal overlap of both photons. More generally, indistinguishability can be quantitatively defined as the mean squared overlap between the wave-functions of two photons and accordingly

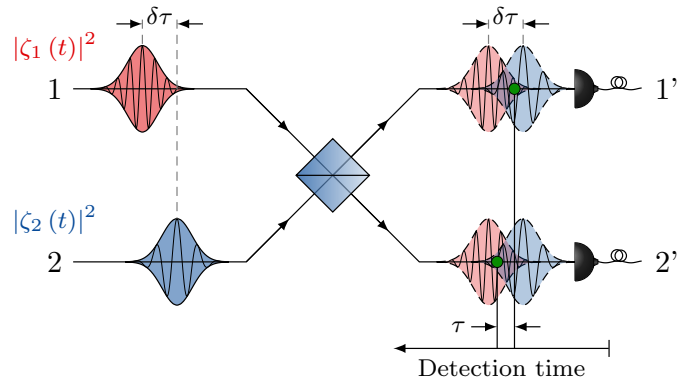


Figure 2.13. Hong-Ou-Mandel experiment considering the temporal input mode. Shown is the same initial situation of a two-photon interference experiment as described in Fig. 2.12. The input and output modes are renamed to 1 and 2 as well as 1' and 2', respectively. The temporal shape of the input photons is described by the wave-functions $\zeta_{1,2}(t)$. The model [217] allows to consider parameters such as the arrival of both photons with a delay $\delta\tau$ or a carrier frequency mismatch $\delta\nu$ and enables to evaluate the coincidence probability of detection events in both channels with a time lag of τ (see green circles). Adapted with permission from [217], © 2003 by Springer Nature.

varies between zero and one for entirely distinguishable and indistinguishable, respectively [221]. In view of our later requirements, we here introduce the well established formalism reported in [217, 218], which enables to describe the temporal pattern of HOM coincidence measurements based on the spectro-temporal properties of the input photons. The results can be used to extract the coincidence probability and thereby the degree of indistinguishability. Moreover, the model derived in Chap. 3 will be built upon the considerations presented in the following.

We start by rearranging our nomenclature in a more suitable manner: all input and output modes are now labeled by numbers i and i' , respectively, and the corresponding creation operators are denoted \hat{a}_i^\dagger and $\hat{a}_{i'}^\dagger$ (compare Fig. 2.13). To describe photons in temporally extended field modes defined by normalized wave-functions $\zeta_i(t)$, we employ the field-operators for mode i reading

$$\hat{E}_i^+(t) = \zeta_i(t) \hat{a}_i \quad \text{and} \quad \hat{E}_i^-(t) = \zeta_i^*(t) \hat{a}_i^\dagger. \quad (2.43)$$

Accordingly, the BS transformation relations (2.39) for the output modes 1' and 2' can be modified to

$$\begin{aligned} \hat{E}'_1(t) &= [\zeta_1(t) \hat{a}_1 + \zeta_2(t) \hat{a}_2] / \sqrt{2} \quad \text{and} \\ \hat{E}'_2(t) &= [\zeta_1(t) \hat{a}_1 - \zeta_2(t) \hat{a}_2] / \sqrt{2}. \end{aligned} \quad (2.44)$$

The quantity of interest is the joint photon-detection probability $P_{\text{joint}}(t_0, \tau)$, which yields the probability to detect one photon at time t_0 in output mode 1' and the other photon at $t_0 + \tau$ in output mode 2' (see green circles in Fig. 2.13). Using the input state $|\Psi_{\text{in}}\rangle = \hat{a}_1^\dagger \hat{a}_2^\dagger |0\rangle$ and Eq. (2.44) it can be evaluated to

$$\begin{aligned} P_{\text{joint}}(t_0, \tau) &= \langle \Psi_{\text{in}} | \hat{E}_1'^-(t_0) \hat{E}_2'^-(t_0 + \tau) \hat{E}_2'^+(t_0 + \tau) \hat{E}_1'^+(t_0) | \Psi_{\text{in}} \rangle \\ &= \frac{1}{4} |\zeta_1(t_0 + \tau) \zeta_2(t_0) - \zeta_2(t_0 + \tau) \zeta_1(t_0)|^2. \end{aligned} \quad (2.45)$$

This result is particularly convenient, as the quantum mechanical ansatz is reduced to an expression that only requires knowledge of the input photons' temporal modes. It can be expanded and separated into an incoherent contribution and an interference term according to $P_{\text{joint}}(t_0, \tau) = P_0(t_0, \tau) + P_{\text{int}}(t_0, \tau)$ with

$$\begin{aligned} P_0(t_0, \tau) &= \frac{|\zeta_1(t_0 + \tau) \zeta_2(t_0)|^2 + |\zeta_2(t_0 + \tau) \zeta_1(t_0)|^2}{4} \quad \text{and} \\ P_{\text{int}}(t_0, \tau) &= -2\text{Re}[\zeta_1(t_0 + \tau) \zeta_2(t_0) \zeta_2^*(t_0 + \tau) \zeta_1^*(t_0)]. \end{aligned} \quad (2.46)$$

The latter term is responsible for the two-photon interference and converges towards zero for $\tau \gg \tau_{\text{coh}}$, if averaged over an ensemble, where τ_{coh} is the mutual coherence time of both photons.

2.4.3 Quantum Beats and Hong-Ou-Mandel Dip

To illustrate possible predictions of this model, we here review the discussion presented in [217], which considers two input photons propagating in normalized Gaussian wave-packets that read (compare Fig. 2.13)

$$\zeta_{1,2}(t) = \sqrt[4]{2/\pi} \exp\left[-(t \pm \delta\tau/2)^2 - 2\pi i(\nu \pm \delta\nu/2)t\right], \quad (2.47)$$

where the indices '1' and '2' refer to '+' and '-', respectively. The maxima of both wave-packets are separated by a temporal delay of $\delta\tau$ and their carrier frequencies are detuned by $\delta\nu$. Plugging these wave-functions into Eq. (2.45), we obtain the joint detection probability

$$\begin{aligned} P_{\text{joint}}(t_0, \tau; \delta\tau, \delta\nu) &= \frac{\cosh(2\tau\delta\tau) - \cos(2\pi\tau\delta\nu)}{\pi} \\ &\quad \times \exp[-4t_0(t_0 + \tau) - \delta\tau^2 - 2\tau^2], \end{aligned} \quad (2.48)$$

where $\delta\tau$ and $\delta\nu$ appear as additional parameters. For a full coincidence measurement all recorded coincidences are accumulated over a large number of repetitions yielding the cross-correlation function $g^{(2)}(\tau)$, which, in its limit,

2. FUNDAMENTALS

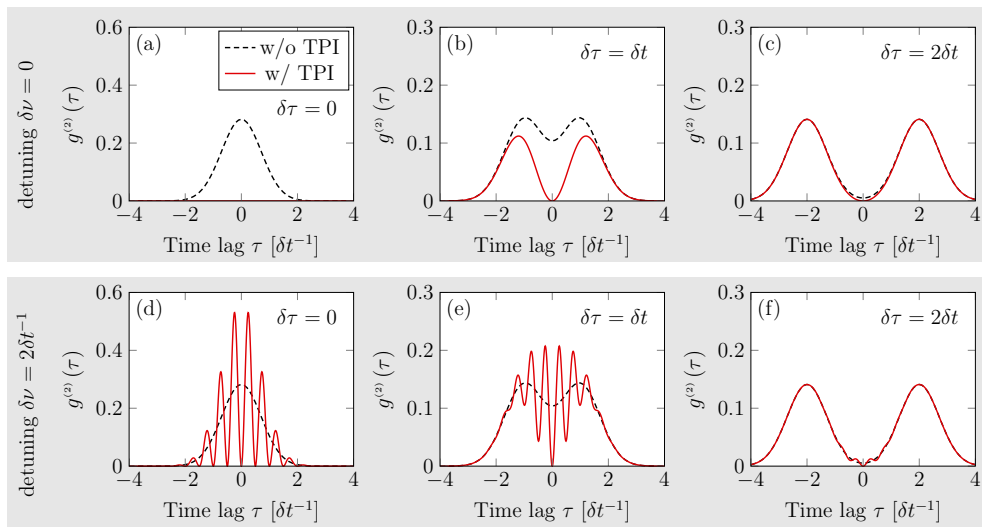


Figure 2.14. Quantum beats observed in a Hong-Ou-Mandel experiment with Gaussian wave-packets. Shown are examples according to Eq. (2.49) for no detuning $\delta\nu = 0$ (top row) and $\delta\nu = 2\delta t^{-1}$ (bottom row), where δt is the width of the wave-packets. Each detuning is shown with 3 relative delays $\delta\tau$ between the photons. The dashed line shows the result expected in absence of two-photon interference (TPI), while the red curves include TPI. The oscillations in the red curves are known as quantum beats.

equals an integration of P_{joint} over all possible detection times t_0 . The result of this integration step is

$$\begin{aligned}
 g^{(2)}(\tau; \delta\tau, \delta\nu) &= \int_{-\infty}^{\infty} P_{\text{joint}}(t_0, \tau; \delta\tau, \delta\nu) dt_0 \\
 &= \frac{\cosh(2\tau\delta\tau) - \cos(2\pi\tau\delta\nu)}{2\sqrt{\pi}} \cdot \exp(-\delta\tau^2 - \tau^2),
 \end{aligned}
 \tag{2.49}$$

which is illustrated in Fig. 2.14. Therein, examples for different relative delays $\delta\tau$ and detunings $\delta\nu$ are depicted, where all values are presented in units of the half width at $1/e$ maximum of the wave-packet δt . Shown are a black dashed and red solid curve, which differ by the interference term $\cos(2\pi\tau\delta\nu)$ in Eq. (2.49) (set to zero for black dashed). In part (a) we see that for $\delta\tau = 0$ and $\delta\nu = 0$ no coincidences appear, if the interference term is included (missing red curve), which corresponds to entirely indistinguishable photons. With increasing $\delta\tau$ [(a) through (c)] the red curve converges towards its incoherent limit, revealing decreasing indistinguishability due to a decreasing temporal overlap of both photons.

In case of an additional detuning [(d) through (f)] the cross-correlation starts to oscillate with a period of $\delta\nu^{-1}$ in regions where both photons are

temporally well overlapping. This beat is a signature of the quantum mechanical uncertainty which of the two photons has been detected first. The second photon subsequently propagates in a superposition state of $\zeta_1(t)$ and $\zeta_2(t)$. As both field modes evolve at different rates corresponding to $\delta\nu$, their relative phase changes in time causing classical interference fringes between both BS outputs. This phenomenon is commonly referred to as *quantum beats* and has first been observed in [222]. Note that the quantum beats always start with both photons being in phase at $\tau = 0$, i.e. it is $g^{(2)}(0) = 0$. We find that this is a general result, as Eq. (2.45) predicts $P_{\text{joint}}(t_0, 0) = 0$ no matter how different both input photons are. Therefore, it is important to keep in mind that $g^{(2)}(0) \neq 0$ is not a sign of a non-ideal indistinguishability, but rather a timing jitter present in the system, typically caused by limited detector resolution or the photon emission process.

While Eq. (2.49) yields the probability to obtain two detection events separated by τ , the overall coincidence probability p_{coinc} discussed in Sect. 2.4.1 is a cumulative quantity and can be obtained via the integration

$$p_{\text{coinc}} = \int_{-\infty}^{+\infty} g^{(2)}(\tau) d\tau. \quad (2.50)$$

Based on the cross-correlation function Eq. (2.49) for the Gaussian input photons under consideration, this integration leads to

$$p_{\text{coinc}}(\delta\tau, \delta\nu) = \frac{1}{2} [1 - \exp(-\delta\tau^2 - \pi^2\delta\nu^2)], \quad (2.51)$$

which is plotted against the delay $\delta\tau$ in Fig. 2.15 (a) for no detuning (red curve) and two non-zero detunings. All three curves converge towards $p_{\text{coinc}} =$

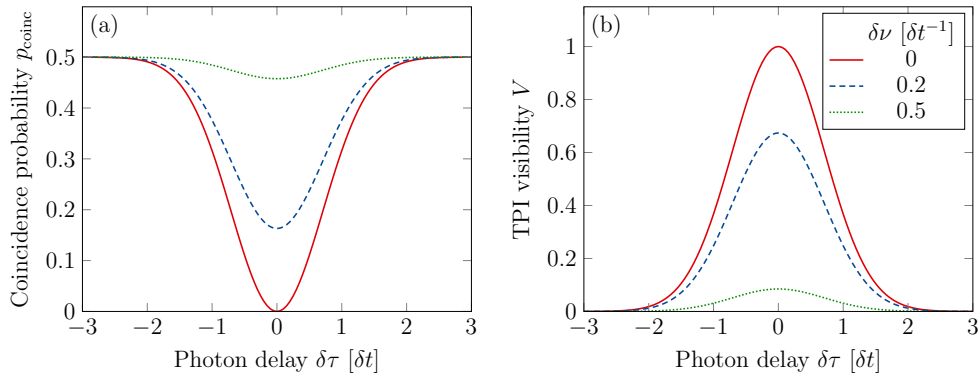


Figure 2.15. Coincidence probability for temporal and spectral detuning. (a) Coincidence probability and (b) two-photon interference visibility as function of the photon delay $\delta\tau$ for no detuning (red solid), $\delta\nu = 0.2\delta t^{-1}$ (blue dashed), and $\delta\nu = 0.5\delta t^{-1}$ (green dotted). For increasing $\delta\tau$ and $\delta\nu$ both quantities converge towards their classical limits $p_{\text{coinc}} = 0.5$ and $V = 0$. The drop of p_{coinc} around $\tau = 0$ is known as HOM dip.

$1/2$ for $\delta\tau \rightarrow \pm\infty$, but drop to lower values around $\delta\tau = 0$, which is known as *HOM dip*. The HOM dip indicates that the indistinguishability is maximized when both photons perfectly overlapping in time. While ideal indistinguishability can be obtained at $\delta\tau = 0$ and $\delta\nu = 0$, an additional detuning (blue dashed and green dotted) leads to a less pronounced HOM dip, showing that both photons are now partially distinguishable in the frequency domain. Eventually it is possible to compute a TPI visibility V based on the coincidence probability, which reads

$$V = 1 - 2p_{\text{coinc}}. \quad (2.52)$$

The TPI visibility is illustrated in Fig. 2.15 (b) and resembles an inverted HOM dip. It is an important figure-of-merit, as it is easily accessible in experiment and identical to the desired indistinguishability under ideal conditions (symmetric BS, perfect spatial mode overlap) [221].

Quantum Interference of Independent Photons

Copyright notice: All results presented in this chapter except for Sect. 3.2.3 were originally published in [197] (Copyright © 2018 The Authors. Published by IOP Publishing Ltd on behalf of Deutsche Physikalische Gesellschaft).

The main goal of the present work is to investigate the impact of QFDC on photon indistinguishabilities. Therefore, it is inevitable to quantify all effects limiting the wave-packet overlap of the photons. In experiment we are able to ensure a virtually ideal spatial, temporal, as well as polarization mode match, but are rather limited in manipulating the frequency domain. In particular frequency fluctuations of solid state emitters as described in Sect. 2.2 are known to be a limiting factor for quantum interference applications.

Here we establish a theoretical framework based on [217] describing TPI experiments with arbitrary quantum gates using dissimilar input photons. The model incorporates differing radiative lifetimes and emission frequencies as well as spectral diffusion (SD) and pure dephasing (PD). We obtain a set of equations describing the temporal pattern of cross-correlation measurements between the gate outputs and the respective overall coincidence probability. The model goes beyond existing formalisms, which focus only on single beam splitter TPI measurements with a more restricted parameter space [151, 152, 196, 223]. The results enable us to explain all TPI visibilities presented in chapters 5 and 6 based on independently measured emitter parameters.

3.1 Derivation

The following derivation adopts the basic ansatz discussed in Sect. 2.4.2 and 2.4.3. Accordingly, further details can be found in [217, 218] as well as the

supplement of [197].

3.1.1 Joint Detection Probability for Linear Optical Gates

Linear optical quantum computing provides a general framework for quantum computing solely based on linear optical components, such as beam splitters, phase shifters and mirrors [220]. Its implementations include boson sampling [224], which is expected to be superior to classical computers for certain problems, or even universal quantum computers in the scope of the scheme after Knill, Laflamme, and Milburn [146]. LOQC protocols typically rely on the conditional phase shift introduced by TPI (compare Sect. 2.4.1) and therefore directly depend on the indistinguishability of the employed photons. Accordingly, it is valuable to establish a formalism, which allows to predict the performance of given photons in elaborate LOQC schemes based on their assessment using simple HOM experiments [217] to arbitrary linear optical gates. The result will then be integrated for photons as emitted by solid state emitters under the influence of PD and SD.

A generic linear optical gate is depicted in Fig. 3.1. It consists of N input and N output modes which are interconnected by a network of beam splitters and phase shifters. Such a gate can be represented by an $N \times N$ unitary

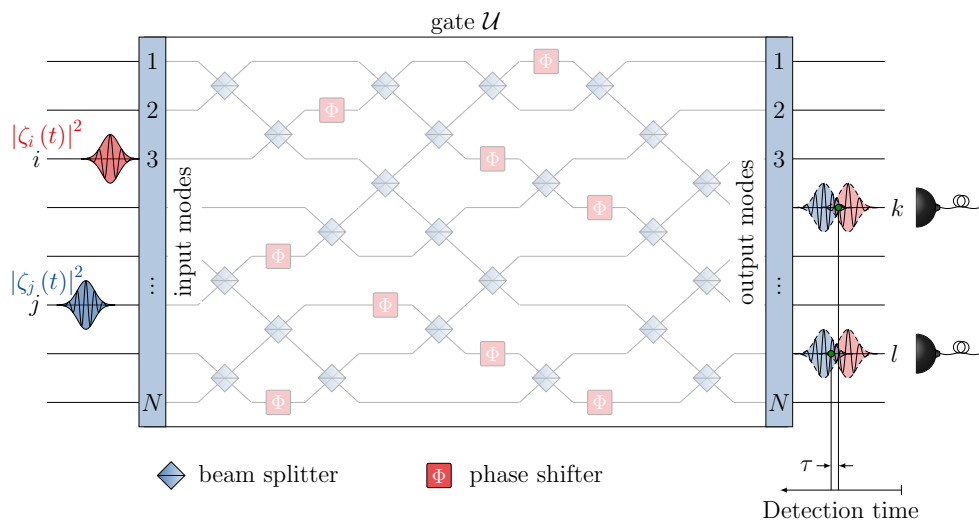


Figure 3.1. Scattering of two photons at a linear optical gate. The gate consists of beam splitters and phase shifters connecting N input and output modes and can be described by a unitary matrix \mathcal{U} . The presented formalism yields the probability to detect two photons at the outputs k and l with a time difference of τ , if the gate was fed with two photons via the input i and j propagating in the temporal modes $|\zeta_{i,j}(t)|^2$.

matrix \mathcal{U} . Given a set of input field operators $\hat{E}_l^\pm(t)$ with l referring to the respective input mode, the output field operators can be expressed as

$$\hat{E}_k^{\prime+}(t) = \sum_l \mathcal{U}_{kl} \hat{E}_l^+(t) \quad \text{and} \quad \hat{E}_k^{\prime-}(t) = \sum_l \mathcal{U}_{kl}^* \hat{E}_l^-(t), \quad (3.1)$$

where \mathcal{U}_{kl} are the elements of \mathcal{U} . Given any input state $|\Psi_{\text{in}}\rangle$, the probability $P_{\text{joint}}(t_0, \tau)$ to detect a photon at time t_0 in output mode k and a second photon at $t_0 + \tau$ in mode l reads according to Eq. (2.45)¹

$$P_{\text{joint}}(t_0, \tau) = \langle \Psi_{\text{in}} | \hat{E}_k^{\prime-}(t_0) \hat{E}_l^{\prime-}(t_0 + \tau) \hat{E}_l^{\prime+}(t_0 + \tau) \hat{E}_k^{\prime+}(t_0) | \Psi_{\text{in}} \rangle. \quad (3.2)$$

We now restrict $|\Psi_{\text{in}}\rangle$ to two input photons in modes i and j by setting $|\Psi_{\text{in}}\rangle = |1_i 1_j\rangle$. Furthermore, we employ the transformation relations (3.1) and use the definition of field operators (2.43), which leads to

$$P_{\text{joint}}(t_0, \tau) = \sum_{r,s,u,v} \mathcal{U}_{kr}^* \mathcal{U}_{ls}^* \mathcal{U}_{lu} \mathcal{U}_{kv} \zeta_r^*(t_0) \zeta_s^*(t_0 + \tau) \zeta_u(t_0 + \tau) \zeta_v(t_0) \\ \times \langle 1_i 1_j | \hat{a}_r^\dagger \hat{a}_s^\dagger \hat{a}_u \hat{a}_v | 1_i 1_j \rangle. \quad (3.3)$$

The summation over $r, s, u,$ and v covers all input modes $1 \dots N$, which can be reduced to 16 summands, as the only occupied modes are i and j . In order to be nonzero, those terms must fulfill $r \neq s$ as well as either $r = u$ and $s = v$ or $r = v$ and $s = u$, which is straightforward to verify using $\hat{a} |0\rangle = 0$ and corresponding orthogonality relations. Due to this condition we are left with only 4 terms. Eventually, these can be factorized to

$$P_{\text{joint}}(t_0, \tau) = |\mathcal{U}_{li} \mathcal{U}_{kj} \zeta_i(t_0 + \tau) \zeta_j(t_0) + \mathcal{U}_{lj} \mathcal{U}_{ki} \zeta_j(t_0 + \tau) \zeta_i(t_0)|^2, \quad (3.4)$$

which is equivalent to Eq. (2.45), but applicable to arbitrary linear optical gates represented by a unitary matrix \mathcal{U} . Indeed, for a symmetric 50:50 beam splitter described by

$$\mathcal{U}_{BS} = \begin{pmatrix} \mathcal{U}_{11} & \mathcal{U}_{12} \\ \mathcal{U}_{21} & \mathcal{U}_{22} \end{pmatrix} = \frac{1}{\sqrt{2}} \begin{pmatrix} 1 & 1 \\ 1 & -1 \end{pmatrix}, \quad (3.5)$$

we find that both expressions agree. In particular, this implies that all quantities, which used to be evaluated based on Eq. (2.45) for single beam splitter experiments, can be obtained for any linear optical gate using Eq. (3.4) without any further efforts, if only the underlying gate matrix is known.

Note that existing input-output theories of quantum networks such as the SLH-framework [225] fully cover linear optical gates and even go well beyond them, as components and architectures such as atoms in cavities or coherent feedback can be treated. However, the advantage of Eq. (3.4) resides in its simple implementation, as the quantum mechanical ansatz necessary to treat TPI applications is reduced to an expression that only requires knowledge of the wave-functions and gate matrix.

¹Note that the dependency of $P_{\text{joint}}(t_0, \tau)$ on the input and output modes $i, j, k,$ and l was omitted in the chosen notation in favor of a legibility.

3.1.2 Cross-Correlation Function

In the following we focus on input fields $\zeta_{i,j}(t)$ tailored to our needs, i.e. fields, which describe single photons as emitted by solid state quantum emitters. Therefore, we adopt the wave-function already introduced in Sect. 2.2.2 reading

$$\zeta_{i,j}(t) = \frac{1}{\sqrt{\tau_{i,j}}} \text{H}(t) \cdot \exp \left\{ -t/2\tau_{i,j} - i [2\pi\nu_{i,j}t + \varphi_{i,j}(t)] \right\}. \quad (3.6)$$

Note that we allow both input photons to differ in radiative lifetime $\tau_{i,j}$, carrier frequency $\nu_{i,j}$, as well as instantaneous phase $\varphi_{i,j}(t)$, which enables us to model independent, dissimilar sources. As before, PD is captured by a rapidly fluctuating $\varphi_{i,j}(t)$ while SD is accounted for by a static distribution of $\nu_{i,j}$. All experiments performed in the scope of this work are based on pulsed excitation schemes allowing us to synchronize the input photons. Therefore, it is sufficient to consider both photons starting at $t = 0$ as in Eq. (3.6). It is important to keep in mind, however, that due to this restriction our results are not applicable, if the photon arrival times were uncertain, e.g. in case of cw-excitation.

In the following we use the abbreviations $\Phi_{\mathcal{U}} = \arg(\mathcal{U}_i \mathcal{U}_{kj} \mathcal{U}_{ki}^* \mathcal{U}_j^*)$ for the phase introduced by the gate, $\Delta\nu = \nu_i - \nu_j$ being the carrier frequency displacement between both emitters, $\Delta\varphi_{i,j} = \varphi_{i,j}(t_0 + \tau) - \varphi_{i,j}(t_0)$ the instantaneous phase differences, as well as $1/T_+ = 1/\tau_i + 1/\tau_j$. Thereby, we can express the joint detection probability via

$$P_{\text{joint}}(t_0, \tau) = \frac{1}{\tau_i \tau_j} \cdot f(t_0, \tau) \cdot g(t_0, \tau) \quad (3.7)$$

with the terms

$$\begin{aligned} f(t_0, \tau) &= |\mathcal{U}_i|^2 |\mathcal{U}_{kj}|^2 \cdot \exp(-\tau/\tau_i) + |\mathcal{U}_j|^2 |\mathcal{U}_{ki}|^2 \cdot \exp(-\tau/\tau_j) \\ &\quad + |\mathcal{U}_i \mathcal{U}_{kj} \mathcal{U}_{ki}^* \mathcal{U}_j^*| \cdot \exp(-\tau/2T_+) \cdot h(t_0, \tau), \\ g(t_0, \tau) &= \text{H}(t_0) \text{H}(t_0 + \tau) \cdot \exp(-t_0/T_+), \quad \text{and} \\ h(t_0, \tau) &= 2 \cos(2\pi\Delta\nu\tau + \Delta\varphi_i - \Delta\varphi_j + \Phi_{\mathcal{U}}). \end{aligned} \quad (3.8)$$

According to Eq. (2.49), the cross-correlation function $g^{(2)}(\tau)$ can be obtained from $P_{\text{joint}}(t_0, \tau)$ via integration over t_0 . However, the result is insufficient to describe a realistic cross-correlation measurement, as SD and PD lead to randomly fluctuating $\Delta\nu$ and $\Delta\varphi_{i,j}$ throughout the measurement run. Therefore, it is necessary to include a statistical averaging step denoted by $\langle\langle \cdot \rangle\rangle$ via

$$\mathcal{G}^{(2)}(\tau) = \langle\langle g^{(2)}(\tau) \rangle\rangle = \int_{-\infty}^{+\infty} \langle\langle P_{\text{joint}}(t_0, \tau) \rangle\rangle dt_0, \quad (3.9)$$

which covers all available frequencies and phases. The models we apply for both PD and SD describe ergodic stochastic processes (cf. Sect. 2.2 and [186,

187]), i.e. we can expect that any possible phase or frequency jump which might occur at a fixed time in an ensemble of identical emitters will also be encountered when observing a single emitter over a sufficiently long time. This property of the emitted photon field justifies the interchange of statistical average and time average in Eq. (3.9). From Eq. (3.8) we recognize that only $h(t_0, \tau)$ is phase-sensitive and therefore affected by the statistical average. Assuming that SD and PD independently act on the emitter, we can write

$$\begin{aligned} \langle\langle h(t_0, \tau) \rangle\rangle &= \langle\langle h(t_0, \tau) \rangle\rangle_{\text{SD}} \text{PD} \\ &= 2 \langle\langle \cos(2\pi\Delta\nu\tau + \Delta\varphi_i - \Delta\varphi_j + \Phi_U) \rangle\rangle_{\text{SD}} \text{PD} \\ &= \langle e^{i2\pi\Delta\nu\tau} \rangle_{\text{SD}} \langle e^{i\Delta\varphi_i} \rangle_{\text{PD}} \langle e^{-i\Delta\varphi_j} \rangle_{\text{PD}} \cdot e^{i\Phi_U} \\ &\quad + \langle e^{-i2\pi\Delta\nu\tau} \rangle_{\text{SD}} \langle e^{-i\Delta\varphi_i} \rangle_{\text{PD}} \langle e^{i\Delta\varphi_j} \rangle_{\text{PD}} \cdot e^{-i\Phi_U}, \end{aligned} \quad (3.10)$$

where $\langle \cdot \rangle_{\text{SD}}$ and $\langle \cdot \rangle_{\text{PD}}$ denote the averaging due to SD and PD, respectively. For the PD contribution, we employ Eq. (2.13) and find

$$\langle e^{\pm i\Delta\varphi_{i,j}} \rangle_{\text{PD}} = \exp(-\Gamma_{i,j}^* |\tau|) \quad (3.11)$$

with $\Gamma_{i,j}^*$ corresponding to the pure dephasing rate of the photon in mode i or j . To evaluate $\langle \cdot \rangle_{\text{SD}}$, we are in need of a distribution $\varrho(\Delta\nu)$, which yields the probability of both photons having a spectral displacement $\Delta\nu$. Assume the emitters are indeed independent and their frequency range is given by the normal distributions $S_{i,j}(\nu_{i,j})$ with standard deviations $\sigma_{i,j}$ and central frequencies $\nu_{0,i}$ and $\nu_{0,j}$ according to Eq. (2.10). In this case, we find the probability $p(\nu, \Delta\nu)$ of emitter i being at frequency $\nu_i = \nu$ and emitter j being at $\nu_j = \nu + \Delta\nu$ as

$$\begin{aligned} p(\nu, \Delta\nu) &= S_i(\nu) \cdot S_j(\nu + \Delta\nu) \\ &= \frac{1}{2\pi\sigma_i\sigma_j} \exp\left[-\frac{(\nu - \nu_{0,i})^2}{2\sigma_i^2} - \frac{(\nu + \Delta\nu - \nu_{0,j})^2}{2\sigma_j^2}\right]. \end{aligned} \quad (3.12)$$

The desired distribution $\varrho(\Delta\nu)$ simply equals an integration of $p(\nu, \Delta\nu)$ over all occurring frequencies ν , which mathematically corresponds to a cross-correlation between the individual distributions S_i and S_j . Its result is given by

$$\varrho(\Delta\nu) = \int_{-\infty}^{+\infty} p(\nu, \Delta\nu) \, d\nu = \frac{1}{\sqrt{2\pi\Sigma^2}} \exp\left[-\frac{(\Delta\nu + \delta\nu)^2}{2\Sigma^2}\right], \quad (3.13)$$

where $\delta\nu = \nu_{0,i} - \nu_{0,j}$ is the relative detuning of both emission lines and $\Sigma^2 = \sigma_i^2 + \sigma_j^2$. We can use Eq. (3.13) to obtain the required statistical average

$$\begin{aligned} \langle e^{\pm i2\pi\Delta\nu\tau} \rangle_{\text{SD}} &= \int_{-\infty}^{+\infty} \varrho(\Delta\nu) \cdot e^{\pm i2\pi\Delta\nu\tau} \, d\Delta\nu \\ &= \exp(-2\pi^2\Sigma^2\tau^2 \mp i2\pi\delta\nu\tau), \end{aligned} \quad (3.14)$$

3. QUANTUM INTERFERENCE OF INDEPENDENT PHOTONS

which is simply the Fourier transformation of $\varrho(\Delta\nu)$ taken at $\mp 2\pi\tau$. Eventually, Eq. (3.11) and Eq. (3.14) enable us to write the overall statistical average as

$$\langle\langle h(t_0, \tau) \rangle\rangle = 2 \exp[-(\Gamma_i^* + \Gamma_j^*)|\tau| - 2\pi^2\Sigma^2\tau^2] \cos(2\pi\delta\nu\tau - \Phi_{\mathcal{U}}). \quad (3.15)$$

As can be seen $\langle\langle h(t_0, \tau) \rangle\rangle$ lost its t_0 -dependency and so has $\langle\langle f(t_0, \tau) \rangle\rangle$ in Eq. (3.8) as a consequence. Therefore, the integration over t_0 in Eq. (3.9) only affects $g(t_0, \tau)$, which is given by

$$\int_{-\infty}^{+\infty} g(t_0, \tau) dt_0 = T_+ [\text{H}(\tau) + \text{H}(-\tau) \exp(\tau/T_+)]. \quad (3.16)$$

Given Eq. (3.8) and our results (3.15) as well as (3.16) we find the cross-correlation function to be

$$\mathcal{G}^{(2)}(\tau) = \mathcal{G}_0^{(2)}(\tau) + \mathcal{G}_{\text{int}}^{(2)}(\tau) \quad (3.17)$$

with

$$\begin{aligned} \mathcal{G}_0^{(2)}(\tau) = \frac{1}{\tau_i + \tau_j} & \left\{ |\mathcal{U}_{li}|^2 |\mathcal{U}_{kj}|^2 [\text{H}(\tau) \cdot \exp(-\tau/\tau_i) + \text{H}(-\tau) \cdot \exp(\tau/\tau_j)] \right. \\ & \left. + |\mathcal{U}_{lj}|^2 |\mathcal{U}_{ki}|^2 [\text{H}(\tau) \cdot \exp(-\tau/\tau_j) + \text{H}(-\tau) \cdot \exp(\tau/\tau_i)] \right\} \end{aligned} \quad (3.18)$$

and

$$\mathcal{G}_{\text{int}}^{(2)}(\tau) = \frac{2 \left| \mathcal{U}_{li} \mathcal{U}_{kj} \mathcal{U}_{ki}^* \mathcal{U}_{lj}^* \right|}{\tau_i + \tau_j} \cdot \exp(-\gamma|\tau| - 2\pi^2\Sigma^2\tau^2) \cdot \cos(2\pi\delta\nu\tau - \Phi_{\mathcal{U}}), \quad (3.19)$$

where we introduced $\gamma = \gamma_i + \gamma_j$ with $\gamma_{i,j} = 1/(2\tau_{i,j}) + \Gamma_{i,j}^*$ specifying the width of the homogeneous linewidth contribution of each emitter.

Summarizing, Eq. (3.17) yields the time structure of a cross-correlation measurements between the outputs labeled k and l of a linear optical gate described by the unitary matrix \mathcal{U} , if the gate was fed with two single photons via the input modes i and j . While the incoherent contribution $\mathcal{G}_0^{(2)}(\tau)$ solely depends on the gate and temporal envelope of both photons, it can be seen that the interference term $\mathcal{G}_{\text{int}}^{(2)}(\tau)$ additionally gives rise to quantum beats depending on the spectral detuning $\delta\nu$ between both emitters. Moreover, we find that $\mathcal{G}_{\text{int}}^{(2)}(\tau)$ converges towards zero with increasing γ and Σ , which indicates a loss of mutual coherence due to PD and SD. Note that we use the standard deviation σ only in favor of a concise notation. In the following, we often quantify the inhomogeneous broadening with the more common FWHM given by $\sigma' = 2\sqrt{2 \ln 2} \sigma$ instead. It is worth mentioning that the phase of the quantum beats is determined by the gate via $\Phi_{\mathcal{U}}$. In Sect. 2.4.3 we found that $\mathcal{G}^{(2)}(0) = 0$ is a general property of HOM experiments. Here we realize that $\mathcal{G}^{(2)}(0)$ reaches a local minimum (which is not necessarily zero) only if $\Phi_{\mathcal{U}} = \pi$, i.e. in case of specific gates and combinations of input and output modes.

3.1.3 Overall Coincidence Probability

For the assessment of photons in a given quantum information processing scheme the cross-correlation function is only of limited value. Instead, the efficiency of a gate is more commonly determined via the overall probability to obtain coincidences [226, 227]. According to Eq. (2.50) it can be obtained via

$$\begin{aligned}
 p_{\text{coinc}} &= \int_{-\infty}^{+\infty} \mathcal{G}^{(2)}(\tau) \, d\tau \\
 &= \int_{-\infty}^{+\infty} \mathcal{G}_0^{(2)}(\tau) \, d\tau + \int_{-\infty}^{+\infty} \mathcal{G}_{\text{int}}^{(2)}(\tau) \, d\tau \\
 &= p_{\text{coinc},0} + p_{\text{coinc,int}}.
 \end{aligned} \tag{3.20}$$

Evaluating p_{coinc} using Eq. (3.17) we first find

$$p_{\text{coinc},0} = \int_{-\infty}^{+\infty} \mathcal{G}_0^{(2)}(\tau) \, d\tau = |\mathcal{U}_{li}|^2 |\mathcal{U}_{kj}|^2 + |\mathcal{U}_{lj}|^2 |\mathcal{U}_{ki}|^2. \tag{3.21}$$

To find the solution for the interference term, we first simplify by using the abbreviations $\alpha = 2\pi\Sigma$ and $\omega = 2\pi\delta\nu$ as well as defining the functions $a(\tau) = \exp(-\gamma|\tau|)$ and $b(\tau) = \exp(-\alpha^2\tau^2/2)$. This enables us to write

$$\begin{aligned}
 p_{\text{coinc,int}} &= \int_{-\infty}^{+\infty} \mathcal{G}_{\text{int}}^{(2)}(\tau) \, d\tau \\
 &= \frac{|\mathcal{U}_{li}\mathcal{U}_{kj}\mathcal{U}_{ki}^*\mathcal{U}_{lj}^*|}{\tau_i + \tau_j} \cdot \int_{-\infty}^{+\infty} a(\tau) \cdot b(\tau) (e^{i\omega\tau - i\Phi_U} + c.c.) \, d\tau \\
 &= \frac{|\mathcal{U}_{li}\mathcal{U}_{kj}\mathcal{U}_{ki}^*\mathcal{U}_{lj}^*|}{\tau_i + \tau_j} \cdot \left[e^{-i\Phi_U} \int_{-\infty}^{+\infty} a(\tau) \cdot b(\tau) e^{i\omega\tau} \, d\tau \right. \\
 &\quad \left. + e^{+i\Phi_U} \int_{-\infty}^{+\infty} a(\tau) \cdot b(\tau) e^{-i\omega\tau} \, d\tau \right].
 \end{aligned} \tag{3.22}$$

Substituting $\tau \rightarrow -\tau$ in the first integral and considering that both $a(\tau)$ and $b(\tau)$ are mirror-symmetric around $\tau = 0$ leads to

$$p_{\text{coinc,int}} = \frac{2|\mathcal{U}_{li}\mathcal{U}_{kj}\mathcal{U}_{ki}^*\mathcal{U}_{lj}^*|}{\tau_i + \tau_j} \cdot \cos(\Phi_U) \cdot \underbrace{\int_{-\infty}^{+\infty} a(\tau) \cdot b(\tau) e^{-i\omega\tau} \, d\tau}_{=\sqrt{2\pi}\mathcal{F}[a(\tau)\cdot b(\tau)](\omega)}. \tag{3.23}$$

As indicated, the integral constitutes a unitary Fourier transformation of the product $a(\tau) \cdot b(\tau)$. In the course of Sect. 2.2.2 we encountered the same integral while computing the power spectral density of a single photon field

under the influence of PD and SD. Therefore, we adopt the same solution, i.e. we apply the Fourier convolution theorem and express the result in terms of the real part of the Faddeeva function $w(z)$ with $z = (2\pi\delta\nu + i\gamma) / (2\pi\sqrt{2}\Sigma)$, which results in

$$p_{\text{coinc, int}} = 2 |\mathcal{U}_{li}\mathcal{U}_{kj}\mathcal{U}_{ki}^*\mathcal{U}_{lj}^*| \cdot \cos(\Phi_{\mathcal{U}}) \cdot \frac{\text{Re}[w(z)]}{\sqrt{2\pi}\Sigma(\tau_i + \tau_j)}. \quad (3.24)$$

Eventually, with help of Eq. (3.21) and Eq. (3.24) we find the overall coincidence probability to be

$$p_{\text{coinc}} = |\mathcal{U}_{li}|^2 |\mathcal{U}_{kj}|^2 + |\mathcal{U}_{lj}|^2 |\mathcal{U}_{ki}|^2 + 2 |\mathcal{U}_{li}\mathcal{U}_{kj}\mathcal{U}_{ki}^*\mathcal{U}_{lj}^*| \cdot \cos(\Phi_{\mathcal{U}}) \cdot \frac{\text{Re}[w(z)]}{\sqrt{2\pi}\Sigma(\tau_i + \tau_j)}. \quad (3.25)$$

We see that p_{coinc} follows a Voigt-lineshape as function of the spectral detuning $\delta\nu$, whose width and height is determined by homogeneous and inhomogeneous linewidth contributions of both emitters. The following section focuses on possible predictions for HOM experiments that can be extracted from Eq. (3.17) and Eq. (3.25). Applications going beyond single beam splitter experiments will be addressed in Sect. 7.1. An extension of the formalism including asynchronous arrival and a polarization mismatch of both input photons can be found in the supplement of [197].

3.2 Experiments after Hong-Ou-Mandel

In the present work we are mainly concerned with the fundamental HOM experiment as introduced in Sect. 2.4. Therefore, we restrict the following discussions to symmetric beam splitters represented by the unitary matrix (3.5). In this case we find $|\mathcal{U}_{11}|^2 |\mathcal{U}_{22}|^2 = |\mathcal{U}_{12}|^2 |\mathcal{U}_{21}|^2 = |\mathcal{U}_{11}\mathcal{U}_{22}\mathcal{U}_{12}^*\mathcal{U}_{21}^*| = 1/4$ as well as $\Phi_{\mathcal{U}} = \pi$. This reduces the cross-correlation function (3.17) to

$$\mathcal{G}^{(2)}(\tau) = \frac{1}{4(\tau_1 + \tau_2)} \cdot [\exp(-|\tau|/\tau_1) + \exp(-|\tau|/\tau_2) - 2 \exp(-\gamma|\tau| - 2\pi^2\Sigma^2\tau^2) \cos(2\pi\delta\nu\tau)] \quad (3.26)$$

and the overall coincidence probability Eq. (3.25) to

$$p_{\text{coinc}} = \frac{1}{2} \cdot \left(1 - \frac{\text{Re}[w(z)]}{\sqrt{2\pi}\Sigma(\tau_1 + \tau_2)} \right). \quad (3.27)$$

In particular, we are interested in the TPI visibility V , which is related to p_{coinc} via Eq. (2.52) and accordingly reads

$$V = \frac{\text{Re}[w(z)]}{\sqrt{2\pi}\Sigma(\tau_1 + \tau_2)}. \quad (3.28)$$

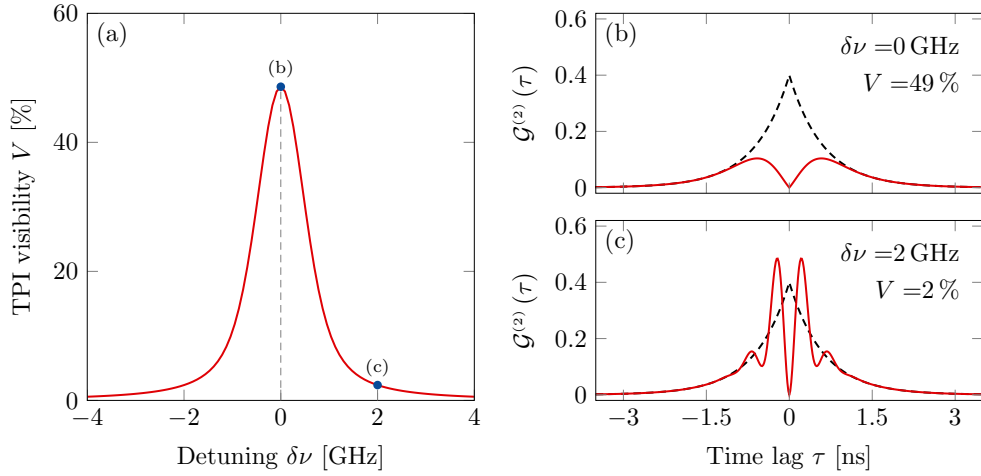


Figure 3.2. Impact of spectral tuning on the two-photon interference visibility. The illustrated example employs the radiative lifetimes $\tau_1 = 700$ ps, $\tau_2 = 550$ ps, pure dephasing rates $\Gamma_1^* = 400$ MHz, $\Gamma_2^* = 200$ MHz, and inhomogeneous broadening $\sigma'_1 = 600$ MHz, $\sigma'_2 = 500$ MHz. Shown is (a) Two-photon interference visibility as function of spectral detuning, (b) and (c) corresponding cross-correlation functions at detunings $\delta\nu = 0$ GHz and $\delta\nu = 2$ GHz, respectively (red). The black dashed curves correspond to the incoherent limits $\mathcal{G}_0^{(2)}(\tau)$. Adapted with permission from [197], IOP Publishing Ltd on behalf of Deutsche Physikalische Gesellschaft.

HOM experiments using solid state emitters typically require tuning mechanisms to match the emission frequencies of both sources. It is common to verify an ideal spectral overlap by measuring the TPI visibility V as function of the detuning $\delta\nu$. A tuning curve of this kind based on Eq. (3.28) is depicted in Fig. 3.2 (a) for an arbitrarily chosen emitter pair (see caption for parameters). Corresponding cross-correlation functions according to Eq. (3.26) are shown in (b) and (c) as red curves. If both emitters are in tune with each other [$\delta\nu = 0$ GHz, (b)], a maximum visibility of $V = 49\%$ is obtained. For a detuning of $\delta\nu = 2$ GHz as shown in (c), the visibility is reduced to only $V = 2\%$, reflecting the poor spectral overlap of both photons. Additionally, quantum beats appear for nonzero detuning rising from the interference term in Eq. (3.26).

3.2.1 Comparison to Literature

The novelty and advantage of the presented formalism mainly resides in the simultaneous consideration of PD and SD in a framework for HOM experiments based on compact equations. However, the impact of either of the two effects separated has been investigated before. In [152], for instance, a pair

of dissimilar photons under the influence of only PD is considered and an expression for the TPI visibility is derived. The absence of SD corresponds to $\Sigma = 0$, but the answer of Eq. (3.28) in this limit is not obvious. Therefore, we need to reevaluate the Fourier transformation (3.23) with $g(\tau) = 1$, which leads to

$$V = \frac{4}{\tau_1 + \tau_2} \cdot \frac{1/\tau_1 + 1/\tau_2 + 2\Gamma_1^* + 2\Gamma_2^*}{(1/\tau_1 + 1/\tau_2 + 2\Gamma_1^* + 2\Gamma_2^*)^2 + 16\pi^2\delta\nu^2}. \quad (3.29)$$

This is indeed in agreement with the expression found in [152]. If we further restrict Eq. (3.29) to two identical photons with $\tau_{1,2} = \tau_r$, $\Gamma_{1,2}^* = \Gamma^*$, as well as $\delta\nu = 0$, we find $V = \tau_{\text{coh}}/(2\tau_r)$ with the coherence time given by $1/\tau_{\text{coh}} = 1/(2\tau_r) + \Gamma^*$. This equals the expression derived in [196] for two identical, but independently dephasing emitters. It is worth noting that this definition of the optical coherence time is equivalent to the well-known expression [228]

$$\frac{1}{T_2^*} = \frac{1}{2T_1} + \frac{1}{T_2} \quad (3.30)$$

for the free induction decay time T_2^* of electron spins originally introduced for nuclear magnetic resonance. It is composed of the spin-lattice and spin-spin relaxation times T_1 and T_2 describing the decay and decoherence of the longitudinal and transversal magnetization components, respectively.

In order to theoretically describe the experiments presented in [151] the authors establish a model for two emitters of equal radiative lifetime that disregards PD, but includes inhomogeneous broadening based on a distribution comparable to Eq. (3.13). In the scope of our work, this limit is covered by equations (3.26) and (3.28) by simply setting $\Gamma_{1,2}^* = 0$. However, despite a similar approach we find that both cross-correlation function and visibility do not agree with [151]. In particular, one finds that for sufficiently large inhomogeneous broadening the formalism in [151] yields negative visibilities. As the coincidence probability is restricted to $p_{\text{coinc}} = 1/2$ in its incoherent limit, this is an impossible outcome suggesting that the underlying derivation might be erroneous. Indeed, it can be seen that the employed wave-functions and their frequency distributions are improperly normalized, which might have caused the wrong result.

Moreover, our formalism can be independently tested by reproducing experimental TPI visibilities reported in literature. Although a large number of HOM experiments between photons of independent solid state emitters have been performed, only some of those are suitable for that purpose. On one hand, the experiments presented in [64–68, 154] employ non-resonant or cw-excitation schemes and are therefore exposed to an uncertainty in the photon arrival time, which is not covered by our equations. For other experiments the necessary emitter parameters are not given in an unambiguous way, rendering a reliable application of our equations impossible [152, 153, 229]. Furthermore,

Table 3.1. Application of remote HOM formalism to literature values. Theoretical visibilities V_{th} obtained from Eq. (3.28) are compared to experimental visibilities $V_{\text{exp}}^{\text{ref}}$ and accompanying theoretical predictions $V_{\text{th}}^{\text{ref}}$. Radiative lifetime τ_{r} , coherence time τ_{coh} , inhomogeneous linewidth σ'_{max} , and pure dephasing rate Γ^*_{max} are given in pairs corresponding to emitter 1 / emitter 2. Reproduced with permission from [197], IOP Publishing Ltd on behalf of Deutsche Physikalische Gesellschaft.

Ref.	τ_{r} [ps]	τ_{coh} [ps]	σ'_{max} [GHz]	Γ^*_{max} [GHz]	$V_{\text{exp}}^{\text{ref}}$ [%]	$V_{\text{th}}^{\text{ref}}$ [%]	V_{th} [%]
[151]	670/660	330/420	1.39/1.04	2.28/1.62	39	36	28-32
[155]	256/230	256/256	1.46/1.37	1.95/1.73	51	56	53-57
[156]	155/187	153/123	2.46/3.53	3.31/5.46	41	40	40-44

to the best of our knowledge no report on HOM experiments exists, which provides a full set of parameters consisting of radiative lifetime τ_{r} , pure dephasing rate Γ^* and inhomogeneous linewidth σ' for both emitters. In case of the three experiments [151, 155, 156], however, both radiative lifetimes and coherence times τ_{coh} are stated instead. From Eq. (2.15) we find that Γ^* can be expressed in terms of σ' according to

$$\Gamma^* = \frac{1}{\tau_{\text{coh}}} - \frac{1}{2\tau_{\text{r}}} - \frac{\pi^2 \sigma'^2 \tau_{\text{coh}}}{4 \ln 2}. \quad (3.31)$$

The solution of this equation yields pairs of Γ^* and σ' for the given τ_{r} and τ_{coh} . Their maxima Γ^*_{max} and σ'_{max} correspond to the respective boundaries $\sigma' = 0$ as well as $\Gamma^* = 0$ and are given by

$$\Gamma^*_{\text{max}} = \frac{1}{\tau_{\text{coh}}} - \frac{1}{2\tau_{\text{r}}} \quad \text{and} \quad \sigma'_{\text{max}} = \left[\frac{4 \ln 2}{\pi^2 \tau_{\text{coh}}} \left(\frac{1}{\tau_{\text{coh}}} - \frac{1}{2\tau_{\text{r}}} \right) \right]^{\frac{1}{2}}. \quad (3.32)$$

Eventually, considering all possible combinations of Γ^* and σ' we find a range of TPI visibilities V_{th} according to Eq. (3.28) at $\delta\nu = 0$, which are summarized in Tab. 3.1. Comparing V_{th} to the experimentally obtained visibilities, we find excellent agreement for [155, 156]. In case of [151] our prediction underestimates the experimental visibility by almost 10%, while the accompanying theoretical value $V_{\text{th}}^{\text{ref}}$ matches far better. Note, however, that the theory provided in [151] is erroneous (see preceding paragraph) and $V_{\text{th}}^{\text{ref}}$ therefore not reliable. The reason for the disagreement between experimental value and V_{th} , on the other hand, can not be unambiguously identified.

3.2.2 Remote HOM Visibility and Coherence Time

In order to shed more light on the simultaneous impact of PD and SD on TPI visibilities, we restrict ourselves to an ideal scenario of an experiment with two identical emitters, i.e. we assume $\tau_{1,2} = \tau_r$, $\Gamma_{1,2}^* = \Gamma^* \rightarrow \gamma = 2\Gamma^* + 1/\tau_r$, $\sigma_{1,2} = \sigma \rightarrow \Sigma^2 = 2\sigma^2$, as well as $\delta\nu = 0$. In the following, we divide both broadening contributions by the decay rate $1/\tau_r$, which leads to the normalized homogeneous and inhomogeneous linewidths $\vartheta_{\text{PD}} = \gamma \cdot \tau_r$ and $\vartheta_{\text{SD}} = \sigma' \cdot \tau_r$. Both parameters enable us to assess the emitter pair independent of the radiative lifetime. Note that the Fourier limit corresponds to $\vartheta_{\text{PD}} = 1$ as well as $\vartheta_{\text{SD}} = 0$ and increasing values indicate a loss of coherence. We are now able to rewrite the TPI visibility (3.28) as

$$V = \sqrt{\frac{2 \ln 2}{\pi}} \cdot \frac{\text{Re}[w(z)]}{2\vartheta_{\text{SD}}} \quad \text{with} \quad z = i \sqrt{\frac{\ln 2}{2\pi^2}} \cdot \frac{\vartheta_{\text{PD}}}{\vartheta_{\text{SD}}} \quad (3.33)$$

which is depicted in Fig. 3.3 (a) as contour plot over both ϑ_{PD} and ϑ_{SD} . Emitter pairs at the Fourier limit with a TPI visibility of 100% can be found at the bottom left corner. The black solid and dashed contour lines indicate levels of constant visibility and normalized coherence time $x_c = \tau_{\text{coh}}/(2\tau_r)$. While the iso-visibility lines were found numerically, the iso-coherence time lines can be obtained from Eq. (2.15) and read

$$x_c = -\frac{\ln 2}{2\pi^2} \cdot \frac{\vartheta_{\text{PD}}}{\vartheta_{\text{SD}}^2} + \sqrt{\left(\frac{\ln 2}{2\pi^2} \cdot \frac{\vartheta_{\text{PD}}}{\vartheta_{\text{SD}}^2}\right)^2 + \frac{\ln 2}{\pi^2 \cdot \vartheta_{\text{SD}}^2}}. \quad (3.34)$$

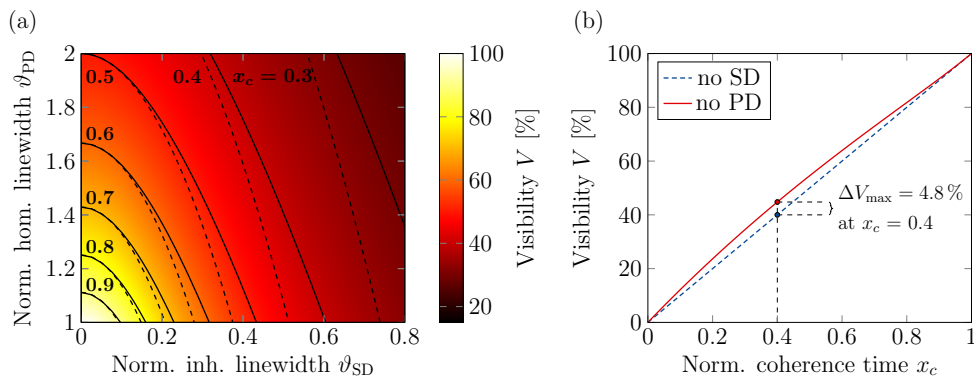


Figure 3.3. Simultaneous influence of pure dephasing and spectral diffusion on remote HOM visibility. (a) Visibility plotted as function of normalized homogeneous and inhomogeneous linewidths ϑ_{PD} and ϑ_{SD} as defined in main text. Solid and dashed contour lines indicate levels of constant visibility and normalized coherence time x_c , respectively. (b) Visibility over normalized coherence time for the two limiting cases of no pure dephasing (PD, red) and no spectral diffusion (SD, blue dashed). Reproduced with permission from [197], IOP Publishing Ltd on behalf of Deutsche Physikalische Gesellschaft.

Comparing both contour lines we recognize, as expected, that high TPI visibilities generally require high coherence times. In [196] it was shown that for two identical, but independently dephasing, emitters it is $V = x_c$ in absence of SD. While this indeed holds for $\vartheta_{\text{SD}} = 0$, we see that V and x_c disagree for an increasing inhomogeneous linewidth, i.e. $\vartheta_{\text{SD}} > 0$. This is further illustrated in Fig. 3.3 (b). Here, the visibility is plotted against x_c in the two limiting cases of vanishing pure dephasing resulting in $V_{\text{noPD}} = V(\vartheta_{\text{PD}} = 1, \vartheta_{\text{SD}})$ as well as vanishing spectral diffusion corresponding to $V_{\text{noSD}} = V(\vartheta_{\text{PD}}, \vartheta_{\text{SD}} = 0) = x_c$. The graph reveals $V_{\text{noPD}} \geq V_{\text{noSD}}$, which indicates that V cannot be generally expressed as function of x_c . The maximum deviation, however, is no more than $\Delta V_{\text{max}} = 4.8\%$ at $x_c = 0.4$ so that V_{noSD} can be used as a reasonably accurate lower bound.

From this direct comparison of PD and SD we realize that both homogeneous and inhomogeneous line broadening mechanisms corrupt remote TPI applications to a comparable extent. This might seem counter-intuitive considering that each individual photon is Fourier-limited in absence of PD. The impact of an independent frequency-jitter completely unfolds, however, for long measurement runs, which enable both emitters to explore their entire frequency ranges.

3.2.3 Quantum Interference of Consecutively Emitted Photons

Up to this point we restricted ourselves to HOM experiments with photons emitted by two independent sources, whose emission frequencies are entirely uncorrelated. In Sect. 5.3 we will encounter a different situation: Following the experimental scheme first presented in [230], we investigate TPI between photons consecutively emitted by the same source. With the experimental details being addressed in Sect. 5.3.1, it is sufficient at this point to consider that both photons were emitted with a given delay τ_{mzi} ². Typically, τ_{mzi} significantly exceeds the radiative lifetime τ_r (e.g. $\tau_{\text{mzi}} > 5 \cdot \tau_r$ in [230]). In this case any phase correlation between the individual photons is certainly lost and the treatment of PD as presented in Sect. 3.1.2 can be adopted without further modifications. In contrast SD diffusion processes act on a time scale comparable to or larger than τ_r [192–195] entailing a correlation of the carrier frequencies. Accordingly, the static distribution $\varrho(\Delta\nu)$ of the frequency displacement $\Delta\nu$ introduced in Eq. (3.13) is not applicable here.

In order to adjust our formalism, we employ the time dependent description of SD given in Sect. 2.2.3 in the following way: Assume that the emission spectrum is centered around ν_0 and exhibits an inhomogeneous width σ_0 . The probability $p_1(\nu')$ of the first emitted photon having a carrier frequency ν' is

²Note that the index *mzi* refers to the Mach-Zehnder interferometer, which was employed to set the delay throughout all experiments. See Sect. 5.3.1 for further details.

simply given by the equilibrium distribution

$$p_1(\nu') = \frac{1}{\sqrt{2\pi\sigma_0^2}} \cdot \exp\left[-\frac{(\nu' - \nu_0)}{2\sigma_0^2}\right]. \quad (3.35)$$

The carrier frequency of the second photon, however, depends on ν' and must therefore be described by Eq. (2.20). In particular, the probability to find it at $\nu = \nu' + \Delta\nu$ is

$$p_2(\nu' + \Delta\nu, \tau_{\text{mzi}}) = \frac{1}{\sqrt{2\pi\sigma^2(\tau_{\text{mzi}})}} \cdot \exp\left\{-\frac{[\nu' + \Delta\nu - \nu_c(\tau_{\text{mzi}})]^2}{2\sigma^2(\tau_{\text{mzi}})}\right\} \quad \text{with} \quad (3.36)$$

$$\begin{aligned} \sigma^2(\tau_{\text{mzi}}) &= \sigma_0^2 \cdot [1 - \exp(-2\tau_{\text{mzi}}/\tau_{\text{sd}})] \quad \text{and} \\ \nu_c(\tau_{\text{mzi}}) &= \nu_0 + (\nu' - \nu_0) \cdot \exp(-\tau_{\text{mzi}}/\tau_{\text{sd}}), \end{aligned}$$

where we substituted $\tau_{\text{sd}} = 1/\beta$ with τ_{sd} being the frequency correlation time associated with SD (or *memory depth* [192]). In agreement with Eq. (3.13), the modified distribution $\varrho(\Delta\nu, \tau_{\text{mzi}})$ equals the cross-correlation of p_1 and p_2 reading

$$\varrho(\Delta\nu, \tau_{\text{mzi}}) = \int_{-\infty}^{+\infty} p_1(\nu') \cdot p_2(\nu' + \Delta\nu, \tau_{\text{mzi}}) d\nu' \quad (3.37)$$

$$\begin{aligned} &= \frac{1}{\sqrt{2\pi\Sigma^2(\tau_{\text{mzi}})}} \exp\left[-\frac{\Delta\nu^2}{2\Sigma^2(\tau_{\text{mzi}})}\right] \quad \text{with} \\ \Sigma^2(\tau_{\text{mzi}}) &= 2\sigma_0^2 \cdot [1 - \exp(-\tau_{\text{mzi}}/\tau_{\text{sd}})]. \end{aligned} \quad (3.38)$$

Comparing Eq. (3.37) to our former result Eq. (3.13), we recognize only two differences being **(i)** the absence of detuning, i.e. $\delta\nu = 0$, and **(ii)** the new width of the distribution $\Sigma(\tau_{\text{mzi}})$, which now includes an explicit dependency on τ_{mzi} according to Eq. (3.38). Taking these modifications into account and considering $\tau_{1,2} = \tau_r$ as well as $\Gamma_{1,2}^* = \Gamma^* \rightarrow \gamma = 2\Gamma^* + 1/\tau_r$, it is straightforward to rewrite the cross-correlation function (3.26) as

$$\mathcal{G}^{(2)}(\tau) = \frac{1}{4\tau_r} \cdot [\exp(-|\tau|/\tau_r) - \exp(-\gamma|\tau| - 2\pi^2\Sigma^2(\tau_{\text{mzi}})\tau^2)] \quad (3.39)$$

and the TPI visibility (3.28) as

$$V(\tau_{\text{mzi}}) = \frac{\text{Re}[w(z)]}{2\sqrt{2\pi} \cdot \tau_r \cdot \Sigma(\tau_{\text{mzi}})} \quad \text{with} \quad z = i \frac{1/\tau_r + 2\Gamma^*}{2\pi\sqrt{2} \cdot \Sigma(\tau_{\text{mzi}})}. \quad (3.40)$$

The resulting visibility is illustrated for an arbitrary emitter in Fig. 3.4 as red curve (see caption for emitter parameters). It can be seen that the visibility converges towards constant values for both $\tau_{\text{mzi}} \rightarrow 0$ and $\tau_{\text{mzi}} \rightarrow \infty$. The limit for small τ_{mzi} is set by PD, which affects each photon to its full

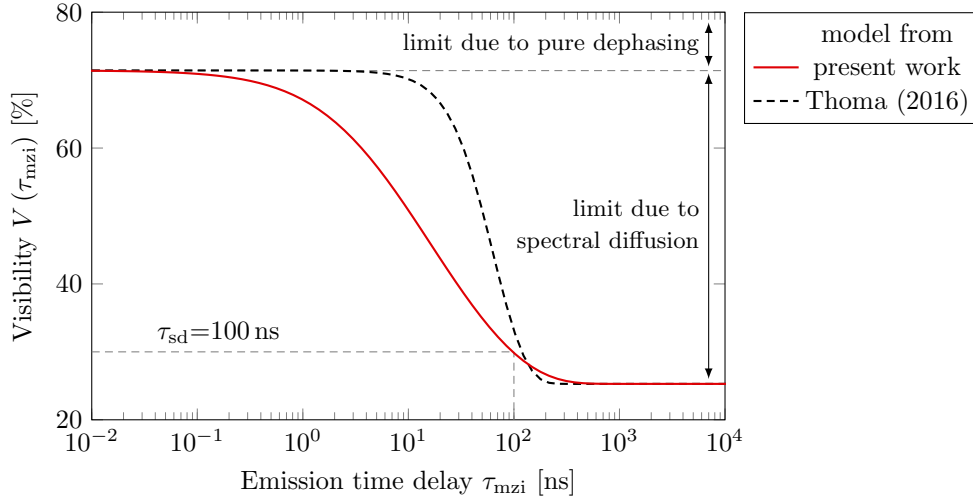


Figure 3.4. Dependency of two-photon interference visibility on emission time delay. Comparison of model presented here (red) with model derived in [192] (black dashed) for an emitter with $\tau_r=1$ ns, $\Gamma^*=200$ MHz, $\sigma'_0=1$ GHz, and $\tau_{sd}=100$ ns. The dephasing rate Γ'_0 appearing in [192] was set to 975 MHz to match the limits of both models for $\tau_{mzi} \rightarrow \infty$.

extent independent of the emission time delay, while the influence of SD can be neglected. For intermediate τ_{mzi} the visibility drops due to SD indicating a progressing loss of frequency correlation between both photons. Accordingly, the limit at large delays corresponds to uncorrelated photons and is best described by the frequency distributions at equilibrium. Furthermore, we recognize that for $\tau_{mzi} = \tau_{sd}$ SD almost fully unfolded.

An alternative model was proposed in [192], which also has been used to describe the data presented in [193, 195]. The model does not include SD as an inhomogeneous broadening of the emission line, but rather as an effect increasing the PD rate as function of τ_{mzi} . On that account, it is split into two parts: a static contribution, which equals Γ^* in our model, and a time dependent term reading

$$\Gamma'(\tau_{mzi}) = \Gamma'_0 \cdot \left\{ 1 - \exp \left[-(\tau_{mzi}/\tau_{sd})^2 \right] \right\}. \quad (3.41)$$

It is then possible to write the overall visibility using Eq. (3.29) for two photons from the same source as

$$V(\tau_{mzi}) = \frac{1/\tau_r}{1/\tau_r + 2 \cdot [\Gamma^* + \Gamma'(\tau_{mzi})]}. \quad (3.42)$$

This equation agrees with [192] except for the factor of '2', which, however, only stems from a different definition of the PD rate. The result is plotted in

Fig. 3.4 as black dashed curve based on the previously used parameters. The visibility exhibits the same limits we observed before, but drops later and more rapidly instead. As consequence, this model yields small frequency correlation times compared Eq. (3.40), if used as fitting function for experimental data. We like to mention that the approach used in [192] is sufficient to qualitatively describe the visibility as function of τ_{mzi} , but significantly overstretches the scope of pure dephasing. The phase correlation (2.13), which is typically used to describe the regime of PD, is only valid in the limit of fluctuations, which are fast compared to τ_r (see Sect. 2.2.1). Here, it is used, however, for emitter systems, whose memory depth τ_{sd} is several orders of magnitude larger than τ_r . Accordingly, we suggest that Eq. (3.40) is more appropriate to model the time dependent impact of SD on TPI visibilities.

3.3 Summary

In this chapter we established a theoretical framework to describe correlation measurements taken during TPI experiments on arbitrary linear optical gates. The equations generalize the well-known formalism introduced in [217]. It was then applied to obtain expressions for the cross-correlation function and overall coincidence probability, if the gate was fed with two independent, dissimilar photons stemming from solid state emitters being subject to pure dephasing and spectral diffusion. The result was discussed in the special case of HOM experiments and compared to existing formalisms as found in literature. Eventually, the results were adapted to be applicable to consecutively emitted photons, which exhibit a net correlation between their carrier frequencies. The main results are additionally summarized in the *highlights*-box.

CHAPTER 3 - HIGHLIGHTS

Joint Detection Probability

- The well established formalism for HOM experiments [217] was extended to arbitrary linear optical gates represented by a unitary $N \times N$ matrix (Sect. 3.1.1 and

Sect. 3.1.3).

- Given two arbitrary input photons described by dissimilar wave-functions, the resulting Eq. (3.4) yields the probability to obtain two detection events at times t_0 and $t_0 + \tau$ at two distinct output modes.

CHAPTER 3 - HIGHLIGHTS CONTINUED

Solid State Emitters

- The formalism was applied to two photons emitted by independent solid state emitters (Sect. 3.1.2).
- The photons exhibit differing radiative lifetime, relative detuning and an independent phase- and frequency-jitter to account for pure dephasing and spectral diffusion.
- An integration step over the detection time t_0 leads to the cross-correlation (3.17) function yielding the probability to obtain correlated detection events with a time lag of τ .
- Additional integration over τ yields the overall probability to obtain a coincidence [Eq. (3.25)], which follows a Voigt-lineshape as function of the detuning reflecting the homogeneously and inhomogeneously broadened joint spectra of both photons.

HOM Experiments

- The two-photon interference visibility for HOM experiments is given by restricting the result to a symmetric beam-splitter [Eq. (3.28)]
- A comparison to existing formalisms and an application to experimentally obtained visibilities confirms the validity of our equations (Sect. 3.2.1).
- Focusing on the joint impact of homogeneous and inhomogeneous broadening mechanisms reveals that spectral diffusion and pure dephasing have a comparable impact on the interference visibility (Sect. 3.2.2).
- The formalism was extended to describe HOM experiments with consecutively emitted, i.e. non-independent, photons considering their carrier-frequency correlation (Sect. 3.2.3).

Frequency Conversion Setup

The frequency converter (FC) is at the heart of all experiments presented in this work. In the following we outline the setup as a whole and offer detailed information about its principal components and their interplay. Note that the design shown here corresponds to the frequency converter used for the quantum frequency conversion (QFC) experiment with indistinguishable photons from a single QD presented in the next chapter. The setup employed in Chap. 6 exhibits a number of modifications that will be addressed separately. Furthermore, we here discuss measurements quantifying the converter performance and its limitations.

4.1 Overview

The optical setup is illustrated in Fig. 4.1. Its main component is a magnesium oxide doped, periodically poled lithium niobate (MgO:PPLN) waveguide chip designed to support the DFG process defined by $1/905 \text{ nm} - 1/2175 \text{ nm} = 1/1550 \text{ nm}$ (NTT ELECTRONICS, Japan). The signal light at 905 nm is fed into the setup via an optical fiber and collected by an aspherical lens. We use a fiber polarization controller to minimize the optical power transmitted through the subsequent polarizing beam splitter (PBS) in order to ensure the desired vertical polarization. The pump light field at 2175 nm is delivered by a $\text{Cr}^{2+}:\text{ZnS}$ laser in cw-operation (IPG PHOTONICS, USA). A combination of half-wave plate (HWP) and Glan-Taylor calcite-prism (GTP) are used for two purposes: **(i)** to set the initially horizontally polarized pump light to vertical polarization and **(ii)** to control the optical power of the pump light to the level required for maximal conversion efficiency.

Both signal and pump light are overlapped on a dichroic mirror (DM, custom made item, charge O414G037, LAYERTEC, Germany) and simultaneously coupled via an anti-reflection coated zinc selenide aspheric lens (ZnSe AL, II-IV DEUTSCHLAND, Germany) to the WG. To enable simultaneous optimal coupling of both beams, an additional spherical lens (SL) is introduced to the

4. FREQUENCY CONVERSION SETUP

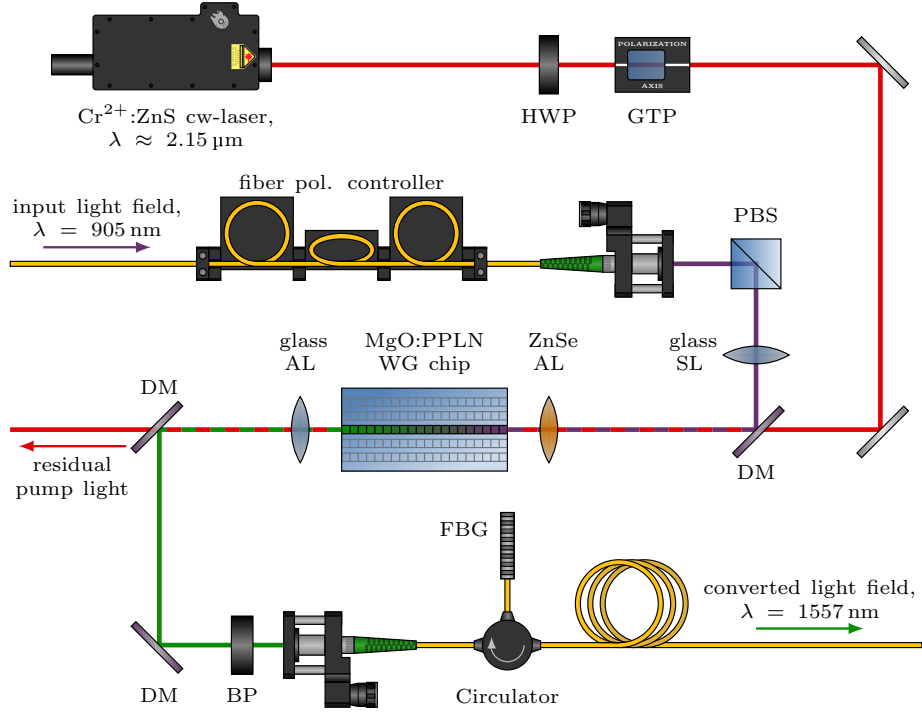


Figure 4.1. Illustration of the Frequency Converter. The pump light (red) is provided by a $\text{Cr}^{2+}:\text{ZnS}$ cw-laser. The combination of a half-wave plate (HWP) and Glan-Taylor prism (GTP) is used to set the pump power. Both pump light and signal light (violet) are set to vertical polarization at the GT and a polarizing beam splitter (PBS), respectively, where a fiber polarization controller is used for the signal light. Combined on a dichroic mirror (DM), both light fields are simultaneously coupled to the waveguide through a ZnSe aspheric lens (AL). The spherical lens (SL) in the signal beam path aids the optimal coupling. The converted telecom light (green) is separated from residual pump light (red) at a second DM and spectrally filtered by a bandpass filter (BP) and the combination of a fiber based circulator and reflective fiber Bragg grating (FBG).

signal beam path (details in Sect. 4.3). In order to achieve the maximum conversion efficiencies the phase-matching condition for the desired DFG-process has to be met. As periodicity of the periodic poling and WG dimension are fixed parameters, the only remaining degree of freedom is the crystal temperature, which is here stabilized with help of a commercially available temperature controller (model TED200C, THORLABS, USA). To measure and control the temperature a thermistor with negative temperature coefficient and a thermoelectric Peltier element are used, respectively. Eventually, the converted light at 1550 nm is coupled out of the WG and collimated with an anti-reflection coated AL.

The last essential step is spectral filtering of the converted photons in order to isolate them from any other present light field, which may stem from **(i)** residual pump light, **(ii)** light from non-phase-matched nonlinear optical processes of second and higher order, as well as **(iii)** parametric fluorescence [102] and **(iv)** Raman scattering [101, 231] of the pump. In order to minimize these unwanted contributions we use two different components being an optical bandpass filter with central wavelength 1550 nm and bandwidth 20 nm (BP, item 1550BP20, OMEGA OPTICAL, USA) as well as a system consisting of fiber Bragg grating (FBG, AOS GmbH, Germany) and circulator acting as another 120 GHz wide bandpass filter centered at 1557 nm. The relevance of all noise sources will be detailed in sections 4.5, 5.1.2, and 6.2.2.

4.1.1 Nonlinear Waveguide Chip

All nonlinear optical devices employed in the present work rely on periodically poled lithium niobate (LN) crystals [97]. The material is known for its comparatively large nonlinear coefficients [205–208], wide transparency range from 0.35 μm to $>4\mu\text{m}$ [207], and ferroelectricity, which enables QPM via ferroelectric poling [232] [compare Fig. 4.2 (a)]. Typically LN single crystals are not available in their stoichiometric composition LiNbO_3 , but in a congruent composition, in which up to 3% of all Li ions are substituted by Nb ions [233]. However, it has been observed that congruent LN is prone to photorefractive effects, which significantly degrade its nonlinear optical properties [234]. A common approach to minimize the photorefractive effect is to dope the LN crystal, for instance with MgO or ZnO. Therefore, we here exclusively use LN crystals with 5 mol% MgO doping.

Both frequency converters used for the experiments presented in chapters 5 and 6 utilize LN crystals purchased from NTT ELECTRONICS, Japan (model WD-1550-000-A-C-C-S009, S/N 3071357 and 3071358). The LN is bonded on a 40 mm long, 6 mm wide, and 0.5 mm high lithium tantalate (LT) substrate [Fig. 4.2 (b) and (c)]. The crystal is z -cut, thus the largest nonlinear coefficient d_{33} [205, 208] can be exploited if all interacting light fields are vertically polarized, i.e. their polarization is parallel to the z -axis [compare Fig. 4.2 (a) and (c)]. To achieve high conversion efficiencies at moderate pump power the LN crystal is furthermore shaped into WGs by mechanically thinning it to a thickness of 10 μm and cutting ridge WGs using a dicing saw. Both WG chips feature 9 groups of WGs with QPM pitches ranging from 24.3 μm to 24.5 μm in steps of 25 nm. The chosen QPM pitches support the desired DFG process $1/905\text{ nm} - 1/2175\text{ nm} = 1/1550\text{ nm}$ for moderate temperatures below 100 $^\circ\text{C}$. Each group contains 2 WGs with a width of 10.8 μm and 11.6 μm , respectively. The input and output facets of the crystal are coated with dielectric coatings minimizing reflection losses for all participating light fields.

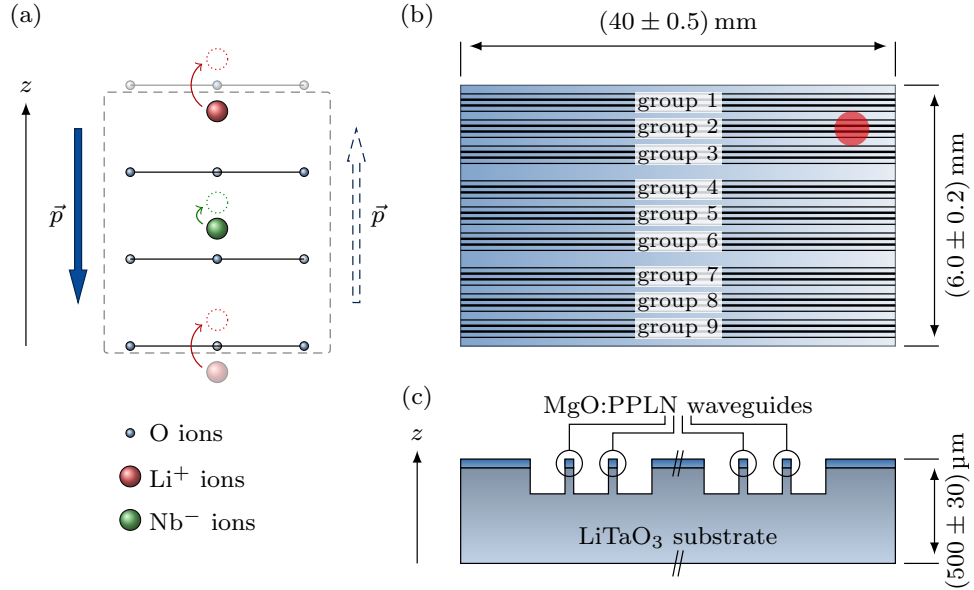


Figure 4.2. Lithium niobate as platform for nonlinear optics.

(a) Illustration of ferroelectric poling (after [97]): Both Nb and Li ions have two stable positions along the z -axis of the crystal. In the configuration indicated by solid spheres a positively charged Li ion resides in the upper part of the unit cell (gray dashed box) causing a dipole moment \vec{p} anti-parallel to the z -axis. Upon ferroelectric poling the ions change to the dashed positions. The unit cell now contains a Li ion in its lower part, i.e. the dipole moment turned by 180° pointing along the z -axis. (b) Top view and (c) cross-section of the geometry of the employed LN WG chips (reproduced based on [235]). The red circle in (b) is physically present on the chip to indicate its orientation.

4.1.2 Pump Laser System

To stimulate the down-conversion process $905\text{ nm} \rightarrow 1550\text{ nm}$ a pump light source at around 2175 nm is required, which meets a number of criteria: **(i)** an output power exceeding 1 W to achieve the maximum conversion efficiency, **(ii)** single frequency operation with small linewidth and high coherence time for minimum degradation of the single photon spectral and temporal properties (QD emission: linewidth $\mathcal{O}(1\text{ GHz})$, coherence time $\mathcal{O}(100\text{ ps})$, see e.g. [236]), **(iii)** single transversal mode operation for high coupling efficiencies to the WGs and optimal mode overlap with other participating light fields, as well as **(iv)** a broad tuning range, as both the exact QD emission wavelength and converted target-wavelength within the telecom C-band are not known a priori.

In preceding QFC experiments within our working group [231, 237], home-built optical parametric oscillators (OPO) have been employed for this task, as

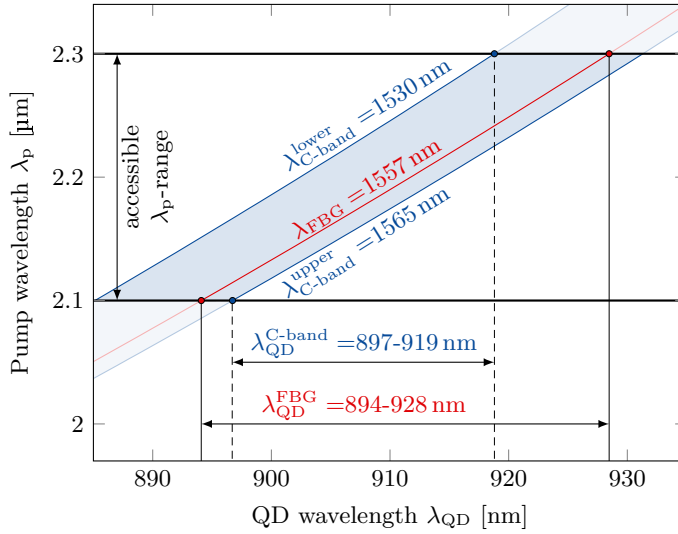


Figure 4.3. Telecom wavelengths accessible with the $\text{Cr}^{2+}:\text{ZnS}$ pump laser system. Pump laser wavelength required for conversion of a given QD emission wavelength to the telecom C-band (blue shaded area, $\lambda_{\text{C-band}} = 1530\text{-}1565$ nm). Exploiting the available pump laser tuning range $\lambda_p = 2.1\text{-}2.3$ μm , it is possible to tune the converted light from any QD emitting in the range $\lambda_{\text{QD}}^{\text{C-band}} = 897\text{-}919$ nm across the entire telecom C-band. Considering the FBG filter-window centered around $\lambda_{\text{FBG}} = 1557$ nm (red curve), QDs with $\lambda_{\text{QD}}^{\text{FBG}} = 894\text{-}928$ nm can be converted.

appropriate laser systems were not available. However, recent progress in the development of lasers based on transition metal doped II-IV chalcogenides led to laser systems fulfilling all requirements mentioned above [238]. Here, we use single frequency tunable lasers in cw operation based on $\text{Cr}^{2+}:\text{ZnS}$ as active laser medium (model CLT-2175/200-1SF, S/N 1411145 and 1411146, IPG PHOTONICS, USA). The lasers are optically pumped by an integrated Erbium-doped fiber laser at 1567 nm (model ELR-20-1567-LP, IPG PHOTONICS, USA) and deliver linearly polarized light at an optical power of > 1.5 W in a tuning range from 2.1 μm to 2.3 μm with a spectral linewidth of around 1 MHz [239]. Fig. 4.3 illustrates accessible telecom wavelengths λ_{tel} as obtained from the underlying energy conservation law of a DFG process for different QD emission wavelengths λ_{QD} and considering the available pump laser tuning range. It can be seen that converted light from QDs with $\lambda_{\text{QD}} = 897\text{-}919$ nm can be tuned within the entire telecom C-band (blue shaded area, $\lambda_{\text{tel}} = 1530\text{-}1565$ nm). In our experiments the target-wavelength is determined by the FBG-based bandpass filter with center-wavelength $\lambda_{\text{tel}} = 1557$ nm, which corresponds to $\lambda_{\text{QD}} = 894\text{-}928$ nm (red curve).

4.2 Temperature Tuning

In the remainder of this chapter, we present a number of performance tests, all of which conducted on the first-built frequency converter prior to the experiments shown in Chap. 5. In particular this means that these measurements were performed using the WG-chip with S/N 3071357 and pump laser with S/N 1411145.

First we measure SPDC spectra and investigate their temperature dependencies in order to identify ideal operation conditions for each WG. In the scope of only this section we employ the conventional nomenclature for parametric fluorescence, i.e. we denote the light field with highest energy as pump, as it exhibits by far the highest field amplitudes and drives the process. Accordingly, we call the other two fields signal and idler, where idler corresponds to the field with lowest photon-energy. As pump, we use light at $\lambda=904.7$ nm (i.e. around the anticipated QD emission wavelength) with a power of 31 mW provided by a green-pumped cw singly resonant OPO [231, 240], couple it into a WG, and measure the spectral distribution of its parametric fluorescence at telecom wavelengths using an optical spectrum analyzer (OSA, model AQ6370B, YOKOGAWA, Japan). The black curve in Fig. 4.4 (a) shows a typical spectrum, here taken from WG 1 in group 6 (poling period $\Lambda=24.425$ μm , nominal WG width $b_{\text{nom}}=10.8$ μm) at a crystal temperature of 26.4 °C. Its most prominent feature is the presence of two peaks located at 1415 nm and 1543 nm. It is important to note that these peaks do not correspond to a signal/idler wavelength-combination, as the idler wavelength is at >2 μm . Instead both peaks stem from the signal light-field, i.e. the phase-matching condition $\Delta\beta = 0$ [cf. sections 2.3.1 and 2.3.2, in particular Eq. (2.31)] is fulfilled for two different wavelengths and the phase-mismatch reaches an extremum in between. Moreover, both peaks are extraordinarily broad with a FWHM of 40 nm and 75 nm (compared to ≈ 10 nm in [231, 237]), which indicates a small slope of the phase-mismatch in this region. Figures 4.4 (c) and (d) show the center-wavelengths of both peaks measured at different temperatures for WGs with the nominal width $b_{\text{nom}}=10.8$ μm and 11.6 μm , respectively. Only for 10 out of 18 WGs phase-matching was achieved with accessible temperatures ranging from 20 °C to 55 °C. However, it can be seen that all of those WGs enable frequency conversion into the telecom C-band (blue shaded region).

According to our considerations in Sect. 2.3.2, a theoretical description of these data needs to consider the impact of waveguide dispersion on phase mismatch $\Delta\beta$ and normalized interaction length ΓL . To that end, we implement a MATLAB-based simulation of SPDC-spectra and tuning curves that incorporates multiple steps, being

- (i) thermal expansion regarding the set-temperature of the WG chip including change of width b , thickness d , length L and poling period Λ using expansion coefficients of LN given in [241],

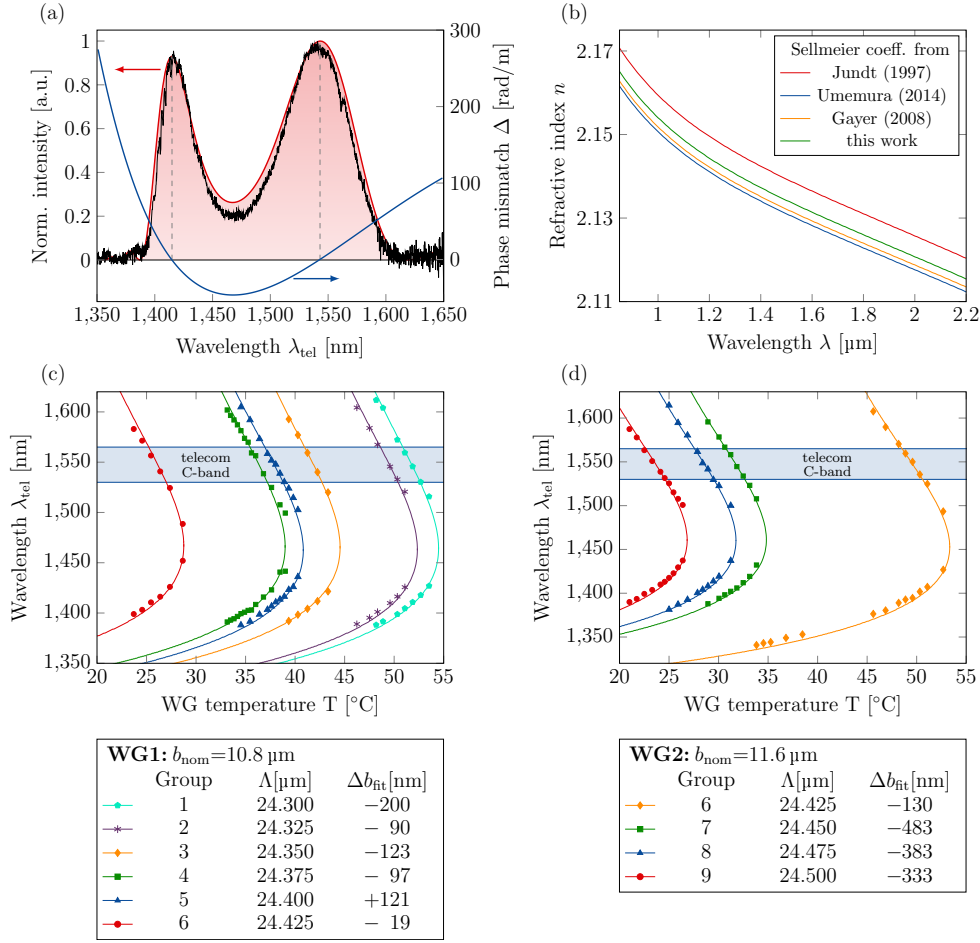


Figure 4.4. Temperature tunability of SPDC spectra. (a) Spectral distribution of parametric fluorescence for pump-light at $\lambda=904.7 \text{ nm}$ with 31 mW obtained from WG 1 of group 6 at a crystal temperature of $26.4 \text{ }^{\circ}\text{C}$ (data black, simulation red). The simulated phase-mismatch Δ (blue) shows zero-crossings at two different signal-wavelengths, leading to two signal-peaks. (b) Refractive index for LN calculated with various sets of Sellmeier-coefficients. The green curve corresponds to the modified Sellmeier-coefficients from [212] used for the presented simulations. (c), (d) Center-wavelengths of both signal-peaks for WGs with $b_{\text{nom}}=10.8 \mu\text{m}$ and $b_{\text{nom}}=11.6 \mu\text{m}$, respectively. Measured data as marks, simulations as solid lines.

- (ii) evaluating refractive indices of all participating light-fields using temperature dependent Sellmeier-coefficients for air [214] and LT [213] as well as modified coefficients for LN [212],
- (iii) numerical solution of the eigenvalue equations given in Appx. A yielding transversal wavenumbers and displacement of the fundamental guided

mode, which in turn lead to the transversal electrical field component E_x Eq. (2.29) and the effective refractive indices n_{eff} Eq. (2.30), and

- (iv) evaluating phase-mismatch $\Delta\beta$ Eq. (2.31) using n_{eff} as well as
- (v) the desired SPDC-spectrum Eq. (2.37), where the normalized interaction length ΓL is obtained using E_x and the effective nonlinear coefficient d_{eff} . The latter is approximated based on Miller's rule [208, 242].

Using the nominal WG dimensions given in the datasheet [235] and available Sellmeier-coefficients [212, 243–245] both simulated spectra and tuning curves are far off the measurements. However, a fit of the Sellmeier-coefficients taken from [212] leads to a good qualitative agreement with the spectrum shown in Fig. 4.4 (a) [corresponding refractive index shown as green curve in Fig. 4.4 (b), coefficients given in Appx. B]. While these fitted coefficients are sufficient to explain spectrum and tuning curve of this particular WG, the tuning curves of all other waveguides still strongly disagree with the data. Another possibility to adjust the simulations can be found in the WG dimensions: both width b and thickness d differ from their nominal values b_{nom} and d_{nom} due to a limited precision of the fabrication process, i.e. we assume to have $b = b_{\text{nom}} + \Delta b$ and $d = d_{\text{nom}} + \Delta d$. These deviations have a significant impact on the phase-mismatch, which we exploit in a fitting routine that treats all Δb as free parameters. Furthermore, we optimize the WG thickness, but assume it is the same for each WG. The results are plotted as solid curves in Fig. 4.4 (a), (c), and (d) and show a good agreement with all data. The blue curve in Fig. 4.4 (a) corresponds to the simulated phase-mismatch. It confirms our initial assertions that the phase-matching condition $\Delta = 0$ is fulfilled at both signal-peaks. Also, it can be seen that its slope is smaller for the broader peak at 1543 nm. The obtained deviations Δb_{fit} are summarized for all WGs within the legends of Fig. 4.4 (c) and (d). Apart from WG1 in group 5 all WGs appear to be thinner than stated in the datasheet. In average we find $\langle \Delta b_{\text{wg1}} \rangle = -68$ nm and $\langle \Delta b_{\text{wg2}} \rangle = -332$ nm for WGs 1 and 2, respectively, which agrees with an estimated margin of error of ± 0.1 μm stated by the manufacturer¹.

We like to stress that the applied fit should be treated with some caution, as the overall model depends on a large amount of input parameters. Although our selection of free parameters is reasonable, it is also arbitrary to some extent and therefore likely to be not unique.

4.3 Dichroic Waveguide Coupling

Knowing the appropriate phase-matching temperatures, the next step is to approach a stimulated DFG-process. On that account it is necessary to com-

¹Personal communication: Y. Nishida, NTT ELECTRONICS, email, November 20th 2018.

bine the signal- and pump field at 905 nm and 2175 nm on the dichroic mirror and simultaneously couple both to the fundamental mode of the desired WG (compare Fig. 4.1). A technical complication arises from the wavelength dependent focal length shift of the ZnSe aspheric lens due to dispersion: the lens is designed to have an effective focal length of $f_{\text{des}} = 11$ mm at the pump wavelength, while the focal length at 905 nm is only $f_{\text{foc}} = 10.52$ mm [246]. Therefore it is not possible to achieve simultaneous optimal coupling, if both input beams are initially collimated. In the following we present considerations, which lead to a simple optical assembly that allows for high coupling efficiencies of both beams.

First, we assume the ZnSe AL to be at a distance of $d_{\text{foc}} = f_{\text{des}} = 11$ mm to the WG facet, i.e. optimized for the coupling of the pump (see setup schematic in Fig. 4.5). The distance between PBS and AL for coupling is $d_{\text{al}} = 377$ mm. It can be varied only in a limited range due to space limitations of the setup and is therefore considered fixed. The signal light is guided to the setup in a single mode fiber with a mode field diameter of $\text{MFD} = 5.0$ μm (type 780HP, THORLABS, USA) and collected via an aspheric lens with focal length $f_{\text{col}} = 6.31$ mm (model C110TMD-B², THORLABS, USA). The distance between fiber facet and lens d_{col} as well as lens and PBS d_{pbs} are considered free parameters, which should offer sufficient flexibility to achieve optimal coupling. However, it turns out that optimal coupling requires the fiber coupler to be closer to the WG than the PBS, which is not feasible. To compensate this shortcoming, we introduce an additional spherical lens (SL) with focal length 50 mm at a variable distance of d_{sl} to the PBS.

In order to evaluate the coupling efficiency to the WG, we use the ray tracing method of Gaussian beams [247]. The input beam has an initial radius of $w = \text{MFD}/2 = 2.5$ μm determined by the fiber and infinite radius of curvature, as the fiber facet constitutes a focal spot. After propagation through the optical system the input beam at the position of the WG is described by its electrical field E_{in} . The coupling efficiency η_{coup} can now be evaluated by [248]

$$\eta_{\text{coup}} = \frac{|\langle E_{\text{in}}, E_{\text{wg}} \rangle|^2}{\langle E_{\text{in}}, E_{\text{in}} \rangle \cdot \langle E_{\text{wg}}, E_{\text{wg}} \rangle}, \quad (4.1)$$

where E_{wg} is the fundamental WG mode and $\langle E_{\text{in}}, E_{\text{wg}} \rangle$ denotes the spatial overlap integral of E_{in} and E_{wg} . The intensity profile of the guided mode obtained by the method described in Sect. 2.3.2 is depicted in Fig. 4.5 (c). It can be seen that the cross section of the mode reproduces the rectangular shape of the WG, i.e. a unity mode overlap with a rotationally symmetric Gaussian input beam is impossible to achieve. Fig. 4.5 (a) shows the beam diameter evolution for optimized coupling efficiency yielding $\eta_{\text{coup}} = 99\%$

²The specified focal length of $f_{\text{col}} = 6.24$ mm is valid at the design wavelength of 780 nm. Material dispersion leads to $f_{\text{col}} = 6.31$ mm at 905 nm.

4. FREQUENCY CONVERSION SETUP

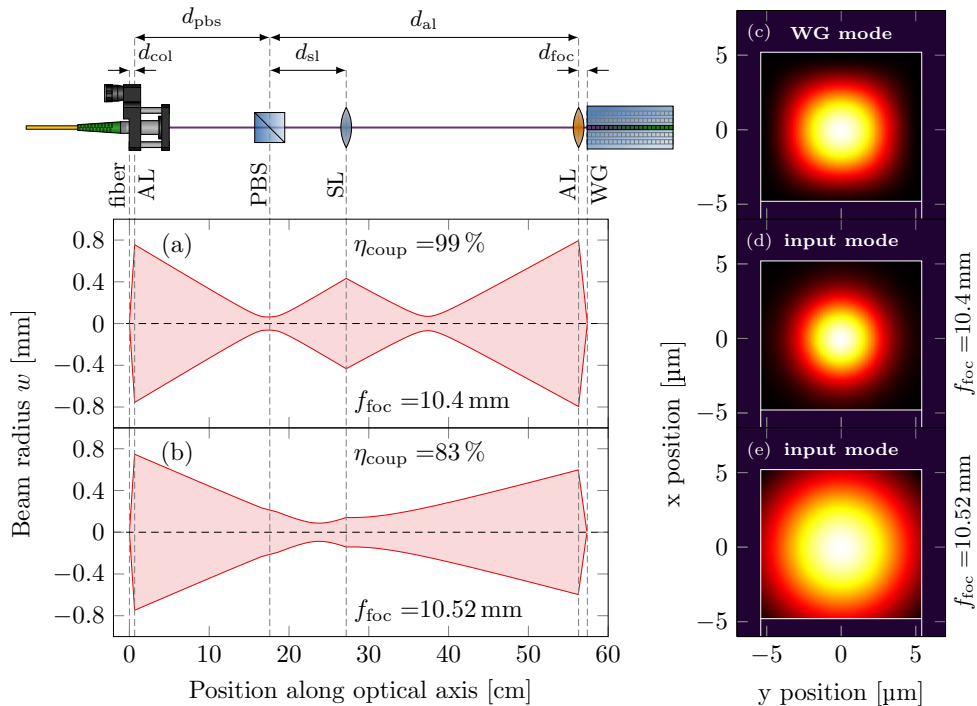


Figure 4.5. Optimal coupling of the signal light. Top left: Schematic of optical system for the signal light, which enters the setup via an optical fiber and is collimated with an aspheric lens (AL). Other optical components are the polarizing beam splitter (PBS), a spherical lens (SL), the ZnSe AL and eventually the waveguide (WG). (a) and (b) depict the evolution of the beam diameter for our optimization using $f_{\text{foc}} = 10.4$ mm and the actual focal length $f_{\text{foc}} = 10.52$ mm of the ZnSe AL, respectively. (c), (d), and (e) are the mode profiles of the fundamental WG mode and the input modes corresponding to (a) and (b).

at $d_{\text{col}} = 6.56$ mm, $d_{\text{pbs}} = 159$ mm, and $d_{\text{sl}} = 86$ mm. The intensity profile of E_{in} shown in Fig. 4.5 (d) illustrates the good overlap with WG mode (c). However, this optimization was performed assuming a focal length of the ZnSe AL of 10.4 mm, as the correct value of 10.52 mm was unknown at the time. The actual setup was built using d_{pbs} and d_{sl} as obtained from the optimization, while d_{col} remained a free parameter during setup alignment. In experiment we measure optical powers of the signal of $P_2 = 7.36$ mW prior to and $P_3 = 5.12$ mW behind the WG at the positions 2 and 3 as indicated in Fig. 4.6 (d). Considering the limited transmittance of $\approx 90\%$ of both dichroic mirrors and aspheric lenses situated in the optical path, we obtain a coupling efficiency of 77%. A simulation with d_{pbs} and d_{sl} taken from the initial optimization as well as the correct focal length $f_{\text{foc}} = 10.52$ mm as fixed parameters is presented in Fig. 4.6 (b) and (e). Corresponding to the real con-

figuration the coupling efficiency was only optimized with respect to d_{col} and evaluates to $\eta_{\text{coup}} = 83\%$, which compares well to the experimentally achieved value. This demonstrates that the applied method is a suitable approach to simultaneously achieve high coupling efficiencies at different wavelengths despite chromatic dispersion. Note that the design of polarization preserving frequency converters recently established within our working group exploits and extends this method to simultaneous coupling at three different wavelengths [249].

4.4 Stimulated Down-Conversion

In this section we present a first test of stimulated down-conversion with classical light fields and assess its efficiency. The measurements were performed with the OPO and pump-laser set to output wavelengths of $\lambda_s = 905.1$ nm and $\lambda_p = 2167$ nm, respectively, corresponding to a telecom wavelength of $\lambda_{\text{tel}} = 1554$ nm. For the conversion we employed WG 1 in group 5 at a crystal temperature of 41°C . Fig. 4.6 (a) shows the spectrum of light collected from the WG output around the telecom C-band center, measured with the OSA. The black curve was obtained in absence of pump light and reveals the typical broad spectral distribution of parametric fluorescence we already encountered in Sect. 4.2. Once the pump light is added, the spectrum changes to a sharp peak at the anticipated telecom wavelength (red curve), corresponding to idler light from the stimulated down-conversion process. It can be seen that the maxima of both curves coincide, indicating that the crystal temperature is set at the ideal operating point to achieve phase-matching. Note that the SPDC spectrum was magnified by a factor of about 10^8 , as the parametric fluorescence is significantly weaker than the telecom light from the DFG process (pW-range vs. mW-range).

The efficiency of a frequency converter is typically assessed by two complementary quantities: the internal conversion efficiency η_{int} and the external device efficiency η_{ext} . While the former is defined as the fraction of signal photons that are transduced to the idler wavelength during propagation in the nonlinear medium, the latter can be interpreted as an input-fiber to output-fiber efficiency of the entire converter. That means it additionally includes all losses that occur on the signal path between input fiber and WG as well as on the telecom path between the WG and the output fiber. The external device efficiency plays a crucial role in the design of fiber-based quantum networks, as it determines the minimum channel length, which is necessary to benefit from the implementation of QFC-devices [237].

A direct measurement of the internal conversion efficiency is elaborate and error-prone, as it requires precise knowledge of coupling efficiencies, losses and detection efficiencies at both the signal and telecom wavelength. However, a good approximation can be obtained measuring the signal depletion η_s as a

4. FREQUENCY CONVERSION SETUP

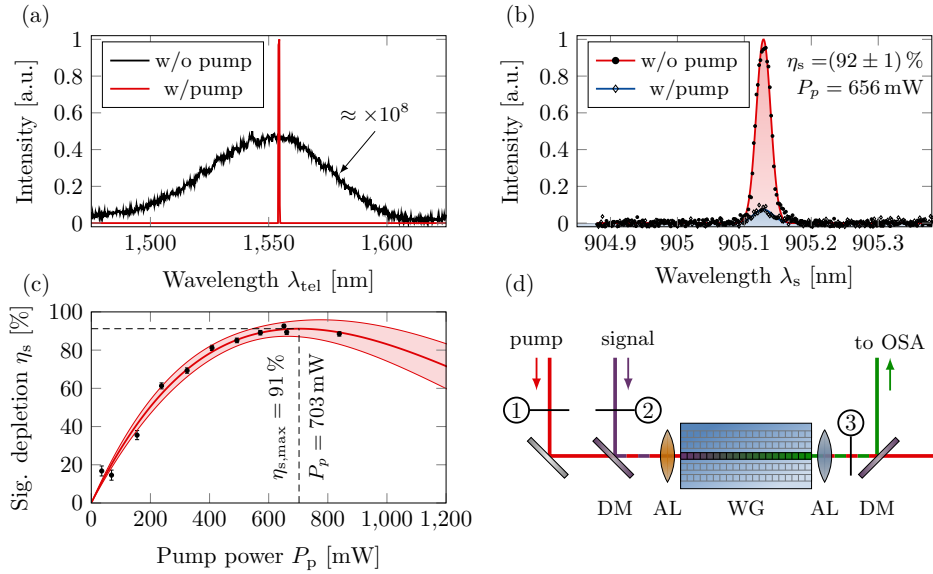


Figure 4.6. Analysis of signal depletion at 905 nm. (a) Spectrum of WG output at the telecom C-band with and without pump laser (red and black, resp.). The black curve stems from parametric fluorescence. (b) The presence of pump light depletes the signal (blue curve). Here, the signal is reduced by 92% at a pump power of 656 mW. (c) Signal depletion as function of pump power (data: black dots, fit: red curve). (d) Illustration of positions, at which optical powers were measured (see main text).

function of the pump power P_p instead, which is defined by

$$\eta_s(P_p) = 1 - \frac{P_s(P_p)}{P_s(0)}. \quad (4.2)$$

Here, P_s is the optical power of the signal taken at any point behind the WG. To understand the similarities and distinction between signal depletion and internal conversion efficiency it is instructive to write P_s as

$$P_s = T [1 - L(P_p)] P_{\text{in}}, \quad (4.3)$$

where P_{in} is the input power of the signal and T the pump-power-independent transmittance accounting for loss channels such as absorption and scattering as well as nonlinear optical processes that do not include the pump. In contrast $L(P_p)$ denotes the pump-power-*dependent* losses, or more specifically losses due to conversion processes that include the pump. Using this definition and $L(0) = 0$ it follows $\eta_s(P_p) = L(P_p)$, i.e. the signal depletion is a cumulative measure of all nonlinear optical processes scaling with pump power. Being the only quasi-phase-matched TWM-process, the desired DFG certainly governs the signal depletion, thus we expect to find $\eta_s \approx \eta_{\text{int}}$. However, one should

keep in mind that strictly speaking η_s is only an upper bound for the internal conversion efficiency, as non-phase-matched processes and phase-matched processes of higher order also contribute to the signal depletion.

To obtain η_s , we first determine P_s by integrating the corresponding signal peaks measured on the OSA. Fig. 4.6 (b) shows the spectra of the signal light at zero pump power (data: black circles, fit: red curve) and at $P_p = 656$ mW (data: black diamonds, fit: blue curve), yielding a signal depletion of $\eta_s = (92 \pm 1) \%$. The black data points shown in Fig. 4.6 (c) correspond to η_s taken at different pump powers and reveal that the depletion reaches a maximum at around 700 mW. For higher powers the efficiency drops due to SFG transferring the telecom light back to the signal wavelength. Assuming $\eta_s = \eta_{\text{int}}$, the signal depletion follows the same pump power dependency as the internal conversion efficiency given by [compare Eq. (2.36)]

$$\eta_s(P_p) = \eta_{\text{max}} \sin^2 \left(\sqrt{\kappa_{\text{norm}} P_p L} \right). \quad (4.4)$$

From a fit to the data (see red curve) we obtain $\eta_{\text{max}} = (91 \pm 4) \%$ at $P_p = 703$ mW, which we consider as the maximum achievable internal conversion efficiency $\eta_{\text{int}}^{\text{max}}$. To estimate the external device efficiency, we additionally include all losses that occur between converter-input and output, i.e. we write

$$\eta_{\text{ext}}^{\text{max}} = T_{\text{nir}} \cdot \eta_{\text{coup}}^{\text{WG}} \cdot \eta_{\text{int}}^{\text{max}} \cdot T_{\text{tel}} \cdot \eta_{\text{coup}}^{\text{fiber}} \cdot T_{\text{FBG}}. \quad (4.5)$$

The cumulative transmittances of the unconverted signal and converted telecom light through all optical bulk components are $T_{\text{nir}} = 92 \%$ and $T_{\text{tel}} = 95 \%$, respectively. The coupling efficiencies are $\eta_{\text{coup}}^{\text{WG}} = 77 \%$ for the signal light to the WG (see last section) and $\eta_{\text{coup}}^{\text{fiber}} = 80 \%$ for the telecom light to the output fiber. The FBG-filtering system constitutes a major loss channel with a transmittance of only $T_{\text{FBG}} = 60 \%$, which mainly originates from significant attenuation in the fiber-based circulator. These values lead to a maximally attainable external device efficiency of $\eta_{\text{ext}}^{\text{max}} = 29 \%$ being in good agreement with all values reported in the following chapters.

We like to note that the pump-power P_p used here and in the following refers to the optical power inside the WG. As it is typically measured in front of the WG [position 1 in Fig. 4.6 (d)], the specified power incorporates the known cumulative transmittance and coupling efficiency of 72%.

4.5 Converter Noise

As mentioned before, frequency converters add a significant amount of noise stemming from a plethora of different processes, most of which include the strong pump field. Despite being very weak compared to macroscopic optical powers, the noise has a considerable impact at the single photon level and therefore needs to be removed. In the following we consider contributions

that merely originate from the pump, i.e. noise, which is independent of the converter's input light field. Mixing processes of residual QD excitation and pump light will be discussed in sections 5.1.2 and 6.2.2.

With an optical power of around 500 mW, the residual pump light is by far the largest potential noise source. However, as the optical path behind the WG is optimized for the transmission and detection of telecom C-band light, the pump is strongly attenuated, which can be estimated as follows:

- (i) Both dichroic mirrors after the WG have reflectivities of $< 1\%$.
- (ii) Bandpass filter attenuation of the pump of > 30 dB [inset Fig. 4.7 (d)].
- (iii) The SMF-28 output fiber is not designed to guide light at wavelengths > 1625 nm, but assuming properties of a SM2000 fiber we estimate
 - a coupling efficiency of 0.3% mainly limited due to the focal length shift of collimation and coupling lens from 1550 nm to the pump wavelength, as well as
 - transmission losses of 15 dB (fiber length ≈ 100 m with 150 dB/km).
- (iv) FBG attenuation of 35 dB outside its reflection band.
- (v) The detection efficiency of the employed superconducting-nanowire single photon detectors (SNSPD, SINGLE QUANTUM, Netherlands) is approximately 1% at 1700 nm, [250].

All effects combined, we obtain an attenuation of > 165 dB, which corresponds to around 174 cps of detected noise photons stemming from the pump at an initial power of 500 mW. As SMF-28 fibers in fact have significant bending losses at the pump wavelength and the detection efficiency of our SNSPDs is expected to drop abruptly above 1800 nm³, the actual attenuation certainly exceeds the value estimated here. Therefore, we believe that residual pump light does not contribute to the observed noise count rate at all.

Fig. 4.7 (a) to (c) show spectra of the converter output in the range of 1100-1700 nm recorded with help of a grating spectrometer (model SP2500A with an InGaAs camera, PRINCETON INSTRUMENTS, USA). In (a) and (c) the converter was fed with strongly attenuated OPO-light at 905 nm to emulate single photon input. Corresponding to a pump wavelength of 2162 nm, the converted light emerges at 1557 nm (see peak 2). We recorded spectrum (a) without the C-band bandpass filter and observe a rich peak structure over the entire measured range. The transmission spectrum of the filter (d) reveals that light outside a window of 1515-1590 nm is attenuated with more than 30 dB. Accordingly, only the converted light remains for a measurement employing

³Personal communication: J. Qin-Dregely, SINGLE QUANTUM., email, November 30th 2018

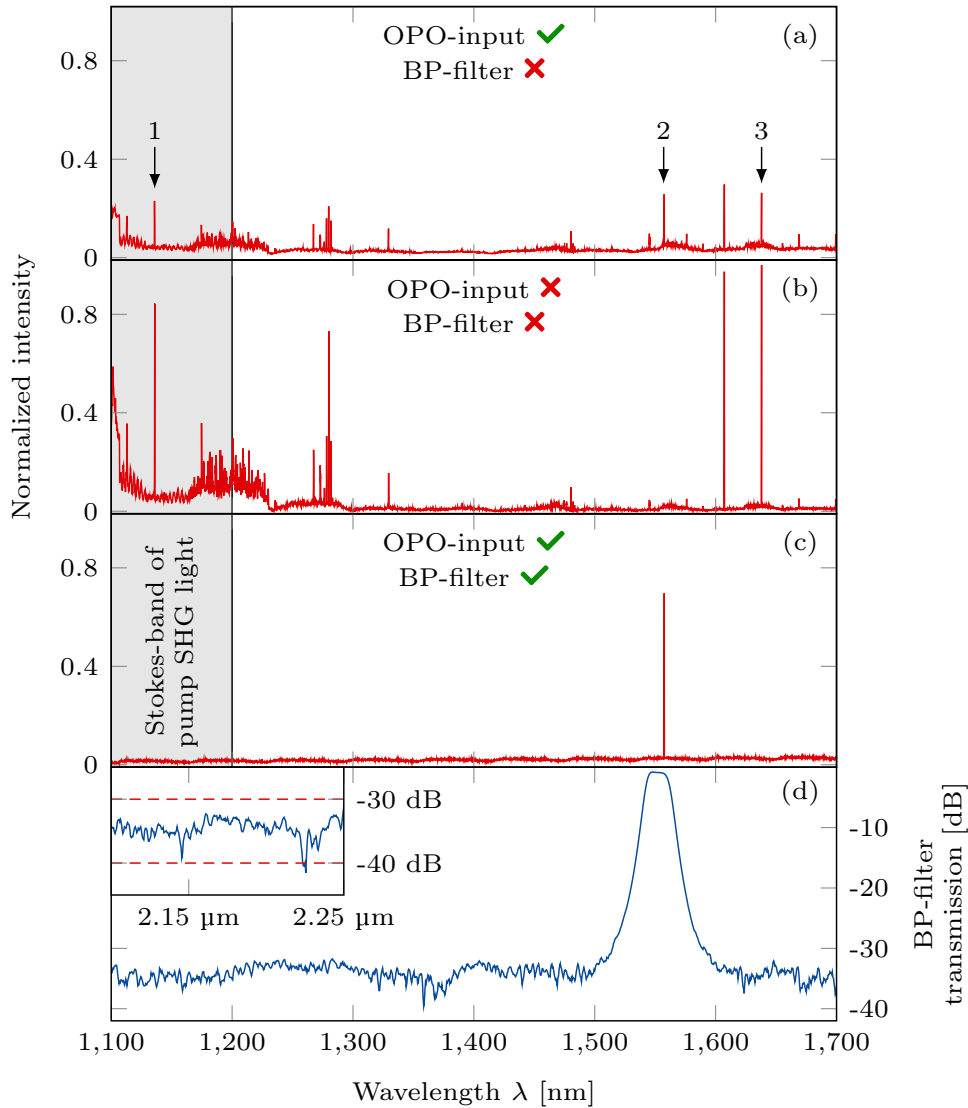


Figure 4.7. Noise spectra stemming from pump light. The converter is fed with OPO-input at 905 nm in spectra (a) and (c). Accordingly, converted light appears at 1557 nm (peak 3). Plots (a) and (b) reveal a rich noise spectrum, which is largely removed by the BP-filter in (c). (d) shows a measured transmission spectrum of the BP-filter.

the filter [compare (c)]. Spectrum (b) was recorded without the OPO-input. Apart from the now missing converted light (peak 2), the measurement qualitatively resembles spectrum (a), from which we conclude that all observable noise results from processes merely including the pump light.

Both parametric fluorescence [102] and Raman scattering [101, 231] are known effects that create broadband noise around the pump wavelength stem-

ming from interactions with the nonlinear medium. Parametric fluorescence naturally only appears on the long wavelength side of the pump. Therefore, it can be simply avoided by choosing a DFG process with the pump wavelength being longer than the target wavelength, as has been done here. Raman scattering on the other hand can shift the pump field to longer wavelengths (Stokes-shift) as well as to shorter wavelengths (Anti-Stokes-shift). The detailed analysis of Raman scattering in LN waveguides given in [101,231] reveals that the largest Anti-Stokes-shift corresponds to a peak at a wavenumber of 574 cm^{-1} , while its tail reaches to approximately 800 cm^{-1} . For the shortest pump wavelength of 2154 nm employed in our experiments (see Sect. 5.1.2) this leads to Raman scattered pump light at about 1840 nm , being well above the telecom C-band. In [100], however, it was shown that broadband Anti-Stokes Raman light extends until at least 1800 cm^{-1} ($\equiv 1553\text{ nm}$) and presumably continues even further, even though its intensity drops to $< 1\%$ compared to the strongest Raman transition. In conclusion, parametric fluorescence as well as Raman scattering of the pump can be mostly ruled out as sources for the noise observed in Fig. 4.7, with the caveat that a minor contribution might stem from Anti-Stokes light.

Despite being non-phase-matched, we observed a considerable amount of SHG light of the pump [$\mathcal{O}(100\text{ nW})$] throughout all experiments, here at a wavelength of 1081 nm . Using a maximum Stokes-shift of 920 cm^{-1} ($=875\text{ cm}^{-1}$ peak-center plus estimated tail [101]), its Raman light can stretch until $\approx 1200\text{ nm}$ [see blue shaded area in Fig. 4.7 (a)-(c)], which offers a possible explanation of this part of the observed noise. A less predictable, but equally probable source of noise are nonlinear mixing processes between any existing Raman light or parametric fluorescence and pump light. These processes can be phase-matched by higher order QPM and result in peaks appearing at arbitrary positions. For instance peak 1 is located at 1136 nm according to SFG of pump light and 2394 nm , which in turn is well within the Stokes-band of the pump. Peak 3 on the other hand resides at 1638 nm , which might stem from DFG of pump and 932 nm . The latter possibly originates from Anti-Stokes scattered SHG light of the pump. More generally, all peaks might result from similar nonlinear processes of second or higher order and additionally from cascaded effects, such that a conclusive assignment of the observed noise is virtually impossible.

4.6 Summary

In this chapter we presented the design considerations and performance assessment of the frequency converter employed for the experiments presented in Chap. 5. This converter moreover serves as a blueprint for the second one set up in the scope of the subsequent experiments discussed in Chap. 6. Its main features are summarized in the following *highlights*-box.

CHAPTER 4 - HIGHLIGHTS

Principal Components

- Lithium niobate waveguides on a lithium tantalate substrate serve as nonlinear medium. The waveguides are 40 mm long, 10 μm high, and 10.8 μm or 11.6 μm wide. Quasi phase-matching poling periods ranging from 24.3 μm to 24.5 μm support the DFG process defined by $1/905 \text{ nm} - 1/2175 \text{ nm} = 1/1550 \text{ nm}$ (Sect. 4.1.1).
- As pump light source driving the DFG process a single frequency cw-laser based on $\text{Cr}^{2+}:\text{ZnS}$ as active medium is employed. The laser delivers optical powers exceeding 1.5 W in a tuning range from 2.1 μm to about 2.3 μm with a linewidth of around 1 MHz (Sect. 4.1.2).

Converter Performance

- Parametric fluorescence spectra of input light at 904.7 nm for 10 out of 18 available waveguides were investigated. The telecom C-band light exhibits two peaks with a very broad spectral distribution (40 nm and 75 nm), indicating a flat phase-mismatch curve with two zero-crossings in this region. Temperature tuning reveals that all investigated waveguides are suitable for conversion into the telecom C-band (Sect. 4.2).
- The spectra and tuning curves could be reconstructed taking into account material

and waveguide dispersion. The material dispersion was modeled based on Sellmeier-coefficients found in [212] fitted to our data. It was found that small processing errors of the waveguide dimensions in the range of $\pm 0.1 \mu\text{m}$ have a severe impact on the resulting phase-mismatch (Sect. 4.2 and Appx. B).

- Stimulated down-conversion was tested with signal and pump light at 905.1 nm and 2167 nm, leading to converted telecom light at 1554 nm. A signal depletion of 91 % at a pump power of 703 mW was measured, which is an upper bound for the internal conversion efficiency. The external device efficiency at this set point was estimated to be 29 %, which matches values reported in literature [95,96,104] (Sect. 4.4).
- The spectral distribution of pump light induced noise was investigated in the range from 1.1 μm to 1.7 μm . A broadband noise floor as well as a plethora of distinct peaks were observed. Parametric fluorescence as noise source can be ruled out due to process design. A minor contribution might stem from Anti-stokes Raman scattered pump light. The distinct peaks most likely stem from non-phase matched cascaded conversion processes. A conclusive assignment, however, is not possible (Sect. 4.5).

Quantum Interference between Down-Converted Photons from a Single Quantum Dot

Contributions and copyright notice: The experimental results presented in the scope of this chapter were obtained within a collaborative project under the joint supervision of Prof. Peter Michler (Stuttgart University) and Prof. Christoph Becher. The investigated sample was designed and fabricated by Robert Roßbach and Michael Jetter at Stuttgart University. The frequency converter was designed, set up, and operated by Benjamin Kambs (B.K.) with help of Andreas Lenhard and Matthias Bock (M.B.). The Michelson interferometer was set up by Richard Nelz. All experiments were performed by B.K., Jan Kettler (J.K., Stuttgart University), M.B. and Jonas Nils Becker at Saarland University. The data were analyzed by B.K. with input from J.K. and M.B.

Note that the main results presented in this chapter were originally published in [251] (Copyright © 2016 by Optical Society of America).

In this chapter we present results obtained from a HOM-experiment between photons consecutively emitted by a single InAs QD. The experiment was designed based on the scheme reported in [230] and performed on unconverted photons in the near infrared (NIR) regime as well as converted photons in the telecom C-band. The results reveal that quantum frequency down-conversion does not impair the indistinguishability of single photons and thereby fill a gap between experiments demonstrating the same for up-converted single photons [104] as well as down-converted single photons coalescing with an attenuated laser field [150].

In the course of this chapter we first outline the experimental setup used to excite the QD sample and extract the emitted photons. After assessing the conversion efficiency, we offer a detailed analysis of all relevant spectral and temporal properties of the selected QD with both unconverted and converted photons. Eventually, we describe the HOM-experiment and discuss the achieved two-photon interference visibilities.

5.1 Single Photon Generation

The TPI experiments presented here rely on a pulsed single photon input to enable synchronized arrival of exactly two photons at the HOM beam splitter. In the following we describe the QD sample and the experimental methods used to obtain single photons at 903.6 nm as well as at the converted target wavelength of 1557 nm. To assess the brightness of the photon source, we investigate the achievable photon flux in both wavelength regimes. The experimental verification of the *single* photon nature of the emitted light will be provided as part of the subsequent section on spectral and temporal properties.

5.1.1 Confocal Microscope and Quantum Dot Selection

The investigated single photons stem from a sample containing InAs quantum dots residing in a GaAs matrix, designed and fabricated using a MOVPE process at Stuttgart university (sample identifier *M5059*). The sample is described in detail in [252, 253]. It exhibits emission in the range from 885 nm to 910 nm, covering the design wavelength of the frequency converter of 905 nm (compare Sect. 4.1). To improve the directionality of the emitted fluorescence, the sample is terminated by GaAs/AlAs DBR mirrors on bottom and top, which act as a low finesse planar cavity. The layer containing quantum dots resides about 700 nm under the surface.

The principal components of the setup used to excite the QDs and collect their fluorescence are illustrated in Fig. 5.1 (a). The sample is mounted inside a cryostat and cooled to a temperature of $T=10$ K in order to decrease lattice vibrations and thus minimize line broadening mechanisms, for instance caused by pure dephasing or emission into phonon sidebands [126, 179, 180]. For optical excitation we use a pulsed Ti:Sa laser (model Tsunami, SPECTRA-PHYSICS, USA) set to an emission wavelength of 884 nm (red beam path), resonantly creating excitons in the p -shell of the QD. The pulse separation of the laser emission was measured to be $T_{\text{rep}} = 12.47$ ns, which closely matches its nominal repetition rate of 80 MHz. Using an intensity autocorrelator the pulse width was measured to be 4.3 ps, which implies an FWHM pulse duration of 3.0 ps. The Mach-Zehnder interferometer (MZI) placed in the excitation beam path is used to obtain double pulses separated by approximately 4 ns. It is a vital part of the subsequent HOM experiments and will be addressed

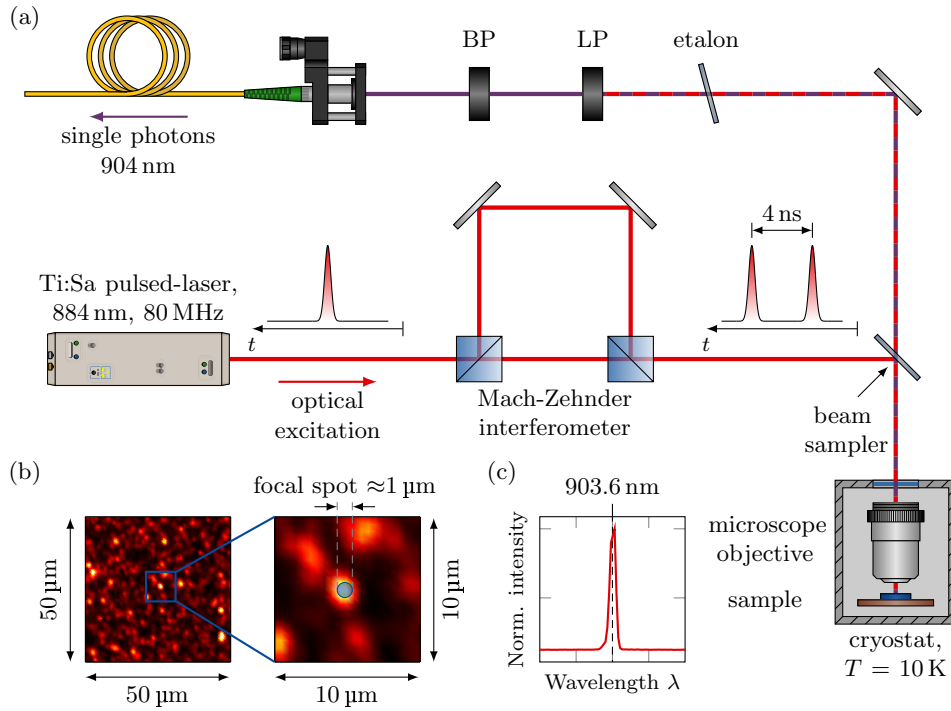


Figure 5.1. Setup for quantum dot excitation and fluorescence collection. (a) The InAs/GaAs sample is placed within a cryostat at a temperature of $T=10$ K. For optical excitation a pulsed Ti:Sa laser is employed at an emission wavelength of 884 nm (red line, p -shell excitation). The Mach-Zehnder interferometer is used to generate double pulses with a spacing of 4 ns within each repetition cycle of the excitation laser. A microscope objective ($100\times$ magnification, $NA = 0.8$) is used to focus the excitation light onto the sample and collect the emitted fluorescence at 904 nm (violet line). The fluorescence is then spectrally filtered by an etalon, longpass- (LP), as well as a bandpass-filter (BP) before being coupled to a single mode fiber via an aspheric lens. Microscope objective, aspheric lens, and single mode fiber constitute a confocal microscope for spatial quantum dot selection. (b) Fluorescence map of an area of $50 \times 50 \mu\text{m}^2$ (left) around the investigated quantum dot. On the right a zoom into an area of $10 \times 10 \mu\text{m}^2$ can be seen. The blue transparent disc illustrates the excitation spot with a $1/e^2$ -diameter of approximately $1 \mu\text{m}$. (c) Spectrum of the selected QD with a center wavelength of 903.6 nm. Note that the spectrum shows a very narrow region around the emission line concealing surrounding spectral features. For a more detailed spectrum cf. Fig. 5.5. Adapted with permission from [251], Optical Society of America.

in Sect. 5.3.1. A small fraction of the excitation light is reflected from a beam sampler towards a microscope objective ($100\times$ magnification, NA = 0.8, model LMPLFLN, OLYMPUS, Japan), which focuses the excitation light onto the sample and collects the emitted fluorescence around 905 nm (violet beam path). The collimated emission is then transmitted through the beam sampler and spectrally separated from residual excitation light, undesired QD transition lines, and broadband background by an etalon (finesse $\mathcal{F} \approx 25$, free spectral range 341 GHz), a 900 nm longpass filter (LP), and a 905 nm bandpass filter (BP, joint transmission of filter components $\approx 42\%$). Eventually, the fluorescence light is coupled via an aspheric lens into a single mode fiber and forwarded to subsequent experiments.

The configuration of microscope objective, aspheric lens, and optical fiber constitutes a confocal microscope, imaging fluorescence collected from only a small segment of the sample surface onto the core of the optical fiber. Although the focal spot of the excitation laser has a diameter of around $d_{\text{foc}} = 1\ \mu\text{m}$, the fluorescence stems from a larger confocal area with an estimated diameter of $d_{\text{con}} \approx 2\ \mu\text{m}$ [compare Fig. 5.1 (c)]. Theoretically, it is $d_{\text{con}} \leq d_{\text{foc}}$, but this assumes an ideally aligned confocal microscope as well as a medium with a homogeneous refractive index profile. In particular the latter is not given due to the air-semiconductor interface as well as the DBR-cavity structure of the sample. To obtain an overall fluorescence map, the sample is scanned perpendicular to the propagation direction of light, while the collected photons are detected and pointwise integrated for 50 ms with help of a silicon avalanche photodiode (Si-APD). Fig. 5.1 (b) shows a representative scan over an area of $50\times 50\ \mu\text{m}^2$ with a step size of $0.5\ \mu\text{m}$. We count 260 QDs in this region, corresponding to a density of 0.1 QDs per μm^2 , or an average of 0.08 QDs per excitation spot (compare blue circle). Note that the fluorescence map was obtained using p -shell excitation at a fixed wavelength, i.e. not all QDs were optically addressed. Accordingly, the actual QD density is likely to be higher. On the right, a zoom into an area of $10\times 10\ \mu\text{m}^2$ is shown. All experiments discussed in the following were performed using photons emitted by the QD situated at its center. The QD emits at a central wavelength of 903.6 nm [Fig. 5.1 (c), cf. Sect. 5.2.3 for a detailed analysis of the spectrum], being suitable for down-conversion. A detection rate of 38,800 counts per second (cps) could be achieved at an excitation power of 12 μW . Note that this value was obtained using double pulse excitation, i.e. at an effective repetition rate of 160 MHz. Considering the quantum efficiency of 33 % of the Si-APD, this corresponds to a flux of 117,600 photons per second in the output fiber. Additionally accounting for the spectral filter and beam sampler transmission of 42 % and 90 %¹, respectively, as well as an estimated fiber coupling efficiency of 80 %,

¹The stated transmission is calculated using Fresnel equations for unpolarized light impinging on the beam sampler (NBK7, $n = 1.51$ at 904 nm) with an angle of incidence of 45° .

we find that with a probability of 0.24 % each excitation pulse yields a photon collected by the microscope objective. This value is more than one order of magnitude below typical extraction efficiencies of photons from GaAs samples terminated by DBR mirrors [171]. It includes, however, further limitations such as a non-ideal excitation efficiency and radiative quantum yield, which were not quantified in scope of the present experiment.

5.1.2 Frequency Converter Performance

In order to transduce the fluorescence photons from their initial wavelength at 903.6 nm to the telecom C-band, we use the output fiber of the confocal microscope as input of the frequency converter detailed in Chap. 4. Etalon, longpass- and bandpass-filter in the NIR beam path could be removed throughout all conversion experiments, as the narrow acceptance bandwidth of the PPLN waveguide along with both telecom C-band filters described in Sect. 4.1 provide sufficient suppression of undesired background photons entering the converter (details provided in Sect. 5.2.3). Accordingly, the input photon flux is increased to $\Phi_{\text{in}} = 280,000$ photons per second [compare Fig. 5.2 (a)]. The unconverted single photons are coupled to WG1 in group 1 with the WG chip set to a temperature of 41 °C. The pump laser of the frequency converter was operated at an output wavelength of 2154 nm, which leads to a target wavelength of 1557 nm [Fig. 5.2 (b)], matching the filter window of the fiber Bragg grating. Starting from the converter output, the telecom photons propagate through ≈ 90 m of optical fiber (SMF-28, 0.2 dB/km at 1550 nm) with a transmission of $T_{\text{tel}} = 99.6$ % and are detected by our SNSPDs (quantum efficiency $\eta_{\text{SNSPD}} = 10$ % at 1550 nm, [250]).

Fig. 5.2 (c) shows a measurement of the telecom photon count rate ν_{det} (right ordinate) as a function of the pump power P_{P} present in the WG. The flux of telecom photons available at the converter output is given by

$$\Phi_{\text{out}} = \frac{\nu_{\text{det}} - \nu_{\text{dc}}}{T_{\text{tel}} \cdot \eta_{\text{SNSPD}}} \quad (5.1)$$

with the detection dark count rate being $\nu_{\text{dc}} = 350$ cps. Knowing Φ_{out} , the external device efficiency can be obtained via $\eta_{\text{ext}} = \Phi_{\text{out}} / \Phi_{\text{in}}$, which is plotted along the left ordinate. The red curve constitutes a fit of model Eq. (2.36) to the measured data and reveals a maximum external device efficiency of $\eta_{\text{ext}}^{\text{max}} = (30.9 \pm 0.5)$ % at a pump power of 295 mW. At this set point we achieve a detection count rate of 8,980 cps, respectively a flux of $\Phi_{\text{out}} = 86,700$ telecom photons per second. The achieved external device efficiency slightly exceeds the value estimated in Sect. 4.4. This deviation most likely stems from the SNSPD detection efficiency, which is not known for certain. Other possible reasons include improved coupling efficiencies to WG as well as output fiber of

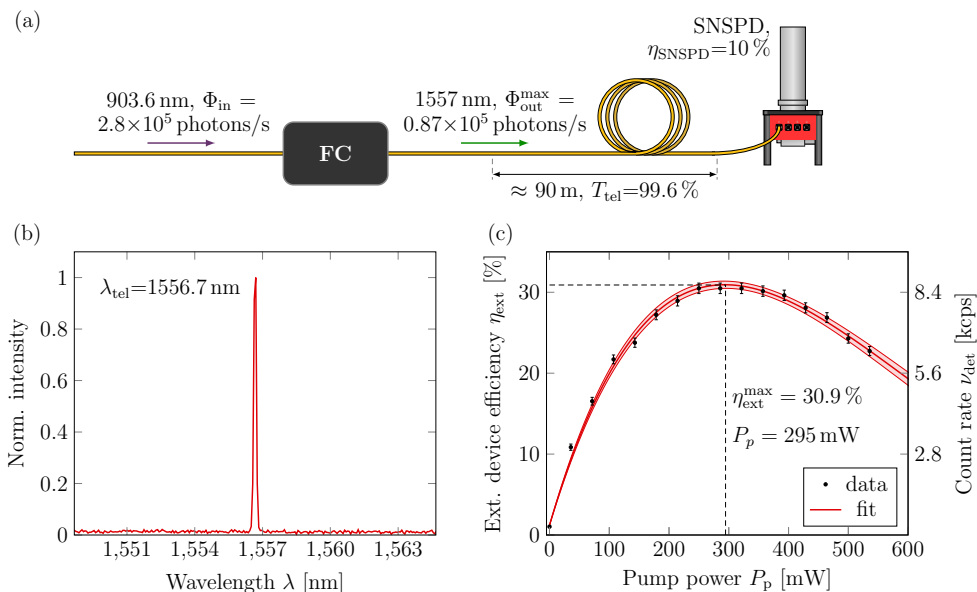


Figure 5.2. External device efficiency for the down-conversion during single quantum-dot experiments. (a) 280,000 photons/s at 903.6 nm enter the frequency converter (FC), of which 86,700 photons/s are down-converted to 1557 nm and available at the converter output. The detection count rate is reduced due to limited fiber transmission (99.6%) and detection efficiency (10%). (b) Spectrum of converted telecom C-band photons centered around 1557 nm, taken by a grating spectrometer with InGaAs camera. Note that the linewidth is limited by the spectrometer resolution. (c) A maximum external device efficiency of $\eta_{ext}^{max} = (30.9 \pm 0.5)\%$ could be achieved at a pump power of 295 mW. The shown error bars were calculated as twofold standard error of the measured count rates.

the converter, or a higher internal conversion efficiency of the WG employed for this experiment².

Coupling only the pump, but no single photons to the WG at the chosen operating point, the SNSPD detection count rate equals its dark count level. This suggests that none of the noise peaks or broadband noise discussed in Sect. 4.5 considerably leak into the filter window. However, this conclusion should be taken with a grain of salt, as minor noise contributions ($\nu_{noise} \lesssim 0.1 \times \nu_{dc}$) require a long integration of the count rates to be detectable, which was not performed here. A different conceivable noise source is the QD excitation light centered at 884 nm. Its direct down-conversion leads to 1499 nm, which is outside the spectral filter windows. Possible two-step processes such as Raman-scattering or parametric fluorescence transducing

²In this experiment we employed WG1 in group 1, while in Sect. 4.4 we assessed the device efficiency of WG1 in group 5.

photons from 884 nm to 904 nm and subsequent down-conversion potentially create noise at the target wavelength. As these noise photons originate from the pulsed excitation light, they are temporally correlated with the emitted single photons. In Sect. 5.2.4 we conclude, however, that this type of correlated noise can be completely attributed to background fluorescence emitted by the QD sample. Accordingly, the excitation laser can be ruled out as noise source.

5.2 Spectral and Temporal Properties

For a thorough analysis of the HOM experiments a profound knowledge of the single photons' properties is essential. In Sect. 3.2 we saw that the mutual indistinguishability of two photons is mainly determined by their radiative lifetimes and mechanisms that broaden the emission lines beyond the Fourier limit. In the scope of this section, these are quantified both for converted and unconverted photons by time-correlated single photon counting (TCSPC) and a measurement of the degree of first-order coherence using Michelson interferometry. Furthermore we estimate the amount of uncorrelated and correlated background photons superimposed with the single photon field by an analysis of their spectra as well as a measurement of the degree of second-order coherence. For all measurements presented in the following, one arm of the MZI is blocked, i.e. the QD is excited at a repetition rate of 80 MHz.

5.2.1 Radiative Lifetime

To obtain the radiative lifetime we employ TCSPC, being a widespread standard method for that purpose [254–256]. Both clock-signal of excitation laser and output pulse of the single photon detector are registered by an electronic correlation device (model PicoHarp 300, PICOQUANT, Germany), which then computes the time lag τ between their arrival with a resolution of 4 ps. The time lag is repeatedly recorded throughout multiple excitation cycles and eventually plotted as a histogram, which can be seen as black line in Fig. 5.3 (a) and (b) for unconverted and converted photons, respectively. The data show the anticipated one-sided exponential decay corresponding to the idealized model of a two-level quantum emitter and is described by

$$f(\tau) = N_0 \cdot \text{H}(\tau - \tau_0) \exp\left(-\frac{\tau - \tau_0}{\tau_r}\right). \quad (5.2)$$

Here N_0 is the amplitude, τ_r the desired radiative lifetime, and τ_0 an offset stemming from differing travel times of start- and stop-signal. The Heaviside-function $\text{H}(\tau)$ accounts for the fact that photons can be emitted only after the excitation step. From the data it is evident, however, that the instantaneous rise of $f(\tau)$ at τ_0 caused by the Heaviside-function is blurred, in particular

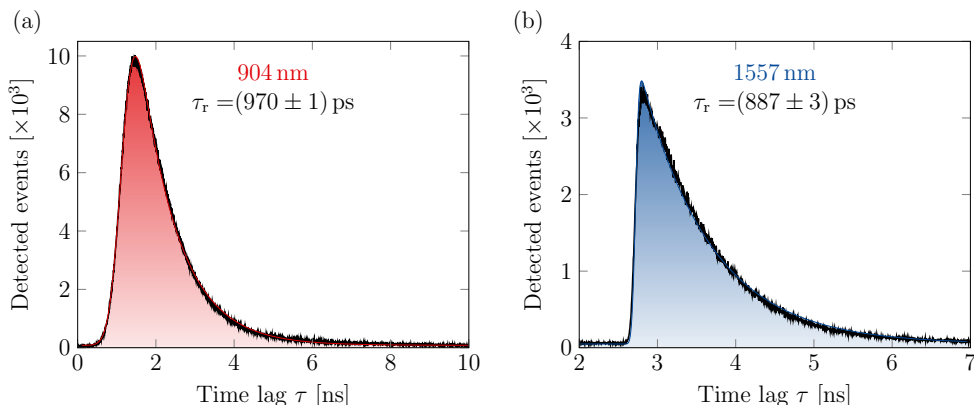


Figure 5.3. Measurement of the radiative lifetime of the quantum dot. TCSPC histogram data are shown as black curves for (a) unconverted and (b) converted photons. The red and blue shaded areas constitute fits revealing radiative lifetimes of $\tau_r = (970 \pm 1)$ ps and $\tau_r = (887 \pm 3)$ ps, respectively.

for Fig. 5.3 (a). This is caused by an uncertainty in the response-time of the overall detection system and typically referred to as jitter. Here, we model the detector response as a normal distribution $g(\tau)$ assuming an FWHM of $\tau_{\text{jit}}=300$ ps for the Si-APD as well as $\tau_{\text{jit}}=50$ ps for the SNSPD. The final model function is then obtained by a convolution of Eq. (5.2) with $g(\tau)$ and reads

$$h(\tau) = N_0 \exp\left(-\frac{\tau - \tau_0}{\tau_r}\right) \cdot \left[1 + \operatorname{erf}\left(\frac{\tau - \tau_0}{\sqrt{2}\sigma_{\text{jit}}} - \frac{\sigma_{\text{jit}}}{\sqrt{2}\tau_r}\right)\right], \quad (5.3)$$

where it is $\tau_{\text{jit}} = 2\sqrt{2\ln 2}\sigma_{\text{jit}}$. Note that N_0 is modified compared to Eq. (5.2), as all constant prefactors appearing during the convolution were merged into it. The red and blue shaded curves in Fig. 5.3 (a) and (b) constitute a fit of model (5.3) to the data, where τ_{jit} was fixed, but all other parameters were treated as free. We find radiative lifetimes of $\tau_r = (970 \pm 1)$ ps and $\tau_r = (887 \pm 3)$ ps for unconverted and converted photons, respectively. Both values are in good agreement with typical lifetimes measured for InAs QDs [161], but differ with respect to each other by almost 10%. This might stem from an inaccurate specification of the detector jitter. Including the jitter as fit parameter, however, does not significantly change the resulting lifetimes. Apart from a measurement-related origin, it is certainly also possible that the temporal distribution of detected photons indeed changed between both measurements. On one hand, the exciton recombination rate depends on the excitation power [162], which was not explicitly kept constant. On the other hand, the unconverted photon field contains more background photons from spectrally distinct transitions (Sect. 5.2.3), which might exhibit different

lifetimes. As neither has been independently measured, however, the actual reason cannot be identified beyond any doubt.

5.2.2 Coherence Time

From the TCSPC measurements, the lifetime limited coherence time can be derived for both wavelength regimes as $\tau_{\text{coh}} = 2\tau_r = 1,940$ ps and $1,774$ ps, corresponding to natural linewidths of $1/(2\pi\tau_r) = 164$ MHz and 179 MHz. The emission line is homogeneously and inhomogeneously broadened beyond this limit, quantified by the pure dephasing rate Γ^* and FWHM σ' of the underlying normal distribution, respectively. As discussed in Sect. 3.2, these linewidth contributions are essential in assessing the photon indistinguishability. In the following, we present interferometric measurements of the first-order coherence function. According to Eq. (2.14), both Γ^* and σ' can be extracted from its temporal shape³.

Fig. 5.4 (a) illustrates the Michelson interferometer (MI) employed for the measurement. Split up at a non-polarizing BS, the light propagates in two different arms, is reflected at retroreflectors (RR), and eventually recombined. The retroreflector RR1 is mounted on a translation stage in order to change the time delay τ_{mi} between both interferometer arms. For any fixed τ_{mi} , the piezoelectric actuator attached to RR2 is repeatedly scanned over a given voltage range, thereby changing the relative phase $\Delta\Phi$ between both interferometer arms. This phase determines the probability with which the photons leave the BS towards detector or beam block, appearing as interference fringes in the detected count rate ν_{det} according to

$$\nu_{\text{det}} = \nu_{\text{dc}} + \bar{\nu} \cdot (1 + V \cos \Delta\Phi), \quad (5.4)$$

where ν_{dc} is the detector dark count rate, $\bar{\nu}$ the average count rate, and V the visibility of the interference pattern. Fig. 5.4 (b) and (c) show representative measurements in both wavelength regimes and for each at a small and a large time delay. The solid curves are fits of the measured data to Eq. (5.4). All visibilities extracted from these fits are plotted against τ_{mi} in Fig. 5.4 (d) and (e). Their error bars correspond to the standard deviation of a set of visibilities, which were obtained from several fits in different regions of the measurements. Note that the shown values are normalized to a maximum visibility of one in order to compensate limitations caused by the interferometer, such as a polarization mismatch between both interferometer arms or a non-ideal spatial mode overlap at the BS. The observed decrease in visibility for increasing τ_{mi} occurs at a high rate compared to the Fourier-limited case (compare inset). This is on one hand symptomatic of the elevated probability of phase jumps occurring between distant points of a single wave train. On

³Note that Eq. (2.14) employs the standard deviation σ instead of the corresponding FWHM σ' to account for inhomogeneous line broadening.

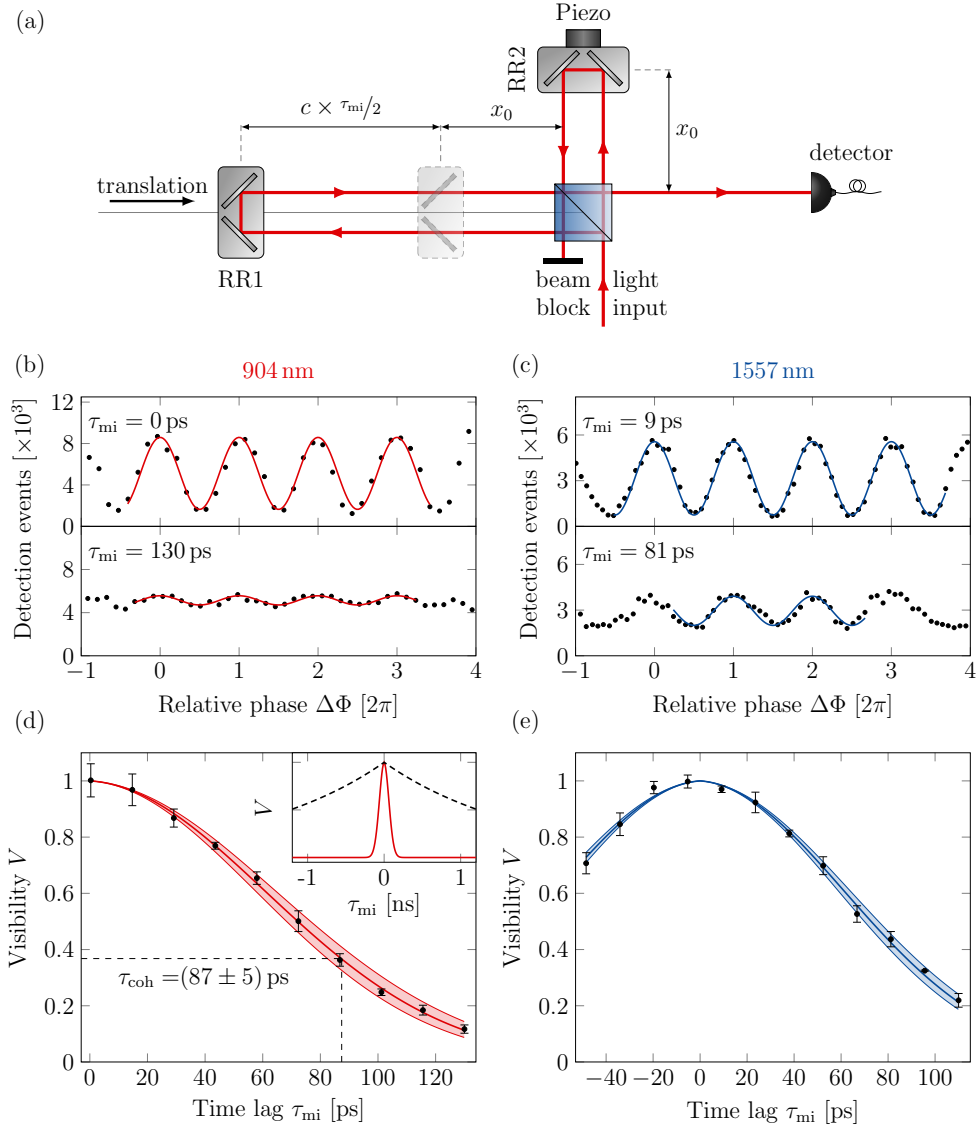


Figure 5.4. Measurement of coherence time. (a) Illustration of the Michelson-interferometer used for the measurement. The input light is split up at a beam splitter and in each arm reflected by retroreflectors (RR). RR1 is mounted on a translation stage in order to vary the delay τ_{mi} introduced by the interferometer. The piezoelectric actuator attached to RR2 is used to scan the relative phase $\Delta\Phi$ of both arms. (b) and (c) show measured interference fringes at different τ_{mi} for unconverted and converted photons, respectively (data: black circles, fit: solid curve). The obtained interference visibilities are plotted against τ_{mi} in (d) and (e). The red solid curve shown in (d) is a fitted coherence function $|g^{(1)}(\tau_{mi})|$ revealing a coherence time of $\tau_{coh} = (87 \pm 5)$ ps. At the inset a comparison of the fitted fringe visibility (red) to the Fourier limit (black dashed) can be seen. In (e) the data are accompanied by a plot of $|g^{(1)}(\tau_{mi})|$ (blue curve) using the parameters found from the fit in (d).

the other hand it also indicates frequency jumps between successive photons, as the interference fringes were integrated over tens of milliseconds, i.e. over $\mathcal{O}(10^6)$ excitation cycles. In other words, the visibility bears the signature of both pure dephasing and spectral diffusion. With Eq. (2.14) we presented an expression for the first order coherence function depending on pure dephasing rate Γ^* and inhomogeneous linewidth σ' . Its absolute value equals the fringe visibility $V(\tau_{\text{mi}})$ (see e.g. [257, Chapter 2]), i.e. it is an appropriate model function for the presented data. In our case, however, it is not possible to simultaneously fit both Γ^* and σ' , as the inhomogeneous broadening exceeds the homogeneous broadening by two orders of magnitude, thereby mostly concealing the impact of Γ^* . Instead we estimate the dephasing rate using the approach presented in the supplement of [192]. Therein, Γ^* is treated proportional to the square of the phonon number within the scope of the Markovian approximation [258], while the phonon number follows Bose-Einstein statistics. Assuming the model parameters for InAs QDs reported in [192] and the sample temperature of $T=10$ K, we obtain $\Gamma^*=47$ MHz. Eventually, this enables us to fit the visibility shown in Fig. 5.4 (d) using the known radiative lifetime and pure dephasing rate as fixed parameters (see red curve). From the fit we extract $\sigma'=(5.9 \pm 0.4)$ GHz corresponding to a coherence time of $\tau_{\text{coh}}=(87 \pm 5)$ ps [cf. Eq. (2.15)]. The inset of Fig. 5.4 (d) compares the fitted fringe visibility to the Fourier limited case, visualizing that the coherence of the emitted photons is severely degraded, possibly indicating a very strong coupling of the QD to its electrostatic environment or non-ideal operating conditions. Also it has been observed that the coherence is further reduced when both fine structure components of the emission line are collected [160], which is the case in the present experiment. The blue curve shown in Fig. 5.4 (e) is a plot of the fit obtained for (d). It is in excellent agreement with the data obtained from converted photons, thereby confirming the conservation of the degree of first-order coherence during the down-conversion step reported in [95].

5.2.3 Spectral Background Analysis

In the upcoming section we present correlation measurements to test the photon source under investigation for antibunching. We find, however, a non-negligible amount of simultaneous emission of two or more photons. In preparation for that, we here investigate the measured spectra in order to quantify the amount of background photons stemming from the QD sample.

We start from the spectrum of unconverted photons, shown in Fig. 5.5 (a) as red curve. The spectrum was recorded without the etalon and reveals a plethora of emission peaks besides the main line, in particular in the region from 906 to 910 nm. Additionally, the transmission spectrum of the etalon is shown in gray, which was calculated based on equations presented in [259] and using the specified coating reflectivity of 90 % and thickness of 300 μm

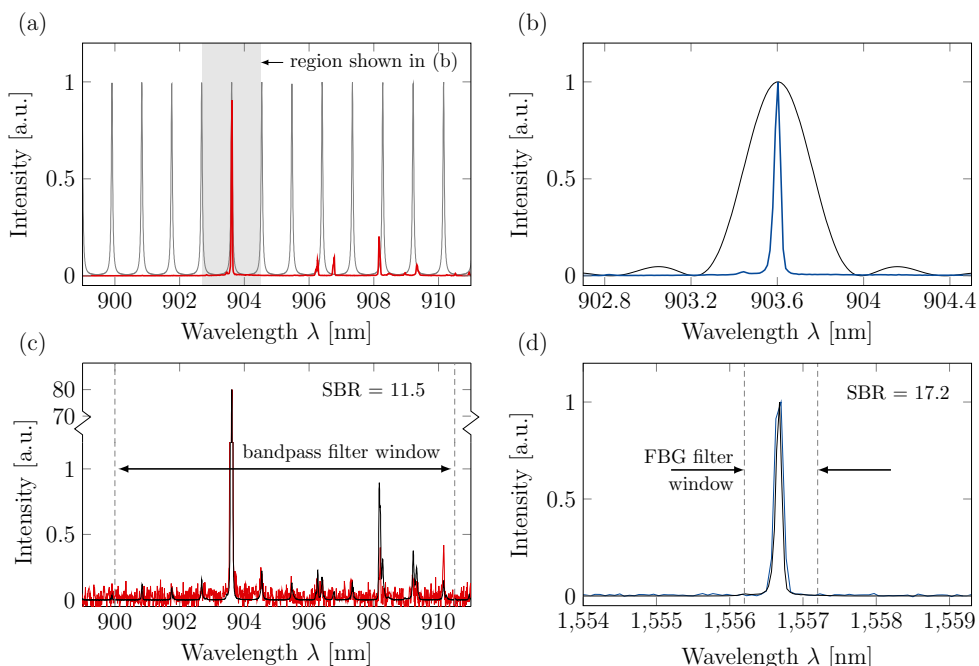


Figure 5.5. Spectra of unconverted and converted photons. (a) Measured spectrum of unconverted photons without etalon (red) and calculated transmission spectrum of etalon (gray). (b) Magnification of the spectrum shown in (a) (blue) along with the spectral, relative conversion efficiency (black). (c) Measured spectrum with etalon (red) compared to product of both curves in (a) (black). (d) Measured spectrum of converted photons (blue) compared to the product of both curves shown in (b) (black). Integration within the bandpass filter window (Fiber-Bragg-grating window) yields a signal-to-background ratio of SBR=11.5 (17.2). Adapted with permission from [251], Optical Society of America.

as well as the refractive index of fused silica of 1.452 at 904 nm [260]. The measured spectrum of unconverted photons including etalon filtering and after subtracting spectrometer dark counts is depicted in Fig. 5.5 (c) as red curve. Although some peak amplitudes do not fully match, the filtered spectrum is qualitatively well reproduced by the multiplication of the unfiltered spectrum and etalon transmission taken from (a), here shown in black. The gray dashed lines indicate the transmission window of the bandpass filter. Integrating the spectrum in this region yields a measure of the joint QD emission and background intensity. Additionally considering the area under the isolated QD emission line, we find a signal-to-background ratio (SBR) of 11.5.

To obtain a similar estimation for converted photons, we first consider the narrow spectral region around the QD emission line for unconverted and unfiltered photons shown in Fig. 5.5 (b) (blue). The spectrum is accompanied by a curve illustrating the relative conversion efficiency (black), which was obtained

for WG1 in group 1 at a WG temperature of 41 °C using the same method and parameters discussed in Sect. 4.2. However, in contrast to the simulation of SPDC spectra, we here fix the target wavelength of 1557 nm and vary the NIR input wavelength in the region of interest instead. Multiplying both curves in (b) and shifting the wavelength to the telecom C-band yields the spectral distribution of converted photons shown in Fig. 5.5 (d) (black), agreeing well with the measured spectrum (blue). Integration within the bounds set by the FBG now yields an SBR of 17.2, considerably improved compared to the unconverted photons. It is worth noting that this does not stem from the central linewidth of the filters - both FBG and conversion efficiency exhibit an FWHM of around 120 GHz, while the etalon linewidth is as low as 14 GHz. The stronger background at the NIR regime is rather a consequence of various emission lines leaking through neighboring transmission peaks as can be seen in Fig. 5.5 (c). These peaks, however, are well outside the acceptance bandwidth of the converter and therefore efficiently suppressed.

5.2.4 Antibunching

The key attribute of an ideal on-demand single photon source resides in its photon statistics. In contrast to light sources, whose emission can be modeled by classical electromagnetic fields, a single quantum emitter cannot emit more than one photon at a time [255], which is often referred to as antibunching. An established method to verify antibunching is to measure the intensity auto-correlation function $g^{(2)}(\tau)$ of the light source using a Hanbury-Brown-Twiss (HBT) interferometer [261, 262]. A theoretical treatment of antibunched light fields reveals that $g^{(2)}(\tau) < 1$ for $\tau \rightarrow 0$, assuming $g^{(2)}(\tau)$ to be normalized [255, 263]. For a Fock-state $|n\rangle$ with mean photon number n one generally finds $g^{(2)}(0) = 1 - 1/n$, which motivates the frequently used, but not strictly unambiguous, criterion for single photon emission $g^{(2)}(0) < 0.5$.

In the following we show measurements demonstrating antibunched photon emission from the QD under investigation. The HBT interferometer is built using a bulk BS and two free-space Si-APDs (quantum efficiency 30 %, detection jitter 300 ps, dark count rate 300 Hz) in case of unconverted photons. For converted photons, we use a fiber-based BS and two SNSPDs instead (quantum efficiency 10 %, detection jitter 50 ps, dark count rate 350 Hz). The respectively measured $g^{(2)}(\tau)$ functions are shown in Fig. 5.6 (a) and (b) (black circles). Their most prominent feature is the repetitive pattern of peaks every 12.47 ns stemming from the pulsed excitation. Each peak shows a double-sided exponential decay, which corresponds to the auto-correlation of the radiative decay including detector jitter described by Eq. (5.3). All coincidences within peaks not centered around $\tau = 0$ originate from photons of distinct excitation cycles, while simultaneously emitted photons produce coincidences at $\tau = 0$ according to our preceding considerations. To extract a measure for the antibunching value we evaluate

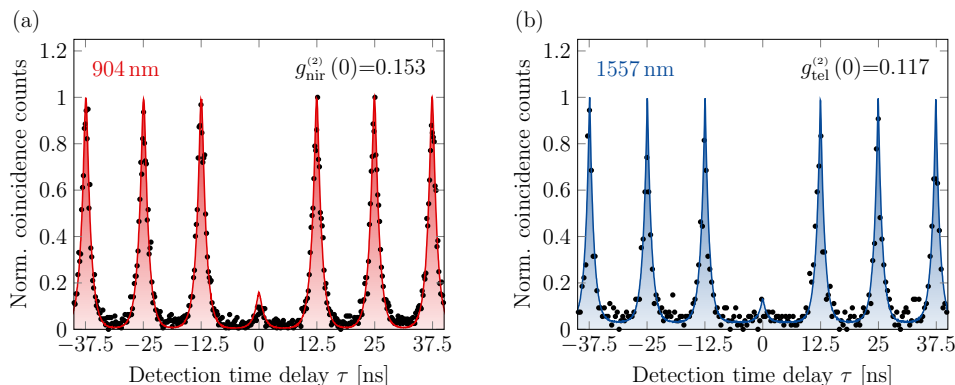


Figure 5.6. Measurement of the intensity auto-correlation function. The coincidence measurements reveal detector dark count corrected antibunching values of $g_{\text{nir}}^{(2)}(0)=0.153$ and $g_{\text{tel}}^{(2)}(0)=0.117$ for unconverted and converted photons, respectively. The shaded areas correspond to Monte-Carlo simulations based on all known emitter parameters. Adapted with permission from [251], Optical Society of America.

Table 5.1. Summary of antibunching values. All obtained values for $g^{(2)}(0)$ are listed, i.e. for unconverted and converted photons, from measurement and simulation, as well as with and without detector dark count correction. Note that the SBR limit closely reproduces the dark count corrected values. Adapted with permission from [251], Optical Society of America.

		904 nm	1557 nm
	SBR limit	0.154	0.107
Measured	w/ dark counts	0.171	0.290
	w/o dark counts	0.153	0.117
Simulated	w/ dark counts	0.172	0.278
	w/o dark counts	0.154	0.109

$$g^{(2)}(0) = \frac{A_0}{C} \quad \text{with} \quad C = \frac{1}{2N} \sum_{\substack{i=-N \\ i \neq 0}}^N A_i, \quad (5.5)$$

where A_i is the integrated total number of coincidences under the i th peak. We choose $N = 16$, which corresponds to an average over a region of ± 200 ns around the central peak. For the raw data, this leads to $g_{\text{nir}}^{(2)}(0)=0.171$ and $g_{\text{tel}}^{(2)}(0)=0.290$ with 'nir' and 'tel' referring to values obtained for unconverted and converted photons, respectively (see also Tab. 5.1 for a summary of all antibunching values).

Even though both values are below 0.5 and therefore point towards single photon emission, there is a considerable amount of coincidences around $\tau = 0$.

Table 5.2. Noise floor estimation. List of all relevant parameters to evaluate the number of coincidences caused by detector dark counts per bin N_{dc} for both wavelength regimes according to Eq. (5.6).

	ν_{det} [kHz]	ν_{dc} [Hz]	T [s]	$\Delta\tau$ [ps]	N_{dc} [1]
904 nm	28.29	300	191	200	0.652
1557 nm	3.73	350	1580	400	1.73

One major source are detector dark counts that occur temporally uncorrelated to photon detection events and therefore cause a constant noise floor. As this contribution is only related to the detection system, but not the single photon field, it is reasonable to subtract it from the raw data. The number of coincidences per bin N_{dc} caused by detector noise is given by (derivation in Appx. C, see also supplement of [141])

$$N_{\text{dc}} = (2\nu_{\text{det}} - \nu_{\text{dc}}) \cdot \nu_{\text{dc}} T \Delta\tau, \quad (5.6)$$

where ν_{det} is the average count rate per detector, T the measurement duration, and $\Delta\tau$ the bin width of the histogram. Also, we assumed that both detectors exhibit equal dark count rates ν_{dc} , which is approximately valid. Based on the known parameters listed in Tab. 5.2 we obtain $N_{\text{dc,nir}}=0.652$ and $N_{\text{dc,tel}}=1.73$, which leads to dark count corrected antibunching values of $g_{\text{nir}}^{(2)}(0)=0.153$ and $g_{\text{tel}}^{(2)}(0)=0.117$.

The remaining deviation from zero stems from the area under the peak centered at $\tau=0$ and therefore indicates a minor contribution of multi-photon emission. It is possible to relate the SBRs found in Sect. 5.2.3 to an expected $g^{(2)}(0)$ value via [264]

$$g^{(2)}(0) = 1 - \left(\frac{\text{SBR}}{\text{SBR} + 1} \right)^2, \quad (5.7)$$

which yields $g_{\text{nir}}^{(2)}(0)=0.154$ and $g_{\text{tel}}^{(2)}(0)=0.107$ being in excellent agreement with the dark count corrected values. This finding suggests that the observed multi-photon emission is not caused by successive emission events from the transition line at 903.6 nm during a single excitation cycle, but rather by spectrally distinct transitions [compare Fig. 5.5 (a)]. Accordingly, we conclude that more rigorous spectral filtering will help to significantly improve the antibunching of the single photon source at hand.

To independently verify our analysis we perform Monte Carlo simulations, which reproduce the measured $g^{(2)}$ -functions (see Appx. D for corresponding MATLAB-code). The simulations emulate a large number of excitation cycles, each of which containing a single photon released from the QD. During each cycle a set of decisions is made based on appropriately distributed random

numbers yielding click lists for both detectors. These decisions determine **(i)** the number of background photons n_{bg} and detector dark counts n_{dc} per excitation cycle, **(ii)** the path each photon takes at the BS of the HBT interferometer, **(iii)** the detection time of each photon relative to the respective excitation pulse including detector jitter, as well as **(iv)** the recording time of dark counts. As the number of dark counts is random, we use a Poissonian distribution, whose mean value $\langle n_{\text{dc}} \rangle$ is given by

$$\langle n_{\text{dc}} \rangle = \frac{1}{\text{SNR} + 1} \quad \text{with} \quad \text{SNR} = \frac{\nu_{\text{det}} - \nu_{\text{dc}}}{\nu_{\text{dc}}} \quad (5.8)$$

in order to comply with the observed dark count rates. The necessary signal-to-noise ratios (SNR) can be calculated based on the values stated in Tab. 5.2, which yields $\text{SNR}_{\text{nir}}=93$ and $\text{SNR}_{\text{tel}}=9.7$. The physical process leading to background photon emission is not investigated for our sample. Therefore, we model it as a random process as well using the known SBR instead of SNR in Eq. (5.8) to obtain $\langle n_{\text{bg}} \rangle$. While the recording time of detector dark counts is uniformly distributed within each excitation cycle, the detection time t_{det} of QD and background photons must follow the expected exponential decay. This can be achieved applying the method of inverse transform sampling [265], for which the inverse of the cumulative distribution function of Eq. (5.2)

$$t_{\text{det}} = \tau_r \cdot \ln \frac{1}{1 - x} \quad (5.9)$$

has to be evaluated. Here, $x \in [0, 1]$ is a uniformly distributed random number and τ_r equals the measured value for both QD and background photons. Eventually, we add a detector jitter to t_{det} following a Gaussian distribution with an FWHM as specified by the manufacturer. Although reflection or transmission at the BS happens prior to detection in experiment, we include it as a final randomized decision, which writes t_{det} with equal probability to one of the click-lists. The desired intensity auto-correlation can now be obtained from a correlation of the click-lists.

The results of the simulations are depicted as shaded curves in Fig. 5.6 (a) and (b). As all necessary input parameters were known from independent measurements, no additional fit of simulation to measurement was necessary except for a normalization. From the simulation we extract raw antibunching values of $g_{\text{nir}}^{(2)}(0)=0.172$ and $g_{\text{tel}}^{(2)}(0)=0.278$, while the dark count correction now yields $g_{\text{nir}}^{(2)}(0)=0.154$ and $g_{\text{tel}}^{(2)}(0)=0.109$. These values are in perfect agreement with measurement and calculated SBR-limit, supporting our preceding analysis. While the spread of $g^{(2)}(0)$ -values for unconverted photons is as low as 0.001, we find that the measured value differs by 0.012 from the simulated one for converted photons. This is a direct consequence, however, from the lower SNR encountered at the telecom regime, which was not compensated by a higher integration time, thereby causing a larger statistical error.

5.3 Preservation of Indistinguishability during Quantum Frequency Conversion

We conclude this chapter by presenting our results from HOM experiments performed on consecutively emitted single photons. The observed TPI visibilities are consistently explained using all available setup and emitter parameters, allowing the conclusion that QFDC does not alter the indistinguishability of single photons. Before showing the experimental results and their analysis, we will briefly review the underlying idea of the experiment.

5.3.1 Experimental Concept

For our HOM experiments we adapt the scheme presented in [230], which is schematically shown in Fig. 5.7 (a). In both excitation and emission beam path a Mach-Zehnder interferometer (MZI) is introduced, exhibiting equal delays τ_{mzi} . The excitation pulses (red) are split up at the MZI entrance and reunited at its exit, leading to a temporal pattern of double pulses separated by τ_{mzi} that repeats every $T_{\text{rep}}=12.47$ ns. As will be detailed in the upcoming sections, we here employ $\tau_{\text{mzi}}=3.98$ ns and 8.03 ns for unconverted and converted photons, respectively. The subsequently emitted single fluorescence photons (violet) reveal the same pattern. For a HOM experiment, we need two photons simultaneously arriving at one BS via distinct input ports, which is realized by the second MZI. Consider two photons emitted with a delay of τ_{mzi} . If the early photon took the long path and the late photon the short path at BS1, they will meet at BS2. Whether or not both photons coalesce with a non-classical probability >0.5 can be tested once more recording and correlating the detection events at both BS outputs yielding an intensity correlation function $g^{(2)}(\tau)$. In case of ideal indistinguishability no correlated events will appear around $\tau = 0$. For all considerations regarding the temporal pattern of $g^{(2)}(\tau)$ in the remainder of this section, we assume the photons to be entirely distinguishable.

Besides the central peak, the resulting intensity correlation has a rich structure of neighboring peaks, which requires some further clarification. First, consider two photons that were emitted subsequent to the double pulse excitation of a single excitation cycle. As each photon can take two different paths at BS1, there are four possible outcomes, all of which illustrated in Fig. 5.7 (b). The left column therein shows where early and late photon go after BS1 (dashed and dotted beam path, resp.). If both photons are either transmitted or reflected (first and third case), their relative delay does not change during propagation in the MZI. Accordingly, a coincidence appears at a time bin with $\tau = \pm\tau_{\text{mzi}}$, corresponding to the blue and red bar depicted on the right hand side. The sign of τ depends on whether the early (positive sign) or late photon (negative sign) leaves BS2 towards the *start*-detector 2 as illustrated in the middle column. Similar considerations show that we obtain coincidences at

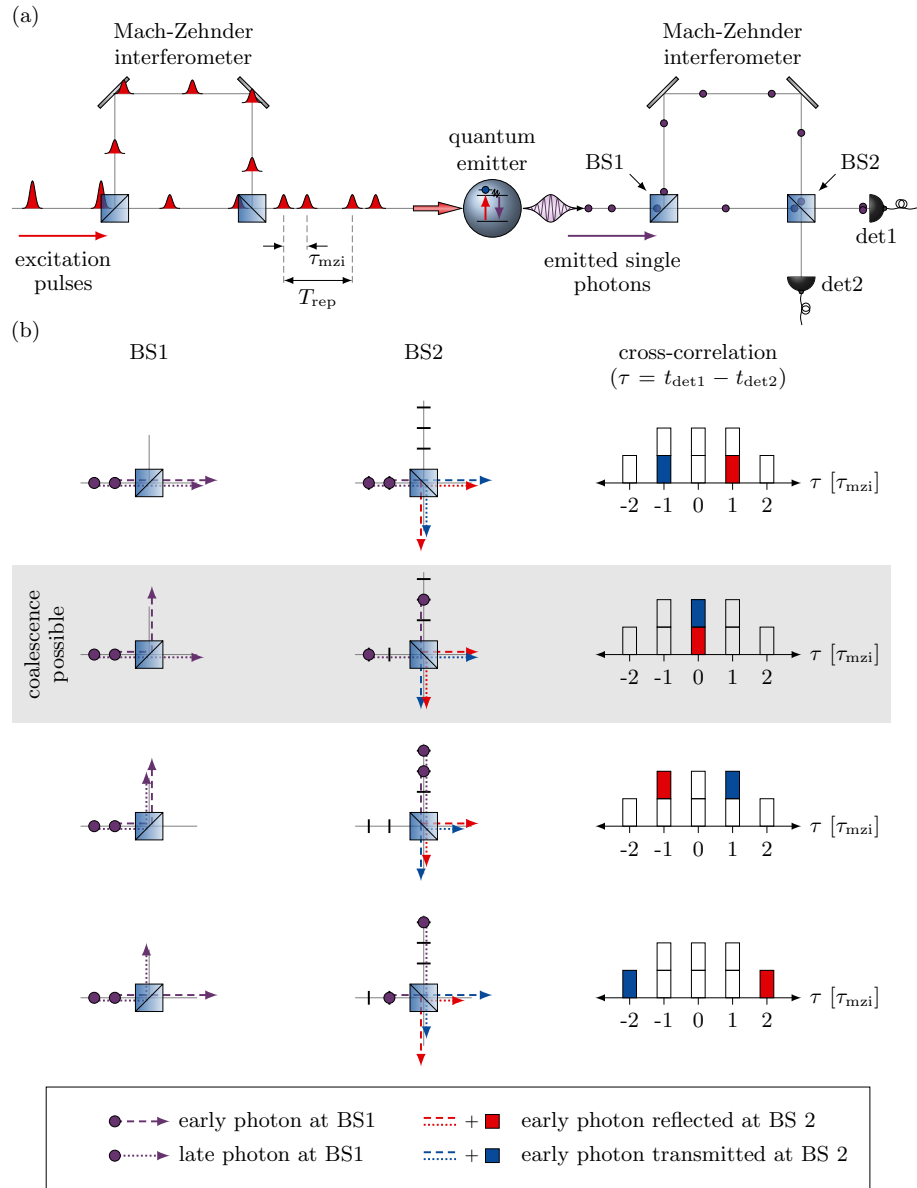


Figure 5.7. Experimental concept of two-photon interference with consecutively emitted single photons. (a) A Mach-Zehnder interferometer (MZI) in the excitation beam path (red) creates double pulses separated by τ_{mzi} . A second MZI compensates the delay between consecutively emitted single photons (violet). (b) Depending on the path the two single photons take at the entrance and exit of the second MZI, coincidences will appear in 5 different time slots of the resulting histogram. Only in case the early photon takes the long path and the late photon the short path both will simultaneously arrive at BS2 making coalescence possible.

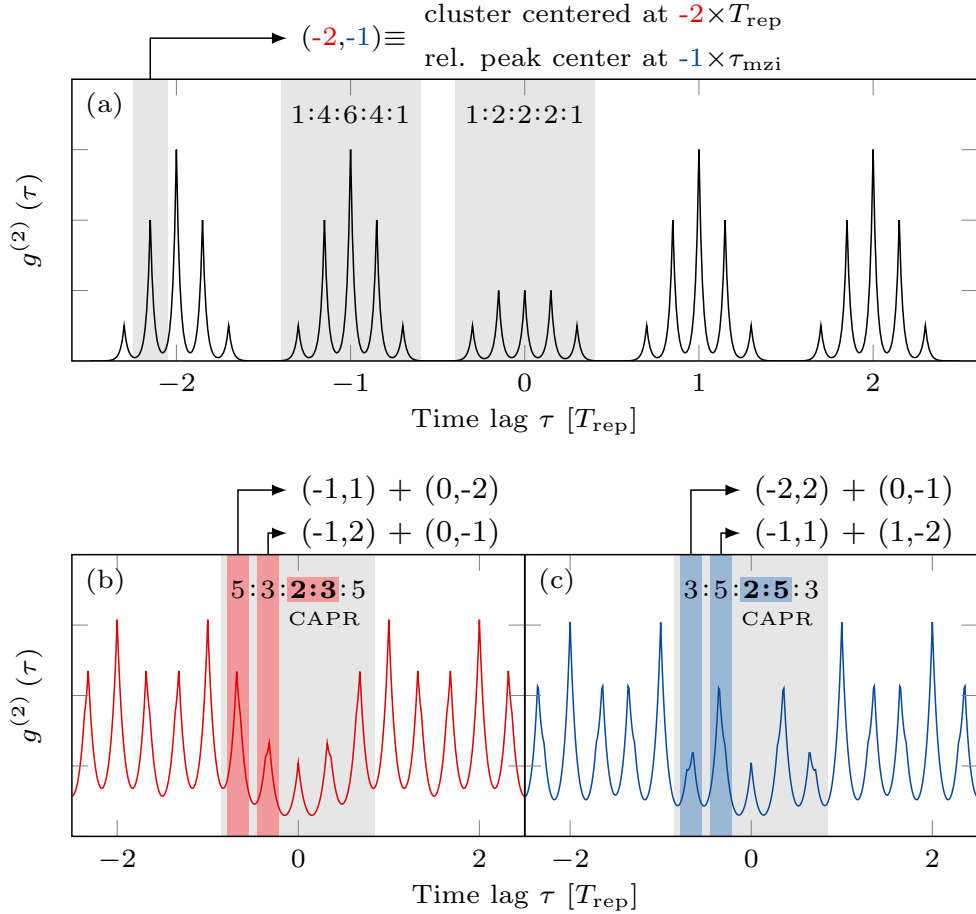


Figure 5.8. Temporal pattern of intensity correlation in HOM experiment. (a) Idealized example with well separated peaks corresponding to $\tau_{\text{mzi}}=0.15 \cdot T_{\text{rep}}$ and $\tau_r=0.02 \cdot T_{\text{rep}}$. The peaks of the central cluster have relative intensities of $1:2:2:2:1$, while all neighboring ones exhibit $1:4:6:4:1$. We identify each peak by a tuple (n, l) , meaning the peak originates from the cluster centered around $n \cdot T_{\text{rep}}$ and is at a relative position of $l \cdot \tau_{\text{mzi}}$. (b) and (c) show the patterns obtained in experiment with unconverted and converted photons, i.e. using (b) $\tau_{\text{mzi}}=0.32 \cdot T_{\text{rep}}$ and $\tau_r=0.08 \cdot T_{\text{rep}}$ as well as (c) $\tau_{\text{mzi}}=0.64 \cdot T_{\text{rep}}$ and $\tau_r=0.07 \cdot T_{\text{rep}}$. Note the change in the central-to-adjacent-peak-ratio (CAPR) as a result of different overlapping peaks (compare notes on top of plot). Also, all central peaks are plotted with an intensity of '2', corresponding to entirely distinguishable photons.

$\tau = 0$ and $\tau = \pm 2\tau_{\text{mzi}}$ when both photons part ways at BS1 with the early one taking the long and short path, respectively (second and forth case). The former case leads to the previously discussed and desired initial situation of a HOM experiment. Altogether we obtain a cluster of 5 coincidence peaks with relative intensities of 1:2:2:2:1 centered at $(-2:-1:0:1:2)\tau_{\text{mzi}}$.

Fig. 5.8 (a) shows the full intensity correlation for $\tau_{\text{mzi}}=0.15\cdot T_{\text{rep}}$ incorporating the temporal shape of each peak corresponding to $\tau_r=0.02\cdot T_{\text{rep}}$. In this example all peaks are well separated making it easy to understand their origin and all relative intensities. Besides the central cluster we just discussed, further clusters can be seen centered around $\pm T_{\text{rep}}$, $\pm 2\cdot T_{\text{rep}}$, etc. These stem from coincidences between photons emitted during distinct excitation cycles and exhibit relative intensities of 1:4:6:4:1. Besides all contributions considered in the preceding paragraph, additional coincidences arise, as both photons might impinge on the interferometer either in the early or late time bin of the respective excitation cycle. More specifically, two early or two late photons both being reflected or transmitted at BS1 lead to 8 more coincidences - each 4 at $\tau = \pm T_{\text{rep}}$. Another 8 coincidences appear for one photon being reflected and one transmitted at BS1, which are equally distributed to the 4 distinct time bins at $\tau = +T_{\text{rep}} \pm \tau_{\text{mzi}}$ and $\tau = -T_{\text{rep}} \mp \tau_{\text{mzi}}$. For ideal single photons, these cases are impossible within a single excitation cycle and therefore do not appear in the central cluster.

Eventually, we introduce the tuple (n, l) in Fig. 5.8 (a) used to identify each peak, where n refers to the cluster and l to its relative position, i.e. the peak is centered at $\tau_{n,l} = n\cdot T_{\text{rep}} + l\cdot \tau_{\text{mzi}}$. Fig. 5.8 (b) and (c) show the $g^{(2)}(\tau)$ -functions we expect to measure in the present experiment for unconverted and converted photons, respectively (see caption for parameters). It is important to note the change in the intensity ratio of central to adjacent peak. As in (b) the adjacent peak is composed of $(-1,2)$ and $(0,-1)$, we find a ratio of 2:3 [compare red box denoted CAPR in (b)]. In contrast, the adjacent peak in (c) is the sum of $(-1,1)$ and $(1,-2)$, leading to 2:5 instead [blue box in (c)].

5.3.2 Mach-Zehnder Interferometers

The MZI in the excitation beam path as well as the emission interferometer for unconverted photons are built with bulk optics. The emission interferometer at the telecom regime, on the other hand, is constructed using fiber-based components. All interferometers are aligned such that they exhibit classical interference visibilities close to unity, which was assessed using coherent light sources. Besides an optimization of the spatial mode overlap at the output BS of the free-space interferometers, this requires a polarization match between both interferometer arms. On that note the polarization in one arm of each interferometer was controlled using half-wave plates in case of the free-space MZIs and a fiber polarization controller for the telecom MZI. In order to match the delays of both interferometers, the mirrors of the excitation MZI

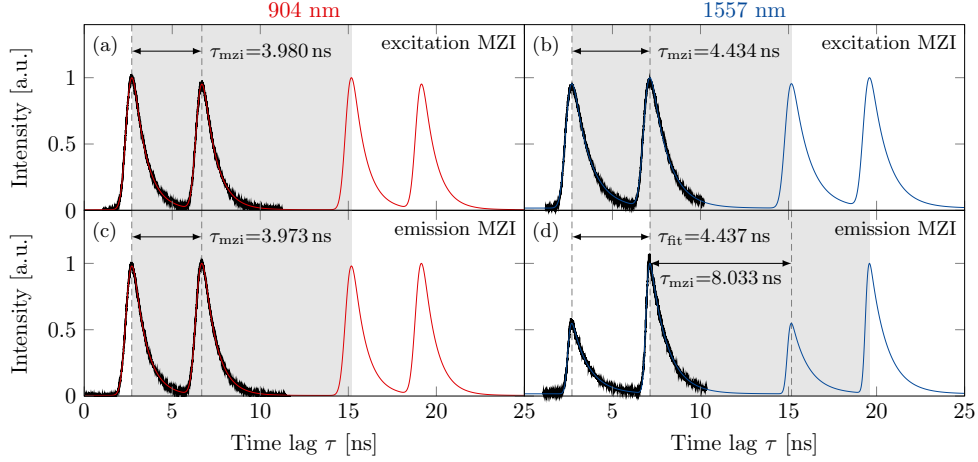


Figure 5.9. TCSPC measurements of Mach-Zehnder interferometer delays. The measurements of the delays τ_{mzi} introduced by excitation and emission Mach-Zehnder interferometers are shown in (a) and (c) for unconverted and in (b) and (d) converted photons (data in black, fits and extrapolation in red and blue). The gray areas indicate one full excitation with a length $T_{\text{rep}}=12.47$ ns chosen such that they start at the fundamental pulse entering the interferometer. The retarded pulse is accordingly within the gray area.

are shifted with help of a translation stage. As we have seen, the temporal pattern of the intensity correlation is determined by repetition time T_{rep} , MZI delay τ_{mzi} , as well as radiative lifetime τ_r . The only parameter we are free to choose is τ_{mzi} , which should be small enough to minimize the overlap of adjacent clusters, but also large enough compared to τ_r so that all peaks can be sufficiently resolved (compare Fig. 5.8 (a) or examples given in [89, 150, 230]). Due to the comparatively large lifetime of the QD under investigation, both conditions cannot be simultaneously met. Therefore, we chose $\tau_{\text{mzi}} \approx 4$ ns as reasonable trade-off, which leads to the pattern already presented in Fig. 5.8 (b).

In order to determine each τ_{mzi} we repeat the TCSPC measurements presented in Sect. 5.2.1 with the associated MZI being integrated to the beam path. As the measured data in Fig. 5.9 (black) show, we thereby obtain two exponential decays, whose centers are separated by τ_{mzi} . All data are accordingly fitted using using Eq. (5.3). For the excitation and emission interferometers used for unconverted photons [(a) and (c), fit: red] we obtain $\tau_{\text{mzi}}=3.980$ ns and 3.973 ns, respectively. The remaining difference of $\delta\tau_{\text{mzi}}=7$ ps is close to the resolution limit of the correlation electronics (4 ps) and well below the detector jitter, so that the interferometers can be deemed as matched. Following the discussion on the asynchronous arrival of photons given in the supplement of [197], $\delta\tau_{\text{mzi}}$ corresponds to a reduction of TPI

contrast of only $1 - \exp(-\delta\tau_{\text{mzi}}/\tau_r)=0.7\%$, which will be neglected in the following.

The equivalent measurements for the converted photon experiment are shown in Fig. 5.9 (b) and (d). While the excitation interferometer exhibits $\tau_{\text{mzi}}=4.434$ ns, there is a twist in the data for the emission MZI, which we only became aware of in the aftermath of the experiments: The fitted delay of $\tau_{\text{fit}}=4.437$ ns does not equal the desired τ_{mzi} , but corresponds to the difference between a pulse retarded in the long arm of the interferometer and the fundamental pulse of the subsequent excitation cycle. Therefore, the actual MZI delay is given by $\tau_{\text{mzi}} = T_{\text{rep}} - \tau_{\text{fit}}=8.033$ ns. This is further visualized by the gray regions plotted in Fig. 5.9, each of which spanning an entire excitation cycle starting and ending at a fundamental pulse. While all data shown in (a) - (c) were recorded within a single cycle, the last measurement extends over two adjacent cycles. We like to mention that the MZI delay of 8 ns was unintended, but resulted from an unnoticed mistake in the interferometer design.

Although we are dealing with two differently imbalanced interferometers for the experiment including QFDC, we still have a valid HOM experimental situation on hand. As the delays meet the condition $T_{\text{rep}} = \tau_{\text{mzi,em}} + \tau_{\text{mzi,ex}}$, a pulse, which took the long path in both interferometers, will meet with a pulse of the subsequent cycle that took two times the short one. In fact, the situation is completely equivalent to both interferometers having a delay of 8.033 ns, whose correlation pattern we discussed in Fig. 5.8 (c).

5.3.3 Correlation Measurements

The $g^{(2)}(\tau)$ -functions measured in the HOM experiment are depicted in Fig. 5.10 (a) and (b) as black circles. The observed structures agree with the predicted patterns in Fig. 5.8 (b) and (c). Merely the central peak at $\tau=0$ reveals a reduced intensity, which is particularly evident for the measurement in the NIR regime. This observation indicates that photons, which simultaneously arrive at the HOM beam splitter, coalesce with a probability higher than the classical value of 0.5, being the signature of partial indistinguishability we expect to encounter.

To extract the TPI contrast from the experiment we perform Monte-Carlo simulations with the method and parameters presented in Sect. 5.2.4. We additionally assume two single photons per excitation cycle separated by τ_{mzi} and incorporate the emission MZI to the simulation via two corresponding reflection/transmission decisions. If both fluorescence photons meet at the last BS, we have to consider TPI to obtain the correct temporal distribution of coincidences. In this respect, our simulations follow the cross-correlation function given by Eq. (3.39), which includes all spectral properties of the emitter. Its numerical implementation, however, is involved and therefore separately detailed in Appx. D.

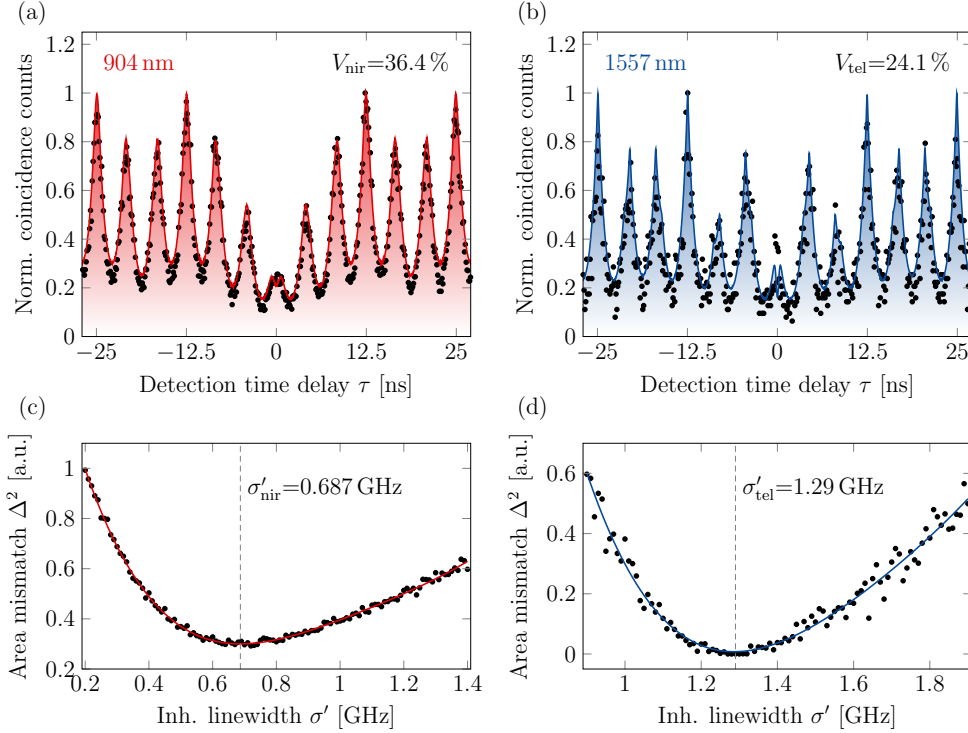


Figure 5.10. Intensity correlations from two-photon interference experiments. (a) and (b) show measured correlations (black circles) and Monte-Carlo simulations (shaded areas) revealing two-photon interference visibilities of $V_{\text{nir}}=36.4\%$ and $V_{\text{tel}}=24.1\%$ for unconverted and converted photons. The visibilities result from a minimization of the squared mismatch Δ^2 between the areas of the center peaks of data and simulation with respect to the inhomogeneous linewidth σ' . The minimization results are depicted in (c) and (d). Adapted with permission from [251], Optical Society of America.

The most essential step of our analysis is to account for the different interferometer delays in both wavelength regimes, as they determine the time passing between the emission events of both photons. As τ_{mzi} is in the same order of or below typical memory depths associated with spectral diffusion [192–195], the effective inhomogeneous linewidth σ' increases with τ_{mzi} , which causes the TPI contrast to decline. Therefore, our main objective is to determine the underlying σ' . On that note, we first simulate the expected correlation measurement for a given guess of σ' and after proper normalization evaluate the mismatch between data and simulation via the squared deviation of the central peak areas $\Delta^2 = (A_{\text{data}} - A_{\text{sim}})^2$. The mismatch Δ^2 is calculated for various σ' , which is plotted in Fig. 5.10 (c) and (d). From a fit to a fourth order polynomial, we find minimal deviations at $\sigma'_{\text{nir}} = (0.687 \pm 0.005)$ GHz and $\sigma'_{\text{tel}} = (1.29 \pm 0.01)$ GHz, which correspond

to TPI visibilities of $V_{\text{nir}} = (36.4 \pm 0.2) \%$ and $V_{\text{tel}} = (24.1 \pm 0.2) \%$, respectively⁴. The simulated intensity correlations at these optimized inhomogeneous linewidths are shown as shaded areas in Fig. 5.10 (a) and (b). While the simulation excellently reproduces the data for the unconverted photons, it clearly underestimates the correlation of converted photons for a few bins around $\tau=0$. However, it is important to keep in mind that this simulation corresponds to a best fit regarding the peak area. Indeed it can be seen that all adjacent bins are overestimated instead. Therefore, we conclude that the measured time structure of the central peak results from an unfortunate distribution of correlated events due to insufficient integration time, i.e. a large statistical error.

In Fig. 5.11 both experimentally determined visibilities are plotted against the corresponding MZI delay, visualizing the observed drop of V with increasing τ_{mzi} . In Sect. 2.2.3 we have seen that a fluctuating occupation of charge traps in the vicinity of the QD leads to a diffusion of its transition energy following the dynamics of a random walker in a harmonic potential. Accordingly, the carrier frequencies of two consecutively emitted photons are correlated if not $\tau_{\text{mzi}} \gg \tau_{\text{sd}}$, where τ_{sd} is the memory depth of spectral diffusion. Following our discussion in Sect. 3.2.3, the visibility in this case is given by Eq. (3.40), which reads⁵

$$V(\tau_{\text{mzi}}) = \sqrt{\frac{\ln 2}{2\pi}} \cdot \frac{\text{Re}[w(z)]}{\tau_{\text{r}} \cdot \sigma'(\tau_{\text{mzi}})} \quad \text{with} \quad z = i \sqrt{\frac{\ln 2}{2\pi^2}} \cdot \frac{1/\tau_{\text{r}} + 2\Gamma^*}{\sigma'(\tau_{\text{mzi}})} \quad (5.10)$$

with the time-dependent inhomogeneous linewidth

$$\sigma'(\tau_{\text{mzi}}) = \sigma'_0 \cdot \sqrt{1 - e^{-\tau_{\text{mzi}}/\tau_{\text{sd}}}}. \quad (5.11)$$

Taking radiative lifetime τ_{r} , pure dephasing rate Γ^* , and inhomogeneous linewidth σ'_0 as determined in Sect. 5.2.1 and 5.2.2, we fit Eq. (5.10) to the measured visibilities. The result is shown in Fig. 5.11 as red curve and reveals $\tau_{\text{sd}} = (230 \pm 30) \text{ ns}$, being well within the range of values found in literature [192–195]. Therefore, we conclude that the change in the interferometer length between the HOM experiments with unconverted and converted photons is the source of loss of interference contrast. This implies that quantum frequency down-conversion does not alter the indistinguishability of single photons.

From the shape of the curve we furthermore recognize the limits of V . For small delays, the inhomogeneous broadening vanishes. However, fast pure dephasing processes remain, so that the visibility will rise no higher than 92 % corresponding to $\Gamma^* = 47 \text{ MHz}$ (compare upper dashed line). In the opposite

⁴The analysis presented in [251] did not include the explicit time structure of $g^{(2)}(\tau)$, leading to different visibilities obtained therein.

⁵Note that we here use the FWHM σ'_0 instead of the corresponding standard deviation σ_0 in contrast to Eq. (3.40).

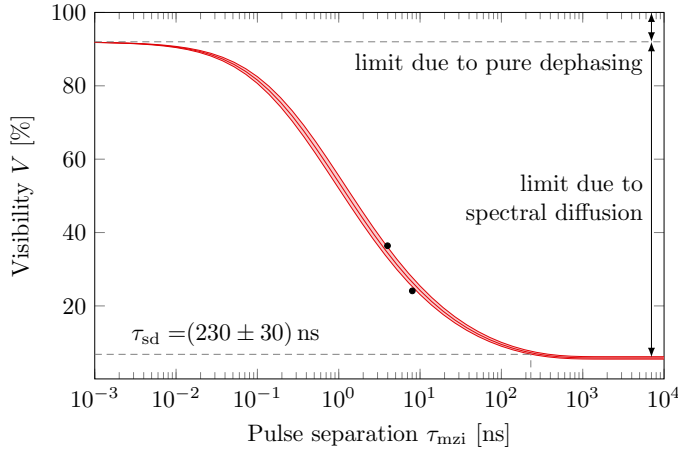


Figure 5.11. Two-photon interference visibility as function of the timelag between consecutive emission events. The two black data points correspond to the measured visibilities for unconverted (left) and converted photons (right). The red curve is a fit of the visibility, assuming a time-dependency of the line broadening due to spectral diffusion. It reveals a memory depth of $\tau_{sd} = (90 \pm 7)$ ns. The dashed lines illustrate an upper and lower bound for the visibility corresponding to the pure dephasing rate and inhomogeneous linewidth determined in Sect. 5.2.2.

limit of large delays, the inhomogeneous broadening reaches its equilibrium value σ'_0 , resembling a HOM experiment with two photons, whose carrier frequencies explore the same spectral distribution, but in a mutually uncorrelated fashion. This situation leads to a TPI visibility of around 6% (lower dashed line).

5.4 Summary

In the course of this chapter, we have presented experimental results proving that QFDC does not alter the indistinguishability of single photons. The experiments were performed using fluorescence photons emitted by an InAs QD. All spectral and temporal properties necessary to assess the HOM measurements were determined - both for unconverted near-infrared photons as well as converted photons in the telecom C-band. It was shown that the differences in TPI contrast between both wavelength regimes solely result from setup related parameters and not the down-conversion step itself. An overview over the primary results and conclusions is given in the *highlights*-box below.

CHAPTER 5 - HIGHLIGHTS

Photon Source

- Investigated were single photon emitted by an InAs QD at 903.6 nm with a photon flux of 117,600 photons/s after spectral filtering (Sect. 5.1.1).
- The single photons were obtained after *p*-shell excitation with a pulsed laser at a repetition rate of 80 MHz (Sect. 5.1.1).
- The unconverted photons show a radiative lifetime of 970 ps and a coherence time of 87 ps. The coherence is reduced due to pure dephasing at a rate of 47 MHz and spectral diffusion of the emission line in a range of 5.9 GHz (Sect. 5.2.1 and 5.2.2).
- A clear antibunching was observed with an intensity correlation value of $g_{\text{nir}}^{(2)}(0)=0.153$. The deviation from zero can be related to emission collected from spectrally distinct transitions. From the spectra an SBR of 11.5 was extracted matching the antibunching value (Sect. 5.2.3 and 5.2.4).

Frequency Conversion

- A quantum frequency down-conversion scheme was applied mixing the single photons with a pump field at 2154 nm inside a PPLN waveguide, leading to a target wavelength of 1557 nm (Sect. 5.1.2).
- The frequency converter was operated at an external device efficiency of 30.9% being comparable to [95, 96, 104] or better than [103, 105] values reported in literature. The process yielded 86,700 telecom photons per second (Sect. 5.1.2).
- At the telecom regime a radiative lifetime of 887 ps was observed. The SBR improved to 17.2 involving a smaller antibunching value of $g_{\text{tel}}^{(2)}(0)=0.117$ (Sect. 5.2.1, 5.2.3, and 5.2.4).
- Perfect agreement of measured antibunching and SBR limit extracted from spectra for unconverted as well as converted photons indicates ideal conservation of photon statistics during quantum frequency conversion (Sect. 5.2.4).

CHAPTER 5 - HIGHLIGHTS CONTINUED

Two-Photon Interference

- Hong-Ou-Mandel measurements revealed TPI visibilities of 36.4% and 24.1% for unconverted and converted photons, respectively (Sect. 5.3.3).
- The loss of visibility was quantitatively attributed to spectral diffusion of the quantum dot's emission wavelength. It has a larger impact at the telecom regime due to an increased time lag between the emission processes of both photons. Accordingly, the photon indistinguishability is conserved throughout quantum frequency conversion. The memory depth of spectral diffusion was estimated to be 230 ns (Sect. 5.3.3).
- Both antibunching and Hong-Ou-Mandel measurements were additionally emulated by Monte-Carlo simulations. The simulations were performed based on independently determined model parameters and perfectly reproduce the correlation measurements. This underlines that all relevant aspects of the experiments are completely understood (Sect. 5.2.4 and 5.3.3).

Quantum Interference between Down-Converted Photons from Remote Quantum Dots

Contributions and copyright notice: The experimental results presented in the scope of this chapter were obtained within a collaborative project under the joint supervision of Prof. Peter Michler (Stuttgart University) and Prof. Christoph Becher. The investigated sample was designed and fabricated by Robert Roßbach and Michael Jetter at Stuttgart University. The frequency converter was designed, set up, and operated by Benjamin Kambs (B.K.) with help of Matthias Bock. All experiments were performed at Stuttgart University by B.K., Jonas Heinrich Weber (J.H.W.), Simon Kern, and Simone Luca Portalupi with support of Jan Kettler (all Stuttgart University except for B.K.). The data were analyzed by B.K. and J.H.W.

Note that the main results presented in this chapter were originally published in [266] (Copyright © 2018 The Authors. Published by Springer Nature).

In the preceding chapter we provided the experimental proof of principle that QFDC does not impair the indistinguishability of single photons. This enables us to implement and test down-conversion schemes in more complex situations, which aim at quantum information processing applications based on TPI. The coalescence of two photons from independent emitters at a single beam splitter is a key ingredient for long-haul quantum repeater networks, which are naturally composed of a large number of remote stationary quantum memories [31–33]. This type of experiment has been successfully performed on various platforms including spontaneous parametric down-conversion sources [62], trapped ions [63] and atoms [61], as well as solid state

single photon emitters including QDs [65, 151, 152, 155], color centers in diamond [66–68], or single molecules in crystalline materials [64]. In this chapter, we demonstrate quantum interference with photons from remote InAs QDs, but additionally integrate two independent frequency converters - one for each emitter. The HOM experiment is then performed with the converted photons at the telecom C-band. Besides the commonly quoted advantage of an interface to the low-loss regime of optical fibers, frequency conversion offers yet another benefit to the overall scheme at hand: in case of solid state sources the emission frequencies of both emitters typically differ and therefore need to be actively matched. To that end the emitters can be tuned with help of various control parameters, such as temperature [151–153], strain [154–156], as well as static electric [64–67] or magnetic fields [157, 158]. All of those parameters, however, directly or indirectly act on the electronic structure of the emitter and thereby potentially degrade the spectral properties of the emitted photons. In contrast, we tune the C-band photons during down-conversion via control of the pump-laser frequency instead, which renders invasive tuning mechanisms unnecessary.

In the following, we will outline the overall experimental scheme and highlight the main differences in QD excitation, photon extraction, and QFC compared to the experiment presented in Chap. 5. After the assessment of spectral and temporal properties of both single photon sources individually, we present the mutual HOM experiment and fully explain the outcome based on all predetermined parameters.

6.1 Experimental Overview

The remote HOM experiment reduced to its principal components is illustrated in Fig. 6.1 (a). As single photon source we use two InAs/GaAs quantum dots, here denoted QD1 and QD2, which stem from the same sample *M5059* investigated in the preceding chapter (compare Sect. 5.1.1 for details), but are located in two distinct fragments of it that are installed in two independent cryostats. Based on the measured radiative lifetime and coherence time presented in Sect. 5.2.1 and 5.2.2, we expect remote HOM visibilities of no more than $\tau_{\text{coh}}/(2\tau_{\text{r}}) \approx 5\%$ for photons from this sample mainly due to the large inhomogeneous linewidth of almost 6 GHz. To achieve superior photon indistinguishabilities we mainly take two measures in the QD operation that go beyond the methods employed in the preceding experiment: **(i)** the QDs are optically excited with π -pulses resonant with the *s*-shell (as opposed to *p*-shell excitation) to minimize interactions between excitons and environment as well as to reduce the timing jitter in their creation process, and **(ii)** a weak above-band cw-laser at 808 nm is added to the excitation light, which generates free charges in the conduction band. These keep charge traps in the vicinity of the emitter constantly occupied and thereby further stabilize the

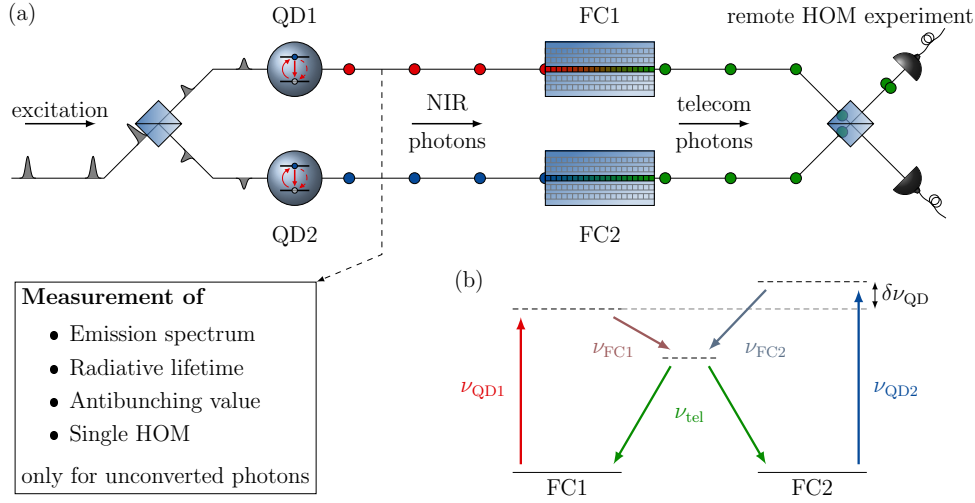


Figure 6.1. Illustration of the overall remote Hong-Ou-Mandel experiment. (a) Both quantum dots, denoted QD1 and QD2, are resonantly excited by the same pulsed laser. The emitted single near infrared (NIR) photons are detuned with respect to each other (red and blue color, resp.). The frequency converters FC1 and FC2 are set to convert the photons of both sources to a common wavelength at the telecom C-band (green photons). Eventually, the photons are overlapped on a beam splitter to test their indistinguishability in a Hong-Ou-Mandel (HOM) type experiment. All single photon properties such as emission spectra, radiative lifetimes, antibunching-values, and indistinguishabilities of consecutively emitted photons are measured with unconverted photons prior to conversion. (b) Energy scheme of both frequency conversion processes. The initial NIR photons exhibit a frequency offset of $\delta\nu_{\text{QD}} = \nu_{\text{QD2}} - \nu_{\text{QD1}}$. If the pump lasers of both converters fulfill $\nu_{\text{FC2}} - \nu_{\text{FC1}} = \delta\nu_{\text{QD}}$, the converted telecom photons are spectrally overlapped at ν_{tel} .

emission frequency [131, 132]. For excitation, a single pulsed laser is used, which is split at a free space BS and then forwarded via optical fibers to both confocal microscopes containing the respective QDs. The QD emission lines are located at the NIR regime and detuned by about $\delta\nu_{\text{QD}} = \nu_{\text{QD2}} - \nu_{\text{QD1}} \approx 8$ GHz (compare Sect. 6.2.1). However, the spectral width of the excitation laser light is >160 GHz, i.e. sufficiently large to simultaneously cover both resonances.

The emitted photons are virtually distinguishable, as the detuning $\delta\nu_{\text{QD}}$ is significantly larger than their respective linewidths (illustrated by red and blue colored photons). To compensate the detuning we employ two independent frequency converters, FC1 and FC2, both operated at differing pump laser frequencies ν_{FC1} and ν_{FC2} . If these fulfill $\nu_{\text{FC2}} - \nu_{\text{FC1}} = \delta\nu_{\text{QD}}$ according to the energy scheme shown in Fig. 6.1 (b), the converted output photons of both

sources will exhibit a common wavelength inside the telecom C-band (green photons). The telecom photons are then forwarded within optical fibers over a distance of ≈ 60 m before being overlapped on a symmetric fiber-based BS. Here, the photons coalesce, if indistinguishable, which is tested by a coincidence measurement between both BS outputs.

The outcome of the remote HOM experiment will be assessed based on the temporal and spectral properties of both emitters. These include radiative lifetimes, spectral line-broadening contributions, antibunching values, as well as indistinguishabilities of consecutively emitted photons for each source individually. The parameters of interest are measured with unconverted photons prior to the down-conversion step, as their conservation during QFC has been sufficiently demonstrated elsewhere (see [95] and Chap. 5).

6.2 Single Photon Generation

In the following we describe the confocal microscopes and frequency converters, which were used to obtain the single photons at telecom wavelengths necessary for the intended remote HOM experiment. The setup is comparable to the one presented in Sect. 5.1 for the most part. However, some differences arise due to the resonant excitation scheme as well as the more rigorous requirements regarding frequency stability of the frequency converters, which will be discussed in this section. As the confocal microscopes were designed, set up, and operated by our collaboration partner at Stuttgart University, we here only elaborate on specific features necessary to understand experimental aspects relevant to this chapter. A more detailed treatment can be found in [162].

6.2.1 Confocal Microscope for Resonant Excitation of Trions

A scheme of the employed confocal microscope is depicted in Fig. 6.2 (a). The InAs/GaAs sample is located inside a flow-cryostat and cooled to a temperature of 4 K. In Sect. 5.1.1 we have pointed out that the QDs from this sample emit in a range from 885 nm to 910 nm. Accordingly, we need an excitation source in the same wavelength regime in order to *resonantly* address the *s*-shell transition. For that purpose we use a Ti:Sa laser (model Mira 900P, COHERENT, USA), which emits optical pulses with a duration of around 3 ps at a repetition rate of 76.2 MHz. The excitation light (200-300 nW) is superimposed with light from the aforementioned non-resonant cw-laser (10-20 nW) and guided through a delay stage before entering the confocal microscope. The delay stage is inserted only in front of one of the microscopes and used to synchronize the photons emitted by both QDs for the final remote HOM experiment. Furthermore, for HOM experiments with consecutively emitted photons from a single QD (compare Sect. 5.3), the delay stage can be

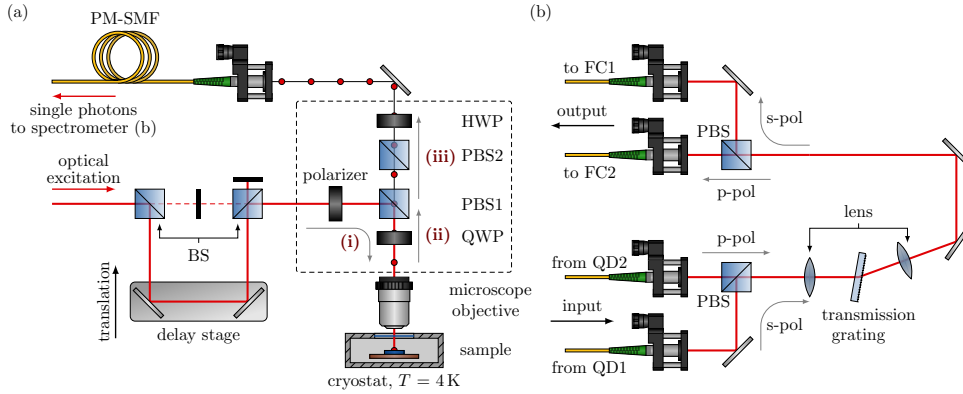


Figure 6.2. Confocal microscope for resonant excitation of quantum dots.

(a) The sample is located inside a cryostat and cooled to 4 K. To separate the optical excitation light (red line) from the emitted photons (red circles) a setup for polarization suppression is used (see dashed frame). Its principal components are a linear polarizer, two polarizing beam splitters (PBS), as well as a quarter and a half wave plate (QWP and HWP). The steps of the suppression process are labeled (i) - (iii) and detailed in the main text. The photons are eventually coupled to a polarization-maintaining single-mode fiber (PM-SMF). The shown delay stage is used to either synchronize the converted photons in the final HOM experiment or as Mach-Zehnder interferometer, if the beam block (black bar) is removed. (b) Illustration of the filter-spectrometer used to spectrally clean up the fluorescence photons. The photons from QD1 and QD2 enter the spectrometer in s- and p-polarized states, respectively and are overlapped on a PBS. Both pass a transmission grating and subsequently disperse. On a second PBS both polarization components are separated, coupled to a single-mode fiber and forwarded to the respective frequency converters (FC). The spectrometer is aligned such that a band of ≈ 15 GHz around the central emission frequency of each QD is efficiently coupled to the corresponding fiber.

converted to a Mach-Zehnder interferometer with variable delay by simply removing the beam block between both beam splitters (black bar).

The resonant excitation scheme is a necessity to achieve competitive indistinguishabilities, but it entails an experimental inconvenience, as the excitation light can no longer be removed from the fluorescence photons via spectral filtering. One alternative is to use orthogonal excitation and detection beam paths, which allow to spatially separate both fields [176]. Furthermore, a recent experiment demonstrated coherent excitation using dichromatic laser pulses, which are red- and blue-detuned with respect to the resonance [267]. We follow another option, however, by suppressing the excitation laser via polarization rejection [130, 177]. The corresponding components of the setup are shown within the dashed box in Fig. 6.2 (a). The basic suppression process

can be reduced to three main steps: **(i)** The s-polarized, incident excitation light is reflected from PBS1 and focused via the microscope objective onto the sample normal to its surface. **(ii)** Subsequent to the excitation step, the resonance fluorescence - being in an arbitrary polarization state - is collected and collimated by the microscope objective and propagates towards PBS1. Simultaneously, it is superimposed by residual excitation light, which we assume to be still s-polarized. **(iii)** The p-polarized fraction of the fluorescence is transmitted through PBS1, while the excitation light is reflected. Thereby, it is mostly removed from the transmitted fluorescence. The additional optical components depicted in Fig. 6.2 (a) fulfill various tasks to ensure an operation of the polarization suppression as close to ideal as possible. The polarizer is employed to generate a clean linear polarization of the excitation light, which is moreover aligned with the s-polarization axis of PBS1. As microscope objective, cryostat window, and sample surface alter the polarization of the impinging light, its back-reflected fraction does not necessarily possess s-polarization anymore. To partially restore the initial polarization a quarter-wave plate (QWP) is inserted between PBS1 and objective, which is passed twice by the excitation light. The maximum suppression attainable with a single PBS is capped by its extinction coefficient¹, which is typically no more than 30 to 40 dB. To obtain a better suppression, a second polarizing beam splitter (PBS2) is put in series with PBS1. Note, however, that the suppression does not benefit from even more PBSs, as each of them partially re-polarizes the impinging light, which ultimately limits the best possible performance. Eventually, the fluorescence is coupled into a polarization-maintaining single mode fiber (PM-SMF). The half-wave plate (HWP) is used to match the fluorescence polarization with one of the symmetry axes of the PM-fiber. Using the shown setup a maximal laser suppression of ≈ 60 dB is reported in [162].

Fig. 6.3 (a) shows an exemplary spectrum of the fluorescence from QD1 as collected by the detection fiber, taken with a commercial grating spectrometer (model SP2500i with an InGaAs camera, PRINCETON INSTRUMENTS, USA). The spectrum reveals a distinct peak at a wavelength of 904.44 nm, which corresponds to the ZPL of the QD. Additionally, we observe a broad background signal roughly ranging from 903-906 nm. The background is composed of residual excitation light and a phonon sideband stemming from acoustic phonons. As the phonon sideband generally has a complicated asymmetric structure [179, 180], it is not possible to specify a certain fitting function. Therefore, we only use a heuristic function consisting of 4 Gaussian peaks - one of which describes the ZPL, while the others are used to fit the background. From the resulting fit (red curve) we extract a signal-to-background ratio (SBR) of 1.6 by integrating over the entire shown spectral range. As this SBR is not sufficient for any of the subsequent experiments, the fluorescence

¹The extinction coefficient is defined as the intensity ratio of p-polarized over s-polarized transmitted light.

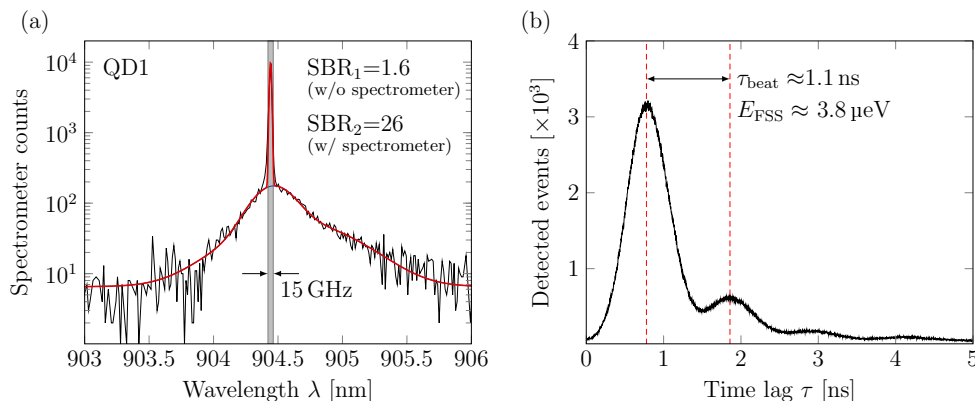


Figure 6.3. Properties of single photons after polarization suppression.

(a) Fluorescence spectrum of QD1 at the output of the confocal microscope (data: black, fit: red). A sharp fluorescence peak resides at 904.44 nm, while a broad background stemming from residual laser light and a phonon sideband ranges from 903-906 nm. Integration yields signal-to-background ratios (SBR) of 1.6 and 26 before and after additional filtering by a spectrometer (filter window of 15 GHz shown in gray). (b) Lifetime measurement of fluorescence photons collected from an exciton transition of an arbitrary QD. Due to the polarization suppression setup both emitted fine-structure components are projected to a common polarization leading to a beat in the observed decay. The beat period is estimated to be $\tau_{\text{beat}} \approx 1.1$ ns, corresponding to a fine-structure splitting (FSS) of 3.8 μeV . Due to the undesired beat node of excitons, all experiments were performed with photons emitted by trions instead.

photons are additionally passed through a homebuilt filter-spectrometer [268], which is schematically depicted in Fig. 6.2 (b). The spectrometer is designed such that it can be simultaneously used for the fluorescence from both QDs. On that account, the arriving photons are fed into the two inputs of a PBS. Their polarization states are set to be linear, perpendicular with respect to each other, and matched with the axes of the PBS. This ensures that they can be combined at the first and separated at the second PBS without any significant cross-talk between the individual polarization channels. On the common beam path, the photons are first guided through a transmission grating and subsequently disperse. Eventually, following the second PBS, they are coupled to SMFs and forwarded to the frequency converters. The cores of the SMFs act as exit slits of the spectrometer leading to an overall passband width of around 15 GHz [compare narrow gray area centered around the QD peak in Fig. 6.3 (a)]. Integrating the spectrum within the spectrometer window leads to a SBR of 26, which is only slightly below the value reported in [162] and superior to the SBR found in the scope of Sect. 5.2.3.

A unique phenomenon caused by the polarization suppression scheme emerges in radiative lifetime measurements of photons emitted during the

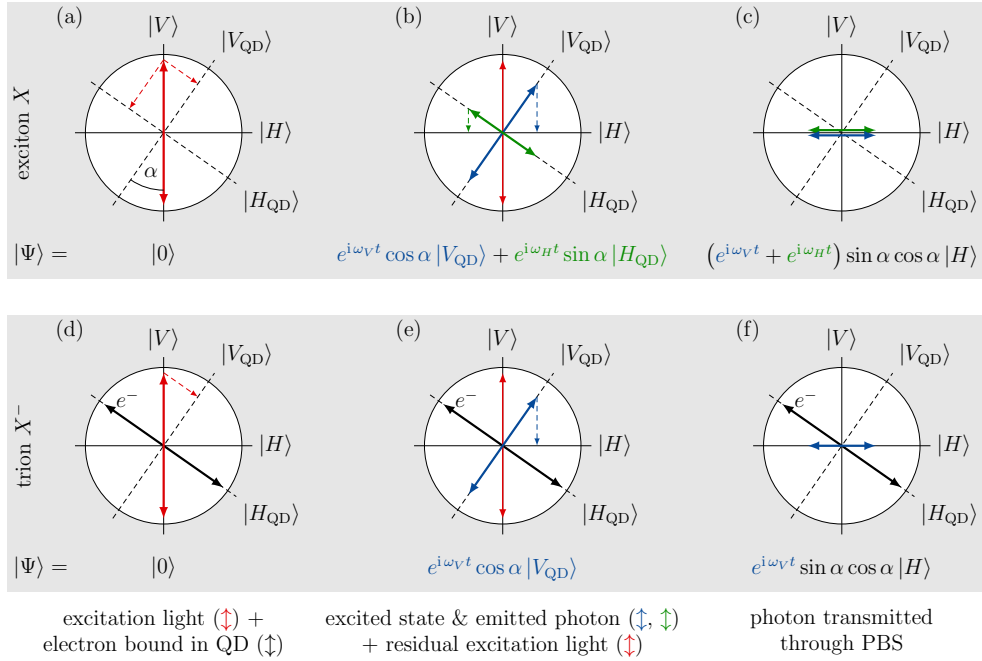


Figure 6.4. View on the polarization states of excitation and fluorescence light in the polarization suppression setup. Comparison of the excitation of excitons [(a)-(c)] and trions [(d)-(f)]. The lab frame is defined by the principal axes $|H\rangle$ and $|V\rangle$ of the polarizing beam splitter (PBS) inside the polarization suppression setup. The principal axes of the quantum dot $|H_{\text{QD}}\rangle$ and $|V_{\text{QD}}\rangle$ are rotated by α with respect to the lab frame. The fluorescence photon state is defined by $|\Psi\rangle$. Three steps in the process are illustrated [also indicated in Fig. 6.2 (a)]: **(i)** (a) and (d) show the polarization of excitation light (red), which **(ii)** creates an exciton in a superposition state of both fine structure components of the quantum dot [blue and green in (b) and (e)]. **(iii)** Transmission through the PBS projects the photon to horizontal polarization and blocks residual excitation light [(c) and (f)]. In contrast to the exciton, the trion and emitted photon only consist of a single frequency and polarization component. For details see main text.

recombination of excitons. Fig. 6.3 (b) shows a corresponding TCSPC measurement of an arbitrary QD. In contrast to the simple one sided exponential decay according to Eq. (5.3), the decay measured here clearly oscillates. These oscillations have been observed before and are commonly attributed to a beat between the fine-structure components of the QD [269,270]. To illustrate this relation we review the three steps of the laser suppression with a detailed view on the polarization state of the emitted photon from the exciton transition in Fig. 6.4 (a)-(c). Therein, the axes of the lab frame are denoted $|H\rangle$ and $|V\rangle$, while the principal axes of the QD and emitted photon $|H_{\text{QD}}\rangle$ and $|V_{\text{QD}}\rangle$ form an angle α with the lab frame and are defined by

$$|H_{\text{QD}}\rangle = \cos \alpha |H\rangle - \sin \alpha |V\rangle \quad \text{and} \quad (6.1)$$

$$|V_{\text{QD}}\rangle = \sin \alpha |H\rangle + \cos \alpha |V\rangle. \quad (6.2)$$

The s-polarized excitation light is aligned along $|V\rangle$ [red arrow in (a)]. The excitation process creates an exciton, whose spin is in a superposition state of both fine structure components [blue and green arrows in (b)]. Subsequently, the spin state is imprinted on the polarization of the emitted photon, which can therefore be written as

$$|\Psi\rangle = e^{i\omega_V t} \cos \alpha |V_{\text{QD}}\rangle + e^{i\omega_H t} \sin \alpha |H_{\text{QD}}\rangle \quad (6.3)$$

prior to PBS1. Here, the amplitudes $\cos \alpha$ as well as $\sin \alpha$ result from the projection of the laser light onto the QD axes and the phases of both fine-structure components evolve at different frequencies ω_V and ω_H . These frequencies are connected to the fine-structure splitting (FSS) via $E_{\text{FSS}} = \hbar |\omega_V - \omega_H|$. Upon transmission through PBS1 both components are projected along $|H\rangle$ leading to the output state

$$|\Psi\rangle = (e^{i\omega_V t} + e^{i\omega_H t}) \sin \alpha \cos \alpha |H\rangle. \quad (6.4)$$

In particular, a TCSPC measurements yields a signal proportional to the squared modulus of $|\Psi\rangle$, for which we find $\langle \Psi | \Psi \rangle \propto 1 + \cos [(\omega_V - \omega_H) t]$, i.e. the observed beat signature. From Fig. 6.3 (b) we read a beat period of $\tau_{\text{beat}} \approx 1.1$ ns, which corresponds to $E_{\text{FSS}} \approx 3.8$ μeV .

The fine-structure of excitons does not only complicate the interpretation of TCSPC and consequently all intensity correlation measurements, but it also has a negative impact on the intended remote HOM experiment. As both emitters generally exhibit distinct FSSs, we need to consider four different frequency components, of which only two can be matched by tuning the emission lines. The other components remain detuned, which in turn reduces the overall indistinguishability. In the scope of our experiments, we therefore choose to work with trions instead. Simply put, the additional charge present in the QD occupies one of its fine-structure components and thereby prevents the emitted photon from oscillating at two different frequencies [compare Fig. 6.4 (d)-(f)].

Fig. 6.5 (a) shows the emission spectra of trion transitions of both QD1 and QD2, which were selected for the remote HOM experiment. The lines are centered around $\lambda_{\text{QD1}} = 904.442$ nm and $\lambda_{\text{QD2}} = 904.420$ nm, respectively, i.e. they exhibit a detuning of $\delta\nu_{\text{QD}} = 8.06$ GHz. The spectra suggest that both emission lines possess a spectral overlap, which implies that a TPI signature might be observed even without tuning both emitters into resonance. Note, however, that the apparent spectral overlap only results from the limited spectrometer resolution of ≈ 6 GHz and not the actual emitter parameters. This will be detailed in the following Sect. 6.3. Feeding the output of the filter-spectrometer into a Si-APD, we obtain detection rates of $\nu_{\text{det,QD1}} =$

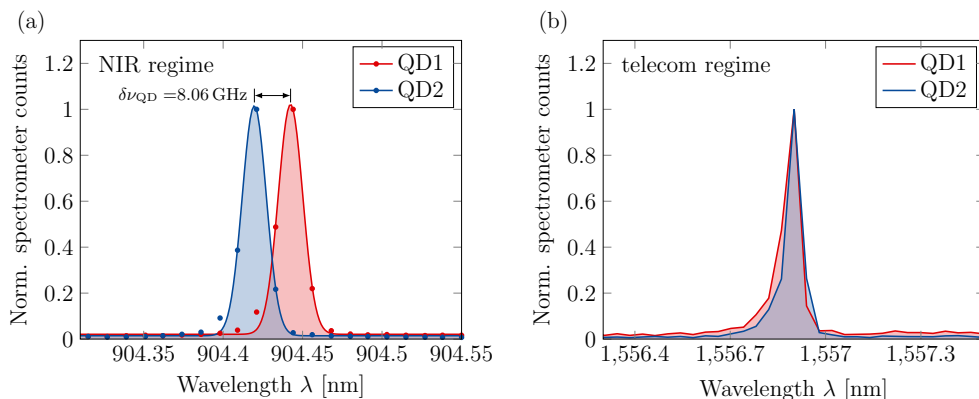


Figure 6.5. Emission spectra of both selected quantum dots.

(a) Data (dots) and fit (solid line) of unconverted photons at the NIR regime for QD1 (red) and QD2 (blue). The emission lines are centered around $\lambda_{\text{QD1}} = 904.442 \text{ nm}$ and $\lambda_{\text{QD2}} = 904.420 \text{ nm}$ and relatively detuned by $\delta\nu_{\text{QD}} = 8.06 \text{ GHz}$. (b) Exemplary spectrum of converted photons at the telecom regime when the relative pump laser detuning is set to compensate the QD detuning. It can be seen that both photons appear at the same telecom wavelength.

28-32 kHz and $\nu_{\text{det,QD2}} = 81\text{-}92 \text{ kHz}$. Taking the quantum efficiency of the detector of $\approx 30\%$ into account, we find that the QDs yield photon fluxes of around $\Phi_{\text{QD1}} = 100,000$ and $\Phi_{\text{QD2}} = 290,000$ photons per second within the output fibers of the confocal microscopes. Note that 5-10% of these photons do not stem from the resonant excitation, but are caused by the additional non-resonant cw-laser, which is used for the stabilization of the resonance.

6.2.2 Frequency Converter Performance

The wavelength of the down-converted telecom photons is determined by the pump laser employed in the frequency converter. Accordingly, any frequency fluctuation of its optical output will be imprinted on the converted photons, which potentially degrades their mutual indistinguishability. In Chap. 5 we have identified pure dephasing and spectral diffusion as the only sources of frequency noise. Pump laser fluctuations, on the other hand, did apparently not decrease the measured TPI visibilities, even though significant mode hopping was observed in the aftermath of the experiments. This suggests that pump laser instabilities act on a time-scale long compared to the emission delay of 8 ns between both QD photons, rendering them irrelevant. The situation has to be reconsidered, however, for the present remote HOM experiment. Here, both photons are independently converted and we must assume that the impact of pump laser fluctuations on both telecom photons are no longer correlated. In this case we obtain an additional contribution to the inhomoge-

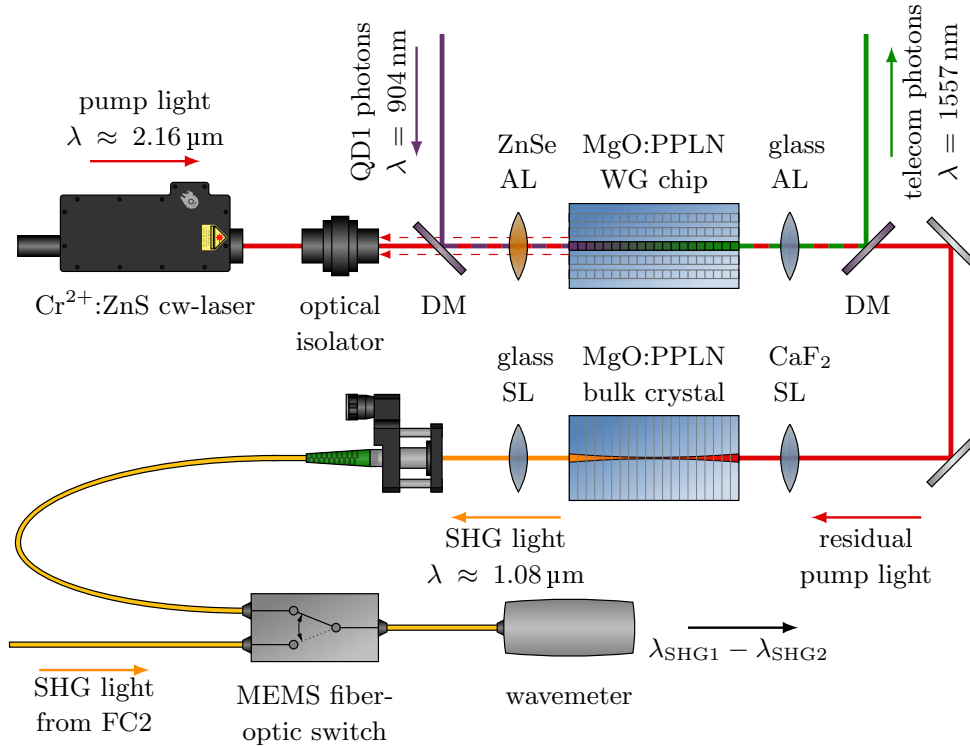


Figure 6.6. Frequency conversion setup with pump frequency monitoring. The setup mostly conforms with the one presented in Fig. 4.1. An additional optical isolator was inserted to protect the laser from light reflected at the waveguide (WG) facet. The residual pump light transmitted through the second dichroic mirror (DM) is converted to $\approx 1.08 \mu\text{m}$ via second harmonic generation (SHG) in a MgO:PPLN bulk crystal. After coupling to a fiber, the SHG light of both converters is alternately forwarded to a wavemeter by turns with help of a MEMS fiber-optic switch. SL and AL: spherical and aspheric lens.

neous broadening of the single photons, quantified by its standard deviation σ_{pump} .

Fig. 6.6 shows a simplified version of the frequency converter already discussed in Sect. 4.1². The main modification for the present experiment is the additional optical isolator (model IO-4-2150-HP, THORLABS, USA) inserted between the pump laser and dichroic mirror (DM). It protects the laser from pump light reflected at the facet of the PPLN waveguide (dashed red beam) and thereby averts the aforementioned mode hopping. Moreover, we need to determine the relative detuning of the pump lasers $\delta\nu_{\text{pump}} = \nu_{\text{FC2}} - \nu_{\text{FC1}}$ and quantify its stability by measuring σ_{pump} . On that account, we first convert

²Missing components compared to Fig. 4.1 are here only omitted for simplicity, but were still present in the actual setup.

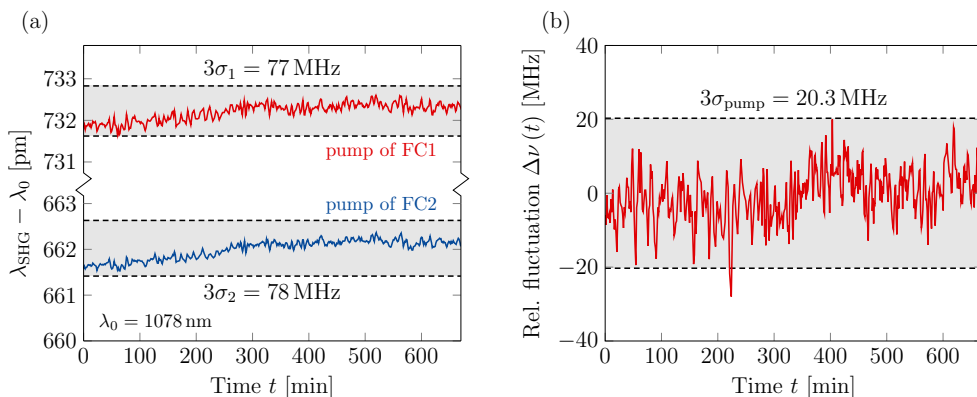


Figure 6.7. Measurement of long-time stability of both pump lasers. (a) Time trace of second harmonic generation wavelength λ_{SHG} of the pump lasers for frequency converter 1 (red) and 2 (blue) over ≈ 11 h. The wavelengths are shifted by $\lambda_0 = 1078$ nm. It can be seen that both pump lasers evolve similarly over ranges characterized by the threefold standard deviations $3\sigma_1 = 77$ MHz and $3\sigma_2 = 78$ MHz. (b) The common evolution of both pump lasers becomes more clear in their relative fluctuation $\Delta\nu(t) = \delta\nu_{\text{pump}}(t) - \langle\delta\nu_{\text{pump}}\rangle$, which has a standard deviation of only $3\sigma_{\text{pump}} = 20.3$ MHz.

the residual pump light to a wavelength of $1.08 \mu\text{m}$ by means of second harmonic generation (SHG), which is then constantly monitored by a wavemeter (model WS6-200, HIGHFINESSE, Germany) throughout all experiments. The SHG process takes place in a MgO:PPLN bulk crystal (PHOTONIK-ZENTRUM KAISERSLAUTERN E.V., Germany). The crystal is 20 mm long and possesses poling periods ranging from $31.8 \mu\text{m}$ to $32.1 \mu\text{m}$. To achieve phase matching for the desired process, it was heated to a temperature of around 240°C . With a residual pump power of some 100 mW we obtain SHG light at a few μW , which is a sufficient input level for the wavemeter. Prior to the wavemeter, a MEMS fiber-optic switch (model SL1x2-9N, SERCALO, Switzerland) is inserted, whose two input ports are fed with the SHG light of both converters, respectively. The switch is operated at a frequency of around 1 Hz and thereby enables us to simultaneously monitor both pump lasers. Fig. 6.7 (a) shows the wavelengths λ_{SHG} of both FC1 (red) and FC2 (blue) taken over a time of ≈ 11 h. Both frequencies fluctuate in a range with threefold standard deviations of $3\sigma_1 = 77$ MHz and $3\sigma_2 = 78$ MHz, respectively (compare gray areas). Assuming that the frequencies of both pump lasers evolve uncorrelated, it is possible to estimate the fluctuation range of the relative detuning $\delta\nu_{\text{pump}}$ via the Gaussian sum $\sigma_{\text{pump}}^2 = \sigma_1^2 + \sigma_2^2$ leading to $3\sigma_{\text{pump}} = 110$ MHz. It can be seen, however, that both frequencies are in fact not uncorrelated, but follow almost the same time trace. This might be the case, as both lasers were placed in the same lab and on the same optical table, i.e. they were subject

to the same environmental conditions. For further illustration, the evolution of $\delta\nu_{\text{pump}}$ around its mean $\langle\delta\nu_{\text{pump}}\rangle$ is depicted in Fig. 6.7 (b). The relative frequency fluctuates in a range of no more than $3\sigma_{\text{pump}} = 20.3$ MHz. Although this might be the more appropriate error for our purpose, we will assume the aforementioned $3\sigma_{\text{pump}} = 110$ MHz as a more careful estimate in the following.

Eventually, we assess the external device efficiency η_{ext} of both converters using a diode laser (model DL 100, TOPTICA, Germany), which is tuned to the QD resonances, as optical input signal. In order for both FCs to have a common output wavelength at around $\lambda_{\text{tel}} = 1557$ nm within the FBG filter window [compare Fig. 6.5 (b)], the pump lasers were set to $\lambda_{\text{FC1}} = 2157.46$ nm and $\lambda_{\text{FC2}} = 2157.32$ nm, respectively. Both converters were operated using WG1 in group 5 of the PPLN waveguide chip. Optimal phase matching was achieved at temperatures of 29.6°C and 46.7°C for FC1 and FC2, respectively. To obtain η_{ext} as a function of the pump power P_p we evaluate

$$\eta_{\text{ext}}(P_p) = \frac{P_{\text{tel}}(P_p)}{P_{\text{sig}}} \cdot \frac{\lambda_{\text{tel}}}{\lambda_{\text{QD}}}, \quad (6.5)$$

where the input power of the signal P_{sig} is measured at the FC input and the converted output power P_{tel} subsequent to the FBG. The factor $\lambda_{\text{tel}}/\lambda_{\text{QD}}$ accounts for the differing photon energies of both wavelength regimes. The measured efficiencies are shown in Fig. 6.8 (a) and (b) for FC1 and FC2, respectively. The solid curves therein represent fits based on the Eq. (2.36) and reveal maximal device efficiencies of $\eta_{\text{ext}}^{\text{FC1}} = (34.8 \pm 1.3)\%$ at 488 mW and $\eta_{\text{ext}}^{\text{FC2}} = (31.4 \pm 0.2)\%$ at 338 mW pump power. As can be seen, the data taken for FC1 strongly scatter compared to FC2, which was due to an unstable input

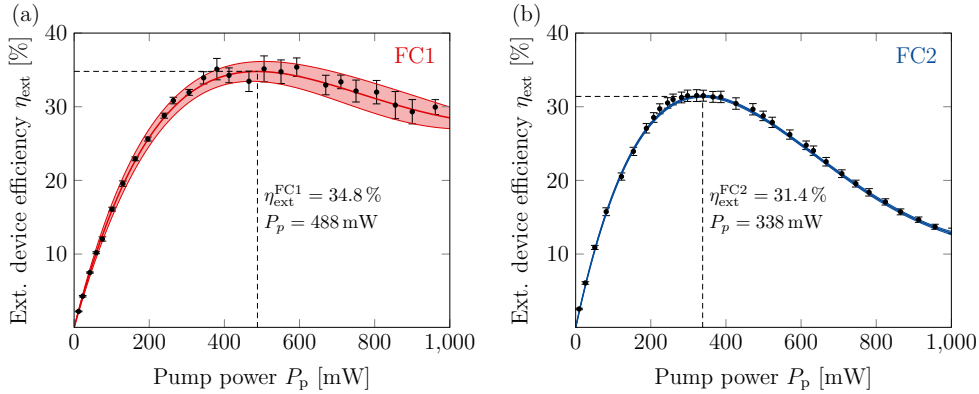


Figure 6.8. External device efficiencies of both frequency converters. Measurements of η_{ext} at different pump powers P_p for (a) FC1 and (b) FC2 are shown. The fits are accompanied by 95 % confidence bands (shaded areas) and reveal maximum efficiencies of $(34.8 \pm 1.3)\%$ and $(31.4 \pm 0.2)\%$.

power of the signal laser. The strong scatter leads to a broader confidence band (shaded area) and consequently a larger error for $\eta_{\text{ext}}^{\text{FC1}}$.

Subsequent to the conversion the telecom photons are forwarded via a 60 m fiber-link to a different lab and pass a short free space section containing further polarization controlling elements as well as the fiber-BS at which the HOM experiment takes place. For this section we measure an overall transmission of $T_{\text{QD1}} = 60.9\%$ for QD1 and $T_{\text{QD2}} = 63.5\%$ for QD2. Considering the SNSPD detection efficiency of $\eta_{\text{det}} = 30\%$ and taking the photon fluxes Φ_{QD1} and Φ_{QD2} at the converter inputs as stated in Sect. 6.2.1, we expect to obtain detection rates of $\nu_{\text{det,QD1}} = 6.4$ kHz and $\nu_{\text{det,QD2}} = 17.3$ kHz according to

$$\nu_{\text{det,QD1/2}} = \Phi_{\text{QD1/2}} \cdot \eta_{\text{ext}}^{\text{FC1/2}} \cdot T_{\text{QD1/2}} \cdot \eta_{\text{det}}. \quad (6.6)$$

In experiment we observe 5.3 kHz and 24.7 kHz, of which 550 Hz and 390 Hz can be attributed to background photons created by the pump lasers and around 50 Hz stemming from detector dark counts. The expected and observed values are in fair agreement. The discrepancy can be mainly attributed to the fact that the NIR and telecom count rates given in Sect. 6.2.1 and here, were measured at separate days, with the QDs and setups being in different conditions. Furthermore, we identify two factors contributing to the deviation: First, switching the unconverted photons from the APDs to the FCs required to exchange the output fiber of the filter spectrometer. Therefore, the precision with which Φ_{QD1} and Φ_{QD2} are known is limited by the reproducibility of the fiber coupling. Second, the detection efficiencies of the SNSPDs are only specified within the telecom O-band. The C-band efficiency of 30%, on the other hand, is merely an estimation provided by the manufacturer and therefore subject to an unknown uncertainty. The observed count rates correspond to 26,000 and 128,000 telecom photons/s at the converter outputs, which are superimposed by around 3,000 and 2,050 background photons/s leading to SBRs of 8.7 and 62.2, respectively.

Note that in Sect. 5.1.2 we did not observe any pump-laser related background although the same down-conversion scheme was used. A possible source are nonlinear mixing processes of the pump with its own Raman-scattered light or parametric fluorescence leading to distinct noise peaks (see discussion in Sect. 4.5). As the positions of these peaks are sensitive to the pump wavelength as well as the chosen WG and its temperature, it is possible that they leak into the FBG filter window in the present experiment, but did not play any role in the preceding one.

6.3 Spectral and Temporal Properties

In this section we present measurements of various properties of the QD emission. These include first of all lifetime measurements and spectral measure-

ments, which resolve all relevant broadening contributions. Based on the obtained parameters it is possible to assess the achieved remote TPI visibilities using Eq. (3.28). Additionally, we provide antibunching as well as HOM measurements with consecutive photon emission from each QD individually. Note that in contrast to Chap. 5 we perform all measurements only with unconverted photons. Consequently, it is necessary to assume that these parameters are conserved throughout the down-conversion step when employing them for the description of our remote HOM measurements. This assertion, however, has been sufficiently proven in the context of numerous preceding experiments (see e.g. [95, 251]). Note that an improvement of the antibunching value throughout the down-conversion step as observed in [95] and Sect. 5.2.4 is not anticipated in the present experiment, as the bandwidth of the filter spectrometer (15 GHz) ensures more rigorous spectral filtering than the acceptance bandwidth of the frequency converter (≈ 120 GHz).

6.3.1 Radiative Lifetime

The radiative lifetime τ_r of both emitters is determined by TCSPC measurements equivalent to Sect. 5.2.1. The obtained measured data are shown as black curves in Fig. 6.9 (a) and (b) for QD1 and QD2, respectively. It can be seen that both measurements follow the expected one-sided exponential decay. In particular, we do not observe any beat signature confirming that the emitted photons indeed stem from the recombination of trions (compare Sect. 6.2.1). To fit the data we convolute the ideal model Eq. (5.2) with the

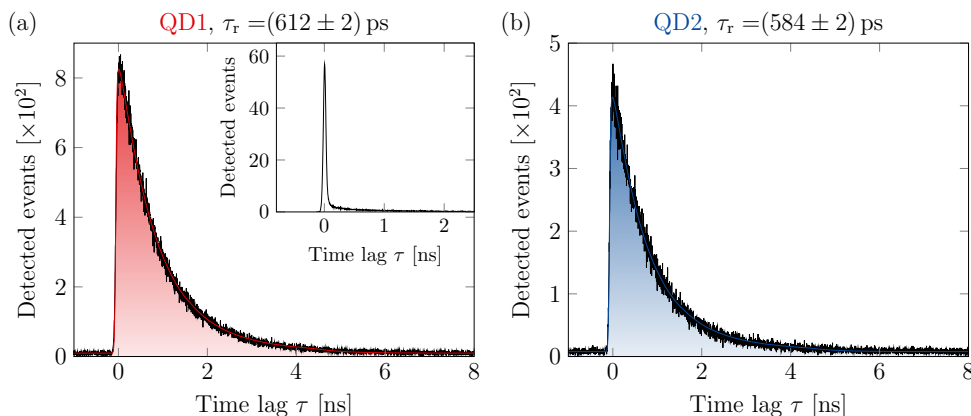


Figure 6.9. Radiative lifetime measurements of both quantum dots. Measured data (black) and corresponding fits (shaded areas) of time-correlated single photon counting measurements for (a) QD1 and (b) QD2 are shown. The data are fitted using a one-sided exponential decay convoluted with the measured detector response (see inset) leading to radiative lifetimes of $\tau_r = (612 \pm 2)$ ps and $\tau_r = (584 \pm 2)$ ps for QD1 and QD2.

measured detector response, which is depicted as inset in Fig. 6.9 (a). The results are plotted as red and blue shaded curves and reveal radiative lifetimes of $\tau_r = (612 \pm 2)$ ps and $\tau_r = (584 \pm 2)$ ps for QD1 and QD2.

6.3.2 High Resolution Emission Spectra

To assess the outcome of the remote HOM experiments it is inevitable to investigate the spectral line shapes of the involved single photon emitters. In particular, according to Eq. (3.28), we need to determine the homogeneous and inhomogeneous linewidths Γ_h and σ' besides the radiative lifetime τ_r . To that end the available commercial grating spectrometer is not suitable, as its resolution is in the same order of or even below the broadening contributions of interest. In Sect. 5.2.2 we solved this issue by means of a coherence time measurement using a Michelson interferometer, which allowed us to determine σ' with a precision of roughly 400 MHz corresponding to the error of the underlying fit. Here, we follow a different approach: the single photons collected at the output of the filter-spectrometer are fed into a scanning Fabry-Pérot interferometer (FPI, Free spectral range FSR = 15 GHz, Finesse $\mathcal{F} = 300$), whose transmission is recorded using a Si-APD. The transmission linewidth of the FPI is given by $\text{FSR}/\mathcal{F} = 50$ MHz, i.e. sufficiently small to resolve both QD emission lines even in their Fourier limits of $1/(2\pi\tau_r) = 260$ MHz and 273 MHz, respectively.

The black lines shown in Fig. 6.10 correspond to measured spectra of both quantum dots. Note that the illustrated spectrum is composed of two measurements of the individual emitters using their known frequency displace-

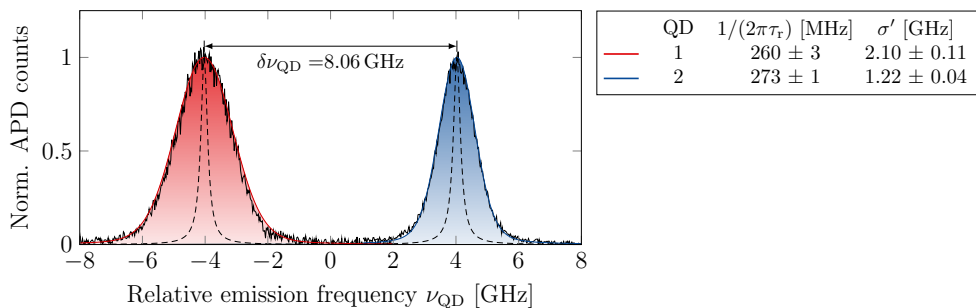


Figure 6.10. Highly resolved quantum dot emission spectra. The spectra were recorded with help of a Fabry-Pérot interferometer and are shown in black. Both emission lines were separately measured and put together using the known spectral displacement of $\delta\nu_{\text{QD}} = 8.06$ GHz. Fits are shown in red and blue for QD1 and QD2, respectively, revealing inhomogeneous linewidths of $\sigma' = (2.10 \pm 0.11)$ GHz and (1.22 ± 0.04) GHz. The lifetime limited emission lines are illustrated as dashed curves for comparison. They possess linewidths of $1/(2\pi\tau_r) = 260$ MHz and 273 MHz for QD1 and QD2.

ment $\delta\nu_{\text{QD}} = 8.06$ GHz. Both peaks are clearly broader than their lifetime limited counterparts (dashed lines). Here, we fit the data using the Voigt profile Eq. (2.16), but fix the pure dephasing rate Γ^* at zero, i.e. both emitters are merely inhomogeneously broadened. Indeed, the resulting fits (red and blue shaded curves) perfectly reproduce the data, which indicates that no further homogeneous broadening is necessary. Moreover, using the same model employed in the scope of Sect. 5.2.2, we estimate the pure dephasing rate to be less than 1 MHz at temperatures below 5 K, which is more than 2 orders of magnitude below the natural linewidths and also not resolvable by the FPI. Averaging the fitted parameters over several spectra taken at different days of the measurement campaign we find inhomogeneous linewidths of $\sigma' = (2.10 \pm 0.11)$ GHz and (1.22 ± 0.04) GHz for QD1 and QD2, respectively. Here, the stated errors correspond to the standard deviation between the individual values. Eventually, we like to mention that both peaks shown in Fig. 6.10 do not overlap. This confirms our assertion that the apparent overlap in Fig. 6.5 (a) is merely caused by the broad spectral response of the spectrometer.

6.3.3 Antibunching

To confirm single photon emission from both QDs, we perform antibunching measurements employing a HBT interferometer as described in Sect. 5.2.4. The obtained correlation measurements are shown in Fig. 6.11 (a) and (b) as black dots. The peaks are centered at multiples of the repetition time of the excitation laser $T_{\text{rep}} = 13.1$ ns and exhibit the expected two-sided exponential decay. It stands out that the central peaks are very small compared to their neighbors, indicating clean single photon emission. In particular for QD1 it is obvious that the peaks bunch towards $\tau = 0$, which is a signature of a blinking emitter [271, 272]. The central peak, however, is not affected by the blinking dynamics, as the contribution of two fluorescence photons emitted from the QD during a single excitation cycle is negligible. Therefore, in order to obtain the desired $g^{(2)}(0)$ -value, it is necessary to normalize the area under the central peak A_0 with respect to the area of a peak at the Poisson level [273], i.e. for $\tau \rightarrow \pm\infty$, according to

$$g^{(2)}(0) = \frac{A_0}{A_\infty} \quad \text{with} \quad A_\infty = \lim_{i \rightarrow \pm\infty} A_i. \quad (6.7)$$

Fig. 6.11 (c) and (d) show the integrated areas of all peaks up to ± 600 ns, corresponding to the first 45 peaks to either side of $\tau = 0$. Following the model proposed in [271], we describe the area of the i 'th peak ($i \neq 0$) via

$$A_i = (A_\infty - D) \cdot \left\{ 1 + B \cdot \exp \left[-(|i| - 1) \cdot \frac{T_{\text{rep}}}{\tau_B} \right] \right\} + D, \quad (6.8)$$

where B and τ_B are the bunching amplitude and bunching time, respectively. Note that we added the constant D to account for a continuous background.

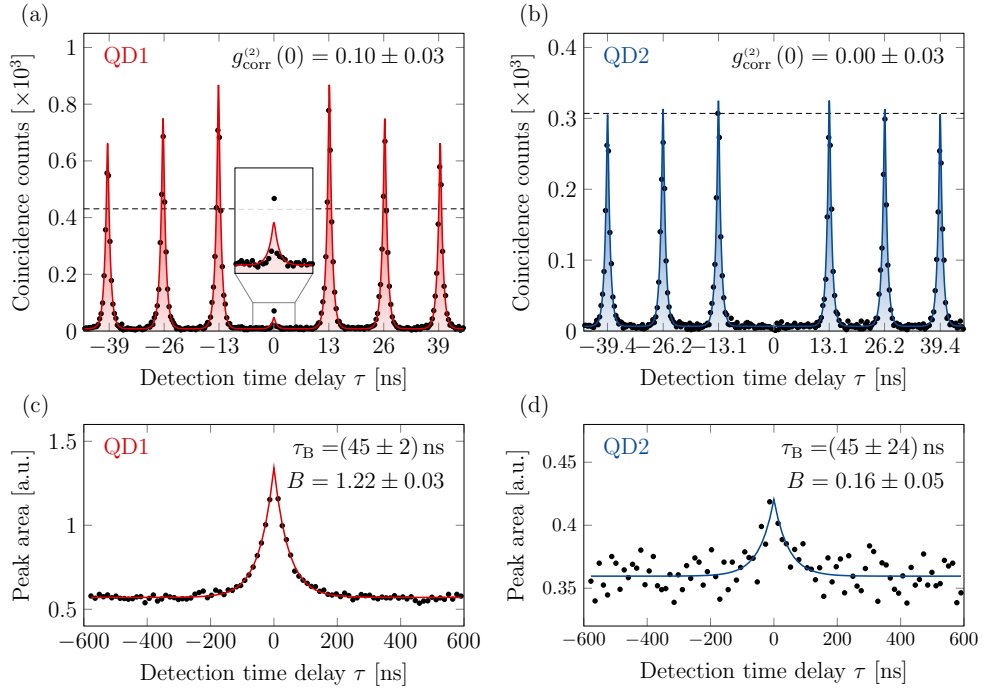


Figure 6.11. Antibunching measurements of both quantum dots under consideration. Measured data are shown as black circles for (a) QD1 and (b) QD2. The area of each peak is plotted in (c) and (d), respectively. The peak area reveals clear bunching, which is quantified by the fitted bunching time τ_B and bunching amplitude B (fits as red and blue curves). The bunching parameters are used in (a) and (b) to reproduce the measured data (shaded curves). Normalizing the central peak at $\tau = 0$ with respect to the Poisson level (dashed line) reveals antibunching values of $g_{\text{QD1}}^{(2)}(0) = 0.10 \pm 0.03$ and $g_{\text{QD2}}^{(2)}(0) = 0.00 \pm 0.03$. The inset in (a) illustrates that the majority of measured coincidences appears in only one bin, pointing towards laser leakage.

Using this notation, A_∞ corresponds to the peak area at the Poisson level *including* background. We determine D by first averaging the measured coincidence counts in between the peaks to obtain the background rate d and subsequently integrating d for the duration of one excitation cycle according to $D = d \cdot T_{\text{rep}}$. Treating the parameters and B , τ_B , and A_∞ as free, we obtain the fits shown as solid curves in (c) and (d). For both emitters we find bunching time constants of $\tau_B = 45$ ns.

Eventually, the raw antibunching values can be evaluated using relation (6.7), leading to $g_{\text{QD1}}^{(2)}(0) = 0.26 \pm 0.02$ and $g_{\text{QD2}}^{(2)}(0) = 0.20 \pm 0.02$, where A_0 was directly integrated from the measured data. Here, the stated errors were propagated from the standard error of A_0 and the confidence interval of A_∞ .

Background-corrected antibunching values according to

$$g_{\text{corr}}^{(2)}(0) = \frac{A_0 - D}{A_\infty - D} \quad (6.9)$$

yield $g_{\text{corr,QD1}}^{(2)}(0) = 0.10 \pm 0.03$ and $g_{\text{corr,QD2}}^{(2)}(0) = 0.00 \pm 0.03$. From our results, we reconstruct the overall measured intensity correlation function by

$$g^{(2)}(\tau) = d + \frac{1}{2\tau_r} \sum_i (A_i - D) \cdot \exp\left[-\frac{|\tau - i \cdot T_{\text{rep}}|}{\tau_r}\right], \quad (6.10)$$

which is illustrated in Fig. 6.11 (a) and (b) as shaded area. The amplitude of coincidence peaks at the Poisson level can be determined by $A_\infty/(2\tau_r)$ and is depicted as dashed line. Eventually, we like to highlight the central peak measured in the intensity auto-correlation of QD1 [see inset of Fig. 6.11 (a)]. It can be seen that most coincidences appear exactly within the central bin at $\tau = 0$ leading to a slight disagreement between measured and reconstructed $g^{(2)}$ -function, although their areas are set to be identical. This suggest that these coincidences were caused by photons that are shorter in time than 350 ps, corresponding to the bin-width of the histogram. The only possible source in this respect is residual excitation light leaking through the polarization suppression - an issue we will occasionally encounter in the upcoming sections.

6.3.4 Indistinguishability of Consecutively Emitted Photons

As a first consistency check between the measured linewidths and the achievable photon indistinguishabilities, we perform HOM measurements on each emitter individually. The experiment is set up as described in Sect. 5.3.1 and the corresponding correlation measurements can be seen in Fig. 6.12 (a) and (b). Due to insufficient integration time, the measurement performed for QD1 suffers from poor statistics. Accordingly, it is not reliable to extract the visibility by a direct fit of the central peak using Eq. (3.26). Instead, we integrate each peak individually. The obtained peak areas along with their standard errors are depicted in (c) and (d) as black dots. The red and blue colored bars therein stem from a fit, which considers both bunching due to emitter blinking as well as the influence of beam splitters with unequal reflectivity and transmission, i.e. $R \neq T$. The derivation of the underlying fitting model is nontrivial and offers no valuable insight at this point. It is therefore omitted here and offered in Appx. E instead. From the fit we extract TPI visibilities of $V_{\text{QD1}} = (34 \pm 18) \%$ and $V_{\text{QD2}} = (61 \pm 7) \%$, where the large error of V_{QD1} results from the aforementioned insufficient statistics. As discussed in Sect. 6.3.2, we assume that both emitters are not affected by phonon-induced pure dephasing. Accordingly, an effective inhomogeneous linewidth can be unambiguously assigned to each given visibility following Eq. (3.33) by setting $\vartheta_{\text{PD}} = 1$ and considering the known radiative lifetime. Here, we obtain

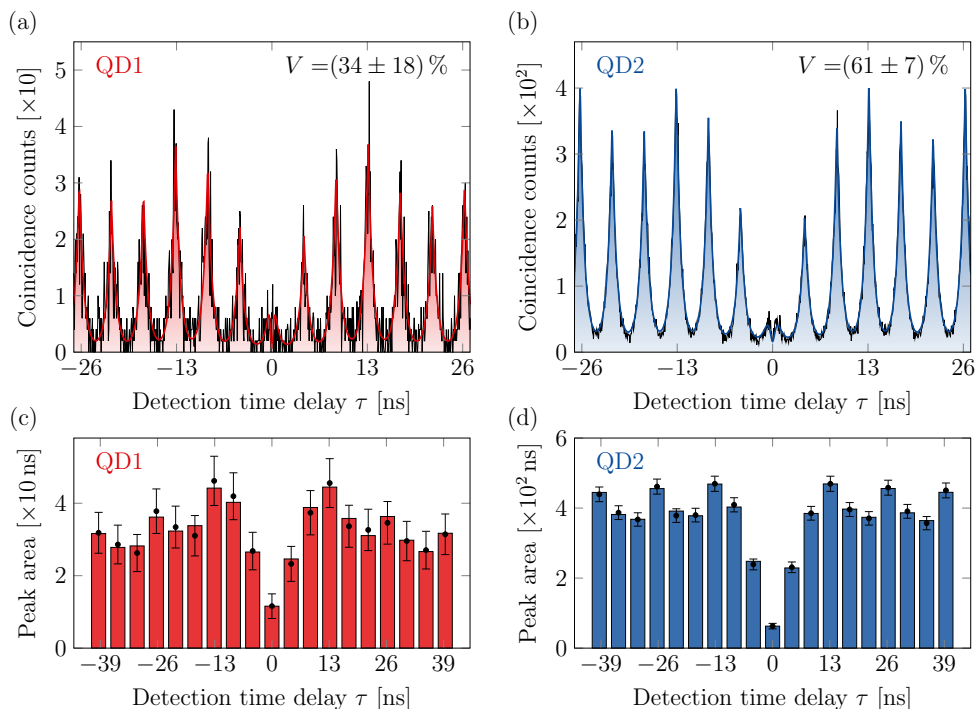


Figure 6.12. Hong-Ou-Mandel correlation measurements of consecutively emitted photons. Data are shown as black lines for (a) QD1 and (b) QD2. The integrated areas of each peak are illustrated in (c) and (d) as black dots. Fits considering the blinking dynamics and beam splitter asymmetry are shown as colored bars. From the fits we extract two-photon interference visibilities of $V = (34 \pm 18) \%$ and $V = (61 \pm 7) \%$. Based on the obtained parameters, the correlation measurements are reconstructed [red and blue shaded curves in (a) and (b)].

$\sigma'_{\text{QD1}} = (1.22 \pm 1.68) \text{ GHz}$ and $\sigma'_{\text{QD2}} = (0.52 \pm 0.13) \text{ GHz}$, which are well below the corresponding equilibrium values of 2.10 GHz and 1.22 GHz reported in Sect. 6.3.2. This observation indicates that SD does not fully unfold within the time set by the Mach-Zehnder interferometer delay of $\tau_{\text{mzi}} = T_{\text{rep}}/3 = 4.37 \text{ ns}$. Based on our model for TPI between consecutively emitted photons (see Sect. 3.2.3), it is possible to extract the memory depth of spectral diffusion τ_{sd} by rearranging Eq. (3.38) according to

$$\tau_{\text{sd}} = -\tau_{\text{mzi}} / \ln \left(1 - \frac{\Sigma^2}{2\sigma_0^2} \right). \quad (6.11)$$

Here, Σ and σ_0 are to be interpreted as effective and equilibrium inhomogeneous linewidths, respectively, which yields time constants of $\tau_{\text{sd,QD1}} = 23 \text{ ns}$ and $\tau_{\text{sd,QD2}} = 46 \text{ ns}$. Eventually, we use the effective inhomogeneous linewidths to reconstruct the time-structure of the measured correlation functions (see

Appx. E). The results are illustrated as red and blue shaded curves in Fig. 6.12 (a) and (b) and reveal a good agreement with the recorded data.

6.4 Recovering Spectral Indistinguishability via Quantum Frequency Down-Conversion

From the spectra shown in Fig. 6.10 it is obvious that the fluorescence emitted by QD1 and QD2 is spectrally disjunct for the most part. Accordingly, a HOM experiment performed between the photons of both remote emitters does not hold out the prospect of any observable quantum interference. More specifically, using the known spectral detuning of $\delta\nu_{\text{QD}} = 8.06$ GHz, the radiative lifetimes $\tau_{\text{r,QD1}} = 612$ ps and $\tau_{\text{r,QD2}} = 584$ ps, as well as the inhomogeneous linewidths $\sigma'_{\text{QD1}} = 2.10$ GHz and $\sigma'_{\text{QD2}} = 1.22$ GHz, we expect the interference contrast to be no more than $V_{\text{rem}} \approx 0.1\%$ following Eq. (3.28). Compensating the spectral mismatch, on the other hand, leads to a maximized contrast of about 27% at $\delta\nu_{\text{QD}} = 0$ GHz, which is now mainly limited by the inhomogeneous broadening of both emission lines.

In the remainder of this chapter we present the results of a set of HOM measurements performed between the photons from both remote QDs. The experimental design follows the concept discussed in the outline of this chapter, i.e. we employ FC1 and FC2 to convert the NIR photons to the telecom C-band and simultaneously reset their relative detuning to any desired value by choosing an appropriate pump laser detuning $\delta\nu_{\text{pump}}$. First, we will present the obtained correlation measurements and illustrate the procedure, which was chosen to extract the desired TPI visibilities. We then discuss the achieved visibilities with respect to the net-detuning between the telecom photons $\delta\nu_{\text{tel}} = \delta\nu_{\text{QD}} - \delta\nu_{\text{pump}}$.

Note that we here only focus on the spectral similarity of the photons, while all other degrees of freedom are assumed to be identical: **(i)** an ideal spatial mode overlap is inherently ensured by use of a fiber-based BS, **(ii)** the arrival of both input photons is synchronized prior to the experiment adjusting the delay stage shown in Fig. 6.2 (a), and **(iii)** the polarization state of both input modes is matched using a set polarization controlling optical elements located in front of the HOM beam splitter.

6.4.1 Correlation Measurements

As has been done for the experiments presented in Sect. 5.3, the desired signature of quantum interference is obtained by correlating the detection events recorded at both BS outputs, i.e. by measuring the intensity correlation function $g^{(2)}(\tau)$. Although the resulting coincidence pattern is straightforward compared to the measurements between consecutively emitted photons [see e.g. Fig. 5.8 (b) and (c)], it exhibits some unique features that need to be ad-

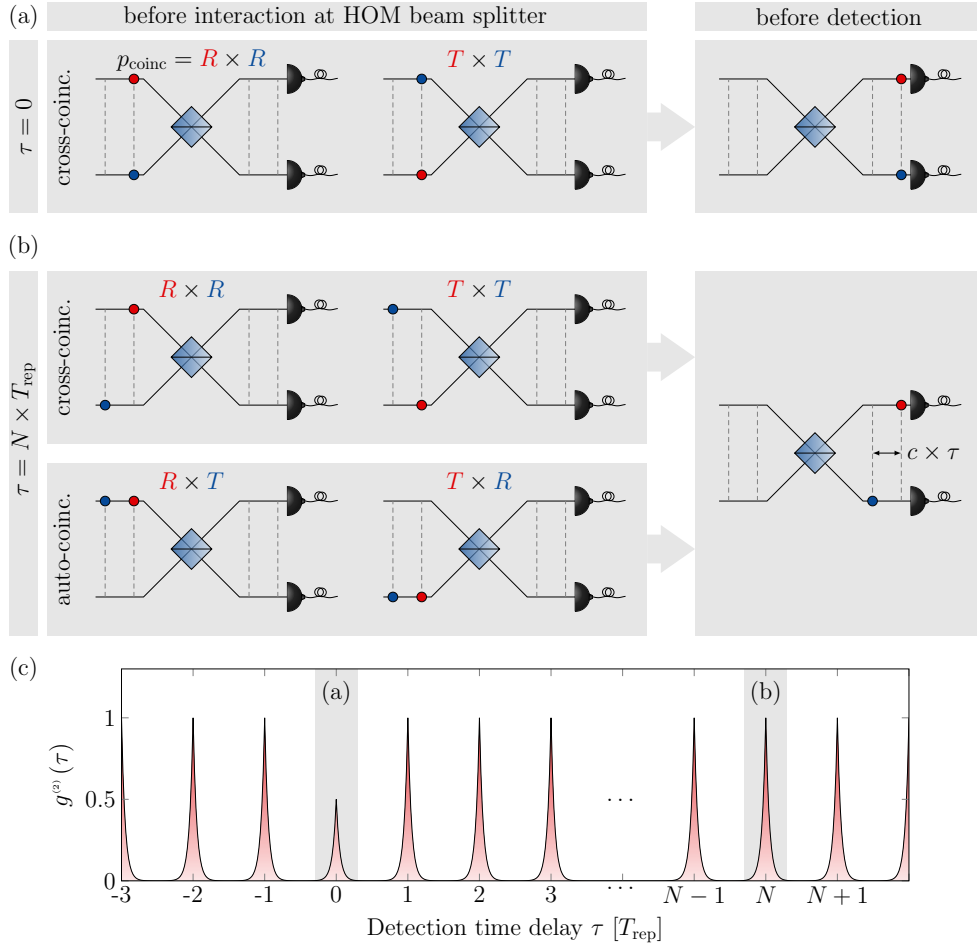


Figure 6.13. Explanation of the obtained coincidence pattern. (a) Coincidences appearing within the central bin at $\tau = 0$ stem from cross-coincidences, i.e. correlated events between detected photons from distinct emitters. (b) In case of off-center bins at $\tau = N \times T_{\text{rep}}$ additional auto-coincidences contribute to the overall pattern, originating from photons subsequently emitted by the same source (see bottom row). (c) Simulation of the pulsed coincidence pattern expected for an ideal single photon source of distinguishable photons. Due to the missing auto-coincidences, the central peak exhibits only half the height of all neighboring peaks.

dressed. On that account, we first discuss the anticipated coincidence pattern in the limit of entirely indistinguishable photons. We further assume that both emitters are ideal single photon sources. This assumption is well sustained by our antibunching measurements presented in Sect. 6.3.3 and necessary to ensure that no two photons arrive within the same time-bin and same input mode of the BS. Additionally, we do not include the blinking of both emitters

for the time being.

All relevant cases contributing to a respective measurement are illustrated in Fig. 6.13. Accordingly, cases in which both photons take the same BS output are not shown. First, consider coincidences appearing in the central time-bin at $\tau = 0$, which we obtain, if there was one photon in each output mode of the beam splitter at the same time [Fig. 6.13 (a), right side]. In case of *single* photons this implies that each emitter contributed one of those photons and both were either reflected or transmitted [Fig. 6.13 (a), left side]. Assuming unit detection efficiencies, the illustrated possible input situations lead to coincidences with a probability of $p_{\text{coinc}} = R^2$ and $p_{\text{coinc}} = T^2$, respectively, and are referred to as cross-coincidences [272]. Correlated events at multiples of the repetition time T_{rep} stem from photons that were detected with a delay of $\tau = N \times T_{\text{rep}}$. In contrast to the situation before, this can not only be realized by cross-coincidences [Fig. 6.13 (b), top row], but also by photons subsequently emitted from the same QD (bottom row). The respective initial situations lead to so-called auto-coincidences with a probability of $p_{\text{coinc}} = R \times T$.

The resulting overall coincidence pattern is illustrated in (c). The pulsed structure of the peaks follow the pulsed excitation scheme. In an ideal scenario all peaks exhibit the same height except for the central peak due to the lack of auto-coincidences. The number of correlated events A_0 and A_N found within the central and all off-center peaks is proportional to the contributing coincidence probabilities. Accordingly, we find the ratio

$$\varrho = \frac{A_0}{A_N} = \frac{P_{\text{cross}}}{P_{\text{cross}} + P_{\text{auto}}} = \frac{R^2 + T^2}{R^2 + T^2 + 2R \times T} = R^2 + T^2, \quad (6.12)$$

where the last equality only holds for a BS without excess loss. Therefore, in case of an ideal symmetric BS with $R = T = 1/2$, the central peak is half as high compared to its neighbors. For the fiber-based BS employed in our experiments, we measure an asymmetry of $R : T = 0.47 : 0.53$, which corresponds to $\varrho = 0.502$. In case of partially indistinguishable photons, we expect that the experimentally obtained number of coincidences in the central peak $A_{0,\text{exp}}$ is reduced by a factor of $1 - V$ compared to A_0 , according to Eq. (2.52). Setting $A_0 = A_{0,\text{exp}} / (1 - V)$ in Eq. (6.12), we can evaluate the TPI visibility as

$$V = 1 - \frac{A_{0,\text{exp}}}{A_N \times \varrho}. \quad (6.13)$$

Fig. 6.14 (a) shows an exemplary correlation measurement between converted telecom photons of both emitters taken at a relative pump laser detuning of $\delta\nu_{\text{pump}} = 8.3$ GHz, which leads to a residual detuning between the telecom photons of $\delta\nu_{\text{tel}} = \delta\nu_{\text{QD}} - \delta\nu_{\text{pump}} = -0.2$ GHz. As reported in Sect. 6.2.2 the telecom photon flux of QD2 is almost fivefold higher than the flux of QD1.

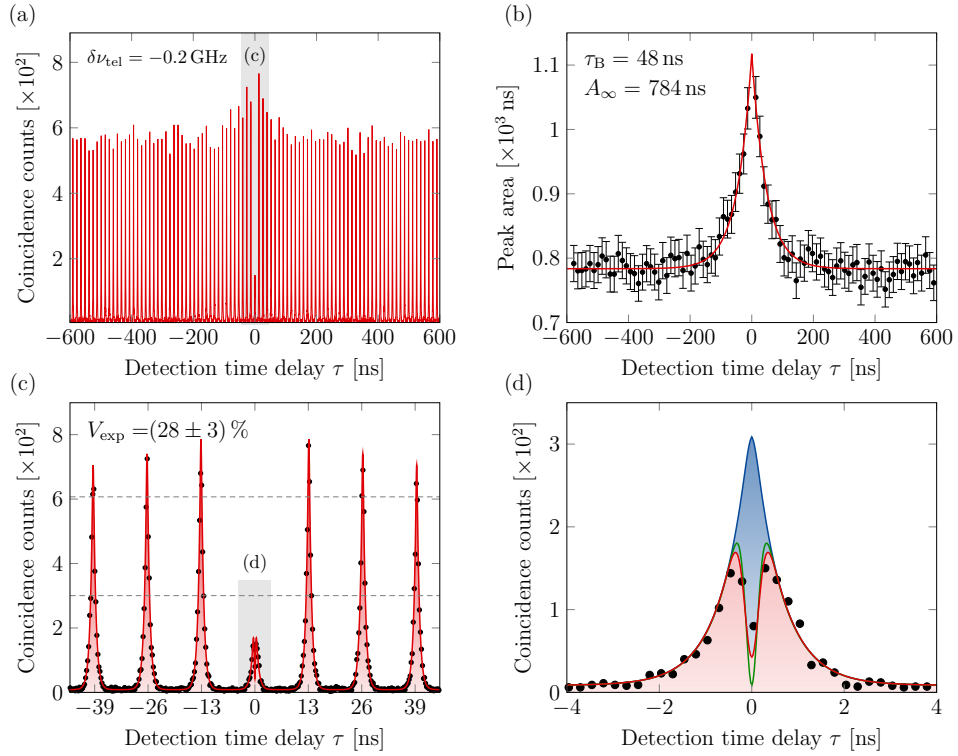


Figure 6.14. Correlation measurement between telecom photons showing quantum interference. (a) Measurement for telecom photons at a net-detuning of $\delta\nu_{\text{tel}} = 0.2$ GHz, i.e. close to resonance. The coincidence peaks show clear bunching in a range of about ± 50 ns. (b) Black dots correspond to integrated area under each peak, shown along with standard error. From a corresponding fit (red curve) we extract a bunching time of $\tau_B = 48$ ns and a peak area at the Poisson-level of $A_\infty = 784$ ns. (c) shows a magnification of the measurement around the central peak. The upper gray dashed line illustrates the Poisson-level, the lower dashed line the anticipated central peak level for entirely distinguishable photons. The missing coincidences of the central peak indicate quantum interference at the HOM beam splitter, for which a contrast of $V_{\text{exp}} = (28 \pm 3)\%$ can be extracted. The red shaded curve corresponds to the reconstructed correlation measurement, based on all known parameters. (d) The central peak is shown along with reconstructed correlation measurements under the influence of detector jitter for actual telecom photon parameters (red) as well as distinguishable photons (blue). The green curve illustrates a measurement with infinite time resolution.

The excess photons of the brighter emitter would superimpose the HOM measurement with a simple antibunching measurement and accordingly lead to overestimated TPI visibilities. Therefore, in the scope of this and the following measurements, we let both telecom photons equally contribute to the overall count rate by attenuating QD2. Similar to the correlation measurements discussed in Sect. 6.3.3 and 6.3.4, the coincidence peaks clearly bunch around the time lag of $\tau = 0$. As a consequence our considerations of the preceding paragraph do not hold for off-center peaks with small N , i.e. for peaks within the bunching range. Instead, it is necessary to determine the peak area in the limit of $N \rightarrow \infty$. On that account, after background subtraction, we individually integrate each peak except for the central one, leading to the data shown in (b). The red curve therein corresponds to a fit using the model function (6.8). From the fit we obtain a bunching time of $\tau_B = 48$ ns and a peak area at the Poisson level of $A_\infty = (784 \pm 4)$ ns. Note that Eq. (6.8) is intended to describe the blinking dynamics of a single emitter. A more general model for the present experiments includes two independent sets of blinking parameters to account for both dissimilar emitters. Based on the analysis presented in Sect. 6.3.3, we assume that both emitters exhibit equal τ_B . Moreover, considering that both emitters contribute to the observed count rate in equal shares, the general model reduces to an expression, which can be effectively described by Eq. (6.8).

The central peak along with its 3 adjacent neighbors is shown in Fig. 6.14 (c). From the bunching fit, we obtain the peak amplitude at the Poisson level C_∞ according to

$$C_\infty = f \cdot \frac{A_\infty}{\tau_{r,QD1} + \tau_{r,QD2}}, \quad (6.14)$$

which corresponds to the upper dashed line in (c). Here, $1/(\tau_{r,QD1} + \tau_{r,QD2})$ simply results from the integration of the two-sided exponential decay in Eq. (3.26) and f accounts for the reduced peak amplitude due to the detector jitter. The latter was numerically determined to be $f = 0.91$, assuming a normally distributed detector response with a FWHM of 200 ps. Following Eq. (6.12) it is possible to find the amplitude of the central peak for entirely distinguishable photons via $C_0 = C_\infty \times \varrho$, which is shown as lower dashed line. Apparently, the central peak stays far below this limit, indicating that both telecom photons coalesce at the HOM beam splitter with non-classical probability, being a signature of quantum interference. In order to quantify the photon indistinguishability, we evaluate the experimentally observed TPI visibility V_{exp} using Eq. (6.13). Due to the observed bunching, however, we need to substitute A_N by A_∞ as obtained from the corresponding fit. We determine $A_{0,\text{exp}}$ by integrating the area under the central peak from the measured data and find a visibility of $V_{\text{exp}} = (29 \pm 3)\%$. The stated error is propagated from the standard error of $A_{0,\text{exp}}$ and the confidence interval of A_∞ . Eventually,

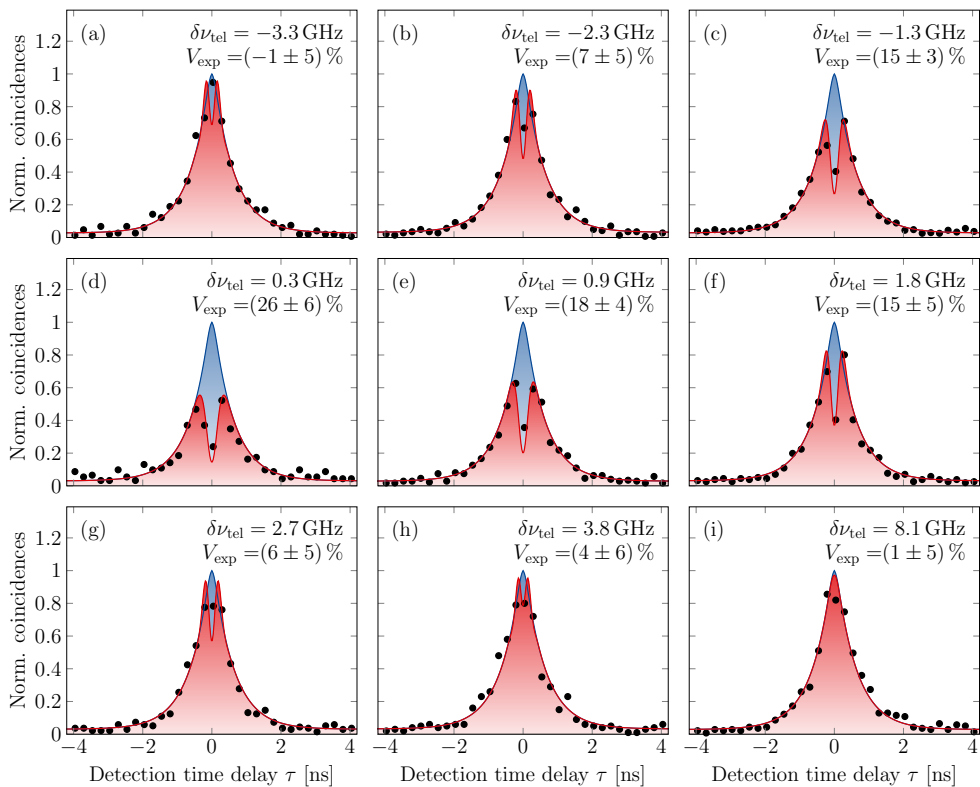


Figure 6.15. Summary of correlation measurements at 9 different detunings. Shown is the central peak of each measurement (black circles) along with the reconstruction of the measurement (red shaded curve) and the limit for distinguishable photons (blue shaded curve) according to the description in the main text. Each plot contains the net-detuning of the telecom photons $\delta\nu_{\text{tel}}$ and the obtained TPI visibility V_{exp} .

we reconstruct the overall correlation measurement according to

$$g^{(2)}(\tau) = y_0 + 2A_\infty \cdot \varrho \cdot \mathcal{G}^{(2)}(\tau) + 2 \sum_{i \neq 0} A_i \cdot \mathcal{G}_0^{(2)}(\tau - i \cdot T_{\text{rep}}), \quad (6.15)$$

where all A_i correspond to the fitted peak areas including bunching [red curve in Fig. 6.14 (b)]. The correlation function $\mathcal{G}^{(2)}(\tau)$ is taken from Eq. (3.26) and describes the central peak based on all known emitter parameters. The off-center peaks are described by $\mathcal{G}_0^{(2)}(\tau)$, which equals to $\mathcal{G}^{(2)}(\tau)$ in the limit of no TPI. The factor of 2 considers that integration over $\mathcal{G}_0^{(2)}(\tau)$ yields 1/2 and y_0 accounts for a constant background. Moreover, in order to take the detector jitter into account, $g^{(2)}(\tau)$ is convoluted with a normal distribution (FWHM = 200 ps). The result is depicted as red shaded area in Fig. 6.14 (c) and (d), revealing good agreement with the data. Additionally, Fig. 6.14 (d) shows the correlation function for entirely distinguishable photons (blue

shaded curve) and for a measurement with infinite time resolution, i.e. without detector jitter (green curve).

This type of correlation measurement was repeated at overall 10 different detunings $\delta\nu_{\text{tel}}$ and evaluated according to the preceding discussion. The measured central peak along with its reconstruction and the limit for entirely distinguishable photons is depicted in Fig. 6.15 for all measurements except the one already presented. The corresponding detunings and obtained visibilities are stated therein. Generally all measurements show a good agreement with the reconstructed correlation functions. For most of the measurements we observe that the central bin at $\tau = 0$ contains more measured coincidences than predicted by the theoretical curve. We attribute them to residual excitation laser superimposing the single photons, which has already been mentioned in Sect. 6.3.3. These coincidences generally reduce the experimentally obtained visibility and can even cause negative values [see Fig. 6.15 (a)].

6.4.2 Relative Spectral Tuning of Converted Telecom Photons

The correlation measurements and extracted visibilities shown in Fig. 6.14 and Fig. 6.15 are clearly sensitive to the chosen pump laser detuning. This already suggests that the fundamental motivation of the present experiment - the relative tunability of both telecom photons via QFC - works as intended. It is of vital importance, however, to investigate, whether the obtained tuning data can be fully understood based on all available information about both emitters and converters. In particular, any negative impact of the down-conversion step on the mutual indistinguishability between the telecom photons needs to be ruled out.

On that account, we first summarize all TPI visibilities V_{exp} and respective errors presented in the last section as black dots in Fig. 6.16 as function of the designated pump laser detuning $\delta\nu_{\text{pump}}$ (top abscissa) and resulting telecom photon detuning $\delta\nu_{\text{tel}} = \delta\nu_{\text{QD}} - \delta\nu_{\text{pump}}$ (bottom abscissa). In Sect. 6.2.2 we obtained an upper limit of 110 MHz for the relative frequency stability between both frequency converters, which we here assume as the error of $\delta\nu_{\text{tel}}$ (horizontal error bars). The rightmost data point was taken at a pump laser detuning of $\delta\nu_{\text{pump}} = 0$ GHz, i.e. the telecom photons exhibit the same spectral detuning as the unconverted NIR photons. As expected we obtain a vanishing TPI visibility of $V_{\text{exp}} = (1 \pm 5) \%$ at this setpoint. The maximum interference contrast of $V_{\text{exp}} = (29 \pm 3) \%$, on the other hand, is achieved at $\delta\nu_{\text{pump}} = 8.3$ GHz, corresponding to a telecom photon detuning of $\delta\nu_{\text{tel}} = -0.2$ GHz. The remaining data points clearly visualize how both telecom photons are first tuned in and then again out of resonance with increasing $\delta\nu_{\text{pump}}$. The additional blue diamond-shaped data point was obtained from an

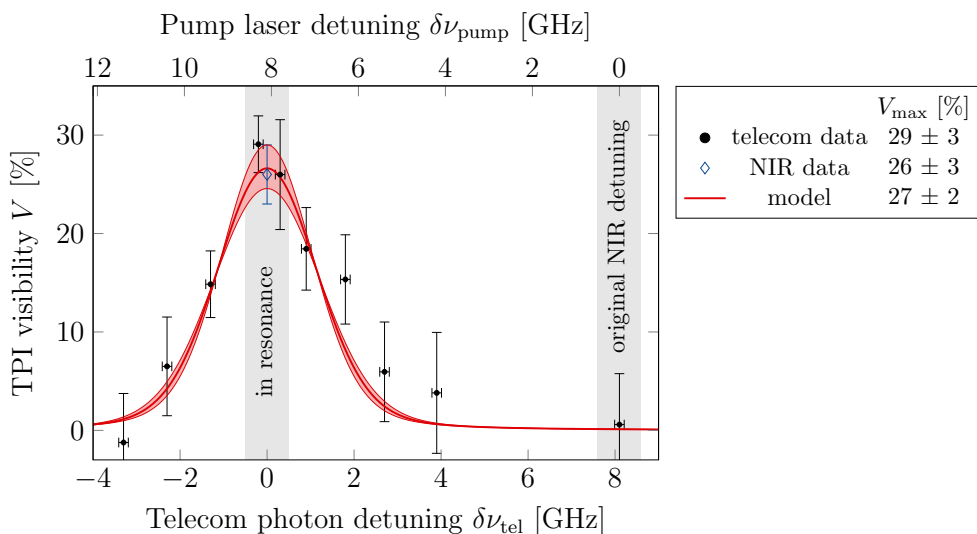


Figure 6.16. Two-photon interference visibility over spectral photon detuning. Shown are data of HOM experiment with telecom photons as performed here (black dots) and with NIR photons from the same emitter pair as reported in [272] (blue diamond). Error bars correspond to errors given in Fig. 6.15 for V_{exp} and frequency converter stability discussed in Sect. 6.2.2 for $\delta\nu_{\text{tel}}$. The experimental data are compared to the model function (3.28) based on the known emitter parameters (red curve). The rightmost data point was taken at $\delta\nu_{\text{pump}} = 0$, i.e. the telecom photons retain the original detuning of the unconverted photons.

independent TPI experiment on the same QD pair and is reported in [272]³. Here, the NIR photons were tuned into resonance by operating QD2 at a temperature of 11 K, while QD1 was kept at 4 K. At this point a TPI visibility of $V_{\text{exp,nir}} = (26 \pm 3)\%$ was observed, being in good agreement with the telecom data.

In order to further assess the obtained visibilities, we apply Eq. (3.28) using the predetermined radiative lifetimes, inhomogeneous linewidths and emitter detuning as reported in Sect. 6.3 as well as Sect. 6.2.1. The result is depicted as red curve along with a confidence band (red shaded area), which was derived from the confidence intervals of all input parameters. The model shows an overall good qualitative and quantitative agreement with the data. Besides the already discussed laser leakage, we attribute deviations between model and theory to long term drifts of the QD emission lines: The emission spectra presented in Sect. 6.3.2 were integrated for ≈ 30 min, while the overall tuning series was taken in course of an entire day. Accordingly,

³Note that both emitters are labeled differently in [272]: QD1 and QD2 correspond to QDR and QDB, respectively.

slow drifts of the emission frequencies might distort the tuning curve, e.g. for the measurements taken at $\delta\nu_{\text{tel}} = 1.8, 2.7,$ and 3.8 GHz. Note that the decreased visibility of the NIR data compared to the telecom data might stem from the elevated sample temperature inducing additional lattice vibrations. According to our estimation given in Sect. 5.2.2, a temperature of 11 K leads to a pure dephasing rate of ≈ 70 MHz. Taking this additional homogeneous broadening of one emitter into account, we obtain only a minor reduction of the visibility of less than 1 %.

It is important to note that the model only incorporates spectral properties of the QD emission without considering any influence of the down-conversion step. Therefore, the good agreement between model and data suggests that QFDC preserves the spectral properties of remotely emitted single photons. This conclusion is further corroborated by the additional HOM measurements with unconverted photons using temperature tuning. Furthermore, the results clearly demonstrate that QFDC is an appropriate tool to tune the telecom photons into resonance and thereby recover their maximally possible mutual indistinguishability.

6.5 Summary

In the course of this chapter we have presented experimental results of a two-photon interference experiment after Hong-Ou-Mandel, which was performed using the independent emission of two remote quantum dots. Prior to the HOM experiment the single photons were transduced to the telecom C-band via quantum frequency down-conversion. Additionally, the down-conversion step was used to compensate the spectral mismatch between the photons of both emitters, rendering other tuning mechanisms redundant. Based on a careful evaluation of all relevant spectral and temporal properties of both quantum dots, it was possible to fully support the obtained experimental interference visibilities using the theoretical model derived in Sect. 3.2. Accordingly, the results demonstrate that QFDC conserves the mutual indistinguishability of independently emitted single photons and can simultaneously be used to reset the relative detuning of the converted photons. Further information and benchmarks obtained throughout this chapter are summarized in the following *highlights*-box.

CHAPTER 6 - HIGHLIGHTS

Photon Source

- Investigation of single photons emitted by two InAs QDs operated in independent cryostats. Both QDs emit at 904.4 nm with a relative detuning of 8.06 GHz and deliver photon fluxes of 10^5 and 2.9×10^5 photons/s (Sect. 6.2.1).
- Stability of emission frequency was improved over Chap. 5 operating the QDs at 4 K, using *s*-shell excitation, and an additional non-resonant cw-laser. Thereby, inhomogeneous broadening could be reduced to 2.10 and 1.22 GHz (Sect. 6.3.2).
- Radiative lifetimes of 612 and 584 ps were measured. Additional homogeneous broadening contributions could be ruled out (Sect. 6.3.1 and 6.3.2).
- Efficient polarization suppression and subsequent narrow spectral filtering allowed to mostly remove the resonant excitation laser, leading to a signal-to-background ratio as high as 26. The polarizations suppression required to use charged QDs, which do not exhibit any fine-structure (Sect. 6.2.1).
- Very pure single photon emission was observed with antibunching values as low as 0.10 ± 0.03 and 0.00 ± 0.03 (Sect. 6.3.3).

- Two-photon interference visibilities of 34% and 61% were observed using consecutively emitted photons from the individual emitters, being well above the limits of 22% and 35% obtained from the emission line shapes for uncorrelated photon emission. From here, spectral diffusion memory depths of 23 and 46 ns could be extracted (Sect. 6.3.4).

Frequency Conversion

- Successful implementation of two identical frequency converters to independently transduce photons of both emitters from NIR regime to 1557 nm (Sect. 6.2.2).
- External device efficiencies of 35% and 31% were obtained, leading to photon fluxes of 26×10^3 and 128×10^3 telecom photons/s at the respective converter outputs, superimposed by about 3×10^3 and 2×10^3 background photons/s (Sect. 6.2.2).
- The relative frequency stability between both converters was determined to be as low as 20 MHz, being almost two orders of magnitude below the frequency jitter of both QDs. A more conservative estimation assuming uncorrelated frequency drift leads to 110 MHz (Sect. 6.2.2).

CHAPTER 6 - HIGHLIGHTS CONTINUED

Quantum Interference with Independent Photons

- A two-photon interference experiment after Hong-Ou-Mandel was performed between the converted telecom photons of both emitters (Sect. 6.4).
- No quantum interference is expected for the unconverted photons, as their relative detuning of >8 GHz exceeds the combined linewidths (Sect. 6.4).
- The possibility to set the target wavelength of each converter individually allowed for relative tuning of the single telecom photons.
- A maximum interference contrast of $(29 \pm 3)\%$ was measured for the telecom photons at a relative detuning close to zero. At the original detuning of 8.1 GHz no non-classical photon-coalescence was observed (Sect. 6.4.2).
- For the same QD pair a contrast of $(26 \pm 3)\%$ is reported in literature, using unconverted photons and temperature tuning instead (Sect. 6.4.2).
- Based on the emitter parameters a contrast of $(27 \pm 2)\%$ is theoretically predicted (Sect. 6.4.2).
- The agreement of all values shows that quantum frequency down-conversion preserves the mutual indistinguishability of independent photons and can be simultaneously used as a tuning mechanism to recover photon indistinguishabilities (Sect. 6.4.2).
- All underlying measured and theoretically predicted intensity correlations were in excellent qualitative and quantitative agreement (Sect. 6.4.1).

Entanglement Generation Based on Quantum Interference

Copyright notice: Note that the results discussed in Sect. 7.1 were originally published in [197] (Copyright © 2018 The Authors. Published by IOP Publishing Ltd on behalf of Deutsche Physikalische Gesellschaft).

A quantum mechanical composite system is said to be entangled, if the states of its components are mutually dependent [2]. As a consequence, measurements performed on the individual states of an entangled system reveal strong correlations that go beyond corresponding classical limits. These correlations can be exploited in a number of quantum information processing applications such as quantum teleportation [274, 275], superdense coding [276–278], and quantum key distribution [13, 33] to name a few. Therefore, it is hardly surprising that the efficient generation of entangled quantum states is at the focus of various research activities. Entangled photon pairs, for instance, can be obtained from spontaneous parametric down-conversion in nonlinear optical materials [78] or radiative decay cascades in single photon emitters [279].

In the scope of this final chapter, we discuss two alternative approaches that take advantage of the effective photon-photon interaction offered by quantum interference:

- (i) Entangling two photons via their interaction within an all-optical controlled-NOT gate (CNOT) as proposed in [147]. The CNOT gate is investigated in light of our theoretical considerations presented in Chap. 3 and assessed with respect to the best available solid state emitter systems up to date.
- (ii) Entanglement swapping as part of standard quantum repeater protocols [31, 32]. In particular, we address the question whether achievable

entanglement rates in long-haul fiber-based quantum repeater networks are mainly limited due to attenuation or dispersion.

7.1 Entanglement via a Controlled NOT Operation

Currently, the most thriving implementation of quantum computers is based on superconducting qubits, as they can be build and operated with readily available and mature integrated circuit and radiofrequency technology [280]. Linear optical quantum computing, on the other hand, aims at an all-optical approach [146,220], which would significantly simplify the integration of quantum computers into quantum communication networks. However, a universal quantum computer needs to be able to conditionally toggle the state of a qubit, which can only be achieved by introducing nonlinear optical gates [281]. As has been suggested by Knill, Laflamme, and Milburn (KLM) [146], the nonlinear phase shift entailing two-photon interference might be exploited on that account.

As an analogue to the XOR gate employed in classical digital computing, an all-optical CNOT gate based on the guidelines of the KLM-protocol has been proposed in [147], while its operation has been demonstrated in a number of experiments [282–284]. One of the most relevant applications of a CNOT gate is the entanglement of the two input photons, which is mediated by quantum interference at a single asymmetric beam splitter. In the following we describe the architecture of an ideal CNOT gate and emulate the generation of a Bell-state including state preparation, CNOT gate operation, as well as a final state tomography using our formalism derived in Chap. 3. In particular, we determine the fidelity of the entangled output state and discuss the limitations set by emitter parameters.

The considered photonic circuit is depicted in Fig. 7.1. It consists of 6 input and 6 output modes. Two photons enter the gate, which are referred to as control (C) and target photon (T). Both photons are regarded qubits in dual rail representation. Accordingly, the states $|0\rangle_C$ and $|1\rangle_C$ of the control photon occupy modes 2 and 3 (called c_0 and c_1), while the target states $|0\rangle_T$ and $|1\rangle_T$ are encoded in modes 4 and 5 (t_0 and t_1). The terminal modes 1 and 6 are typically not fed with any photons and therefore referred to as vacuum modes v_c and v_t , respectively. The CNOT gate resides at the center of the overall optical gate. Basically, it is composed of a Mach-Zehnder interferometer mixing both target modes and three asymmetric beam splitters with a reflectivity of $R = 1/3$. The most crucial part, however, is the central asymmetric beam splitter connecting modes c_1 and t_0 , at which the actual interaction between control and target takes place: In case the control photon is in state $|1\rangle_C$, TPI imprints a phase on state $|0\rangle_T$, which in turn affects the interference between both target modes at the interferometer output. As a result the state of the

7.1. Entanglement via a Controlled NOT Operation

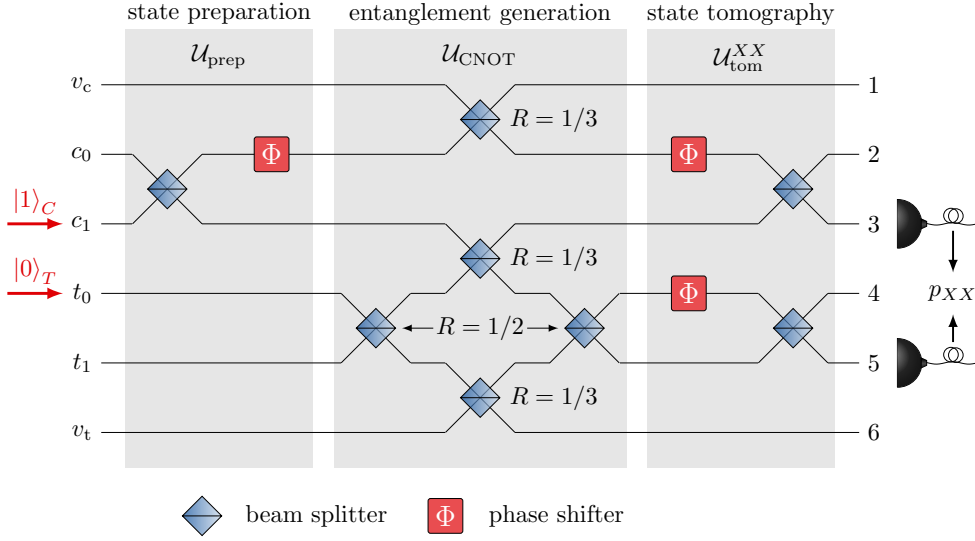


Figure 7.1. Illustration of the overall photonic circuit including the controlled NOT gate. The target and control photon enter the circuit via input modes c_1 and t_0 , respectively. The control photon is then prepared in a superposition state between modes c_0 and c_1 via $\mathcal{U}_{\text{prep}}$. Both photons are entangled with help of the controlled NOT (CNOT) gate represented by $\mathcal{U}_{\text{CNROT}}$, which is designed after [147]. The fidelity of the output state is assessed emulating a state tomography ($\mathcal{U}_{\text{tom}}^{XX}$ and coincidence detection between output modes 3 and 5). Adapted with permission from [197], IOP Publishing Ltd on behalf of Deutsche Physikalische Gesellschaft.

target photon is flipped conditioned on whether $|1\rangle_C$ was occupied or not. The asymmetric beam splitters are a necessity to make TPI possible. On the other hand, they cause the interferometer to be lossy so that the CNOT gate only works as intended in one out of nine cases. Therefore, its operation is often referred to as *probabilistic*. The unsuccessful attempts, however, can be identified and discarded with appropriate coincidence measurements at the gate outputs. For the remaining successful runs it is then valid to note the action of the gate via

$$\mathcal{U}_{\text{CNROT}} |0\rangle_C |0\rangle_T = |0\rangle_C |0\rangle_T, \quad (7.1)$$

$$\mathcal{U}_{\text{CNROT}} |0\rangle_C |1\rangle_T = |0\rangle_C |1\rangle_T, \quad (7.2)$$

$$\mathcal{U}_{\text{CNROT}} |1\rangle_C |0\rangle_T = |1\rangle_C |1\rangle_T, \quad \text{and} \quad (7.3)$$

$$\mathcal{U}_{\text{CNROT}} |1\rangle_C |1\rangle_T = |1\rangle_C |0\rangle_T, \quad (7.4)$$

where $\mathcal{U}_{\text{CNROT}}$ is the unitary matrix representing the CNOT gate. Based on these relations we realize, that both input photons can be entangled via a CNOT operation, if the target photon enters the gate in a superposition state.

In particular, we are able to obtain all four Bell-states according to

$$\begin{aligned} |\Psi^\pm\rangle &= \mathcal{U}_{\text{CNOT}} (|0\rangle_C \pm |1\rangle_C) |1\rangle_T / \sqrt{2} \\ &= (|0\rangle_C |1\rangle_T \pm |1\rangle_C |0\rangle_T) / \sqrt{2} \quad \text{and} \end{aligned} \quad (7.5)$$

$$\begin{aligned} |\Phi^\pm\rangle &= \mathcal{U}_{\text{CNOT}} (|0\rangle_C \pm |1\rangle_C) |0\rangle_T / \sqrt{2} \\ &= (|0\rangle_C |0\rangle_T \pm |1\rangle_C |1\rangle_T) / \sqrt{2}. \end{aligned} \quad (7.6)$$

As all Bell-states yield the same results regarding the following analysis, we only consider creation and assessment of $|\Phi^+\rangle$ for simplicity. A small obstacle arises as our formalisms given by Eq. (3.25) is not applicable to input photons, which are in superposition states. This can be easily met, however, if we include an appropriate state preparation to the overall process. We realize this by feeding the gate with a control photon in state $|1\rangle_C$, which is transferred to the desired superposition using an additional beam splitter and phase shifter, represented by the state preparation matrix $\mathcal{U}_{\text{prep}}$ (Fig. 7.1, left side). We can write the corresponding process as $\mathcal{U}_{\text{prep}} |1\rangle_C = (|0\rangle_C + |1\rangle_C) / \sqrt{2}$.

In order to assess the entanglement quality of the output state, we determine its fidelity. In [227] it is shown that the fidelity can be written as a function of 6 different coincidence probabilities via

$$F^{\Phi^+} = (p_{HH} + p_{VV} + p_{DD} + p_{AA} - p_{RR} - p_{LL}) / 2, \quad (7.7)$$

where the indices of p_{XX} are borrowed from the common notation of polarization states, i.e. we identify the base states as horizontal $|H\rangle = |0\rangle$ and vertical $|V\rangle = |1\rangle$ and obtain the superposition states diagonal $|D\rangle = (|0\rangle + |1\rangle) / \sqrt{2}$ and antidiagonal $|A\rangle = (|0\rangle - |1\rangle) / \sqrt{2}$ as well as right circular $|R\rangle = (|0\rangle + i |1\rangle) / \sqrt{2}$ and left circular $|L\rangle = (|0\rangle - i |1\rangle) / \sqrt{2}$. With that p_{XX} is defined as the coincidence probability measured between control and target photon after projecting the overall output state to $|X\rangle_C |X\rangle_T$. We realize the projection by employing two sets of beam splitter and phase shifter, one of each connecting both control and both target modes, respectively (Fig. 7.1, right side). All four linear optical components are represented by the unitary matrix $\mathcal{U}_{\text{tom}}^{XX}$, whose elements are chosen such that

$$\mathcal{U}_{\text{tom}}^{XX} |X\rangle_C |X\rangle_T = |1\rangle_C |1\rangle_T. \quad (7.8)$$

The desired p_{XX} can now simply be obtained by determining the coincidence probability between the outputs 3 and 5. Summarizing, the procedure is as follows:

- (i) Control and target photon enter the photonic circuit through inputs $i = 3$ and $j = 4$,
- (ii) the control photon is prepared in the necessary superposition state via $\mathcal{U}_{\text{prep}}$,

- (iii) both photons are entangled by means of the CNOT gate $\mathcal{U}_{\text{CNOT}}$ producing the Bell-state $|\Phi^+\rangle$,
- (iv) the output states are rotated via the state tomography matrix $\mathcal{U}_{\text{tom}}^{XX}$,
- (v) the coincidence probabilities p_{XX} between the output ports $k = 3$ and $l = 5$ are calculated using Eq. (3.25) and the overall gate matrix $\mathcal{U}_{\text{gate}} = \mathcal{U}_{\text{tom}}^{XX} \cdot \mathcal{U}_{\text{CNOT}} \cdot \mathcal{U}_{\text{prep}}$, and
- (vi) the desired Bell-state fidelity is eventually obtained applying Eq. (7.7).

The elements of $\mathcal{U}_{\text{prep}}$ and $\mathcal{U}_{\text{tom}}^{XX}$ are adapted from [226], while $\mathcal{U}_{\text{CNOT}}$ is constructed using the elements specified in [147].

It is certainly possible to obtain Bell-state fidelities for arbitrary dissimilar photon pairs using the described procedure. But for the sake of a concise presentation of our results, we only focus on photons with identical lifetimes as well as homogeneous and inhomogeneous line broadening contributions caused by pure dephasing (PD) and spectral diffusion (SD) and no relative detuning. In this case we have $\tau_{1,2} = \tau_r$, $\Gamma_{1,2}^* = \Gamma^* \rightarrow \gamma = 2\Gamma^* + 1/\tau_r$, $\sigma_{1,2} = \sigma \rightarrow \Sigma^2 = 2\sigma^2$, as well as $\delta\nu = 0$ and can use the normalized emitter parameters $\vartheta_{\text{PD}} = \gamma \cdot \tau_r$ and $\vartheta_{\text{SD}} = \sigma' \cdot \tau_r$ already introduced in Sect. 3.2.2. The corresponding Bell-State fidelity F^{Φ^+} as function of ϑ_{PD} and ϑ_{SD} is plotted in Fig. 7.2 (a). The white dashed line therein corresponds to photon pairs that yield $F^{\Phi^+} = 50\%$, being an important limit, as it classifies a given two-photon state as either separable ($F^{\Phi^+} < 50\%$) or non-separable ($F^{\Phi^+} > 50\%$) [227, 285]. Additionally, (b) illustrates the fidelity as function of the normalized coherence time $x_c = \tau_{\text{coh}}/(2\tau_r)$ [compare Eq. (3.34)] for the two limiting cases of photons that are only inhomogeneously (red solid curve, no PD) or only homogeneously broadened (blue dashed curve, no SD). Here, it can be clearly seen that we find $F^{\Phi^+} = 50\%$ for a TPI visibility of $V = 50\%$. Moreover, it is $F^{\Phi^+} < V$ for $50\% < V < 100\%$, which emphasizes the high demands on photon indistinguishabilities necessary to achieve acceptable entanglement fidelities. Note that the relation between F^{Φ^+} and V found here was directly obtained from our numerical simulations. They perfectly agree, however, with the equation $F^{\Phi^+} = (1 + V)/[2 \cdot (2 - V)]$ found e.g. in [284].

Eventually, we use these results to estimate Bell-state fidelities that might be achieved, if the gate was operated with photons from state-of-the-art solid state emitters reported in literature. In particular, we consider selected specimen representing the silicon vacancy (SiV) [286] and nitrogen vacancy (NV) [288] defect centers in diamond, semiconductor QDs [133], as well as single molecules [195]. Typically, the corresponding emission linewidths are not resolved in homogeneous and inhomogeneous contributions. Therefore, using the known radiative lifetime, we numerically find pairs of Γ^* and σ' that yield the stated linewidth assuming the Voigt function defined by Eq. (2.16). These are translated into a function ϑ_{PD} (ϑ_{SD}), which is displayed in Fig. 7.2

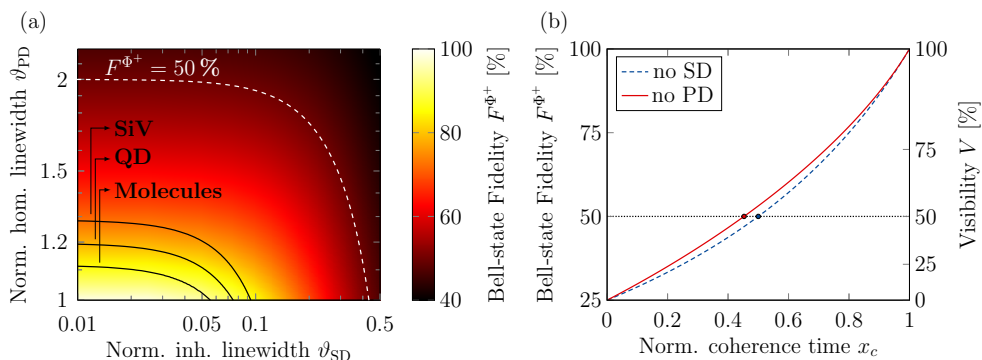


Figure 7.2. Simulation results for the entanglement generation using a controlled NOT gate. (a) Fidelity plotted as function of normalized homogeneous and inhomogeneous linewidths. The limit of $F^{\Phi^+} = 50\%$ distinguishing separable from non-separable is indicated by the white dashed line. For the emitter pair investigated in this work (compare Chap. 6) we find a fidelity of only $\approx 37\%$. Fidelities for selected state-of-the-art emitters shown as black curves: SiV [286], QD [133], molecules [287]. (b) Fidelity as function of normalized coherence time for emitters that do not show pure dephasing (red solid) or spectral diffusion (blue dashed). The curves furthermore indicate that a Bell-state fidelity of 50% is achieved at a two-photon interference visibility of 50%. Adapted with permission from [197], IOP Publishing Ltd on behalf of Deutsche Physikalische Gesellschaft.

(a) for SiV center, QD, and molecules as black solid curves. From these parameterized linewidth functions, we obtain ranges of possible visibilities [using Eq. (3.33)] and fidelities [extracted from Fig. 7.2 (a)], which are summarized in Tab. 7.1. All obtained values consistently reside in a range of moderate fidelities from 73-94%, even though the considered quantum emitters are among the best available in terms of close-to-Fourier-limited single photon emission. It is important to emphasize that these limited values can be entirely attributed to the emitter properties, as the overall optical circuit was modeled as ideal.

In contrast to the other presented emitters, the NV center exhibits a large radiative lifetime of around 12 ns, corresponding to a lifetime limited linewidth of no more than 13 MHz. Even comparatively small line broadening can therefore drastically reduce its coherence time. The most narrow linewidth we are aware of was measured for NV-centers in high-quality bulk diamond and can be found in [221]. Rapidly scanning the excitation laser across the resonance yielded linewidths of <20 MHz, i.e. close to the Fourier-limit. Repeating these scans however, reveals that the emission line shows SD in a range of 100 MHz. In the scope of our simulations, we take the single scan linewidth as an upper bound for PD, but consider the entire 100 MHz as SD range. This leads to a TPI visibility of only 21-23%, corresponding to a Bell-state fidelity of 34-

Table 7.1. Two-photon interference visibilities and Bell-state fidelities simulated for selected solid state emitters. Lifetimes and linewidths are given as stated in literature. Visibilities and fidelities are extracted from the simulations described in the main text.

Ref.	System	Lifetime [ns]	Linewidth [MHz]	V [%]	F^{Φ^+} [%]
[221]	NV	12 ^a	20/100 ^b	21-23	34-35
[286]	SiV	1.72	119	78-91	73-87
[133]	QD	0.85	270	84-93	79-91
[287]	Molecules	9.5	19	90-96	86-94

^aLifetime was obtained from the given Fourier-limited linewidth.

^bValue pair denotes *single scan linewidth / spectral diffusion range*, cf. main text.

35 %. A common strategy to overcome these poor values was applied in [73]. Therein the authors report on the entanglement of two remote NV centers via a projective Bell-state measurement (BSM). TPI visibilities of up to 80 % were achieved using rigorous spectral and temporal filtering, leading to Bell-state fidelities of $F^{\Psi^-} = 73\%$ and $F^{\Psi^+} = 64\%$. This approach, however, comes at the cost of a drastically reduced coincidence count rate. Moreover, from Fig. 7.2 (b) we find that the stated visibility corresponds to a fidelity of 75 %, being in a good agreement with the experimentally obtained values. This comparison is valid as both entanglement procedures using a CNOT gate and a BSM exhibit the same dependency on TPI visibilities as will be elaborated on in the following section.

Eventually, we like to mention that the presented simulations are meant to demonstrate the capabilities of our formalisms derived in Chap. 3. The data shown in Fig. 7.2 (a) correspond to almost 1200 combinations of ϑ_{PD} and ϑ_{SD} . For each data point we emulated the scattering of both photons at overall 11 linear optical elements and subsequent coincidence measurements in 6 different bases. Yet, the entire simulation lasted only $\approx 2\text{s}$ owing to the analytical expression for coincidence probabilities after two-photon scattering at linear optical gates given by Eq. (3.25). Similar performances can be expected for more involved gates and procedures, as long as the underlying gate matrices are known.

7.2 Attenuation and Dispersion in Fiber-Based Quantum Repeater Networks

The field of quantum key distribution (QKD) investigates various strategies that exploit fundamental laws of quantum mechanics in order to establish a secure communication link between two distant parties, which is immune to

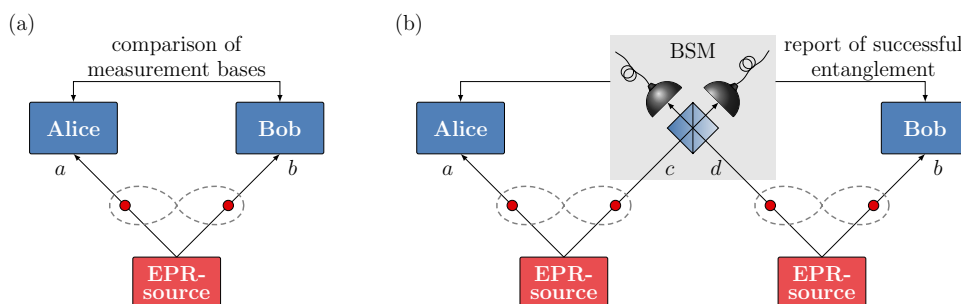


Figure 7.3. Quantum key distribution based on entangled photon pair sources. (a) As part of the E91 protocol [13] an entangled photon pair (red circles with gray lemniscate) is generated by an EPR-source. The photons are separately forwarded to sender (Alice) and receiver (Bob) via channels a and b . Both parties measure the quantum states of the photons in random bases. The bases are later compared via a public channel. (b) To increase the range of quantum key distribution (QKD) schemes, quantum repeaters are used: two EPR sources produce two entangled photon pairs. The photons in mode c and d undergo a projective Bell-state measurement (BSM), which consists of a beam splitter and two detectors at each output port. Whenever a coincidence is detected, both photons in the outer modes a and b are projected to a Bell-state, thus become entangled. The repeater station reports successful entanglement to Alice and Bob, who are then able to use the entangled photons for their QKD protocol.

eavesdropping. One of the most considered approaches is illustrated in Fig. 7.3 (a) and known as the E91-protocol [13], which relies on a source of two entangled qubits, often referred to as *EPR-source* (after Einstein, Podolsky, and Rosen [35]). The two qubits are shared between a sender (Alice) and a receiver (Bob), who measure the qubit states in randomly chosen bases. Whenever Alice and Bob pick the same base, both measurement results are perfectly anticorrelated. Therefore, both parties can agree on a shared quantum key merely by comparing the bases without ever revealing the actual measurement outcome. If, however, an eavesdropper attempts to intercept the quantum key exchange, the entanglement and consequently the anticorrelation are lost. Therefore, it is possible for Alice and Bob to discover eavesdropping simply by publicly announcing some selected measurement results.

In view of long-haul communication applications, photons as information carriers are the natural choice and optical fiber networks seem to offer an ideal infrastructure for QKD. However, as we have discussed in the introduction, the maximum distance between Alice and Bob is capped at a few 100 km for point-to-point schemes due to transmission losses [27–29] and one has to resort to quantum repeaters (QR) [31–33] to exceed this limit. A simplified QR scheme, which can be understood as a quantum relay [75–77], is depicted in Fig. 7.3 (b): two EPR-sources reside in between Alice and Bob. One photon of each

source is sent to a central station via the inner modes c and d . The photons are overlapped on a beam splitter and coincidences between its output modes are detected. In case the photons are indistinguishable, these coincidences project the joint state of the distant photons in outer modes a and b into an entangled Bell-state. This step is commonly referred to as entanglement swapping via Bell-state measurement (BSM). As soon as the central BSM-station registered a coincidence, it reports a successful entanglement generation to Alice and Bob, who are then able to proceed with their quantum key exchange. The key is to recognize that no photon has to travel the entire distance L between sender and receiver, but - in a symmetric arrangement - at maximum $L/2$, which reduces the impact of attenuation.

As we have mentioned, the entanglement swapping crucially depends on the indistinguishability of both photons, which are brought to interaction during the BSM. More specifically, the fidelity of the output Bell-state can be connected to the underlying TPI visibility. The fidelity, on the other hand, needs to be close to unity to retain a high level of correlation between the results of measurements performed by Alice and Bob on the final state. To elaborate on the relation of photon indistinguishability and fidelity we borrow a description offered in [289]: First, it is important to realize that the Bell-states

$$|\Psi^\pm\rangle = (|0\rangle_a |1\rangle_b \pm |1\rangle_a |0\rangle_b) / \sqrt{2} \quad \text{and} \quad (7.9)$$

$$|\Phi^\pm\rangle = (|0\rangle_a |0\rangle_b \pm |1\rangle_a |1\rangle_b) / \sqrt{2} \quad (7.10)$$

constitute a complete orthonormal basis for the two state, two particle Hilbert space describing the photons in modes a and b . We now consider the entanglement swapping scheme shown in Fig. 7.3 (b), where initially a is entangled with c and b with d , and assume that both EPR sources emit entangled photons in a $|\Psi^-\rangle$ state. It is straightforward to show that the composite state of the overall system $|\Psi\rangle_{abcd}$ of four photons can be written as

$$|\Psi\rangle_{abcd} = \frac{1}{2} \sum_{|B\rangle \in \mathcal{M}} |B\rangle_{ab} |B\rangle_{cd}, \quad (7.11)$$

where \mathcal{M} denotes the set of all four Bell-states. Assuming that all photons are entirely indistinguishable, we furthermore see that only state $|\Psi^-\rangle$ is anti-symmetric (fermionic) upon particle exchange, while $|\Psi^+\rangle$ and $|\Phi^\pm\rangle$ are symmetric (bosonic). Therefore, only $|\Psi^-\rangle$ leads to coincidences during the BSM and consequently projects the composite state $|\Psi\rangle_{abcd}$ into the entangled Bell-state $|\Psi^-\rangle_{ab}$. However, this only works ideally for indistinguishable photons. For partially distinguishable photons, the projection leads to a mixed state with decreased fidelity. The fidelity quantifies the probability that a measured coincidence corresponds to a projection to the desired state $|\Psi^-\rangle_{ab}$ and therefore is

$$F = \frac{p_{\Psi^-}}{p_{\Psi^+} + p_{\Psi^-} + p_{\Phi^+} + p_{\Phi^-}}, \quad (7.12)$$

where $p_{\Psi\pm}$ and $p_{\Phi\pm}$ denote the probabilities to obtain a coincidence from the respective Bell-states. Considering the fermionic and bosonic nature of the Bell-states, it can be understood that these probabilities are given by

$$p_{\Psi-} = (1 + V)/2 \quad \text{and} \quad (7.13)$$

$$p_{\Psi+} = p_{\Phi\pm} = (1 - V)/2 \quad (7.14)$$

with V being the TPI visibility. Eventually, this enables us to determine the fidelity as

$$F = \frac{1 + V}{2 \cdot (2 - V)}. \quad (7.15)$$

To review the performance of various QR schemes [33] considers a desired final state fidelity of $F \geq 90\%$ for all discussions. Even in the most simple and ideal case of only a single BSM, unit fidelities of the EPR-sources, and noise-free transmission channels as well as detectors, this demand requires a TPI visibility of $V > 92.9\%$ following Eq. (7.15). Accordingly, visibilities of typically less than 90% as reported in Tab. 7.1 for various solid-state emitters are clearly insufficient. As we have thoroughly discussed throughout this work, these visibilities are mainly limited due to different line broadening mechanisms. One approach to achieve superior indistinguishabilities is to couple the corresponding quantum emitters to high-finesse microcavities [230, 290, 291]. The advantage is even twofold:

- (i) Purcell-enhancement increases the natural linewidth, while additional broadening due to pure dephasing and spectral diffusion remains constant. This improves the relative optical coherence time and thus the indistinguishability of the emitted photons.
- (ii) Moreover, the radiative lifetime is shortened due to Purcell-enhancement, which allows higher system clock rates to be employed.

Shortening photon lifetimes can be considered the course of action, but a new potential problem arises: chromatic dispersion is known to distort the shape of a wave-packet [292]. Group delay dispersion (GDD) for instance, being the leading dispersive term, causes a frequency chirp and pulse broadening. This effect is proportional to the square of the spectral bandwidth and increases linearly with the length of the dispersive medium. Therefore, it is expected to have a more severe impact on temporally short photons and for long fibers. In asymmetric QR setups, where the photons in modes c and d travel different distances prior to the BSM, dispersion will affect both photons to a different extent and therefore decrease their mutual indistinguishability.

Although optical fibers offer the indispensable advantage of guiding photons to any desired location, we see they entail attenuation and dispersion, which ultimately limit the performance of quantum communication. Fig. 7.4

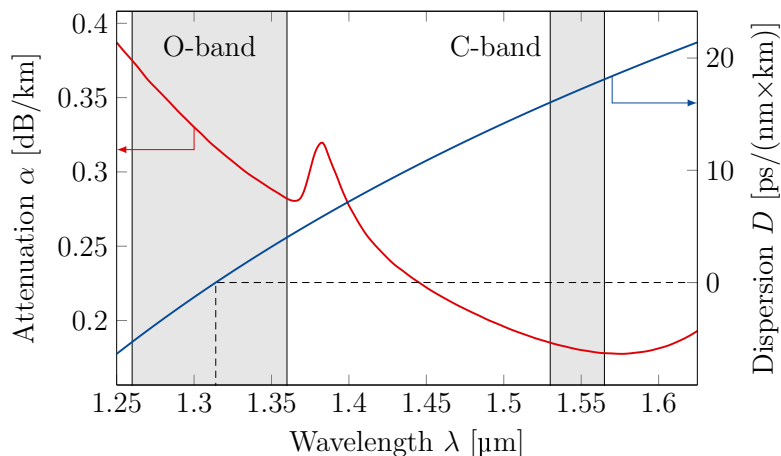


Figure 7.4. Attenuation and dispersion in a SMF-28 fiber at telecom wavelengths. The attenuation (red curve) has a global minimum of ≈ 0.18 dB/km at the telecom C-band around 1550 nm, while dispersion (blue curve) is minimized with the telecom O-band and vanishes at 1314 nm (see dashed line). Both curves were obtained from fiber parameters stated in the datasheet [293].

illustrates both quantities as function of typical telecom wavelengths. The attenuation $\alpha(\lambda)$ was determined using the Hanson-matrix method [294] based on matrix elements reported in [295] and attenuation values at specific wavelengths given in [293]. The dispersion value $D(\lambda)$ can be evaluated using

$$D(\lambda) = \frac{S_0}{4} \cdot \left(\lambda - \frac{\lambda_0^4}{\lambda^3} \right), \quad (7.16)$$

where the zero dispersion slope and wavelength are $S_0 = 0.092$ ps/(nm²·km) and $\lambda_0 = 1314$ nm, respectively [293]. As can be seen, the attenuation is minimal within the telecom C-band, while the dispersion vanishes at λ_0 in the telecom O-band. The low losses and availability of Erbium-doped fiber amplifiers motivated classical optical communication networks to accept the telecom C-band as default wavelength regime, even though pulse broadening due to chromatic dispersion causes temporal cross-talk of neighboring timebins (briefly addressed below). The negative impact of dispersion on photon indistinguishabilities, however, is irrelevant to classical schemes. Therefore, in the scope of quantum communication, the valid question arises, whether and under which conditions the O-band should be preferred to the C-band due to the minimized dispersion.

In the following, we approach this question first by quantifying the effect of dispersion on short single photon pulses using realistic fiber parameters. As figure-of-merit, we calculate the drop of the coincidence rate in an entanglement swapping scheme due to both attenuation and dispersion, if a given

target-fidelity is to be achieved. The results are then discussed for various network designs and emitter parameters comparing the performances in the telecom O- and C-band.

7.2.1 Two-Photon Interference with Dispersed Photons

Dispersion, or more specifically chromatic dispersion, refers to the distortion of a wave-packet in time due to a frequency dependent phase velocity. The effect is most easily described using the spectral phase function $\Phi(\omega)$, which yields the phase that each frequency component ω acquires when traveling through a dispersive medium. It is simply related to the refractive index $n(\omega)$ and the length L of the medium via $\Phi(\omega) = n(\omega)kL$, where k is the wavenumber in vacuum. It is generally very intricate to treat the impact of dispersion for a given wave function $\zeta(t)$ directly in the time domain. In the frequency domain, however, dispersion is nothing but a multiplication with a phase factor that carries $\Phi(\omega)$ as argument. Accordingly, the dispersed wave function $\zeta_{\text{out}}(t)$ can be related to its undispersed counterpart $\zeta_{\text{in}}(t)$ via [292]¹

$$\zeta_{\text{out}}(t) = \mathcal{F}^{-1} \left\{ \mathcal{F}[\zeta_{\text{in}}](\omega) \cdot e^{i\Phi(\omega)} \right\} (t), \quad (7.17)$$

where $\mathcal{F}(\bullet)$ denotes the Fourier transformation. In order to simplify the inverse Fourier transformation, $\Phi(\omega)$ is often expanded into a Taylor series around a given central frequency ω_0 . Its zeroth and first order term are irrelevant for wave-packet distortion, as they only shift phase and envelope of the output pulse. Therefore, we here focus on the second order term, referred to as group delay dispersion (GDD), which leads to pulse broadening and a frequency chirp. Accordingly, we consider the spectral phase to be

$$\Phi(\omega) \approx \frac{1}{2} \Phi^{(2)}(\omega_0) \cdot (\omega - \omega_0)^2 = \kappa \cdot (\omega - \omega_0)^2, \quad (7.18)$$

where $\Phi^{(2)}(\omega_0) = 2\kappa$ is the second derivative of $\Phi(\omega)$ taken at ω_0 . For optical fibers, we find that it can be expressed in terms of the dispersion value D in Eq. (7.16) according to [296]

$$\Phi^{(2)}(\omega_0) = \frac{2\pi cL}{\omega_0^2} \cdot D, \quad (7.19)$$

where c is the speed of light in vacuum. Even despite the approximation of $\Phi(\omega)$, the inverse Fourier transformation in Eq. (7.17) remains complicated when treating single photons with a one-sided exponential decay as given by Eq. (3.6). However, for Gaussian input pulses a simple analytical solution is known. Defining the input wave function as

$$\zeta_{\text{in}}(t) = \sqrt[4]{\frac{2\sigma^2}{\pi}} \cdot \exp(-\sigma^2 t^2 + i\omega_0 t), \quad (7.20)$$

¹Note that [292] is generally used as reference for all remarks regarding the description of dispersed wave functions, if not stated otherwise.

where σ is the standard deviation of its power spectral density, the output pulse after the dispersive medium can be described by

$$\zeta_{\text{out}}(t) = \sqrt[4]{\frac{1}{2\pi\beta\gamma}} \cdot \exp\left[-\frac{t^2}{4\beta\gamma} + i\left(\frac{a}{4}t^2 + \omega_0 t + \frac{\vartheta}{2}\right)\right]. \quad (7.21)$$

Here, the abbreviations

$$\begin{aligned} \gamma &= 1 + 16\sigma^4\kappa^2, & \beta &= \frac{1}{4\sigma^2}, \\ a &= \frac{\kappa}{\beta^2\gamma}, \text{ and} & \vartheta &= \arctan\left(-\frac{\kappa}{\beta}\right). \end{aligned} \quad (7.22)$$

were used. Gaussian pulses certainly do not lead to the same results as exponential decays, but they yield a sufficient first estimation of dispersive effects [292]. To obtain the best possible agreement between a Gaussian pulse of standard deviation σ and a single photon with radiative lifetime τ_r , we set

$$\sigma = \frac{1}{2\sqrt{2\ln 2}\tau_r} \quad (7.23)$$

in the following. In this case the FWHMs of both waveforms are matched in the frequency domain. Fig. 7.5 (a) shows an example of a Gaussian pulse with an initial lifetime of $\tau_{\text{in}} = 10$ ps and an arbitrary carrier frequency ω_0 . Assuming the dispersion value at the telecom C-band of $D = 18$ ps/(nm·km) and an optical fiber length of $L = 20$ km, the output pulse following Eq. (7.21) is illustrated in Fig. 7.5 (b). As can be seen the pulse is stretched to a lifetime of $\tau_{\text{out}} = 19$ ps and the momentary frequency varies across the pulse. The latter effect is referred to as *chirp*. The pulse broadening can be simply quantified by relating the initial to the final pulse width in Eq. (7.20) and Eq. (7.21), which yields

$$\tau_{\text{out}} = \tau_{\text{in}} \cdot \sqrt{1 + \left(\frac{\lambda^2 D}{\pi c}\right)^2 \sigma^4 L^2}. \quad (7.24)$$

From here we realize that the pulse broadening scales quadratically with the spectral bandwidth and linearly with the fiber length in the regime of strong dispersion. Accordingly, spectrally narrow C-band photons with a lifetime of 600 ps as investigated in Chap. 6 would only be broadened by about 2 ps after 100 km of fiber. It is easy to understand that absorption will have a more severe impact at this regime and the telecom C-band is clearly the best choice. Accordingly, we will focus on short photons of a few to a few ten picoseconds as shown in Fig. 7.5 in the following.

In order to include quantum interference into our considerations, we follow the approach already used in Sect. 2.4.2, i.e. we first evaluate the joint

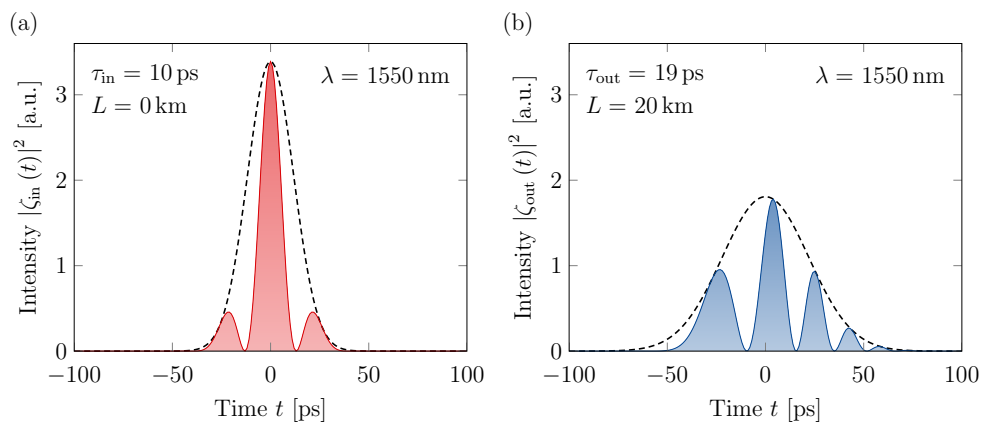


Figure 7.5. Gaussian pulse propagating through 20 km of optical fiber in the telecom C-band. The black dashed curves depict the envelope of the pulse, the red and blue shaded curves illustrate the time-dependent oscillations of the field intensity. (a) shows the initial pulse with a temporal width of $\tau_{\text{in}} = 10$ ps at the entrance of the fiber. (b) corresponds to the output pulse after propagation through the fiber, broadened to a lifetime of $\tau_{\text{out}} = 19$ ps. Additionally, the momentary frequency of the pulse is chirped, i.e. it varies across the pulse. Note that the unrealistically small carrier frequency of $\omega_0 \approx 20 \times 2\pi$ GHz was only chosen for illustrative purposes.

detection probability after the interaction of two input photons in temporal modes $\zeta_{1,2}(t)$ at a single symmetric beam splitter given by

$$P_{\text{joint}}(t_0, \tau) = \frac{1}{4} |\zeta_1(t_0 + \tau) \zeta_2(t_0) - \zeta_2(t_0 + \tau) \zeta_1(t_0)|^2. \quad (7.25)$$

Assuming two dispersed Gaussian input photons according to Eq. (7.21) with distinct linewidths $\sigma_{1,2}$, GDD parameters $\kappa_{1,2}$, and carrier frequencies $\omega_{1,2}$ we obtain

$$P_{\text{joint}}(t_0, \tau) = \frac{1}{2\pi} \sqrt{\frac{1}{\beta_1 \gamma_1 \beta_2 \gamma_2}} \cdot \exp \left[-\frac{1}{4\Gamma} (2t_0^2 + 2t_0\tau + \tau^2) \right] \times \exp \left[i \frac{\Delta a}{4} (\tau^2 + 2t_0\tau) + i \Delta \omega \tau \right] \quad (7.26)$$

with the new abbreviations

$$\frac{1}{\Gamma} = \frac{1}{\beta_1 \gamma_1} + \frac{1}{\beta_2 \gamma_2}, \quad \Delta a = a_1 - a_2, \quad \text{and} \quad \Delta \omega = \omega_1 - \omega_2. \quad (7.27)$$

The cross-correlation function can now be determined via integration over all

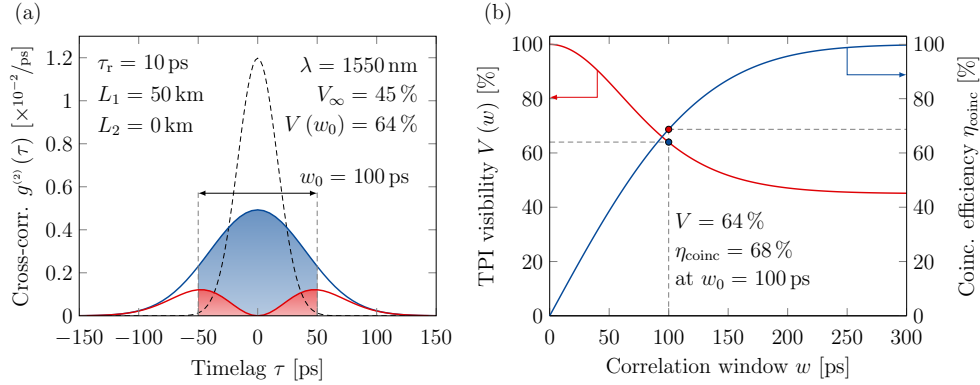


Figure 7.6. Cross-correlation function between chirped and unchirped Gaussian pulses at the telecom C-band. (a) Both photons exhibit $\tau_r = 10$ ps, but one photon travels through $L_1 = 50$ km before the HOM experiment. The red (blue) curve shows correlation with (without) two-photon interference, while the black dashed curve illustrates the limit without interference, if no photon was sent through any fiber. The curves correspond to a visibility of 45%. If only coincidences in a correlation window of $w_0 = 100$ ps are taken into account (shaded areas), the visibility improves to 64%. (b) shows the visibility (red) and coincidence efficiency (blue) for various correlation windows. If the window is chosen sufficiently small, the visibility can be brought close to unity, but only at the cost of a low coincidence efficiency.

possible detection times t_0 , which yields

$$\begin{aligned}
 g^{(2)}(\tau) &= \int_{-\infty}^{\infty} P_{\text{joint}}(t_0, \tau) dt_0 \\
 &= \sqrt{\frac{1}{8\pi\Sigma^2}} \cdot \left[\exp\left(-\frac{\tau^2}{2\Sigma^2}\right) - \exp\left(-\frac{\tau^2}{2\Omega^2}\right) \cdot \cos \Delta\omega\tau \right]
 \end{aligned} \tag{7.28}$$

with

$$\Sigma^2 = \beta_1\gamma_1 + \beta_2\gamma_2 \quad \text{and} \quad \Omega^2 = \frac{4}{1/\Gamma + \Delta a^2\Gamma}. \tag{7.29}$$

A cross-correlation for an identical emitter pair with $\tau_r = 10$ ps, $\Delta\omega = 0$, and $\lambda = 1550$ nm is illustrated in Fig. 7.6 (a) as red curve. One photon traveled through $L_1 = 50$ km, while the other did not ($L_2 = 0$ km). Accordingly both photons became partially distinguishable leading to the non-vanishing cross-correlation. The blue solid curve represents the limit without the interference term in Eq. (7.28) (second summand). The black dashed curve shows a corresponding measurement without TPI for undispersed photons for comparison ($L_1 = L_2 = 0$).

In order to simplify our equations, we only consider photons without a carrier frequency offset in the following, i.e. we set $\Delta\omega = 0$. Using Eq. (2.50)

and Eq. (2.52) we extract the TPI visibility from the cross-correlation function via integration and obtain

$$V = 1 - 2 \int_{-\infty}^{+\infty} g^{(2)}(\tau)|_{\Delta\omega=0} d\tau = \frac{\Omega}{\Sigma}. \quad (7.30)$$

In case of the emitter pair presented in Fig. 7.6, we see that Eq. (7.30) leads to a TPI visibility of merely 45 %, which is only reduced due to the influence of the optical fiber. As already mentioned in Sect. 7.1, a common strategy to improve the visibility is to apply a time filter. In this case we do not consider all recorded correlation events, but only those within a time window of width w centered around $\tau = 0$ [297]. We first obtain the coincidence probabilities

$$p_{\text{coinc},0}(w) = \int_{-\frac{w}{2}}^{+\frac{w}{2}} g_0^{(2)}(\tau)|_{\Delta\omega=0} d\tau = \frac{1}{2} \text{erf}\left(\frac{w}{\sqrt{8}\Sigma}\right) \quad \text{and} \quad (7.31)$$

$$p_{\text{coinc}}(w) = \int_{-\frac{w}{2}}^{+\frac{w}{2}} g^{(2)}(\tau)|_{\Delta\omega=0} d\tau = p_{\text{coinc},0}(w) - \frac{\Omega}{2\Sigma} \text{erf}\left(\frac{w}{\sqrt{8}\Omega}\right),$$

where $\text{erf}(\bullet)$ is the error-function and $g_0^{(2)}(\tau)$ equals $g^{(2)}(\tau)$, but does not include the interference term. These expressions allow us to write the TPI visibility as function of the time window w according to

$$V(w) = 1 - \frac{p_{\text{coinc}}(w)}{p_{\text{coinc},0}(w)} = \frac{\Omega}{\Sigma} \cdot \frac{\text{erf}\left(\frac{w}{\sqrt{8}\Omega}\right)}{\text{erf}\left(\frac{w}{\sqrt{8}\Sigma}\right)}. \quad (7.32)$$

Eventually, we define the coincidence efficiency $\eta_{\text{coinc}}(w)$ as the probability to measure a coincidence when a time window of width w is applied, normalized to its limit for $w \rightarrow \infty$. The efficiency simply reads

$$\eta_{\text{coinc}}(w) = \frac{p_{\text{coinc},0}(w)}{p_{\text{coinc},0}(w \rightarrow \infty)} = \text{erf}\left(\frac{w}{\sqrt{8}\Sigma}\right) \quad (7.33)$$

and describes the reduction of the attainable coincidence count rate in case a time filter was used. Applying these expressions to the emitter pair shown in Fig. 7.6 (a) leads to a visibility of 64 % and a coincidence efficiency of 68 %, if a window of $w_0 = 100$ ps was chosen. A plot of $V(w)$ and $\eta_{\text{coinc}}(w)$ for various w is illustrated in Fig. 7.6 (b) (red and blue curve, respectively). Here, we recognize that visibilities close to unity require rigorous time filters of only a few ps, which entail the loss of most coincidences.

7.2.2 Entanglement Efficiencies in Optical Fiber Networks

Entanglement generation rates depend on a plethora of different parameters such as the emission rate of the EPR-sources, signal latencies, transmission

losses, and detection efficiencies to name a few [33, 298]. As we are only interested in the interplay of attenuation and dispersion, we write the overall rate according to

$$R_{\text{ent}} = R_0 \cdot \eta_{\text{fib}}. \quad (7.34)$$

Here, the efficiency η_{fib} describes the loss of entanglement rate due to the impact of optical fibers, while the rate R_0 summarizes all remaining contributions. Furthermore, we model η_{fib} as

$$\eta_{\text{fib}} = \eta_{\text{coinc}}(w) \cdot T(L_1) \cdot T(L_2), \quad (7.35)$$

where $\eta_{\text{coinc}}(w)$ is the coincidence efficiency according to Eq. (7.33) and $T(L)$ is the transmission of a fiber of length L . The lengths L_1 and L_2 denote the distances of both EPR-sources to the BSM station. Note that this ansatz neglects any error correction, i.e. it is only valid, if the detected signal rate is well above the detector dark count rate [11]. Using the wavelength dependent attenuation $\alpha(\lambda)$ as shown in Fig. 7.4, the transmission is

$$T(L_1) \cdot T(L_2) = 10^{-\alpha L_1/10} \cdot 10^{-\alpha L_2/10} = 10^{-\alpha L/10} \quad (7.36)$$

with $L = L_1 + L_2$ being the overall fiber length. Furthermore, we introduce q as the relative position of the BSM, so that $L_1 = q \cdot L$ and $L_2 = (1 - q) \cdot L$.

The essence of the following simulation is to compare η_{fib} in the telecom O- and C-band for various fiber lengths L , radiative lifetimes τ_r , as well as relative positions of the BSM q . We expect the transmission to be ideal in the telecom C-band. However, at this wavelength range dispersion distorts the single photons and decreases the TPI visibility in asymmetric arrangements ($q \neq 0.5$). Therefore, it is necessary to choose a finite correlation time window w to achieve a desired target fidelity F of the entangled output state [according to Eq. (7.15) and Eq. (7.32)]. This, on the other hand, decreases $\eta_{\text{coinc}}(w)$ and accordingly η_{fib} . In the telecom O-band the situation is vice versa. As target fidelity we choose $F = 90\%$ throughout all simulations, following the suggestion in [33].

As a first example, we assume a pair of equal photons with $\tau_r = 5$ ps and a transmission distance of $L = 40$ km in a maximally asymmetric scenario, where the BSM is performed at the location of EPR-source 1 ($q = 0$). The obtained entanglement efficiency η_{fib} as a function of the wavelength is illustrated in Fig. 7.7 (red curve) and compared to a scenario, in which only attenuation but not dispersion plays a role (black dashed curve). While both curves coincide within the telecom O-band, η_{fib} significantly drops towards longer and shorter wavelengths. In these regimes, dispersion takes effect and it becomes necessary to narrow the coincidence time window w (blue curve) in order to sustain the desired target fidelity. A direct comparison of C-band to O-band reveals that the latter yields a gain factor of

$$g = \frac{\eta_{\text{fib}}(1314 \text{ nm})}{\eta_{\text{fib}}(1550 \text{ nm})} \approx 3.3 \quad (7.37)$$

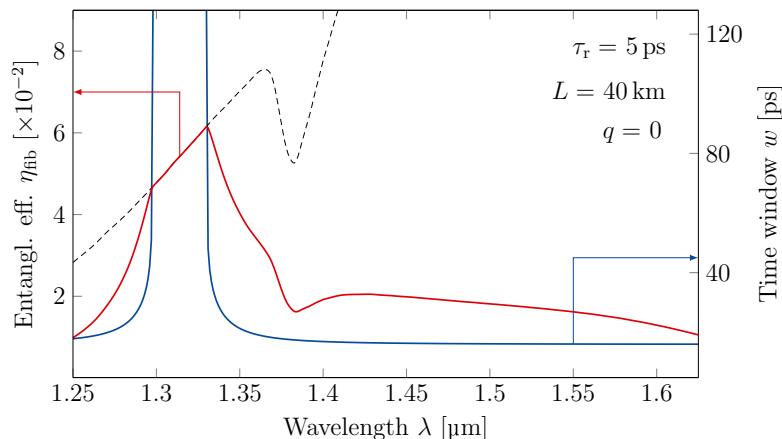


Figure 7.7. Impact of the coincidence time window on the entanglement efficiency. Shown is the entanglement efficiency η_{fib} (red) for an emitter pair with radiative lifetime $\tau_r = 5$ ps, if only one photon traveled through 40 km of optical fiber. The black dashed curve considers the influence of attenuation, but neglects dispersion. Outside the telecom O-band η_{fib} clearly drops below this limit, as the coincidence time window w (blue) has to be narrowed in order to restore the desired entanglement fidelity of 90%. In this example the telecom O-band leads to a gain factor of around 3.3 over the C-band.

for the chosen example.

For a broader view, we consider 4 different radiative lifetimes ranging from $\tau_r = 3$ ps to 10 ps, as the impact of GDD starts to unfold in this regime. For each lifetime we evaluate the O-band gain factor g according to Eq. (7.37), taking fiber lengths of up to 100 km and relative BSM positions between $q = 0$ and 0.5 into account. The results are shown in Fig. 7.8. Generally, we can identify 3 distinct regions as highlighted in (b), all of which are separated by white dashed lines:

- **Region I:** (red shaded) The gain factor is $g > 1$, indicating that the telecom O-band yields the higher entanglement generation rate and should be preferred over the C-band.
- **Region II:** (blue shaded) The gain factor is $g < 1$, implying that the C-band performs better. Furthermore, it is $\eta_{\text{coinc}}(w) < 1$ in region II, i.e. the coincidence measurement needs to be truncated to achieve $F \geq 90\%$. In contrast to region I, however, this loss is overcompensated by the low attenuation in the C-band.
- **Region III:** (blue shaded) Like region II, but we find $\eta_{\text{coinc}}(w) = 1$, meaning that the entanglement rate is only limited due to attenuation, but not dispersion. Therefore, g does not depend on the location of the BSM (parameter q) in this region.

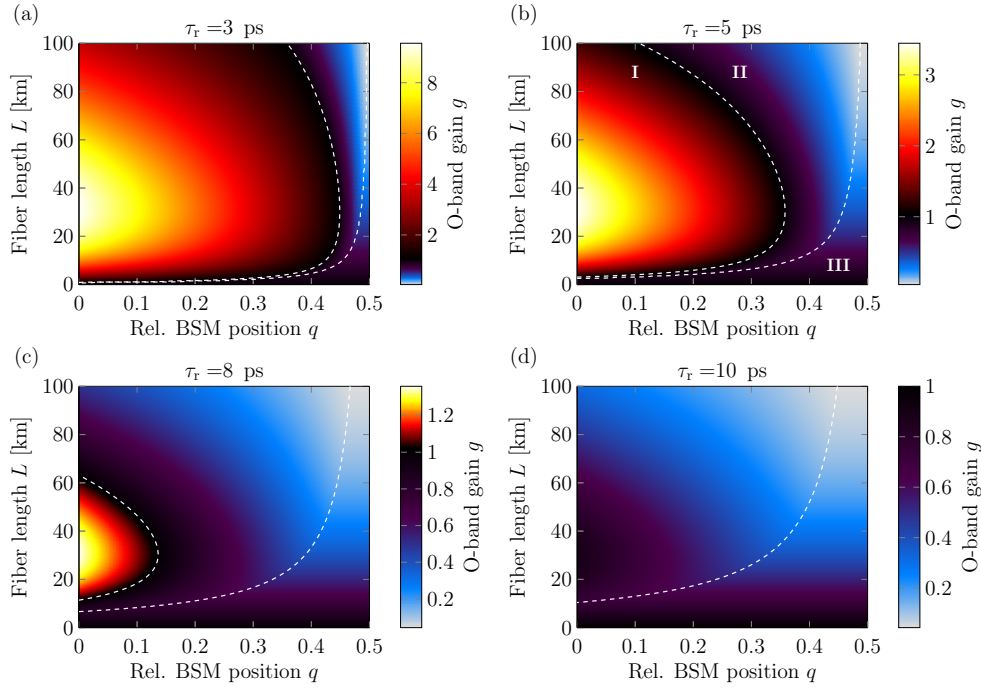


Figure 7.8. Telecom O-band gain factor for different network architectures. Illustrated are simulations for 4 different radiative lifetimes $\tau_r = 3$ ps to 10 ps [(a) to (d)]. For all lifetimes the gain factor g was computed for various fiber lengths L and network asymmetries q . Three regions can be distinguished, separated by white dashed lines [compare (b)]: in region I it is $g > 1$, i.e. the O-band should be preferred. In region II and III the C-band outperforms the O-band. Additionally, in region III it is $\eta_{\text{coinc}}(w) = 1$, i.e. the entanglement rate is only limited by attenuation. In region II dispersion leads to $\eta_{\text{coinc}}(w) < 1$ and therefore further reduces the rate.

The results clearly reveal that under certain conditions the absence of dispersion leads to superior entanglement generation rates in the telecom O-band. As expected the effect is more prominent for short lifetimes and strong asymmetries. Interestingly, we find that the maximal gain factor within region I is always at a fiber length of around $L_{\text{max}} = 31$ km (almost) independent of lifetime and network asymmetry. As it turns out, this corresponds to the length at which the ratio between the transmissions at O- and C-band dropped to $1/e$, i.e. L_{max} is defined by

$$\frac{T(L_{\text{max}}, \lambda_{\text{O}})}{T(L_{\text{max}}, \lambda_{\text{C}})} = 10^{-[\alpha(\lambda_{\text{O}}) - \alpha(\lambda_{\text{C}})] \cdot L_{\text{max}}/10} = 1/e \quad (7.38)$$

with $\lambda_{\text{O}} = 1314$ nm and $\lambda_{\text{C}} = 1550$ nm. Therefore, we conclude that g is maximized at L_{max} , as the attenuation penalty in the O-band becomes dominant beyond this point.

At the maxima $(q_{\max}, L_{\max}) = (0, 31 \text{ km})$, we find gain factors of $g = 9.6$ and 3.4 for $\tau_r = 3 \text{ ps}$ to 5 ps , respectively. On the contrary, as can be seen in the plots (c) and (d) the absence of dispersion within the O-band is not of advantage for long lifetimes, according to our initial guess. Therefore, the present considerations do not matter for a wide range of available emitter systems that typically operate at $\tau_r > 100 \text{ ps}$. Considerable efforts are made, however, to place quantum emitters in optical microcavities and operate them in the strong coupling regime, which increases on one hand the source efficiency, but also the indistinguishability of emitted photons [299, 300]. As mentioned before, the latter effect is partially caused by a decrease of the radiative lifetime. In particular for QD emitters lifetimes of no more than a few 10 ps have been reported [290, 291] and even smaller values are within reach, rendering our considerations relevant for these systems. Moreover note that our discussions have been aimed at solid-state single photon sources, as they are the main subject of the present work. Sources based on spontaneous parametric down conversion, on the other hand, inherit the temporal properties of the employed pump laser and therefore often exhibit pulse durations of only a few ps or even in the fs regime (see e.g. [301–303]). In these cases, dispersion fully unfolds and our considerations should be taken into account.

A possible strategy to counteract dispersion in the C-band is to temporally compress the single photon pulses subsequent to the fiber transmission, e.g. using dispersion-compensating optical fibers or chirped fiber Bragg gratings [304, 305]. Both approaches, however, introduce additional losses, reducing the low-attenuation advantage of the C-band (see e.g. [25]). It is moreover conceivable to mitigate the impact of dispersion by spectrally compressing the employed photon pulses prior to fiber transmission using the concept of time lenses [306, 307]. As this technique in fact requires a dispersive medium, it might be straightforward to implement into fiber transmission channels. Currently, the efficiency of this scheme is capped at a few 10 %, mostly due to losses at the necessary electro-optical modulator. It is also possible to spectrally shape single photons using tailored pump pulses that drive a frequency conversion process [308, 309]. In quantum networks that anyway include QFC to interface atomic with telecom wavelengths, this scheme might entail only a minor efficiency penalty. To avoid GDD altogether, so-called *dispersion-shifted fibers* can be employed [310]. They possess a tailored refractive index profile such that material dispersion is compensated by waveguide dispersion close to or within the C-band. But as most existing networks are not equipped with this type of optical fiber, they can not be considered a general solution for large-scale networks as of yet. Eventually, we like to mention that our considerations did not include the impact of a temporal overlap between photons in neighboring bins caused by dispersion. This effect is commonly known as *inter-symbol interference* and leads to an increasing bit error rate, if neglected [311]. Although it is not a consequence of quantum interference, it underlines the necessity to take dispersion in the telecom C-band into account.

7.3 Summary

In this chapter we theoretically investigated two all-optical schemes to generate entanglement that rely on quantum interference between two independent photons. In the first example, we considered a photonic circuit containing a controlled NOT gate after the design presented in [147] and applied the formalism derived in Chap. 3 to compute entanglement fidelities attainable with state-of-the-art quantum emitters. Thereafter, we turned to entanglement swapping based on Bell-state measurements as employed in quantum repeater networks [31, 32]. Here, we addressed the question whether the low losses in the telecom C-band or the low dispersion in the telecom O-band allow for better entanglement generation rates. The results of both investigations are summarized in the following *highlights*-box.

CHAPTER 7 - HIGHLIGHTS

CNOT Gate Entanglement

- Consideration of a network of 11 linear optical components to create an entangled Bell-state of two photons.
- The network includes elements for state preparation, a CNOT gate, and state tomography.
- Application of theory derived in Chap. 3 to emulate entanglement generation and assess fidelity F of output states with respect to spectral properties of employed photons.
- Despite a high complexity of the investigated system the computation time was as low as 2s owing to the analytical expressions used for the simulation.
- Simulations reveal $V > F$ for two-photon interference (TPI) visibility V in the regime of $F > 50\%$. This underlines high demands on employed single photon sources.
- Best available solid state sources yield fidelities of only 73-94%, if no further filtering or stabilization techniques are employed.

CHAPTER 7 - HIGHLIGHTS CONTINUED**Entanglement Swapping**

- Consideration of asymmetric single quantum repeater networks that employ optical fibers for photon transmission.
- Derivation of cross-correlation function and TPI visibilities in HOM experiments for short Gaussian input pulses under the influence of a fiber-induced group delay dispersion (Sect. 7.2.1).
- Truncation of cross-correlation function was taken into account. Equations for the ensuing improvement of TPI visibilities and decline in the coincidence count rate were given (Sect. 7.2.1).
- Equations were used to model the simultaneous impact of attenuation and dispersion on the entanglement generation rate in a single quantum repeater network. Different fiber lengths, network asymmetries, and pulse durations of single photons were taken into account (Sect. 7.2.2).
- Dispersion at the telecom C-band in asymmetric networks causes partial indistinguishability - for high entanglement fidelity, coincidences need to be truncated. This is a loss channel that does not exist in the O-band. Therefore, the O-band leads to better entanglement rates for high asymmetries and short pulses (Sect. 7.2.2).
- For current emitter systems with lifetimes > 100 ps the effect is negligible, as dispersion is small. For photons from emitters strongly coupled to a microcavity as well as SPDC sources with short and ultrashort pulse durations, the O-band leads to a significant improvement of the entanglement rate (Sect. 7.2.2).

Summary and Conclusion

Throughout the course of this thesis we experimentally investigated quantum frequency conversion (QFC) as tool to transfer indistinguishable photons emitted by InAs semiconductor quantum dots (QD) from the near infrared region to the telecom C-band. The indistinguishability of unconverted and converted photons has been assessed in two-photon interference (TPI) experiments after Hong-Ou-Mandel (HOM) in two distinct settings: **(i)** with photons consecutively emitted by one QD and **(ii)** with photons from two remote QDs and independent frequency converters. Additionally, we established a theoretical framework to describe the interference pattern and attainable TPI visibilities of HOM experiments using non-Fourier-limited photons. The obtained equations were used to consistently explain all experimental results.

The theoretical part of this work was motivated by the lack of an analytical description of HOM experiments, which appropriately covers all spectral features of the photons under consideration. On that account, we applied a well-established formalism [218] assuming two independent two-level emitters, which are subject to both pure dephasing (PD) and spectral diffusion (SD) causing homogeneous and inhomogeneous line broadening, respectively. We moreover allowed the emitters to exhibit differing radiative lifetimes and to be spectrally detuned with respect to each other. Possible phonon-sidebands were not taken into account, as those are typically removed via spectral filtering in experiment. The impact of phonon-sidebands is for instance covered in [183, 312, 313]. The resulting equations yield the temporal structure of cross-correlation measurements taken during a HOM experiment, but also the overall coincidence probabilities and corresponding interference visibility can be computed. The latter follows a Voigt profile as a function of the detuning, whose shape is determined by the joint spectral properties of both emitters. The obtained model was found to agree with existing theories in the limit of independent emitters, which are only subject to PD [152, 196]. Furthermore, the model was verified by comparing its predictions to various HOM experiments with remote solid-state emitters. As our results for the first time

consider the simultaneous impact of PD and SD on indistinguishability, it was possible to put a longstanding notion to the test: in [196] it was shown that optical coherence time and photon indistinguishability are in a fixed relation, if both emitters are only affected by PD. Here, we realized that it is not possible to unambiguously assign a given coherence time to an indistinguishability, if additional SD comes into play. We moreover extended our formalism in two different ways:

- (i) The equations were generalized to describe the scattering of two photons at an arbitrary linear optical gate instead of only a single symmetric beam splitter. This allows to predict the performance of a given set of emitters in more involved schemes based on the results of simple HOM experiments. As an example of intermediate complexity we theoretically discussed the entanglement of two partially indistinguishable photons with help of an all-optical CNOT gate [147]. In this context we could show that state-of-the-art solid-state emitters yield only mediocre entanglement fidelities, typically well below 90 %, if no further spectral or temporal filtering is applied.
- (ii) Eventually, we relaxed the assumption of independent emitters and considered photons consecutively emitted by the same source. In this case both photons are spectrally correlated, if the time delay between the respective emission events τ_{mzi} is less or in the order of the memory depth of SD τ_{sd} . We found that for $\tau_{mzi} \ll \tau_{sd}$ the visibility is dominated by PD, while it converges towards the limit of independent photons for $\tau_{mzi} \gg \tau_{sd}$. Our result qualitatively agrees with a model presented in [192], but is based on a more appropriate description of SD.

At the heart of all experiments was the quantum frequency conversion transducing single photons with a wavelength of around 905 nm to the telecom C-band at 1557 nm. The conversion was realized based on difference frequency generation supported by a periodically poled lithium niobate crystal, shaped into ridge waveguides. The process has an estimated acceptance bandwidth of 120 GHz for the near infrared photons while the target wavelength can be tuned over the entire telecom C-band by changing the crystal temperature. Efficient conversion moreover requires an intense pump light source with an output wavelength of around 2.2 μm . For that purpose we employed a commercial single frequency $\text{Cr}^{2+}:\text{ZnS}$ laser in cw operation, which delivers optical output powers of $>1.5\text{ W}$ over the entire available tuning range from 2.1 μm to 2.3 μm . Throughout all experiments our converters achieved overall device efficiencies exceeding 30 % at optical pump powers of a few 100 mW. Main loss channels were the limited internal conversion efficiency ($\approx 90\%$), coupling efficiencies to the waveguide chip and telecom fiber (each $\approx 80\%$), as well as the transmission of the employed fiber Bragg-grating (FBG) at the telecom regime ($\approx 60\%$). A significantly improved device efficiencies of almost 60 %

has recently been reported in [114]. This value could be achieved mainly owing to a low-loss volume Bragg-grating, which has been used instead of a FBG to remove conversion noise from the converted telecom photons.

In the first experiment, we considered single photons consecutively emitted by an InAs QD. The QD was operated in a confocal microscope at a cryogenic temperature of 10 K and optically addressed via p -shell excitation at a repetition rate of 80 MHz. The emitted photons had a center wavelength of 903.6 nm, a radiative lifetime of 970 ps, and a coherence time of 87 ps. The latter was limited due PD at a rate of 47 MHz as well as SD corresponding to an inhomogeneous linewidth of 5.9 GHz. In an intensity auto-correlation measurement a detector dark-count corrected antibunching value of $g_{\text{nir}}^{(2)}(0)=0.153$ was observed, which was mainly limited due to background photons leaking through the etalon employed for spectral filtering. This is in a quantitative agreement with the signal-to-background ratio (SBR) of 11.5 extracted from the emission spectra. To arrive at the desired target wavelength of 1557 nm, the converter was set to a pump wavelength of 2154 nm. At this operating point a maximum conversion efficiency of 30.9 % was achieved. Radiative lifetime and coherence time of the converted photons are in good agreement with the corresponding near infrared values. The antibunching value improved to $g_{\text{tel}}^{(2)}(0)=0.117$, which can be attributed to the small acceptance bandwidth of the conversion and subsequent filtering entailing a SBR of 17.2. The HOM experiment was conducted after a design first reported in [230], in which two consecutively emitted photons are overlapped on the output beam splitter of a Mach-Zehnder interferometer. Corresponding to the interferometer imbalance, the photons exhibited emission time delays of around 4 ns and 8 ns for the experiments with unconverted and converted photons, respectively. The HOM measurements revealed two-photon interference visibilities (TPI) of 36.4 % at the near infrared and 24.1 % at the telecom regime. The loss of interference visibility directly stems from the increased emission time delay between both experiments, as it is accompanied by a loss of frequency correlation between the photons due to SD. The respective memory depth of SD was found to be 230 ns, which compares well to values reported in literature [192–195]. All intensity correlation measurements, i.e. the antibunching and HOM experiments, were additionally reproduced by Monte-Carlo simulations based on independently measured model parameters, while only the TPI visibility was treated as free parameter. The good agreement of measurement and simulation show that all relevant aspects of the experiment are well understood. The main goal of this experiment was to show that down-conversion does not affect the indistinguishability of photons. Although this was strictly speaking not achieved, the discrepancy between unconverted and converted photons could be conclusively attributed to the change in the interferometer design. Accordingly a loss of indistinguishability due to the QFC step was not observed.

The second experiment was aimed at TPI between photons from remote

quantum emitters. On this account, two InAs QD samples were placed in distinct cryostats at temperatures of 4 K. To achieve superior indistinguishabilities the QDs were driven via s -shell excitation at a clock rate of 76 MHz and by adding weak, non-resonant cw laser light [131,132]. The resonant excitation light was mostly removed by use of a polarization rejection setup [130,177] and subsequent spectral filtering, which resulted in a SBR of 26. However, the polarization suppression required to resort to charged QDs, which do not exhibit any fine-structure splitting. Both chosen QDs exhibited an emission wavelength of around 904.4 nm, but with a relative detuning of 8.06 GHz. The measured radiative lifetimes of 612 ps and 584 ps correspond to natural linewidths of 260 MHz and 273 MHz, respectively, which were inhomogeneously broadened by 2.10 GHz and 1.22 GHz. Accordingly, the emission spectra are well separated and both unconverted photons therefore entirely distinguishable. The antibunching values of both emitters were determined to be 0.10 ± 0.03 and 0.00 ± 0.03 , which were only limited by excitation light leaking through the polarization suppression. The photons of both QDs were shifted to the telecom C-band in two identical but independent frequency converters with device efficiencies of 35 % and 31 %, leading to detected count rates of 5.3 kHz and 24.7 kHz. Of these, around 550 Hz and 390 Hz can be attributed to pump light induced converter noise, corresponding to SBRs of 8.7 and 62.2. Eventually, the converted telecom photons of both emitters were set to overall 10 distinct relative detunings around the target wavelength of 1557 nm. At each detuning a separate HOM measurement was performed and the visibility extracted. For zero detuning a maximum interference contrast of $(29 \pm 3) \%$ was observed. An independent measurement performed with unconverted photons of the same emitter pair yielded a TPI visibility of $(26 \pm 3) \%$ using temperature tuning, which confirms our findings. Note that this experiment was not part of the present thesis, but reported in [272]. Moreover, the measured visibility-over-detuning curve was reproduced using the known emitter parameters as input for our theoretical model. Both measured and model curve are in excellent agreement. The fact that the measurements with unconverted and converted photons yield the same visibility, which moreover can be consistently explained based on the spectral properties of both emitters, suggests that QFC has no negative impact on the mutual indistinguishability of independent single photons. Additionally, our results demonstrate that QFC can be exploited as tuning mechanism to recover spectral indistinguishabilities, which is an interesting option to common schemes for two reasons: **(i)** it is noninvasive in contrast to mechanisms directly acting on the emitter and **(ii)** it reduces the necessary technical overhead in experimental schemes that include QFC anyway.

In conclusion, the experimental results presented in this thesis demonstrate that quantum frequency down-conversion conserves photon indistinguishabilities. As such they provide the missing link in the set of mandatory experiments, which prove that QFC preserves all relevant single photon

properties. Owing to the high device efficiencies and low process-induced noise, frequency converters are not only interesting for academic proof-of-principle experiments, but constitute a serious option for a variety of applications. A big step towards this direction has been taken in a recent experiment demonstrating for the first time a complete quantum repeater segment on a metropolitan fiber network scale made possible by QFC [115]. The experiment uses both single- and two-photon interference following the protocols presented in [32] and [37], respectively, to establish entanglement between two remote Rb ensembles. In particular the latter exploits the preservation of both indistinguishability and matter-photon entanglement [96] during the down-conversion step towards the telecom O-band. Future tasks to refine this scheme might include transferring the photons to the C-band instead and employ polarization-insensitive QFC [114], which will render the transformation of polarization to time-bin encoding performed in [115] unnecessary. A more direct derivation of the present work would be to combine the best available InAs QDs with our frequency converters to obtain a bright source of indistinguishable telecom photons. The emitter employed for a boson sampling experiment in [195], for instance, yielded a detected count rate of 6.5 MHz at a clock rate of 76 MHz. Taking into account the detector system efficiency, this corresponds to a flux of more than 25×10^6 photons per second available at the output of a single mode fiber. Converting these photons with a device efficiency of $\approx 30\%$ as reported in this work would lead to about 7.5×10^6 telecom C-band photons per second that moreover sustain an indistinguishability of $>90\%$ for consecutive emission with a time separation of up to 14 μs - an unparalleled performance compared to available telecom photon emitting quantum dots [88,89]. A different application directly aimed at QKD is to implement QFC in a quantum relay network, which uses polarization-entangled photon pairs. The device presented in [145], for instance, shares entangled photons emitted by an electrically driven InAs QD between a Bell-state measurement station and a receiver. A frequency converter used to shift these photons to the telecom C-band, would need to preserve the photon-photon entanglement, indistinguishability, as well as the polarization encoding. For the latter our devices must be modified to a polarization-insensitive scheme, which approximately reduces the conversion efficiency to 25%. Due to the conversion losses, the overall scheme would not benefit from QFC for optical fibers as short as 350 m, which have been used in [145]. For transmission distances exceeding 2 km, however, the conversion would result in an exponential net gain of the coincidence rate.

As past and ongoing research efforts clearly show, QFC has matured into a versatile tool for quantum technologies, which is regularly integrated into experiments of increasing complexity. At the current stage it offers the most direct and advanced route to release quantum communication from its confinement to lab scale experiments. Therefore, it may be expected that QFC continues its streak of success for the foreseeable future.

Appendices

A Eigenvalue Equations for Rectangular Waveguide Modes

The following equations are taken from [211]. Their solution yields the transversal wavenumbers κ_x and κ_y as well as the mode displacements ξ and η as used in Sect. 2.3.2 and Sect. 4.2. The refractive indices n_i correspond to the respective regions illustrated in Fig. 2.11, d and b are the waveguide dimensions, and k is the vacuum wavenumber of the considered light field. The overall procedure starts from the transcendental equations

$$\tan \kappa_x d = n_1^2 \kappa_x \cdot \frac{n_3^2 \gamma_2 + n_2^2 \gamma_3}{n_3^2 n_2^2 \kappa_x^2 - n_1^4 \gamma_2 \gamma_3} \quad (\text{A.1})$$

$$\tan \kappa_y b = \frac{\kappa_y (\gamma_4 + \gamma_5)}{\kappa_y^2 - \gamma_4 \gamma_5} \quad (\text{A.2})$$

with all γ_i defined by

$$\gamma_2^2 = (n_1^2 - n_2^2) k^2 - \kappa_x^2, \quad (\text{A.3})$$

$$\gamma_3^2 = (n_1^2 - n_3^2) k^2 - \kappa_x^2, \quad (\text{A.4})$$

$$\gamma_4^2 = (n_1^2 - n_4^2) k^2 - \kappa_y^2, \quad \text{and} \quad (\text{A.5})$$

$$\gamma_5^2 = (n_1^2 - n_5^2) k^2 - \kappa_y^2. \quad (\text{A.6})$$

Eq. (A.1) and (A.2) are solved to obtain κ_x and κ_y . These are then used to evaluate ξ and η by solving

$$\tan \kappa_x \xi = -\frac{n_3^2 \kappa_x}{n_1^2 \gamma_3} \quad \text{and} \quad (\text{A.7})$$

$$\tan \kappa_y \eta = -\frac{\gamma_5}{\kappa_y}. \quad (\text{A.8})$$

B Adapted Sellmeier Coefficients for Lithium Niobate

The refractive index of lithium niobate in Sect. 4.2 as function of wavelength λ and temperature T was calculated based on modified Sellmeier-coefficients taken from [212]. The underlying Sellmeier-equation reads

$$n(\lambda, T) = n_0(\lambda) + \Delta n(\lambda, T) \quad (\text{B.1})$$

with the refractive index $n_0(\lambda)$ at $T_0 = 20^\circ\text{C}$ and a temperature dependent correction $\Delta n(\lambda, T)$ given by

$$n_0(\lambda) = \sqrt{a + \frac{b}{\lambda^2 - c} - d\lambda^2} \quad \text{and} \quad (\text{B.2})$$

$$\Delta n(\lambda, T) = \left(\frac{\alpha}{\lambda^3} - \frac{\beta}{\lambda^2} + \frac{\gamma}{\lambda} + \delta - \varepsilon\lambda \right) \cdot (\Delta T + \zeta\Delta T^2) \times 10^{-5} \quad (\text{B.3})$$

with $\Delta T = T - T_0$. Both original parameters found in [212] and the fitted parameters used in Sect. 4.2 are summarized in Tab. B.1. Note that in particular the modification of a and ζ are responsible for the good agreement between measured and simulated tuning curves in Sect. 4.2.

Table B.1. Summary of Sellmeier-coefficients. Unmodified parameters from [212] and fitted parameters from this work as used in Eq. (B.2) and (B.3). The parameters hold for wavelengths given in μm and temperatures in $^\circ\text{C}$.

	[212]	this work		[212]	this work
a	4.54514	4.55849	α	0.4175	0.4175
b	0.096471	0.097819	β	0.6643	0.6643
c	0.043763	0.042794	γ	0.9036	0.9036
d	0.021502	0.021589	δ	3.5332	3.5332
			ε	0.0744	0.0744
			ζ	0.00138	0.00498

C Continuous Noise Floor in Intensity Correlations

We here briefly derive Eq. (5.6) used in Sect. 5.2.4, which yields the number of coincidences per bin in an intensity correlation function $g^{(2)}(\tau)$ with timelag τ stemming from a continuous noise source, which is uncorrelated with the

actual signal. For two measured intensities $I_1(t)$ and $I_2(t)$ as function of time t , the correlation is generally defined as

$$g^{(2)}(\tau) = \langle I_1(t) \cdot I_2(t + \tau) \rangle, \quad (\text{C.1})$$

where $\langle \bullet \rangle$ denotes the integration with respect to t . It is possible to write both intensities as a sum of the signal $s_i(t)$ we are actually interested in and a noise contribution $r_i(t)$. The correlation function can be divided in a signal and noise part as well according to

$$g^{(2)}(\tau) = g_s^{(2)}(\tau) + g_r^{(2)}(\tau) \quad \text{with} \quad (\text{C.2})$$

$$g_s^{(2)}(\tau) = \langle s_1(t) \cdot s_2(t + \tau) \rangle \quad \text{and} \quad (\text{C.3})$$

$$g_r^{(2)}(\tau) = \langle r_1(t) \cdot r_2(t + \tau) \rangle + \langle r_1(t) \cdot s_2(t + \tau) \rangle + \langle r_2(t) \cdot s_1(t + \tau) \rangle. \quad (\text{C.4})$$

Note that the terms in the second line of Eq. (C.4) contribute to the noise part of the correlation although they contain the signals $s_1(t)$ and $s_2(t)$. The correlation with $r_i(t)$, however, deletes any information on the temporal pattern of $s_2(t)$ and it appears as uncorrelated. For this reason it is also valid to model both signal and noise part as rectangular functions following

$$x_i(t) = \begin{cases} X_i & \text{for } -T/2 \leq t \leq T/2 \\ 0 & \text{otherwise} \end{cases} \quad (\text{C.5})$$

even though $s_i(t)$ might in fact be a pulsed signal. Here T is the duration of the overall measurement and $x_i(t)$ as well as X_i correspond to either $s_i(t)$ or $r_i(t)$ with an average rate of S_i or R_i . A correlation of two rectangular functions as given in Eq. (C.4) generally yields a triangular function. However, we are typically only interested in a region around $\tau = 0$, which is small compared to T . In this case the correlation reduces to

$$g_r^{(2)}(\tau) \approx \langle r_1(t) \cdot r_2(t) \rangle + \langle r_1(t) \cdot s_2(t) \rangle + \langle r_2(t) \cdot s_1(t) \rangle = (R_1 R_2 + R_1 S_1 + R_2 S_1) \cdot T. \quad (\text{C.6})$$

This result equals a noise rate for the correlation function. To obtain the number of noise counts N_r within a bin of width $\Delta\tau$, $g_r^{(2)}(\tau)$ needs to be integrated according to

$$N_r = \int_{\tau'}^{\tau'+\Delta\tau} g_r^{(2)}(\tau) d\tau = (R_1 R_2 + R_1 S_1 + R_2 S_1) \cdot T \Delta\tau \quad (\text{C.7})$$

In Sect. 5.2.4 we assume that the only continuous noise source are the detector dark counts, which exhibit equal rates ν_{dc} for both detectors. Accordingly, we set $N_r \rightarrow N_{\text{dc}}$ and $R_1 = R_2 = \nu_{\text{dc}}$. Moreover, using the overall detected count rates $\nu_{\text{det}} = S_1 + \nu_{\text{dc}} = S_2 + \nu_{\text{dc}}$ we obtain

$$N_{\text{dc}} = (2\nu_{\text{det}} - \nu_{\text{dc}}) \cdot \nu_{\text{dc}} T \Delta\tau, \quad (\text{C.8})$$

which corresponds to Eq. (5.6) in the main text.

D Monte Carlo Simulations

All antibunching and HOM measurements presented in Chap. 5 were reproduced using Monte Carlo simulations performed with MATLAB R2016a. In the following we offer the employed scripts. For better performance, the overall simulation is divided into a number of runs, each of which contains several of excitation cycles. For each run, click lists are generated and subsequently correlated. Accordingly, the script can be written in a simplified manner as

```

<initial definitions>
for m = 1:runs % iterate through all runs
    <get click lists>
    <correlate click lists>
    <build histogram>
end
<sum histograms over all runs>

```

Antibunching Measurement Simulations

The *<initial definitions>* span various setup and emitter parameters as specified in the main text as well as settings for the simulation itself. In the following we give the parameters as used for the unconverted antibunching measurement. The respective parameters for the other simulations can be found in the main text:

```

1 % all times and frequencies in s and Hz, resp.
2 %% experimental parameters
3 T      = 12.47e-9;    % repetition time
4 FWHM   = 350e-12;   % detector jitter
5 sigma  = FWHM/2.355; % fwhm to standard deviation
6 CR     = 28290;     % average count rate per detector
7 NR     = 300;       % dark count rate
8 R      = 0.5;      % refl. of HBT beam splitter
9 tau    = 0.969e-9; % radiative lifetime
10 SBR   = 11.5;     % SBR from spectrum
11
12 %% simulation parameters
13 BS     = 200e-12;   % binsize of histogram
14 range  = 40e-9;    % plorange of histogram
15 SF     = 1.3;      % plorange stretch factor
16 bins   = ceil(SF*(range/BS)); % number of bins
17 centers = BS*(-bins:bins); % bin centers
18 NoC    = 1e5;     % cycles per run (one photon / cycle)
19 runs   = 50;      % number of runs

```

```

20 |
21 | %% derived parameters
22 | % probability a detected photons stems from the...
23 | pQD      = SBR/(SBR+1); % ... quantum dot
24 | pBG      = 1-pQD;      % ... background
25 | % noise and background probabilities
26 | % normalized to one emitter photon
27 | QDrate   = 2*(CR-NR)*pQD; % detected counts from QD
28 | pnoise   = NR/QDrate;   % noise probability
29 | pBG      = pBG/pQD;    % background probability
30 |
31 | %% cumulative distributions
32 | % CDF: detection times of N photons
33 | tdet = @(N) -tau*log(1-rand(N,1));

```

Note the function `tdet` defined in line 33. It yields random detection times t_{det} with respect to an excitation pulse and is obtained applying the method of inverse transform sampling [265], which generates random numbers of a desired probability distribution from a uniformly distributed random number x . On that account one has to first calculate the cumulative distribution function (CDF) via

$$P(t_{\text{det}}) = \frac{1}{\tau} \int_0^{t_{\text{det}}} e^{-t/\tau} dt = 1 - e^{-t/\tau}. \quad (\text{D.1})$$

The desired random t_{det} is then obtained by the inverse of $P(t_{\text{det}}) = x$, which yields

$$t_{\text{det}} = -\tau \ln(1 - x) \quad (\text{D.2})$$

and has already been stated in Eq. (5.9).

The *(get click lists)* part within the `for`-loop, generates the detection events for background and fluorescence photons as well as detector noise:

```

1 | %% Generate events of current run
2 | % the following lists for both detectors
3 | % save real detection events and noise
4 | list1 = [];
5 | list2 = [];
6 |
7 | for k = 1:NoC
8 |     % N = number of real photons
9 |     % Poisson distribution for background photons
10 |     % 'plus one' for fluorescence photon
11 |     N = poissrnd(pBG) + 1;

```

```

12
13     % detection times:
14     photons = T*k+tau*log(1./(tau*rand(N,1)));
15     % add detector jitter
16     photons = photons+normrnd(0,sigma,N,1);
17
18     % distribute photons to both detectors
19     % number of reflected photons:
20     nrefl = sum(rand(N,1)<0.5);
21     events1 = photons(1:nrefl);
22     events2 = photons(nrefl+1:end);
23
24     % Poisson distributed number of noise events
25     % uniformly distributed over one cycle
26     noise1 = T*(k+rand(poissrnd(pnoise),1));
27     noise2 = T*(k+rand(poissrnd(pnoise),1));
28
29     % add the noise to the rest
30     events1(end+1:end+length(noise1)) = noise1;
31     events2(end+1:end+length(noise2)) = noise2;
32
33     % sort for correct temporal order
34     list1(end+1:end+length(events1)) = sort(events1);
35     list2(end+1:end+length(events2)) = sort(events2);
36 end

```

The *<correlate click lists>*- and the *<build histogram>*-parts are contained in the following two code snippets. For better performance not all timelags are evaluated, but only those which are within the region of $\pm SF \cdot \text{range}$.

```

1 %% Evaluate correlation for this run
2 timelag = [];
3 for k = 1:length(list1)
4     [~,j] = min(abs(list1(k)-SF*range-list2));
5     while true
6         timelag(end+1) = list1(k)-list2(j);
7         j = j+1;
8         if j>length(list2)||timelag(end)<-SF*range
9             break
10        end
11    end
12 end

```

```

1 %% Evaluate the histogram and save the current run
2 timelag(abs(timelag) > SF * range) = [];
3 counts = hist(timelag,centers);
4 coincidences(m,1:length(counts)) = counts;

```

The overall histogram is generated by in the *(sum histograms over all runs)*-segment, which simply reads `coincidences = sum(coincidences);`. It can be plotted against the timelags contained in the variable `centers`.

HOM Measurement Simulations

The overall structure of the simulations of HOM measurements is identical to that of antibunching measurements. To account for the additional beam splitter decision in the emission MZI as well as the temporal pattern of the central peak including TPI some changes in the parts *(initial definitions)* and *(get click lists)* are necessary. The initial definitions (for unconverted photons) now read

```

1 %% experimental parameters
2 % all times and frequencies in s and Hz, resp.
3 T      = 12.47e-9;    % repetition time
4 FWHM   = 350e-12;    % detector jitter
5 sigma  = FWHM/2.355; % fwhm to standard deviation
6 delay  = 3.978e-9;   % Mach-Zehnder delay
7 CR     = 19370;      % average count rate per detector
8 NR     = 300;        % dark count rate
9 R      = 0.5;        % refl. of beam splitter
10 tau    = 0.969e-9;   % radiative lifetime
11 SBR    = 11.5;      % SBR from spectrum
12 inh    = 687e6;     % inhom. linewidth (sigma')
13 hom    = 47e6;      % hom. linewidth (Gamma*)
14 dnu    = 0;         % emitter detuning (delta nu)
15 b      = [ tau inh hom tau inh hom dnu ];
16
17 %% simulation parameters
18 BS     = 20e-12;    % binsize of histogram
19 range  = 40e-9;    % plotrange of histogram
20 SF     = 1.3;      % plotrange stretch factor
21 bins   = ceil(SF*(range/BS)); % number of bins
22 centers = BS*(-bins:bins); % bin centers
23 NoC    = 5e4;     % cycles per run (one photon / cycle)
24 runs   = 10;      % number of runs
25

```

```

26 %% derived parameters
27 % probability a detected photons stems from the...
28 pQD      = SBR/(SBR+1); % ... quantum dot
29 pBG      = 1-pQD;      % ... background
30 % noise and background probabilities
31 % normalized to one emitter photon
32 QDrate   = 2*(CR-NR)*pQD; % detected counts from QD
33 pnoise   = NR/QDrate;    % noise probability
34 pBG      = pBG/pQD;     % background probability
35
36 %% cumulative distributions
37 % CDF: two photons scattering at a BS
38 MZ = [ ...
39       R^2;...           % both reflected
40       (1-R)^2;...      % both transmitted
41       R*(1-R);...     % late refl., early trans.
42       R*(1-R)];       % early refl., late trans.
43 MZcum = cumsum(MZ); % CDF
44
45 % CDF: central peak with TPI
46 trel    = 0.01*BS*(-50:50)'; % timelag within a bin
47 g2      = mean(TPIg2(b,trel+centers)); % g2 with TPI
48 CDFtpi  = cumsum(g2)*BS;    % CDF
49
50 % CDF: coincidence or no coincidence
51 HOMcum  = [... % photons...
52          CDFtpi(end)...     % ... cause coincidence
53          0.5*(1+CDFtpi(end))... % ... bunch towards det. 1
54          1];                % ... bunch towards det. 2
55 CDFtpi  = CDFtpi/CDFtpi(end); % normalize g2 CDF
56
57 % CDF: detection times of N photons
58 tdet    = @(N) -tau*log(1-rand(N,1));

```

Note that we once more define various CDFs, which are later used to generate appropriate random numbers with inverse transform sampling:

- (i) lines 37-43: the discrete distribution `MZcum` to model the scattering of two consecutive photons at a single beam splitter.
- (ii) lines 45-48 + line 55: `CDFtpi` as CDF of the cross-correlation function Eq. (3.26) (evaluated in line 47 by function `TPIg2`), which here assumes two identical emitters defined by the parameters contained in vector `b`.

- (iii) lines 50-54: the discrete distribution `HOMcum`, which handles the case that two photons simultaneously arrive at the HOM BS. `HOMcum` is used to decide, whether the photons cause a coincidence or bunch.
- (iv) line 58: inverse CDF to determine single photon detection times (see antibunching measurement simulations).

Based on these definitions the *get click lists* part is given by

```

1  for k = 1:NoC
2  % clicks of current circle
3  events1 = [];
4  events2 = [];
5
6  %% background photons
7  bg1 = tdet(poissrnd(pBG)); % in early pulse
8  bg2 = delay+tdet(poissrnd(pBG)); % in late pulse
9  bg = [ bg1 ; bg2];
10
11 for l = 1:length(bg) % add background
12     if rand < R      % first beam splitter
13         if rand < R % second beam splitter
14             events1(end+1) = bg(l)+delay;
15         else
16             events2(end+1) = bg(l)+delay;
17         end
18     else
19         if rand < R
20             events2(end+1) = bg(l);
21         else
22             events1(end+1) = bg(l);
23         end
24     end
25 end
26
27 %% Both QD photons
28 t1      = tdet(1);           % early photon
29 t2      = tdet(1)+delay;    % late photon
30 [~,I1] = max((rand < MZcum)); % decision first BS
31 [~,I2] = max((rand < MZcum)); % decision second BS
32 switch I1
33     case 1 % BS 1: both refl.
34         switch I2
35             case 1 % BS 2: both refl.
36                 events1(end+1) = t1+delay;

```

```
37         events1(end+1) = t2+delay;
38     case 2 % BS 2: both trans.
39         events2(end+1) = t1+delay;
40         events2(end+1) = t2+delay;
41     case 3 % BS 2: late refl., early trans.
42         events2(end+1) = t1+delay;
43         events1(end+1) = t2+delay;
44     case 4 % BS 2: late trans., early refl.
45         events1(end+1) = t1+delay;
46         events2(end+1) = t2+delay;
47     end
48 case 2 % BS 1: both trans.
49     switch I2
50     case 1 % BS 2: both refl.
51         events2(end+1) = t1;
52         events2(end+1) = t2;
53     case 2 % BS 2: both trans.
54         events1(end+1) = t1;
55         events1(end+1) = t2;
56     case 3 % BS 2: late refl., early trans.
57         events1(end+1) = t1;
58         events2(end+1) = t2;
59     case 4 % BS 2: late trans., early refl.
60         events2(end+1) = t1;
61         events1(end+1) = t2;
62     end
63 case 3 % BS 1: late refl., early trans.
64     switch I2
65     case 1 % BS 2: both refl.
66         events2(end+1) = t1;
67         events1(end+1) = t2+delay;
68     case 2 % BS 2: both trans.
69         events1(end+1) = t1;
70         events2(end+1) = t2+delay;
71     case 3 % BS 2: late refl., early trans.
72         events1(end+1) = t1;
73         events1(end+1) = t2+delay;
74     case 4 % BS 2: late trans., early refl.
75         events2(end+1) = t1;
76         events2(end+1) = t2+delay;
77     end
78 % BS 1: late trans., early refl. (HOM possible)
79 case 4
80     [~,I] = max((rand<HOMcum));
```

```

81     switch I
82         case 1 % BS 2: both refl. or trans.
83             % (no coalescence)
84             [~,I] = max((rand<CDFtpi));
85             events1(end+1) = t1+delay;
86             events2(end+1) = t1+centers(I)+delay;
87         case 2 % BS 2: late refl., early trans.
88             events1(end+1) = t1+delay;
89             events1(end+1) = t2;
90         case 3 % BS 2: late trans., early refl.
91             events2(end+1) = t1+delay;
92             events2(end+1) = t2;
93     end
94 end
95
96 % add jitter to all detection events
97 events1 = events1+normrnd(0,sigma,size(events1));
98 events2 = events2+normrnd(0,sigma,size(events2));
99
100 % Poisson distributed number of noise events
101 % uniformly distributed over one cycle
102 noise1 = T*rand(poissrnd(pnoise),1);
103 noise2 = T*rand(poissrnd(pnoise),1);
104
105 % add the noise to the rest
106 events1(end+1:end+length(noise1)) = noise1;
107 events2(end+1:end+length(noise2)) = noise2;
108
109 % sort for correct temporal order
110 list1(end+1:end+length(events1)) = T*k+sort(events1);
111 list2(end+1:end+length(events2)) = T*k+sort(events2);
112 end

```

As the distribution of photons to both detectors depends on the scattering events at both beam splitters and the possibility of TPI requires to simultaneously treat both photons of a single cycle, there is no concise way to model these events, which is comprehensible at the same time. Therefore, we decided to implement the simulation with the rather bulky sequence of nested `switch`-structures given above. Note that the first beam splitter of the emission MZI is modeled by the outer `switch`-statement, the second beam splitter by the inner one. We like to draw attention to `case 4` (lines 79-93) of the outer switch statement. It corresponds to the early and late photon being reflected and transmitted, respectively, and thereby leads to both photons meeting at the output beam splitter. In other words, TPI is possible. In line 80 the CDF

HOMcum is used to decide whether both photons coalesce (**case 2** and **case 3**), or not (**case 1**). In the latter case, the photons must be distributed according to the cross-correlation function Eq. (3.26). This is realized by evaluating a detection time delay `centers(I)` used in line 86, which is determined using the CDF of Eq. (3.26) called `CDFtpi` (line 84). Note that `centers(I)` can be both negative and positive and thereby covers both sides of the central correlation peak.

E Fitting Model for HOM Measurements

The HOM measurements presented in Sect. 6.3.4 were analyzed by first integrating each individual peak and then fitting the obtained peak areas with a model, which beside TPI also incorporates bunching due to emitter blinking and asymmetric beam splitters (BS). In the following, we elaborate on the applied procedure.

First, in order to find the areas F_i of all peaks from the experimental data shown in Fig. 6.12 (a) and (b), we divide the cross-correlation measurements into segments of width $\tau_{\text{mzi}} = 4.37$ ns corresponding to the Mach-Zehnder interferometer (MZI) delay. The segments are centered around each peak, i.e. $0, \pm\tau_{\text{mzi}}, \pm2\tau_{\text{mzi}}, \dots$ corresponding to the indices $i = 0, \pm1, \pm2, \dots$. Assuming each peak to be a two-sided exponential decay, we expect that around $\exp[-\tau_{\text{mzi}}/(2\tau_r)] \approx 3\%$ of the overall peak areas lie outside their respective segment leading to a systematic error. The integrated areas \tilde{F}_n of the n 'th peak can be written as

$$\tilde{F}_i = \tau_{\text{mzi}} \int_{i-\frac{1}{2}}^{i+\frac{1}{2}} \left[D + \frac{F_{i-1}}{2\tau_r} e^{-\frac{|x-(i-1)|}{e}} + \frac{F_i}{2\tau_r} e^{-\frac{|x-i|}{e}} + \frac{F_{i+1}}{2\tau_r} e^{-\frac{|x-(i+1)|}{e}} \right] dx \quad (\text{E.1})$$

with D being a constant background from sources like detector or conversion noise that can be approximated averaging the cross-correlation height in between each peak at $\pm\tau_{\text{mzi}}/2, \pm3\tau_{\text{mzi}}/2, \dots$. The parameters $\varrho = \tau_r/\tau_{\text{mzi}}$ and $x = \tau/\tau_{\text{mzi}}$ constitute normalized radiative lifetime and timelag, respectively. Computing the integral results in

$$\tilde{F}_i = D\tau_{\text{mzi}} + \alpha F_{i-1} + \beta F_i + \alpha F_{i+1} \quad (\text{E.2})$$

with $\alpha = \exp[-\tau_{\text{mzi}}/(2\tau_r)]/2$ and $\beta = (1 - 2\alpha)$. If the peaks $-N$ to N were integrated, Eq. (E.2) defines a set $2N+1$ inhomogeneous linear equations that

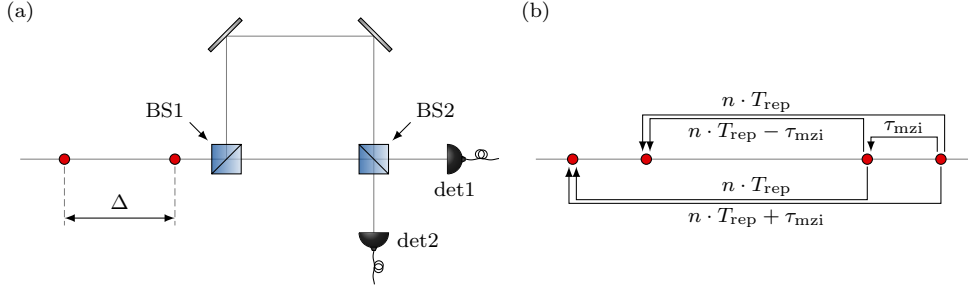


Figure E.1. Illustration of a sequence of photons used for a Hong-Ou-Mandel experiment. (a) Two photons, an early and a late photon, enter a Mach-Zehnder interferometer with a time delay of Δ . They are transmitted or reflected at two beamsplitters (BS1 and BS2) and eventually detected. (b) Four photons in two double pulses. For two photons of one double pulse, there is only one combination of early and late photon. For two distinct double pulses, on the other hand, there are overall four possible combinations.

can be written as

$$\begin{pmatrix} \beta & \alpha & 0 & \dots & 0 \\ \alpha & \beta & 0 & \dots & 0 \\ 0 & 0 & \alpha & \dots & 0 \\ \vdots & \vdots & \vdots & \ddots & \vdots \\ 0 & \dots & 0 & \alpha & \beta \end{pmatrix} \times \begin{pmatrix} F_{-N} \\ \vdots \\ F_0 \\ \vdots \\ F_N \end{pmatrix} = \begin{pmatrix} \tilde{F}_{-N} - D\tau_{mzi} \\ \vdots \\ \tilde{F}_0 - D\tau_{mzi} \\ \vdots \\ \tilde{F}_N - D\tau_{mzi} \end{pmatrix}. \quad (\text{E.3})$$

Solving the system yields the desired F_i , which are plotted in Fig. 6.12 (c) and (d) as black dots. Note that this correction does not account for the contribution of the peaks at $\pm(N+1)\tau_{mzi}$ as well as detector jitter.

To obtain a fitting model for all F_i we need to understand the history of each photon that contributes to the cross-correlation measurement in more detail. On that account we recapitulate the explanation given in Sect. 5.3.1, but in a more general manner: we consider two photons entering a MZI with a time delay Δ [Fig. E.1 (a)]. At two consecutive beam splitters BS1 and BS2 they are either reflected or transmitted and subsequently detected by detector 1 or 2 (det1 or det2) at a time t_{det} . For simplicity, we assume that both BSs are identical but asymmetric, i.e. for reflectivity and transmission we find $R \neq T$. There are overall 16 possibilities, of which only 8 yield a coincidence at a timelag of $\tau = t_{\text{det1}} - t_{\text{det2}}$ with t_{det1} and t_{det2} being the recorded detection times at det1 and det2, respectively. These 8 cases are summarized in Tab. E.2.

To reconstruct all coincidence peaks we have to distinguish photons stemming from the same excitation cycle and distinct excitation cycles. For photons stemming from the same cycle the time delay between early and late

Table E.2. Possible outcomes of 2 photons scattering at a Mach-Zehnder interferometer. The early and late photon enter the MZI with a time delay Δ . If a photon is reflected at BS1 its detection is further delayed by τ_{mzi} . Columns BS1 and BS2 show whether the photons are reflected (*R*) or transmitted (*T*), Det indicates at which detector the photon is recorded, and t_{det} is the detection time. Only cases, where both photons end up at different detectors are listed. The last column states the resulting timelag $\tau = t_{\text{det}1} - t_{\text{det}2}$.

early photon				late photon				timelag τ
BS1	BS2	Det	t_{det}	BS1	BS2	Det	t_{det}	
<i>R</i>	<i>R</i>	1	τ_{mzi}	<i>R</i>	<i>T</i>	2	$\Delta + \tau_{\text{mzi}}$	$-\Delta$
<i>R</i>	<i>R</i>	1	τ_{mzi}	<i>T</i>	<i>R</i>	2	Δ	$-\Delta + \tau_{\text{mzi}}$
<i>R</i>	<i>T</i>	2	τ_{mzi}	<i>R</i>	<i>R</i>	1	$\Delta + \tau_{\text{mzi}}$	Δ
<i>R</i>	<i>T</i>	2	τ_{mzi}	<i>T</i>	<i>T</i>	1	Δ	$\Delta - \tau_{\text{mzi}}$
<i>T</i>	<i>R</i>	2	0	<i>R</i>	<i>R</i>	1	$\Delta + \tau_{\text{mzi}}$	$\Delta + \tau_{\text{mzi}}$
<i>T</i>	<i>R</i>	2	0	<i>T</i>	<i>T</i>	1	Δ	Δ
<i>T</i>	<i>T</i>	1	0	<i>R</i>	<i>T</i>	2	$\Delta + \tau_{\text{mzi}}$	$-\Delta - \tau_{\text{mzi}}$
<i>T</i>	<i>T</i>	1	0	<i>T</i>	<i>R</i>	2	Δ	$-\Delta$

photon can only be $\Delta = \tau_{\text{mzi}}$ [compare 2 photons at the right of Fig. E.1 (b)], which leads to the 8 cases illustrated in Fig. 5.7 (b). These are distributed to 5 peaks centered around $\tau = 0, \pm\tau_{\text{mzi}}$, and $\pm 2\tau_{\text{mzi}}$ with relative intensities of 1:2:2:2:1. The intensities, however, do not yet consider the asymmetric BS and bunching. To include the BS asymmetry each coincidence must be individually weighted with the probability of the preceding reflection and transmission events. The coincidence in the first row of Tab. E.2, for instance, results from the early photon being two times reflected and the late photon being reflected at BS1 and transmitted at BS2, which occurs with the overall probability of R^3T . To account for bunching we employ the coincidence probability given in Eq. (6.8), i.e. a coincidence stemming from two photons being emitted with a delay of Δ must be weighted with the factor

$$A(\Delta) = 1 + B \cdot \exp\left[-\frac{|\Delta| - T_{\text{rep}}}{\tau_{\text{B}}}\right], \quad (\text{E.4})$$

where B and τ_{B} are bunching amplitude and time. For the five peaks of the central cluster, we eventually find the relative intensities $I_{n,l}$

$$I_{0,-2} = RT^3 \cdot A(\tau_{\text{mzi}}) \quad (\text{E.5})$$

$$I_{0,-1} = RT(R^2 + T^2) \cdot A(\tau_{\text{mzi}}) \quad (\text{E.6})$$

$$I_{0,0} = RT(R^2 + T^2) \cdot A(\tau_{\text{mzi}}) \cdot (1 - V) \quad (\text{E.7})$$

$$I_{0,1} = RT(R^2 + T^2) \cdot A(\tau_{\text{mzi}}) \quad (\text{E.8})$$

$$I_{0,2} = R^3T \cdot A(\tau_{\text{mzi}}). \quad (\text{E.9})$$

Note that the indices n and l follow our convention introduced in Sect. 5.3.1, where n refers to the cluster centered at $n \cdot T_{\text{rep}}$ and l to a relative timelag of $l \cdot \tau_{\text{mzi}}$ within the cluster. The factor $(1 - V)$ accounts for TPI with a visibility of V . To obtain the intensities of clusters with $n \neq 0$ one has to consider four different combinations of early and late photon: two photon pairs exhibit $\Delta = n \cdot T_{\text{rep}}$ and each one photon pair has $\Delta = n \cdot T_{\text{rep}} \pm \tau_{\text{mzi}}$ [compare Fig. E.1 (b)]. Each of these 4 possibilities lead to the 8 cases listed in Tab. E.2, which yields overall 32 coincidences. Of these, 16 appear at the cluster at $+n \cdot T_{\text{rep}}$, the other 16 at $-n \cdot T_{\text{rep}}$. Using the abbreviation $A_{n,l} = A(n \cdot T_{\text{rep}} + l \cdot \tau_{\text{mzi}})$ for convenience, we eventually find the intensities

$$I_{\pm n,-2} = RT^3 \cdot A_{n,-1} \quad (\text{E.10})$$

$$I_{\pm n,-1} = 2RT^3 \cdot A_{n,0} + RT(R^2 + T^2) \cdot A_{n,-1} \quad (\text{E.11})$$

$$I_{\pm n,0} = 2RT(R^2 + T^2) \cdot A_{n,0} + R^3T \cdot A_{n,-1} + RT^3 \cdot A_{n,+1} \quad (\text{E.12})$$

$$I_{\pm n,1} = 2R^3T \cdot A_{n,0} + RT(R^2 + T^2) \cdot A_{n,+1} \quad (\text{E.13})$$

$$I_{\pm n,2} = R^3T \cdot A_{n,+1}. \quad (\text{E.14})$$

It is noteworthy, that both clusters at $\pm n \cdot T_{\text{rep}}$ are identical, i.e. they are not sensitive to the sign of $\pm n$, which is the origin of the asymmetry observed in Fig. 6.12. Using all intensities Eq. (E.5) to (E.14), we are now able to compute the area of a peak centered at $i \cdot \tau_{\text{mzi}}$ as

$$G_i = C \cdot \sum_{(n,l) \in \mathcal{M}_i} I_{n,l}. \quad (\text{E.15})$$

The set \mathcal{M}_i includes those individual peaks labeled by (n, l) , which fulfill $n \cdot T_{\text{rep}} + l \cdot \tau_{\text{mzi}} = i \cdot \tau_{\text{mzi}}$ and thereby contribute to the i 'th peak of the overall coincidence pattern. As we have $T_{\text{rep}} = 3\tau_{\text{mzi}}$, this condition can be written as $3n + l = i$. In the final least square fit, which minimizes the expression $\sum_i (G_i - F_i)^2$, the scaling C and the visibility V (included in $I_{0,0}$) are treated as free parameters. The bunching parameters B and τ_B are kept fixed from our analysis in Sect. 6.3.3 and the BS asymmetry was set to $R : T = 0.47 : 0.53$ as stated in Sect. 6.4.1. From the fit, the cross-correlation measurement can be reconstructed via

$$g^{(2)}(\tau) = D + C \cdot \sum_{n=-N}^N \sum_{l=-2}^2 I_{n,l} \cdot f_{n,l}(\tau) \quad \text{with} \quad (\text{E.16})$$

$$f_{n,l}(\tau) = \frac{1}{2\tau_r} \exp \left[-\frac{|\tau - (n \cdot T_{\text{rep}} + l \cdot \tau_{\text{mzi}})|}{\tau_r} \right], \quad (\text{E.17})$$

which is shown in Fig. 6.12 (a) and (b) as red and blue shaded curve.

References

- [1] J. P. Dowling and G. J. Milburn, “Quantum technology: the second quantum revolution,” *Phil. Trans. R. Soc. Lond. A* **361**, 1655–1674 (2003).
- [2] M. A. Nielsen and I. L. Chuang, *Quantum Computation and Quantum Information* (Cambridge University Press, Cambridge, 2005).
- [3] S. Lloyd, “Universal Quantum Simulators,” *Science* **273**, 1073–1078 (1996).
- [4] P. J. J. O’Malley, R. Babbush, I. D. Kivlichan, J. Romero, J. R. McClean, R. Barends, J. Kelly, P. Roushan, A. Tranter, N. Ding, B. Campbell, Y. Chen, Z. Chen, B. Chiaro, A. Dunsworth, A. G. Fowler, E. Jeffrey, E. Lucero, A. Megrant, J. Y. Mutus, M. Neeley, C. Neill, C. Quintana, D. Sank, A. Vainsencher, J. Wenner, T. C. White, P. V. Coveney, P. J. Love, H. Neven, A. Aspuru-Guzik, and J. M. Martinis, “Scalable Quantum Simulation of Molecular Energies,” *Phys. Rev. X* **6**, 031007 (2016).
- [5] C. Hempel, C. Maier, J. Romero, J. McClean, T. Monz, H. Shen, P. Jurcevic, B. P. Lanyon, P. Love, R. Babbush, A. Aspuru-Guzik, R. Blatt, and C. F. Roos, “Quantum Chemistry Calculations on a Trapped-Ion Quantum Simulator,” *Phys. Rev. X* **8**, 031022 (2018).
- [6] M. Reiher, N. Wiebe, K. M. Svore, D. Wecker, and M. Troyer, “Elucidating reaction mechanisms on quantum computers,” *Proc. Natl. Acad. Sci. U.S.A.* **114**, 7555–7560 (2017).
- [7] N. Cherkasov, A. O. Ibadon, and P. Fitzpatrick, “A review of the existing and alternative methods for greener nitrogen fixation,” *Chem. Eng. Process.* **90**, 24–33 (2015).
- [8] P. W. Shor, “Polynomial-Time Algorithms for Prime Factorization and Discrete Logarithms on a Quantum Computer,” *SIAM J. Comput.* **26**, 1484–1509 (1997).

- [9] W. Diffie and M. Hellman, “New directions in cryptography,” *IEEE Trans. Inf. Theory* **22**, 644–654 (1976).
- [10] R. L. Rivest, A. Shamir, and L. Adleman, “A Method for Obtaining Digital Signatures and Public-key Cryptosystems,” *Commun. ACM* **21**, 120–126 (1978).
- [11] N. Gisin, G. Ribordy, W. Tittel, and H. Zbinden, “Quantum cryptography,” *Rev. Mod. Phys.* **74**, 145–195 (2002).
- [12] C. H. Bennett and G. Brassard, “Quantum cryptography: Public key distribution and coin tossing,” *Theor. Comput. Sci.* **560**, 7–11 (2014).
- [13] A. K. Ekert, “Quantum cryptography based on Bell’s theorem,” *Phys. Rev. Lett.* **67**, 661–663 (1991).
- [14] W.-Y. Hwang, “Quantum Key Distribution with High Loss: Toward Global Secure Communication,” *Phys. Rev. Lett.* **91**, 057901 (2003).
- [15] H. J. Kimble, “The quantum internet,” *Nature* **453**, 1023–1030 (2008).
- [16] M. Travagnin and A. M. Lewis, “The impact of quantum technologies on the EU’s future policies. Part 2, Quantum communications: from science to policies,” *EU Publications* (2018).
- [17] J. Qiu, “Quantum communications leap out of the lab,” *Nature* **508**, 441–442 (2014).
- [18] Q. Zhang, F. Xu, Y.-A. Chen, C.-Z. Peng, and J.-W. Pan, “Large scale quantum key distribution: challenges and solutions,” *Opt. Express* **26**, 24260–24273 (2018).
- [19] Quantum Technologies Strategic Advisory Board, “National strategy for quantum technologies,” *Innovate UK* (2015).
- [20] Joint Report by the Committee on Science and the Committee on Homeland and National Security, National Science and Technology Council, “Advancing Quantum Information Science: National Challenges and Opportunities,” *Executive Office of The President* (2016).
- [21] M. G. Raymer and C. Monroe, “The US National Quantum Initiative,” *Quantum Sci. Technol.* **4**, 020504 (2019).
- [22] M. F. Riedel, D. Binosi, R. Thew, and T. Calarco, “The European quantum technologies flagship programme,” *Quantum Sci. Technol.* **2**, 030501 (2017).
- [23] Quantum Flagship, “Strategic Research Agenda (SRA),” draft from July 31st, 2019, available at <https://qt.eu//app/uploads/2019/08/190731-SRA-Draft.docx>.
- [24] H.-L. Yin, T.-Y. Chen, Z.-W. Yu, H. Liu, L.-X. You, Y.-H. Zhou, S.-J. Chen, Y. Mao, M.-Q. Huang, W.-J. Zhang, H. Chen, M. J. Li,

-
- D. Nolan, F. Zhou, X. Jiang, Z. Wang, Q. Zhang, X.-B. Wang, and J.-W. Pan, “Measurement-Device-Independent Quantum Key Distribution Over a 404 km Optical Fiber,” *Phys. Rev. Lett.* **117**, 190501 (2016).
- [25] A. Boaron, G. Boso, D. Rusca, C. Vulliez, C. Autebert, M. Caloz, M. Perrenoud, G. Gras, F. Bussi eres, M.-J. Li, D. Nolan, A. Martin, and H. Zbinden, “Secure Quantum Key Distribution over 421 km of Optical Fiber,” *Phys. Rev. Lett.* **121**, 190502 (2018).
- [26] Corning, *SMF-28[®] ULL Optical Fiber* (2014).
- [27] M. Takeoka, S. Guha, and M. M. Wilde, “Fundamental rate-loss tradeoff for optical quantum key distribution,” *Nat. Commun.* **5**, 5235 (2014).
- [28] S. Pirandola, R. Laurenza, C. Ottaviani, and L. Banchi, “Fundamental limits of repeaterless quantum communications,” *Nat. Commun.* **8**, 15043 (2017).
- [29] A. Pirandola, U. L. Andersen, L. Banchi, M. Berta, D. Bunandar, R. Colbeck, D. Englund, T. Gehring, C. Lupo, V. Ottaviani, J. Pereira, M. Razavi, J. S. Shaari, M. Tomamichel, V. C. Usenko, G. Vallone, P. Villoresi, and P. Wallden, “Advances in Quantum Cryptography,” (2019). Preprint available at [arXiv:1906.01645](https://arxiv.org/abs/1906.01645) [quant-ph].
- [30] W. K. Wootters and W. H. Zurek, “A single quantum cannot be cloned,” *Nature* **299**, 802–803 (1982).
- [31] H.-J. Briegel, W. D ur, J. I. Cirac, and P. Zoller, “Quantum Repeaters: The Role of Imperfect Local Operations in Quantum Communication,” *Phys. Rev. Lett.* **81**, 5932–5935 (1998).
- [32] L.-M. Duan, M. D. Lukin, J. I. Cirac, and P. Zoller, “Long-distance quantum communication with atomic ensembles and linear optics,” *Nature* **414**, 413–418 (2001).
- [33] N. Sangouard, C. Simon, H. de Riedmatten, and N. Gisin, “Quantum repeaters based on atomic ensembles and linear optics,” *Rev. Mod. Phys.* **83**, 33–80 (2011).
- [34] M. Żukowski, A. Zeilinger, M. A. Horne, and A. K. Ekert, “Event-ready-detectors’ Bell experiment via entanglement swapping,” *Phys. Rev. Lett.* **71**, 4287–4290 (1993).
- [35] A. Einstein, B. Podolsky, and N. Rosen, “Can Quantum-Mechanical Description of Physical Reality Be Considered Complete?” *Phys. Rev.* **47**, 777–780 (1935).
- [36] C. Cabrillo, J. I. Cirac, P. Garc a-Fern andez, and P. Zoller, “Creation of entangled states of distant atoms by interference,” *Phys. Rev. A* **59**, 1025–1033 (1999).

- [37] B. Zhao, Z.-B. Chen, Y.-A. Chen, J. Schmiedmayer, and J.-W. Pan, “Robust Creation of Entanglement between Remote Memory Qubits,” *Phys. Rev. Lett.* **98**, 240502 (2007).
- [38] R. Zhao, Y. O. Dudin, S. D. Jenkins, C. J. Campbell, D. N. Matsukevich, T. A. B. Kennedy, and A. Kuzmich, “Long-lived quantum memory,” *Nat. Phys.* **5**, 100–104 (2009).
- [39] P. Farrera, G. Heinze, and H. de Riedmatten, “Entanglement between a Photonic Time-Bin Qubit and a Collective Atomic Spin Excitation,” *Phys. Rev. Lett.* **120**, 100501 (2018).
- [40] K. Hammerer, A. S. Sørensen, and E. S. Polzik, “Quantum interface between light and atomic ensembles,” *Rev. Mod. Phys.* **82**, 1041–1093 (2010).
- [41] M. Gündoğan, P. M. Ledingham, K. Kutluer, M. Mazzerà, and H. de Riedmatten, “Solid State Spin-Wave Quantum Memory for Time-Bin Qubits,” *Phys. Rev. Lett.* **114**, 230501 (2015).
- [42] P. Jobez, N. Timoney, C. Laplane, J. Etesse, A. Ferrier, P. Goldner, N. Gisin, and M. Afzelius, “Towards highly multimode optical quantum memory for quantum repeaters,” *Phys. Rev. A* **93**, 032327 (2016).
- [43] K. Heshami, D. G. England, P. C. Humphreys, P. J. Bustard, V. M. Acosta, J. Nunn, and B. J. Sussman, “Quantum memories: emerging applications and recent advances,” *J. Mod. Opt.* **63**, 2005–2028 (2016).
- [44] S. Lloyd, M. S. Shahriar, J. H. Shapiro, and P. R. Hemmer, “Long Distance, Unconditional Teleportation of Atomic States via Complete Bell State Measurements,” *Phys. Rev. Lett.* **87**, 167903 (2001).
- [45] H. P. Specht, C. Nölleke, A. Reiserer, M. Uphoff, E. Figueroa, S. Ritter, and G. Rempe, “A single-atom quantum memory,” *Nature* **473**, 190–193 (2011).
- [46] T. P. Harty, D. T. C. Allcock, C. J. Ballance, L. Guidoni, H. A. Janacek, N. M. Linke, D. N. Stacey, and D. M. Lucas, “High-Fidelity Preparation, Gates, Memory, and Readout of a Trapped-Ion Quantum Bit,” *Phys. Rev. Lett.* **113**, 220501 (2014).
- [47] P. Müller and J. Eschner, “Single calcium-40 ion as quantum memory for photon polarization: a case study,” *Appl. Phys. B* **114**, 303–306 (2014).
- [48] Y. Wang, M. Um, J. Zhang, S. An, M. Lyu, J.-N. Zhang, L.-M. Duan, D. Yum, and K. Kim, “Single-qubit quantum memory exceeding ten-minute coherence time,” *Nat. Photon.* **11**, 646–650 (2017).

-
- [49] L. Childress and R. Hanson, “Diamond NV centers for quantum computing and quantum networks,” *MRS Bulletin* **38**, 134–138 (2013).
- [50] J. N. Becker and C. Becher, “Coherence Properties and Quantum Control of Silicon Vacancy Color Centers in Diamond,” *Phys. Status Solidi A* **214**, 1700586 (2017).
- [51] P. Lodahl, “Quantum-dot based photonic quantum networks,” *Quantum Sci. Technol.* **3**, 013001 (2017).
- [52] C. Simon and W. T. M. Irvine, “Robust Long-Distance Entanglement and a Loophole-Free Bell Test with Ions and Photons,” *Phys. Rev. Lett.* **91**, 110405 (2003).
- [53] P. G. Kwiat and H. Weinfurter, “Embedded Bell-state analysis,” *Phys. Rev. A* **58**, R2623–R2626 (1998).
- [54] B. B. Blinov, D. L. Moehring, L.-M. Duan, and C. Monroe, “Observation of entanglement between a single trapped atom and a single photon,” *Nature* **428**, 153–157 (2004).
- [55] E. Togan, Y. Chu, A. S. Trifonov, L. Jiang, J. Maze, L. Childress, M. V. G. Dutt, A. S. Sørensen, P. R. Hemmer, A. S. Zibrov, and M. D. Lukin, “Quantum entanglement between an optical photon and a solid-state spin qubit,” *Nature* **466**, 730–734 (2010).
- [56] A. Stute, B. Casabone, P. Schindler, T. Monz, P. O. Schmidt, B. Brandstätter, T. E. Northup, and R. Blatt, “Tunable ion-photon entanglement in an optical cavity,” *Nature* **485**, 482–485 (2012).
- [57] W. B. Gao, P. Fallahi, E. Togan, J. Miguel-Sanchez, and A. Imamoglu, “Observation of entanglement between a quantum dot spin and a single photon,” *Nature* **491**, 426–430 (2012).
- [58] N. Sangouard, C. Simon, J. Minář, H. Zbinden, H. de Riedmatten, and N. Gisin, “Long-distance entanglement distribution with single-photon sources,” *Phys. Rev. A* **76**, 050301(R) (2007).
- [59] C. Simon, H. de Riedmatten, M. Afzelius, N. Sangouard, H. Zbinden, and N. Gisin, “Quantum Repeaters with Photon Pair Sources and Multimode Memories,” *Phys. Rev. Lett.* **98**, 190503 (2007).
- [60] C. K. Hong, Z. Y. Ou, and L. Mandel, “Measurement of Subpicosecond Time Intervals between Two Photons by Interference,” *Phys. Rev. Lett.* **59**, 2044–2046 (1987).
- [61] J. Beugnon, M. P. A. Jones, J. Dingjan, B. Darquié, G. Messin, A. Browaeys, and P. Grangier, “Quantum interference between two single photons emitted by independently trapped atoms,” *Nature* **440**, 779–782 (2006).

- [62] R. Kaltenbaek, B. Blauensteiner, M. Żukowski, M. Aspelmeyer, and A. Zeilinger, “Experimental Interference of Independent Photons,” *Phys. Rev. Lett.* **96**, 240502 (2006).
- [63] P. Maunz, D. L. Moehring, S. Olmschenk, K. C. Younge, D. N. Matsukevich, and C. Monroe, “Quantum interference of photon pairs from two remote trapped atomic ions,” *Nat. Phys.* **3**, 538–541 (2007).
- [64] R. Lettow, Y. L. A. Rezus, A. Renn, G. Zumofen, E. Ikonen, S. Götzinger, and V. Sandoghdar, “Quantum Interference of Tunably Indistinguishable Photons from Remote Organic Molecules,” *Phys. Rev. Lett.* **104**, 123605 (2010).
- [65] R. B. Patel, A. J. Bennett, I. Farrer, C. A. Nicoll, D. A. Ritchie, and A. J. Shields, “Two-photon interference of the emission from electrically tunable remote quantum dots,” *Nat. Photon.* **4**, 632–635 (2010).
- [66] H. Bernien, L. Childress, L. Robledo, M. Markham, D. Twitchen, and R. Hanson, “Two-Photon Quantum Interference from Separate Nitrogen Vacancy Centers in Diamond,” *Phys. Rev. Lett.* **108**, 043604 (2012).
- [67] A. Sipahigil, M. L. Goldman, E. Togan, Y. Chu, M. Markham, D. J. Twitchen, A. S. Zibrov, A. Kubanek, and M. D. Lukin, “Quantum Interference of Single Photons from Remote Nitrogen-Vacancy Centers in Diamond,” *Phys. Rev. Lett.* **108**, 143601 (2012).
- [68] A. Sipahigil, K. D. Jahnke, L. J. Rogers, T. Teraji, J. Isoya, A. S. Zibrov, F. Jelezko, and M. D. Lukin, “Indistinguishable Photons from Separated Silicon-Vacancy Centers in Diamond,” *Phys. Rev. Lett.* **113**, 113602 (2014).
- [69] D. L. Moehring, P. Maunz, S. Olmschenk, K. C. Younge, D. N. Matsukevich, L.-M. Duan, and C. Monroe, “Entanglement of single-atom quantum bits at a distance,” *Nature* **449**, 68–71 (2007).
- [70] Z.-S. Yuan, Y.-A. Chen, B. Zhao, S. Chen, J. Schmiedmayer, and J.-W. Pan, “Experimental demonstration of a BDCZ quantum repeater node,” *Nature* **454**, 1098–1101 (2008).
- [71] L. Slodička, G. Hétet, N. Röck, P. Schindler, M. Hennrich, and R. Blatt, “Atom-Atom Entanglement by Single-Photon Detection,” *Phys. Rev. Lett.* **110**, 083603 (2013).
- [72] J. Hofmann, M. Krug, N. Ortégel, L. Gérard, M. Weber, W. Rosenfeld, and H. Weinfurter, “Heralded Entanglement Between Widely Separated Atoms,” *Science* **337**, 72–75 (2012).
- [73] H. Bernien, B. Hensen, W. Pfaff, G. Koolstra, M. S. Blok, L. Robledo, T. H. Taminiau, M. Markham, D. J. Twitchen, L. Childress, and R. Hanson, “Heralded entanglement between solid-state qubits separated by three metres,” *Nature* **497**, 86–90 (2013).

-
- [74] A. Delteil, Z. Sun, W. Gao, E. Togan, S. Faelt, and A. Imamoglu, “Generation of heralded entanglement between distant hole spins,” *Nat. Phys.* **12**, 218–223 (2016).
- [75] B. C. Jacobs, T. B. Pittman, and J. D. Franson, “Quantum relays and noise suppression using linear optics,” *Phys. Rev. A* **66**, 052307 (2002).
- [76] E. Waks, A. Zeevi, and Y. Yamamoto, “Security of quantum key distribution with entangled photons against individual attacks,” *Phys. Rev. A* **65**, 052310 (2002).
- [77] D. Collins, N. Gisin, and H. de Riedmatten, “Quantum relays for long distance quantum cryptography,” *J. Mod. Opt.* **52**, 735–753 (2005).
- [78] P. G. Kwiat, K. Mattle, H. Weinfurter, A. Zeilinger, A. V. Sergienko, and Y. Shih, “New High-Intensity Source of Polarization-Entangled Photon Pairs,” *Phys. Rev. Lett.* **75**, 4337–4341 (1995).
- [79] O. Benson, C. Santori, M. Pelton, and Y. Yamamoto, “Regulated and Entangled Photons from a Single Quantum Dot,” *Phys. Rev. Lett.* **84**, 2513–2516 (2000).
- [80] D. Huber, M. Reindl, J. Aberl, A. Rastelli, and R. Trotta, “Semiconductor quantum dots as an ideal source of polarization-entangled photon pairs on-demand: a review,” *J. Opt.* **20**, 073002 (2018).
- [81] J.-W. Pan, D. Bouwmeester, H. Weinfurter, and A. Zeilinger, “Experimental Entanglement Swapping: Entangling Photons That Never Interacted,” *Phys. Rev. Lett.* **80**, 3891–3894 (1998).
- [82] Z.-D. Li, R. Zhang, X.-F. Yin, L.-Z. Liu, Y. Hu, Y.-Q. Fang, Y.-Y. Fei, X. Jiang, J. Zhang, L. Li, N.-L. Liu, F. Xu, Y.-A. Chen, and J.-W. Pan, “Experimental quantum repeater without quantum memory,” *Nat. Photon.* **13**, 644–648 (2019).
- [83] B. Hensen, H. Bernien, A. E. Dréau, A. Reiserer, N. Kalb, M. S. Blok, J. Ruitenbergh, R. F. L. Vermeulen, R. N. Schouten, C. Abellán, W. Amaya, V. Pruneri, M. W. Mitchell, M. Markham, D. J. Twitchen, D. Elkouss, S. Wehner, T. H. Taminiau, and R. Hanson, “Loophole-free Bell inequality violation using electron spins separated by 1.3 kilometres,” *Nature* **526**, 682–686 (2015).
- [84] E. Saglamyurek, J. Jin, V. B. Verma, M. D. Shaw, F. Marsili, S. W. Nam, D. Oblak, and W. Tittel, “Quantum storage of entangled telecom-wavelength photons in an erbium-doped optical fibre,” *Nat. Photon.* **9**, 83–87 (2015).
- [85] I. Craiciu, M. Lei, J. Rochman, J. M. Kindem, J. G. Bartholomew, E. Miyazono, T. Zhong, N. Sinclair, and A. Faraon, “Nanophotonic Quantum Storage at Telecommunication Wavelength,” *Phys. Rev. Applied* **12**, 024062 (2019).

- [86] M. B. Ward, M. C. Dean, R. M. Stevenson, A. J. Bennett, D. J. P. Ellis, K. Cooper, I. Farrer, C. A. Nicoll, D. A. Ritchie, and A. J. Shields, “Coherent dynamics of a telecom-wavelength entangled photon source,” *Nat. Commun.* **5**, 3316 (2014).
- [87] K. Takemoto, Y. Nambu, T. Miyazawa, Y. Sakuma, T. Yamamoto, S. Yorozu, and Y. Arakawa, “Quantum key distribution over 120 km using ultrahigh purity single-photon source and superconducting single-photon detectors,” *Sci. Rep.* **5**, 14383 (2015).
- [88] J.-H. Kim, T. Cai, C. J. K. Richardson, R. P. Leavitt, and E. Waks, “Two-photon interference from a bright single-photon source at telecom wavelengths,” *Optica* **3**, 577–584 (2016).
- [89] D. Huber, M. Reindl, Y. Huo, H. Huang, J. S. Wildmann, O. G. Schmidt, A. Rastelli, and R. Trotta, “Highly indistinguishable and strongly entangled photons from symmetric GaAs quantum dots,” *Nat. Commun.* **8**, 15506 (2017).
- [90] P. Kumar, “Quantum frequency conversion,” *Opt. Lett.* **15**, 1476–1478 (1990).
- [91] Z. Y. Ou, “Efficient conversion between photons and between photon and atom by stimulated emission,” *Phys. Rev. A* **78**, 023819 (2008).
- [92] R. W. Boyd, *Nonlinear Optics* (Elsevier, Oxford, 2008), 3rd ed.
- [93] G. Agrawal, “Four-Wave Mixing,” in “Nonlinear Fiber Optics,” (Academic Press, Boston, 2013), chap. 10, pp. 397–456.
- [94] J. Huang and P. Kumar, “Observation of quantum frequency conversion,” *Phys. Rev. Lett.* **68**, 2153–2156 (1992).
- [95] S. Zaske, A. Lenhard, C. A. Keßler, J. Kettler, C. Hepp, C. Arend, R. Albrecht, W. M. Schulz, M. Jetter, P. Michler, and C. Becher, “Visible-to-Telecom Quantum Frequency Conversion of Light from a Single Quantum Emitter,” *Phys. Rev. Lett.* **109**, 147404 (2012).
- [96] M. Bock, P. Eich, S. Kucera, M. Kreis, A. Lenhard, C. Becher, and J. Eschner, “High-fidelity entanglement between a trapped ion and a telecom photon via quantum frequency conversion,” *Nat. Commun.* **9**, 1998 (2018).
- [97] R. S. Weis and T. K. Gaylord, “Lithium niobate: Summary of physical properties and crystal structure,” *Appl. Phys. A* **37**, 191–203 (1985).
- [98] M. M. Fejer, G. A. Magel, D. H. Jundt, and R. L. Byer, “Quasi-phase-matched second harmonic generation: tuning and tolerances,” *IEEE J. Quantum Electron.* **28**, 2631–2654 (1992).
- [99] M. H. Chou, J. Hauden, M. A. Arbore, and M. M. Fejer, “1.5- μm -band wavelength conversion based on difference-frequency generation in

- LiNbO₃ waveguides with integrated coupling structures,” *Opt. Lett.* **23**, 1004–1006 (1998).
- [100] J. S. Pelc, L. Ma, C. R. Phillips, Q. Zhang, C. Langrock, O. Slattery, X. Tang, and M. Fejer, “Long-wavelength-pumped upconversion single-photon detector at 1550 nm: performance and noise analysis,” *Opt. Express* **19**, 21445–21456 (2011).
- [101] S. Zaske, A. Lenhard, and C. Becher, “Efficient frequency downconversion at the single photon level from the red spectral range to the telecommunications C-band,” *Opt. Express* **19**, 12825–12836 (2011).
- [102] J. S. Pelc, C. Langrock, Q. Zhang, and M. Fejer, “Influence of domain disorder on parametric noise in quasi-phasematched quantum frequency converters,” *Opt. Lett.* **35**, 2804–2806 (2010).
- [103] M. T. Rakher, L. Ma, O. Slattery, X. Tang, and K. Srinivasan, “Quantum transduction of telecommunications-band single photons from a quantum dot by frequency upconversion,” *Nat. Photon.* **4**, 786–791 (2010).
- [104] S. Ates, I. Agha, A. Gulinatti, I. Rech, M. T. Rakher, A. Badolato, and K. Srinivasan, “Two-Photon Interference Using Background-Free Quantum Frequency Conversion of Single Photons Emitted by an InAs Quantum Dot,” *Phys. Rev. Lett* **109**, 147405 (2012).
- [105] P. Farrera, N. Maring, B. Albrecht, G. Heinze, and H. de Riedmatten, “Nonclassical correlations between a C-band telecom photon and a stored spin-wave,” *Optica* **3**, 1019–1024 (2016).
- [106] R. Ikuta, T. Kobayashi, K. Matsuki, S. Miki, T. Yamashita, H. Terai, T. Yamamoto, M. Koashi, T. Mukai, and N. Imoto, “Heralded single excitation of atomic ensemble via solid-state-based telecom photon detection,” *Optica* **3**, 1279–1284 (2016).
- [107] S. Tanzilli, W. Tittel, M. Halder, O. Alibart, P. Baldi, N. Gisin, and H. Zbinden, “A photonic quantum information interface,” *Nature* **437**, 116–120 (2005).
- [108] R. Ikuta, Y. Kusaka, T. Kitano, H. Kato, T. Yamamoto, M. Koashi, and N. Imoto, “Wide-band quantum interface for visible-to-telecommunication wavelength conversion,” *Nat. Commun.* **2**, 537 (2011).
- [109] S. Ramelow, A. Fedrizzi, A. Poppe, N. K. Langford, and A. Zeilinger, “Polarization-entanglement-conserving frequency conversion of photons,” *Phys. Rev. A* **85**, 013845 (2012).
- [110] Z.-Y. Zhou, S.-L. Liu, Y. Li, D.-S. Ding, W. Zhang, S. Shi, M.-X. Dong, B.-S. Shi, and G.-C. Guo, “Orbital Angular Momentum-Entanglement Frequency Transducer,” *Phys. Rev. Lett.* **117**, 103601 (2016).

- [111] R. Ikuta, T. Kobayashi, T. Kawakami, S. Miki, M. Yabuno, T. Yamashita, H. Terai, M. Koashi, T. Mukai, T. Yamamoto, and N. Imoto, “Polarization insensitive frequency conversion for an atom-photon entanglement distribution via a telecom network,” *Nat. Commun.* **9**, 1997 (2018).
- [112] A. Tchebotareva, S. L. N. Hermans, P. C. Humphreys, D. Voigt, P. J. Harmsma, L. K. Cheng, A. L. Verlaan, N. Dijkhuizen, W. de Jong, A. Dréau, and R. Hanson, “Entanglement between a Diamond Spin Qubit and a Photonic Time-Bin Qubit at Telecom Wavelength,” *Phys. Rev. Lett.* **123**, 063601 (2019).
- [113] V. Krutyanskiy, M. Meraner, J. Schupp, V. Krcmarsky, H. Hainzer, and B. P. Lanyon, “Light-matter entanglement over 50 km of optical fibre,” *Npj Quantum Inf.* **5**, 72 (2019).
- [114] T. van Leent, M. Bock, R. Garthoff, K. Redeker, W. Zhang, T. Bauer, W. Rosenfeld, C. Becher, and H. Weinfurter, “Long-distance distribution of atom-photon entanglement at telecom wavelength,” (2019). Preprint available at [arXiv:1909.01006](https://arxiv.org/abs/1909.01006) [quant-ph].
- [115] Y. Yu, F. Ma, X.-Y. Luo, B. Jing, P.-F. Sun, R.-Z. Fang, C.-W. Yang, H. Liu, M.-Y. Zheng, X.-P. Xie, W.-J. Zhang, L.-X. You, Z. Wang, T.-Y. Chen, Q. Zhang, X.-H. Bao, and J.-W. Pan, “Entanglement of two quantum memories via metropolitan-scale fibers,” (2019). Preprint available at [arXiv:1903.11284](https://arxiv.org/abs/1903.11284) [quant-ph].
- [116] P. Lodahl, M. Sahand, and S. Stobbe, “Interfacing single photons and single quantum dots with photonic nanostructures,” *Rev. Mod. Phys.* **87**, 347–400 (2015).
- [117] A. K. Nowak, S. L. Portalupi, V. Giesz, O. Gazzano, C. Dal Savio, P. F. Braun, K. Karrai, C. Arnold, L. Lanco, I. Sagnes, A. Lemaître, and P. Senellart, “Deterministic and electrically tunable bright single-photon source,” *Nat. Commun.* **5**, 3240 (2014).
- [118] X. Ding, Y. He, Z. C. Duan, N. Gregersen, M. C. Chen, S. Unsleber, S. Maier, C. Schneider, M. Kamp, S. Höfling, C. Y. Lu, and J. W. Pan, “On-Demand Single Photons with High Extraction Efficiency and Near-Unity Indistinguishability from a Resonantly Driven Quantum Dot in a Micropillar,” *Phys. Rev. Lett.* **116**, 020401 (2016).
- [119] S. Unsleber, Y.-M. He, S. Gerhardt, S. Maier, C.-Y. Lu, J.-W. Pan, N. Gregersen, M. Kamp, C. Schneider, and S. Höfling, “Highly indistinguishable on-demand resonance fluorescence photons from a deterministic quantum dot micropillar device with 74% extraction efficiency,” *Opt. Express* **24**, 8539–8546 (2016).
- [120] J. Claudon, J. Bleuse, N. S. Malik, M. Bazin, P. Jaffrennou, N. Gregersen, C. Sauvan, P. Lalanne, and J.-M. Gérard, “A highly

- efficient single-photon source based on a quantum dot in a photonic nanowire,” *Nat. Photon.* **4**, 174–177 (2010).
- [121] M. Arcari, I. Söllner, A. Javadi, S. Lindskov Hansen, S. Mahmoodian, J. Liu, H. Thyrrestrup, E. H. Lee, J. D. Song, S. Stobbe, and P. Lodahl, “Near-Unity Coupling Efficiency of a Quantum Emitter to a Photonic Crystal Waveguide,” *Phys. Rev. Lett.* **113**, 093603 (2014).
- [122] E. M. Purcell, “Spontaneous Emission Probabilities at Radio Frequencies,” *Phys. Rev.* **69**, 681 (1946).
- [123] J. M. Gérard, B. Sermage, B. Gayral, B. Legrand, E. Costard, and V. Thierry-Mieg, “Enhanced Spontaneous Emission by Quantum Boxes in a Monolithic Optical Microcavity,” *Phys. Rev. Lett.* **81**, 1110–1113 (1998).
- [124] K. J. Vahala, “Optical microcavities,” *Nature* **424**, 839–846 (2003).
- [125] N. Somaschi, V. Giesz, L. De Santis, J. C. Loredó, M. P. Almeida, G. Hornecker, S. L. Portalupi, T. Grange, C. Antón, J. Demory, C. Gómez, I. Sagnes, N. D. Lanzillotti-Kimura, A. Lemaître, A. Aufferes, A. G. White, L. Lanco, and P. Senellart, “Near-optimal single-photon sources in the solid state,” *Nat. Photon.* **10**, 340–345 (2016).
- [126] E. A. Muljarov and R. Zimmermann, “Dephasing in Quantum Dots: Quadratic Coupling to Acoustic Phonons,” *Phys. Rev. Lett.* **93**, 237401 (2004).
- [127] T. Grange, “Decoherence in quantum dots due to real and virtual transitions: A nonperturbative calculation,” *Phys. Rev. B* **80**, 245310 (2009).
- [128] J. Houel, A. V. Kuhlmann, L. Greuter, F. Xue, M. Poggio, B. D. Gerardot, P. A. Dalgarno, A. Badolato, P. M. Petroff, A. Ludwig, D. Reuter, A. D. Wieck, and R. J. Warburton, “Probing Single-Charge Fluctuations at a GaAs/AlAs Interface Using Laser Spectroscopy on a Nearby InGaAs Quantum Dot,” *Phys. Rev. Lett.* **108**, 107401 (2012).
- [129] A. V. Kuhlmann, J. Houel, A. Ludwig, L. Greuter, D. Reuter, A. D. Wieck, M. Poggio, and R. J. Warburton, “Charge noise and spin noise in a semiconductor quantum device,” *Nat. Phys.* **9**, 570–575 (2013).
- [130] A. V. Kuhlmann, J. Houel, D. Brunner, A. Ludwig, D. Reuter, A. D. Wieck, and R. J. Warburton, “A dark-field microscope for background-free detection of resonance fluorescence from single semiconductor quantum dots operating in a set-and-forget mode,” *Rev. Sci. Instrum.* **84**, 073905 (2013).

- [131] O. Gazzano, S. Michaelis de Vasconcellos, C. Arnold, A. Nowak, E. Galopin, I. Sagnes, L. Lanco, A. Lemaître, and P. Senellart, “Bright solid-state sources of indistinguishable single photons,” *Nat. Commun.* **4**, 1425 (2013).
- [132] O. Gazzano, T. Huber, V. Loo, S. Polyakov, E. B. Flagg, and G. S. Solomon, “Effects of resonant-laser excitation on the emission properties in a single quantum dot,” *Optica* **5**, 354–359 (2018).
- [133] A. V. Kuhlmann, J. H. Prechtel, J. Houel, A. Ludwig, D. Reuter, A. D. Wieck, and R. J. Warburton, “Transform-limited single photons from a single quantum dot,” *Nat. Commun.* **6**, 8204 (2015).
- [134] P. Senellart, G. Solomon, and A. White, “High-performance semiconductor quantum-dot single-photon sources,” *Nat. Nanotechnol.* **12**, 1026–1039 (2017).
- [135] S. T. Yilmaz, P. Fallahi, and A. Imamoglu, “Quantum-Dot-Spin Single-Photon Interface,” *Phys. Rev. Lett.* **105**, 033601 (2010).
- [136] A. Javadi, D. Ding, M. H. Appel, S. Mahmoodian, M. C. Löbl, I. Söllner, R. Schott, C. Papon, T. Pregolato, S. Stobbe, L. Midolo, T. Schröder, A. D. Wieck, A. Ludwig, R. J. Warburton, and P. Lodahl, “Spinphoton interface and spin-controlled photon switching in a nanobeam waveguide,” *Nat. Nanotechnol.* **13**, 398–403 (2018).
- [137] K. De Greve, P. L. McMahon, L. Yu, J. S. Pelc, C. Jones, C. M. Nataraajan, N. Y. Kim, E. Abe, S. Maier, C. Schneider, M. Kamp, S. Höfling, R. H. Hadfield, A. Forchel, M. M. Fejer, and Y. Yamamoto, “Complete tomography of a high-fidelity solid-state entangled spinphoton qubit pair,” *Nat. Commun.* **4**, 2228 (2013).
- [138] Y. He, Y.-M. He, Y.-J. Wei, X. Jiang, K. Chen, C.-Y. Lu, J.-W. Pan, C. Schneider, M. Kamp, and S. Höfling, “Quantum State Transfer from a Single Photon to a Distant Quantum-Dot Electron Spin,” *Phys. Rev. Lett.* **119**, 060501 (2017).
- [139] M. Atatüre, D. Englund, N. Vamivakas, S.-Y. Lee, and J. Wrachtrup, “Material platforms for spin-based photonic quantum technologies,” *Nat. Rev. Mater.* **3**, 38–51 (2018).
- [140] A. Dousse, J. Suffczyński, A. Beveratos, O. Krebs, A. Lemaître, I. Sagnes, J. Bloch, P. Voisin, and P. Senellart, “Ultrabright source of entangled photon pairs,” *Nature* **466**, 217–220 (2010).
- [141] M. Müller, S. Bounouar, K. D. Jöns, M. Glässl, and P. Michler, “On-demand generation of indistinguishable polarization-entangled photon pairs,” *Nat. Photon.* **8**, 224–228 (2014).
- [142] K. D. Jöns, L. Schweickert, M. A. M. Versteegh, D. Dalacu, P. J. Poole, A. Gulinatti, A. Giudice, V. Zwiller, and M. E. Reimer, “Bright

- nanoscale source of deterministic entangled photonpairs violating Bells inequality,” *Sci. Rep.* **7**, 1700 (2017).
- [143] D. Huber, M. Reindl, S. F. Covre da Silva, C. Schimpf, J. Martín-Sánchez, H. Huang, G. Piredda, J. Edlinger, A. Rastelli, and R. Trotta, “Strain-Tunable GaAs Quantum Dot: A Nearly Dephasing-Free Source of Entangled Photon Pairs on Demand,” *Phys. Rev. Lett.* **121**, 033902 (2018).
- [144] J. Liu, R. Su, Y. Wei, B. Yao, S. F. C. Silva, Y. Yu, J. Iles-Smith, K. Srinivasan, A. Rastelli, J. Li, and X. Wang, “A solid-state source of strongly entangled photon pairs with high brightness and indistinguishability,” *Nat. Nanotechnol.* **14**, 586–593 (2019).
- [145] C. Varnava, R. M. Stevenson, J. Nilsson, J. Skiba-Szymanska, B. Dzurňák, M. Lucamarini, R. V. Penty, I. Farrer, D. A. Ritchie, and A. J. Shields, “An entangled-LED-driven quantum relay over 1 km,” *Npj Quantum Inf.* **2**, 16006 (2016).
- [146] E. Knill, R. Laflamme, and G. J. Milburn, “A scheme for efficient quantum computation with linear optics,” *Nature* **409**, 46–52 (2001).
- [147] T. C. Ralph, N. K. Langford, T. B. Bell, and A. G. White, “Linear optical controlled-NOT gate in the coincidence basis,” *Phys. Rev. A* **65**, 062324 (2002).
- [148] D. Branning, A. L. Migdall, and A. V. Sergienko, “Simultaneous measurement of group and phase delay between two photons,” *Phys. Rev. A* **62**, 063808 (2000).
- [149] A. F. Abouraddy, M. B. Nasr, B. E. A. Saleh, A. V. Sergienko, and M. C. Teich, “Quantum-optical coherence tomography with dispersion cancellation,” *Phys. Rev. A* **65**, 053817 (2002).
- [150] L. Yu, C. M. Natarajan, T. Horikiri, C. Langrock, J. S. Pelc, M. G. Tanner, E. Abe, S. Maier, C. Schneider, S. Höfling, M. Kamp, R. H. Hadfield, M. M. Fejer, and Y. Yamamoto, “Two-photon interference at telecom wavelengths for time-bin-encoded single photons from quantum-dot spin qubits,” *Nat. Commun.* **6**, 8955 (2015).
- [151] P. Gold, A. Thoma, S. Maier, S. Reitzenstein, C. Schneider, S. Höfling, and M. Kamp, “Two-photon interference from remote quantum dots with inhomogeneously broadened linewidths,” *Phys. Rev. B* **89**, 035313 (2014).
- [152] V. Giesz, S. L. Portalupi, T. Grange, C. Antón, L. De Santis, J. Demory, N. Somaschi, I. Sagnes, A. Lemaître, L. Lanco, A. Auffèves, and P. Senellart, “Cavity-enhanced two-photon interference using remote quantum dot sources,” *Phys. Rev. B* **92**, 161302(R) (2015).

- [153] A. Thoma, P. Schnauber, J. Böhm, M. Gschrey, J. H. Schulze, A. Strittmatter, S. Rodt, T. Heindel, and S. Reitzenstein, “Two-photon interference from remote deterministic quantum dot microlenses,” *Appl. Phys. Lett.* **110**, 011104 (2017).
- [154] E. B. Flagg, A. Muller, S. V. Polyakov, A. Ling, A. Migdall, and G. S. Solomon, “Interference of Single Photons from Two Separate Semiconductor Quantum Dots,” *Phys. Rev. Lett.* **104**, 137401 (2010).
- [155] M. Reindl, K. D. Jöns, D. Huber, C. Schimpf, Y. Huo, V. Zwiller, A. Rastelli, and R. Trotta, “Phonon-Assisted Two-Photon Interference from Remote Quantum Emitters,” *Nano Lett.* **17**, 4090–4095 (2017).
- [156] M. Zopf, T. Macha, R. Keil, E. Uruñuela, Y. Chen, W. Alt, L. Ratschbacher, F. Ding, D. Meschede, and O. G. Schmidt, “Frequency feedback for two-photon interference from separate quantum dots,” *Phys. Rev. B* **98**, 161302(R) (2018).
- [157] R. M. Stevenson, R. J. Young, P. Atkinson, K. Cooper, D. A. Ritchie, and A. J. Shields, “A semiconductor source of triggered entangled photon pairs,” *Nature* **439**, 179–182 (2006).
- [158] M. A. Pooley, A. J. Bennett, R. M. Stevenson, A. J. Shields, I. Farrer, and D. A. Ritchie, “Energy-Tunable Quantum Dot with Minimal Fine Structure Created by Using Simultaneous Electric and Magnetic Fields,” *Phys. Rev. Appl.* **1**, 024002 (2014).
- [159] P. Michler, A. Kiraz, C. Becher, W. V. Schoenfeld, P. M. Petroff, L. Zhang, E. Hu, and A. Imamoglu, “A Quantum Dot Single-Photon Turnstile Device,” *Science* **290**, 2282–2285 (2000).
- [160] C. Santori, D. Fattal, J. Vučković, G. S. Solomon, and Y. Yamamoto, “Single-photon generation with InAs quantum dots,” *New J. Phys.* **6**, 89 (2004).
- [161] S. Buckley, K. Rivoire, and J. Vučković, “Engineered quantum dot single-photon sources,” *Rep. Prog. Phys.* **75**, 126503 (2012).
- [162] J. Kettler, “Telecom-wavelength nonclassical light from single In(Ga)As quantum dots,” Ph.D. thesis, *Universität Stuttgart* (2016).
- [163] P. Michler, ed., *Single Semiconductor Quantum Dots*, NanoScience and Technology (*Springer-Verlag*, Berlin Heidelberg, 2009), 1st ed.
- [164] P. Michler, ed., *Quantum Dots for Quantum Information Technologies*, Nano-Optics and Nanophotonics (*Springer-Verlag*, Berlin Heidelberg, 2017), 1st ed.
- [165] C. B. Murray, C. R. Kagan, and M. G. Bawendi, “Synthesis and Characterization of Monodisperse Nanocrystals and Close-Packed

- Nanocrystal Assemblies,” *Annu. Rev. Mater. Sci.* **30**, 545–610 (2000).
- [166] F. C. Frank, J. H. van der Merwe, and N. F. Mott, “One-dimensional dislocations. I. Static theory,” *Proc. R. Soc. Lond. A* **198**, 205–216 (1949).
- [167] M. Volmer and A. Weber, “Keimbildung in übersättigten Gebilden,” *Z. Phys. Chem* **119**, 277–301 (1926).
- [168] I. N. Stranski and L. Krastanow, “Zur Theorie der orientierten Ausscheidung von Ionenkristallen aufeinander,” *Akad. Wiss. Lit. Mainz Math.-Natur. Kl. Iib* **146**, 797–810 (1939).
- [169] F. Houzay, C. Guille, J. M. Moison, P. Henoc, and F. Barthe, “First stages of the MBE growth of InAs on (001)GaAs,” *J. Cryst. Growth* **81**, 67–72 (1987).
- [170] A. D. Rakić and M. L. Majewski, “Modeling the optical dielectric function of GaAs and AlAs: Extension of Adachi’s model,” *J. Appl. Phys.* **80**, 5909–5914 (1996).
- [171] W. L. Barnes, G. Björk, J. M. Gérard, P. Jonsson, J. A. E. Wasey, P. T. Worthing, and V. Zwiller, “Solid-state single photon sources: light collection strategies,” *Eur. Phys. J. D* **18**, 197210 (2002).
- [172] M. Gschrey, A. Thoma, P. Schnauber, M. Seifried, R. Schmidt, B. Wohlfeil, L. Krüger, J. H. Schulze, T. Heindel, S. Burger, F. Schmidt, A. Strittmatter, S. Rodt, and S. Reitzenstein, “Highly indistinguishable photons from deterministic quantum-dot microlenses utilizing three-dimensional *in situ* electron-beam lithography,” *Nat. Commun.* **6**, 7662 (2015).
- [173] P. Hawrylak and A. Wojs, “Electronic structure and optical properties of self-assembled quantum dots,” *Semicond. Sci. Technol.* **11**, 1516 (1996).
- [174] V. D. Kulakovskii, G. Bacher, R. Weigand, T. Kümmell, A. Forchel, E. Borovitskaya, K. Leonardi, and D. Hommel, “Fine Structure of Biexciton Emission in Symmetric and Asymmetric CdSe/ZnSe Single Quantum Dots,” *Phys. Rev. Lett.* **82**, 1780–1783 (1999).
- [175] M. Bayer, G. Ortner, O. Stern, A. Kuther, A. A. Gorbunov, A. Forchel, P. Hawrylak, A. Fafard, K. Hinzer, T. L. Reinecke, S. N. Walck, J. P. Reithmaier, F. Klopff, and F. Schäfer, “Fine structure of neutral and charged excitons in self-assembled In(Ga)As/(Al)GaAs quantum dots,” *Phys. Rev. B* **65**, 195315 (2002).
- [176] A. Muller, E. B. Flagg, P. Bianucci, X. Y. Wang, D. G. Deppe, W. Ma, J. Zhang, G. J. Salamo, M. Xiao, and C. K. Shih, “Resonance Fluorescence from a Coherently Driven Semiconductor Quantum Dot in a Cavity,” *Phys. Rev. Lett.* **99**, 187402 (2007).

- [177] N. A. Vamivakas, Y. Zhao, C. Y. Lu, and M. Atatüre, “Spin-resolved quantum-dot resonance fluorescence,” *Nat. Phys.* **5**, 198–202 (2009).
- [178] S. Stuffer, P. Machnikowski, P. Ester, M. Bichler, V. M. Axt, T. Kuhn, and A. Zrenner, “Two-photon Rabi oscillations in a single $\text{In}_x\text{Ga}_{1-x}\text{As}/\text{GaAs}$ quantum dot,” *Phys. Rev. B* **73**, 125304 (2006).
- [179] L. Besombes, K. Kheng, L. Marsal, and H. Mariette, “Acoustic phonon broadening mechanism in single quantum dot emission,” *Phys. Rev. B* **63**, 155307 (2001).
- [180] B. Krummheuer, V. M. Axt, and T. Kuhn, “Theory of pure dephasing and the resulting absorption line shape in semiconductor quantum dots,” *Phys. Rev. B* **65**, 195313 (2002).
- [181] I. A. Merkulov, A. L. Efros, and M. Rosen, “Electron spin relaxation by nuclei in semiconductor quantum dots,” *Phys. Rev. B* **65**, 205309 (2002).
- [182] P. Kaer, N. Gregersen, and J. Mørk, “The role of phonon scattering in the indistinguishability of photons emitted from semiconductor cavity QED systems,” *New J. Phys.* **15**, 035027 (2013).
- [183] J. Iles-Smith, D. P. S. McCutcheon, A. Nazir, and J. Mørk, “Phonon scattering inhibits simultaneous near-unity efficiency and indistinguishability in semiconductor single-photon sources,” *Nat. Photon.* **11**, 521–526 (2017).
- [184] R. Kubo, *Fluctuation, Relaxation and Resonance in Magnetic Systems* (Oliver & Boyd, Edinburgh, 1962), 1st ed.
- [185] R. Kubo, “A Stochastic Theory of Line Shape,” *Adv. Chem. Phys.* **15**, 101–127 (1969).
- [186] A. Tokmakoff, “Time-Dependent Quantum Mechanics and Spectroscopy,” online resource published at University of Chicago (2014). <http://tdqms.uchicago.edu>.
- [187] J. L. McHale, *Molecular Spectroscopy* (Taylor & Francis group, Boca Raton, 2017), 2nd ed.
- [188] K. Wódkiewicz, B. W. Shore, and J. H. Eberly, “Pre-Gaussian noise in strong laser–atom interactions,” *J. Opt. Soc. Am. B* **1**, 398–405 (1984).
- [189] A. Berthelot, C. Voisin, C. Delalande, P. Roussignol, R. Ferreira, and G. Cassabois, “From Random Telegraph to Gaussian Stochastic Noises: Decoherence and Spectral Diffusion in a Semiconductor Quantum Dot,” *Adv. Theor. Math. Phys.* **2010**, 494738 (2009).
- [190] E. M. Purcell, R. V. Pound, and N. Bloembergen, “Nuclear Magnetic Resonance Absorption in Hydrogen Gas,” *Phys. Rev.* **70**, 986–987 (1946).

-
- [191] A. Berthelot, I. Favero, G. Cassabois, C. Voisin, C. Delalande, P. Rousignol, R. Ferreira, and J. M. Gérard, “Unconventional motional narrowing in the optical spectrum of a semiconductor quantum dot,” *Nat. Phys.* **2**, 759–764 (2006).
- [192] A. Thoma, P. Schnauber, M. Gschrey, M. Seifried, J. Wolters, J. H. Schulze, A. Strittmatter, S. Rodt, A. Carmele, A. Knorr, T. Heindel, and S. Reitzenstein, “Exploring Dephasing of a Solid-State Quantum Emitter via Time- and Temperature-Dependent Hong-Ou-Mandel Experiments,” *Phys. Rev. Lett.* **116**, 033601 (2016).
- [193] H. Wang, Z. C. Duan, Y. H. Li, S. Chen, J. P. Li, Y. M. He, M. C. Chen, Y. He, X. Ding, C. Z. Peng, C. Schneider, M. Kamp, S. Höfling, C. Y. Lu, and J. W. Pan, “Near-Transform-Limited Single Photons from an Efficient Solid-State Quantum Emitter,” *Phys. Rev. Lett.* **116**, 213601 (2016).
- [194] J. C. Loredó, N. A. Zakaria, N. Somaschi, C. Anton, L. de Santis, V. Giesz, T. Grange, M. A. Broome, O. Gazzano, G. Coppola, I. Sagnes, A. Lemaître, A. Auffeves, P. Senellart, M. P. Almeida, and A. G. White, “Scalable performance in solid-state single-photon sources,” *Optica* **3**, 433–440 (2016).
- [195] H. Wang, Y. He, Y. H. Li, Z. E. Su, B. Li, H. L. Huang, X. Ding, M. C. Chen, C. Liu, J. Qin, J. P. Li, Y. M. He, C. Schneider, M. Kamp, C. Z. Peng, S. Höfling, C. Y. Lu, and J. W. Pan, “High-efficiency multiphoton boson sampling,” *Nat. Photon.* **11**, 361–365 (2017).
- [196] J. Bylander, I. Robert-Philip, and I. Abram, “Interference and correlation of two independent photons,” *Eur. Phys. J. D* **22**, 295–301 (2003).
- [197] B. Kambs and C. Becher, “Limitations on the indistinguishability of photons from remote solid state sources,” *New J. Phys.* **20**, 115003 (2018).
- [198] M. Abramowitz and I. A. Stegun, *Handbook of mathematical functions* (Dover Publications, New York, 1964), 1st ed.
- [199] G. P. M. Poppe and C. M. J. Wijers, “Algorithm 680: evaluation of the complex error function,” *ACM Trans. Math. Softw.* **16**, 47 (1990).
- [200] M. R. Zaghoul and A. N. Ali, “Algorithm 916: Computing the Faddeyeva and Voigt Functions,” *ACM Trans. Math. Softw.* **38**, 1–22 (2011).
- [201] Y. M. Galperin, B. L. Altshuler, J. Bergli, and D. V. Shantsev, “Non-Gaussian Low-Frequency Noise as a Source of Qubit Decoherence,” *Phys. Rev. Lett.* **96**, 097009 (2006).
- [202] M. Kac, “Random Walk and the Theory of Brownian Motion,” *Am. Math. Mon.* **54**, 369–391 (1947).

- [203] G. E. Uhlenbeck and L. S. Ornstein, “On the Theory of the Brownian Motion,” *Phys. Rev.* **36**, 823–841 (1930).
- [204] T. Suhara and M. Fujimura, *Waveguide Nonlinear-Optic Devices*, Springer Series in Photonics (Springer, Berlin Heidelberg, 2003), 1st ed.
- [205] R. C. Miller, W. A. Nordland, and P. M. Bridenbaugh, “Dependence of Second-Harmonic-Generation Coefficients of LiNbO₃ on Melt Composition,” *J. Appl. Phys.* **42**, 4145–4147 (1971).
- [206] R. C. Eckardt, H. Masuda, Y. X. Fan, and R. L. Byer, “Absolute and Relative Nonlinear Optical Coefficients of KDP, KD*P, BaB₂O₄, LiIO₃, MgO:LiNbO₃, and KTP Measured by Phase-Matched Second-Harmonic Generation,” *IEEE J. Quant. Electron.* **26**, 922–933 (1990).
- [207] L. E. Myers, R. C. Eckardt, M. M. Fejer, R. L. Byer, W. R. Bosenberg, and J. W. Pierce, “Quasi-phase-matched optical parametric oscillators in bulk periodically poled LiNbO₃,” *J. Opt. Soc. Am. B* **12**, 2102–2116 (1995).
- [208] I. Shoji, T. Kondo, A. Kitamoto, M. Shirane, and R. Ito, “Absolute scale of second-order nonlinear-optical coefficients,” *J. Opt. Soc. Am. B* **14**, 2268–2294 (1997).
- [209] P. A. Franken and J. F. Ward, “Optical Harmonics and Nonlinear Phenomena,” *Rev. Mod. Phys.* **35**, 23–39 (1963).
- [210] E. A. J. Marcatili, “Dielectric rectangular waveguide and directional coupler for integrated optics,” *Bell Syst. Tech. J.* **48**, 2071–2102 (1969).
- [211] D. Marcuse, *Theory of Dielectric Optical Waveguides* (Academic Press, San Diego, 1991), 2nd ed.
- [212] N. Umemura, D. Matsuda, T. Mizuno, and K. Kato, “Sellmeier and thermo-optic dispersion formulas for the extraordinary ray of 5 mol. % MgO-doped congruent LiNbO₃ in the visible, infrared, and terahertz regions,” *Appl. Opt.* **53**, 5726–5732 (2014).
- [213] I. Dolev, A. Ganany-Padowicz, O. Gayer, A. Arie, J. Mangin, and G. Gadret, “Linear and nonlinear optical properties of MgO:LiTaO₃,” *Appl. Phys. B* **96**, 423–432 (2009).
- [214] P. E. Ciddor, “Refractive index of air: new equations for the visible and near infrared,” *Appl. Opt.* **35**, 1566–1573 (1996).
- [215] A. M. Brańczyk, “Hong-Ou-Mandel Interference,” (2017). Preprint available at [arXiv:1711.00080](https://arxiv.org/abs/1711.00080) [quant-ph].
- [216] Z. Y. J. Ou, *Multi-Photon Quantum Interference* (Springer US, New York, 2007), 1st ed.

-
- [217] T. Legero, T. Wilk, A. Kuhn, and G. Rempe, “Time-resolved two-photon quantum interference,” *Appl. Phys. B* **77**, 797–802 (2003).
- [218] T. Legero, T. Wilk, A. Kuhn, and G. Rempe, “Characterization of Single Photons Using Two-Photon Interference,” *Adv. At. Mol. Opt. Phys.* **53**, 253–289 (2006).
- [219] C. F. Wildfeuer, A. P. Lund, and J. P. Dowling, “Strong violations of Bell-type inequalities for path-entangled number states,” *Phys. Rev. A* **76**, 052101 (2007).
- [220] P. Kok, W. J. Munro, K. Nemoto, T. C. Ralph, J. P. Dowling, and G. J. Milburn, “Linear optical quantum computing with photonic qubits,” *Rev. Mod. Phys.* **79**, 135–174 (2007).
- [221] C. Santori, D. Fattal, and Y. Yamamoto, *Single-photon Devices and Applications* (Wiley-VCH, Berlin, 2010), 1st ed.
- [222] T. Legero, T. Wilk, M. Hennrich, G. Rempe, and A. Kuhn, “Quantum Beat of Two Single Photons,” *Phys. Rev. Lett.* **93**, 070503 (2004).
- [223] A. Kiraz, M. Atatüre, and A. Imamoğlu, “Quantum-dot single-photon sources: Prospects for applications in linear optics quantum-information processing,” *Phys. Rev. A* **69**, 032305 (2004).
- [224] S. Aaronson and A. Arkhipov, “The Computational Complexity of Linear Optics,” *Theory Comput* **9**, 143–252 (2013).
- [225] J. Combes, J. Kerckhoff, and M. Sarovar, “The SLH framework for modeling quantum input-output networks,” *Adv. Phys. X* **2**, 784–888 (2017).
- [226] D. F. V. James, P. G. Kwiat, W. J. Munro, and A. G. White, “Measurement of qubits,” *Phys. Rev. A* **64**, 052312 (2001).
- [227] A. G. White, A. Gilchrist, G. J. Pryde, J. L. O’Brien, M. J. Bremner, and N. K. Langford, “Measuring two-qubit gates,” *J. Opt. Soc. Am. B* **24**, 172–183 (2007).
- [228] R. P. Mildren and J. R. Rabeau, eds., *Optical Engineering of Diamond* (Wiley-VCH, Wiley, Germany, 2013).
- [229] Y. He, Y. M. He, Y. J. Wei, X. Jiang, M. C. Chen, F. L. Xiong, Y. Zhao, C. Schneider, M. Kamp, S. Höfling, C. Y. Lu, and J. W. Pan, “Indistinguishable Tunable Single Photons Emitted by Spin-Flip Raman Transitions in InGaAs Quantum Dots,” *Phys. Rev. Lett.* **111**, 237403 (2013).
- [230] C. Santori, D. Fattal, J. Vučković, G. S. Solomon, and Y. Yamamoto, “Indistinguishable photons from a single-photon device,” *Nature* **419**, 594–597 (2002).

- [231] S. Zaske, “Quantum frequency down-conversion of single photons in nonlinear optical waveguides,” Ph.D. thesis, [Universität des Saarlandes](#) (2013).
- [232] G. D. Miller, “Periodically Poled Lithium Niobate: Modeling, Fabrication, and Nonlinear-Optical Performance,” Ph.D. thesis, [Stanford University](#) (1998).
- [233] A. Kling, J. G. Marques, J. G. Correia, M. F. da Silva, E. Diéguez, F. Agulló-López, and J. C. Soares, “Study of structural differences between stoichiometric and congruent lithium niobate,” [Nucl. Instrum. Methods Phys. Res. B](#) **113**, 293–295 (1996).
- [234] A. Ashkin, G. D. Boyd, J. M. Dziedzic, R. G. Smith, A. A. Ballman, J. J. Levinstein, and K. Nassau, “Optically-Induced Refractive Index Inhomogeneities in LiNbO_3 and LiTaO_3 ,” [Appl. Phys. Lett.](#) **9**, 72–74 (1966).
- [235] NTT Electronics, *Datasheet for PPLN Waveguide Chip, Model WD-1550-000-A-C-C-S009, S/N: 3071357 and 3071358* (2013).
- [236] A. J. Bennett, D. C. Unitt, P. Atkinson, D. A. Ritchie, and A. J. Shields, “High performance single photon sources from photolithographically defined pillar microcavities,” [Opt. Express](#) **13**, 50–55 (2005).
- [237] A. Lenhard, “Quantum photonic interfaces between atomic and telecommunication wavelengths,” Ph.D. thesis, [Universität des Saarlandes](#) (2015).
- [238] S. B. Mirov, V. V. Fedorov, D. Martyshkin, M. I. S, M. Mirov, and S. Vasilyev, “Progress in Mid-IR Lasers Based on Cr and Fe-Doped II-VI Chalcogenides,” [IEEE J. Sel. Top. Quantum Electron.](#) **21**, 1601719 (2015).
- [239] IPG Photonics, *Datasheet for Single-Frequency Tunable $\text{Cr}^{2+}:\text{ZnS}/\text{Se}$ Laser, Model CLT-2175/200-1SF, S/N: 1411145 and 1411146* (2014).
- [240] S. Zaske, D.-H. Lee, and C. Becher, “Green-pumped cw singly resonant optical parametric oscillator based on $\text{MgO}:\text{PPLN}$ with frequency stabilization to an atomic resonance,” [Appl. Phys. B](#) **98**, 729–735 (2010).
- [241] Y. S. Kim and R. T. Smith, “Thermal Expansion of Lithium Tantalate and Lithium Niobate Single Crystals,” [J. Appl. Phys](#) **40**, 4637–4641 (1969).
- [242] R. C. Miller, “Optical second harmonic generation in piezoelectric crystals,” [Appl. Phys. Lett.](#) **5**, 17–19 (1964).

-
- [243] D. H. Jundt, “Temperature-dependent Sellmeier equation for the index of refraction, n_e , in congruent lithium niobate,” *Opt. Lett.* **22**, 1553–1555 (1997).
- [244] O. Paul, A. Quosig, T. Bauer, M. Nittmann, J. Bartschke, G. Anstett, and J. A. L’huillier, “Temperature-dependent Sellmeier equation in the MIR for the extraordinary refractive index of 5% MgO doped congruent LiNbO₃,” *Appl. Phys. B* **86**, 111–115 (2007).
- [245] O. Gayer, Z. Sacks, E. Galun, and A. Arie, “Temperature and wavelength dependent refractive index equations for MgO-doped congruent and stoichiometric LiNbO₃,” *Appl. Phys. B* **91**, 343–348 (2008).
- [246] II-VI Deutschland GmbH, *Datasheet for ZnSe-aspherical lens, model 51610-059-11A* (2013).
- [247] C. C. Davis, *Lasers and Electro-Optics - Fundamentals and Engineering* (Cambridge University Press, Cambridge, 1996), 1st ed.
- [248] K. Kataoka, “Estimation of coupling efficiency of optical fiber by far-field method,” *Opt. Rev.* **17**, 476–480 (2010).
- [249] M. Bock, “Polarization Preserving Quantum Frequency Conversion for Trapped Atom Based Quantum Networks,” Ph.D. thesis, Universität des Saarlandes, in preparation.
- [250] Single Quantum, *Specification sheet for superconducting nanowire single photon detectors, Eos 210 Closed Cycle Detector System* (2013).
- [251] B. Kambs, J. Kettler, M. Bock, J. N. Becker, C. Arend, A. Lenhard, S. L. Portalupi, M. Jetter, P. Michler, and C. Becher, “Low-noise quantum frequency down-conversion of indistinguishable photons,” *Opt. Express* **24**, 22250–22260 (2016).
- [252] A. Ulhaq, S. Wiler, S. M. Ulrich, R. Roßbach, M. Jetter, and P. Michler, “Cascaded single-photon emission from the Mollow triplet sidebands of a quantum dot,” *Nat. Photon.* **6**, 238–242 (2012).
- [253] S. L. Portalupi, M. Widmann, C. Nawrath, M. Jetter, P. Michler, J. Wrachtrup, and I. Gerhardt, “Simultaneous Faraday filtering of the Mollow triplet sidebands with the Cs-D₁ clock transition,” *Nat. Commun.* **7**, 13632 (2016).
- [254] J. R. Lakowicz, *Principles of Fluorescence Spectroscopy* (Springer US, Boston, MA, 2006), 3rd ed.
- [255] M. Fox, *Quantum Optics: An Introduction*, Oxford Master Series in Physics (Oxford University Press, Oxford, 2006), 6th ed.
- [256] D. V. O’Connor and D. Phillips, *Time-correlated single photon counting* (Academic Press Inc., London, 1984), 1st ed.

- [257] I. V. Hertel and C. P. Schulz, *Atoms, Molecules and Optical Physics 2*, Graduate Texts in Physics (**Springer-Verlag**, Berlin Heidelberg, 2015), 1st ed.
- [258] H. J. Carmichael, *Statistical Methods in Quantum Optics 1 - Master Equation and Fokker-Planck Equations*, Texts and Monographs in Physics (**Springer-Verlag**, Berlin Heidelberg, 1999), 1st ed.
- [259] N. Ismail, C. C. Kores, D. Geskus, and M. Pollnau, “Fabry-Pérot resonator: spectral line shapes, generic and related Airy distributions, linewidths, finesses, and performance at low or frequency-dependent reflectivity,” **Opt. Express** **24**, 16366–16389 (2016).
- [260] I. H. Malitson, “Interspecimen Comparison of the Refractive Index of Fused Silica,” **J. Opt. Soc. Am.** **55**, 1205–1209 (1965).
- [261] R. Hanbury Brown and R. Q. Twiss, “Correlation between Photons in two Coherent Beams of Light,” **Nature** **177**, 27–29 (1956).
- [262] H. J. Kimble, M. Dagenais, and L. Mandel, “Photon Antibunching in Resonance Fluorescence,” **Phys. Rev. Lett.** **39**, 691–695 (1977).
- [263] X. T. Zou and L. Mandel, “Photon-antibunching and sub-Poissonian photon statistics,” **Phys. Rev. A** **41**, 475–476 (1990).
- [264] R. Brouri, A. Beveratos, J.-P. Poizat, and P. Grangier, “Photon antibunching in the fluorescence of individual color centers in diamond,” **Opt. Lett.** **25**, 1294–1296 (2000).
- [265] J. E. Gentle, *Random Number Generation and Monte Carlo Methods* (**Springer-Verlag**, New York, 2003), 2nd ed.
- [266] J. H. Weber, B. Kambs, J. Kettler, S. Kern, J. Maisch, H. Vural, M. Jetter, S. L. Portalupi, C. Becher, and P. Michler, “Two-photon interference in the telecom C-band after frequency conversion of photons from remote quantum emitters,” **Nat. Nanotechnol.** **14**, 23–26 (2018).
- [267] Y. M. He, H. Wang, C. Wang, M.-C. Chen, X. Ding, J. Qin, Z.-C. Duan, S. Chen, J.-P. Li, R.-Z. Liu, C. Schneider, M. Atatüre, S. Höfling, C. Y. Lu, and J.-W. Pan, “Coherently driving a single quantum two-level system with dichromatic laser pulses,” **Nat. Phys.** **15**, 941–946 (2019).
- [268] S. Kolatschek, “Aufbau eines Transmissionsspektrometers zur zustandserhaltenden Untersuchung verschränkter Photonen,” Bachelor’s thesis, Universität Stuttgart (2014).
- [269] T. Flissikowski, A. Hundt, M. Lowisch, M. Rabe, and F. Henneberger, “Photon Beats from a Single Semiconductor Quantum Dot,” **Phys. Rev. Lett.** **86**, 3172–3175 (2001).

-
- [270] E. Schöll, L. Hanschke, L. Schweickert, K. D. Zeuner, M. Reindl, S. F. Covre da Silva, T. Lettner, R. Trotta, J. J. Finley, K. Müller, A. Rastelli, V. Zwiller, and K. D. Jöns, “Resonance Fluorescence of GaAs Quantum Dots with Near-Unity Photon Indistinguishability,” *Nano Lett.* **19**, 2404–2410 (2019).
- [271] C. Santori, D. Fattal, J. Vučković, G. S. Solomon, E. Waks, and Y. Yamamoto, “Submicrosecond correlations in photoluminescence from InAs quantum dots,” *Phys. Rev. B* **69**, 205324 (2004).
- [272] J. H. Weber, J. Kettler, H. Vural, M. Müller, J. Maisch, M. Jetter, S. L. Portalupi, and P. Michler, “Overcoming correlation fluctuations in two-photon interference experiments with differently bright and independently blinking remote quantum emitters,” *Phys. Rev. B* **97**, 195414 (2018).
- [273] E. Neu, D. Steinmetz, J. Riedrich-Möller, S. Gsell, M. Fischer, M. Schreck, and C. Becher, “Single photon emission from silicon-vacancy colour centres in chemical vapour deposition nano-diamonds on iridium,” *New J. Phys.* **13**, 025012 (2011).
- [274] C. H. Bennett, G. Brassard, C. Crépeau, R. Jozsa, A. Peres, and W. K. Wootters, “Teleporting an unknown quantum state via dual classical and Einstein-Podolsky-Rosen channels,” *Phys. Rev. Lett.* **70**, 1895–1899 (1993).
- [275] D. Bouwmeester, J.-W. Pan, K. Mattle, M. Eibl, H. Weinfurter, and A. Zeilinger, “Experimental quantum teleportation,” *Nature* **390**, 575–579 (1997).
- [276] C. H. Bennett and S. J. Wiesner, “Communication via one- and two-particle operators on Einstein-Podolsky-Rosen states,” *Phys. Rev. Lett.* **69**, 2881–2884 (1992).
- [277] K. Mattle, H. Weinfurter, P. G. Kwiat, and A. Zeilinger, “Dense Coding in Experimental Quantum Communication,” *Phys. Rev. Lett.* **76**, 4656–4659 (1996).
- [278] R. Jozsa and N. Linden, “On the role of entanglement in quantum-computational speed-up,” *Proc. R. Soc. Lond. A* **459**, 2011–2032 (2003).
- [279] C.-Y. Lu and J.-W. Pan, “Push-button photon entanglement,” *Nat. Photon.* **8**, 174–176 (2014).
- [280] J. Clarke and F. K. Wilhelm, “Superconducting quantum bits,” *Nature* **453**, 1031–1042 (2008).
- [281] S. Lloyd, “Any nonlinear gate, with linear gates, suffices for computation,” *Phys. Lett. A* **167**, 255–260 (1992).

- [282] J. L. O’Brien, G. J. Pryde, A. G. White, T. C. Ralph, and D. Branning, “Demonstration of an all-optical quantum controlled-NOT gate,” *Nature* **426**, 264–267 (2003).
- [283] M. A. Pooley, D. J. P. Ellis, R. B. Patel, A. J. Bennett, K. H. A. Chan, I. Farrer, D. A. Ritchie, and A. J. Shields, “Controlled-NOT gate operating with single photons,” *Appl. Phys. Lett.* **100**, 211103 (2012).
- [284] O. Gazzano, M. P. Almeida, A. K. Nowak, S. L. Portalupi, A. Lemaître, I. Sagnes, A. G. White, and P. Senellart, “Entangling Quantum-Logic Gate Operated with an Ultrabright Semiconductor Single-Photon Source,” *Phys. Rev. Lett.* **110**, 250501 (2013).
- [285] B. M. Terhal and P. Horodecki, “Schmidt number for density matrices,” *Phys. Rev. A* **61**, 040301(R) (2000).
- [286] L. J. Rogers, K. D. Jahnke, T. Teraji, L. Marseglia, C. Müller, B. Naydenov, H. Schauffert, C. Kranz, J. Isoya, L. P. McGuinness, and F. Jelezko, “Multiple intrinsically identical single-photon emitters in the solid state,” *Nat. Commun.* **5**, 4739 (2014).
- [287] A. Walser, A. Renn, S. Götzinger, and V. Sandoghdar, “Lifetime-limited zero-phonon spectra of single molecules in methyl methacrylate,” *Chem. Phys. Lett.* **472**, 44–47 (2009).
- [288] C. Santori, P. E. Barclay, K.-M. C. Fu, R. G. Beausoleil, S. Spillane, and M. Fisch, “Nanophotonics for quantum optics using nitrogen-vacancy centers in diamond,” *Nanotechnology* **21**, 274008 (2010).
- [289] F. Hocke, “Long Distance Atom Photon Entanglement,” Master’s thesis, *Ludwig-Maximilians-Universität München* (2007).
- [290] S. Laurent, S. Varoutsis, L. Le Gratiet, A. Lemaître, I. Sagnes, F. Raineri, A. Levenson, I. Robert-Philip, and I. Abram, “Indistinguishable single photons from a single-quantum dot in a two-dimensional photonic crystal cavity,” *Appl. Phys. Lett.* **87**, 163107 (2005).
- [291] F. Liu, A. J. Brash, J. OHara, L. M. P. P. Martins, C. L. Phillips, R. J. Coles, B. Royall, E. Clarke, C. Bentham, N. Prtljaga, I. E. Itskevich, L. R. Wilson, M. S. Skolnick, and A. M. Fox, “High Purcell factor generation of indistinguishable on-chip single photons,” *Nat. Nanotechnol.* **13**, 835–840 (2018).
- [292] M. Wollenhaupt, A. Assion, and T. Baumert, “Short and Ultrashort Laser Pulses,” in “Handbook of Lasers and Optics,” , F. Träger, ed. (*Springer-Verlag*, Berlin-Heidelberg, 2004), chap. 12, pp. 1047–1094.
- [293] Corning, *SMF-28® Ultra Optical Fiber* (2014).

-
- [294] T. A. Hanson, “Spectral Attenuation Modelling with Matrix Models,” in “Conference Digest NPL Optical Fibre Measurement,” (York, United Kingdom, 1991), pp. 8–11.
- [295] International Telecommunication Union, *Characteristics of a Single-Mode Optical Fibre Cable, ITU-T Recommendation G.652* (1993).
- [296] I. Walmsley, L. Waxer, and C. Dorrer, “The role of dispersion in ultrafast optics,” *Rev. Sci. Instrum.* **72**, 1–29 (2001).
- [297] A. M. Dyckovsky and S. Olmschenk, “Analysis of photon-mediated entanglement between distinguishable matter qubits,” *Phys. Rev. A* **85**, 052322 (2012).
- [298] S. Abruzzo, S. Bratzik, N. K. Bernardes, H. Kampermann, P. van Loock, and D. Bruß, “Quantum repeaters and quantum key distribution: Analysis of secret-key rates,” *Phys. Rev. A* **87**, 052315 (2013).
- [299] T. Grange, G. Hornecker, D. Hunger, J.-P. Poizat, J.-M. Gérard, P. Senellart, and A. Auffèves, “Cavity-Funneled Generation of Indistinguishable Single Photons from Strongly Dissipative Quantum Emitters,” *Phys. Rev. Lett.* **114**, 193601 (2015).
- [300] T. Grange, N. Somaschi, C. Antón, L. De Santis, G. Coppola, V. Giesz, A. Lemaitre, I. Sagnes, A. Auffèves, and P. Senellart, “Reducing Phonon-Induced Decoherence in Solid-State Single-Photon Sources with Cavity Quantum Electrodynamics,” *Phys. Rev. Lett.* **118**, 253602 (2017).
- [301] D. Bonneau, M. Lobino, P. Jiang, C. M. Natarajan, M. G. Tanner, R. H. Hadfield, S. N. Dorenbos, V. Zwiller, M. G. Thompson, and J. L. O’Brien, “Fast Path and Polarization Manipulation of Telecom Wavelength Single Photons in Lithium Niobate Waveguide Devices,” *Phys. Rev. Lett.* **108**, 053601 (2012).
- [302] F. Kaiser, A. Issautier, L. A. Ngah, O. Dănilă, H. Herrmann, W. Sohler, A. Martin, and S. Tanzilli, “High-quality polarization entanglement state preparation and manipulation in standard telecommunication channels,” *New J. Phys.* **14**, 085015 (2012).
- [303] M. Bock, A. Lenhard, C. Chunnillall, and C. Becher, “Highly efficient heralded single-photon source for telecom wavelengths based on a PPLN waveguide,” *Opt. Express* **24**, 23992–24001 (2016).
- [304] L. Gruner-Nielsen, M. Wandel, P. Kristensen, C. Jorgensen, L. V. Jorgensen, B. Edvold, B. Palsdottir, and D. Jakobsen, “Dispersion-compensating fibers,” *J. Light. Technol.* **23**, 3566–3579 (2005).
- [305] S. Ramachandran, *Fiber Based Dispersion Compensation* (Springer-Verlag, New York, 2007), 1st ed.

- [306] M. Karpiński, M. Jachura, L. J. Wright, and B. J. Smith, “Bandwidth manipulation of quantum light by an electro-optic time lens,” *Nat. Photon.* **11**, 53–57 (2017).
- [307] F. Sośnicki and M. Karpiński, “Large-scale spectral bandwidth compression by complex electro-optic temporal phase modulation,” *Opt. Express* **26**, 31307–31316 (2018).
- [308] D. Kielpinski, J. F. Corney, and H. M. Wiseman, “Quantum Optical Waveform Conversion,” *Phys. Rev. Lett.* **106**, 130501 (2011).
- [309] B. Brecht, A. Eckstein, A. Christ, H. Suche, and C. Silberhorn, “From quantum pulse gate to quantum pulse shaper—engineered frequency conversion in nonlinear optical waveguides,” *New J. Phys.* **13**, 065029 (2011).
- [310] L. G. Cohen, C. Lin, and W. G. French, “Tailoring zero chromatic dispersion into the 1.5-1.6 μm low-loss spectral region of single-mode fibres,” *Electron. Lett.* **15**, 334–335 (1979).
- [311] B. E. A. Saleh and M. C. Teich, “Optical Fiber Communications,” in “Fundamentals of Photonics,” (Wiley-VCH, New York, 2019), chap. 25, 3rd ed.
- [312] K. Roy-Choudhury and S. Hughes, “Quantum theory of the emission spectrum from quantum dots coupled to structured photonic reservoirs and acoustic phonons,” *Phys. Rev. B* **92**, 205406 (2015).
- [313] G. Hornecker, A. Auffèves, and T. Grange, “Influence of phonons on solid-state cavity-QED investigated using nonequilibrium Green’s functions,” *Phys. Rev. B* **95**, 035404 (2017).

Publications

- B. Kambs, J. Kettler, M. Bock, J. N. Becker, C. Arend, A. Lenhard, S. L. Portalupi, M. Jetter, P. Michler, and C. Becher, “Low-noise quantum frequency down-conversion of indistinguishable photons,” *Opt. Express* **24**, 22250–22260 (2016).
- B. Kambs and C. Becher, “Limitations on the indistinguishability of photons from remote solid state sources,” *New J. Phys.* **20**, 115003 (2018).
- J. H. Weber, B. Kambs, J. Kettler, S. Kern, J. Maisch, H. Vural, M. Jetter, S. L. Portalupi, C. Becher, and P. Michler, “Two-photon interference in the telecom C-band after frequency conversion of photons from remote quantum emitters,” *Nat. Nanotechnol.* **14**, 23–26 (2018).
- T. Jung, J. Görlitz, B. Kambs, C. Pauly, N. Raatz, R. Nelz, E. Neu, A. M. Edmonds, M. Markham, F. Mücklich, J. Meijer, and C. Becher, “Spin Measurements of NV Centers Coupled to a Photonic Crystal Cavity,” (2019). Preprint available at arXiv:1907.07602 [quant-ph].

Danksagung

Bevor der letzte Vorhang fällt, so geziemt es sich gemäß althergebrachter Tradition, möchte ich den vielen Unterstützern meinen Dank aussprechen, ohne welche diese Arbeit sicherlich nicht zustande gekommen wäre.

Der größte Dank gebührt allem voran natürlich meinem Doktorvater Prof. Dr. Christoph Becher. Mit einem großen Vertrauensvorsprung hat er mich als ihm unbekanntem und nahezu fachfremden Studenten von außerhalb eingestellt und in der zugegeben etwas holprigen Einarbeitungszeit viel Geduld bewiesen. Ob seiner sorgfältig austarierten Mischung aus Forderung und Förderung schuf er für mich in den letzten Jahren die besten Voraussetzungen, um meine definierten Forschungsziele zu erreichen und sie gleichzeitig mit einer persönlichen Note zu versehen. In den kommenden Jahren, die ohne mich leider wohl doch etwas trist werden, wünsche ich ihm ein beständiges *“happy working”*.

I am also very grateful to J.-Prof. Dr. Tim Bartley, who has kindly volunteered to act as the second referee of my thesis.

Dankbar bin ich ebenfalls dem kunterbunten Konglomerat meiner Kollegen. Besonders hervorheben möchte ich dabei Andreas Lenhard und Matthias Bock. Andreas hat mir im ersten Jahr meiner Arbeit sehr geduldig und mit allerhand Fachwissen die vielen Mysterien der nichtlinearen Optik nahe gebracht. In Erinnerung werden mir wohl seine grenzenlose Gelassenheit und sein kompromissloser Optimismus bleiben¹. Der Matthias, auf der anderen Seite, fungiert als steter Quell des Wissens, wandelndes Literaturverzeichnis sowie immenses Energiebündel. Sein Input gab oftmals den benötigten Impuls, um so manch einer Herausforderung Herr zu werden. Ich bin sicher, ^{obwohl} weil er so clever ist, wird Matthias erreichen was auch immer er sich vornimmt. Darüber ^{verplant} hinaus habe ich im Laufe meiner Saarbrücker Lebensdauer die Masterarbeit von Richard Nelz sowie die Bachelorarbeit von Dennis Herrmann betreut. Ich danke euch für euren Fleiß und unermüdlichen Einsatz im Dienste der unhinterfragten Zuarbeit für mich. Eine ganz besondere Rolle wurde in den letzten

¹A. Lenhard, *“Als ich hier anfing, schien draußen noch die Sonne”*, Proceedings of the Nonlinear Optics Office **2.05**, 854→1310 (probably 2014).

Jahren ebenfalls Alexander Bommer zuteil. In unzähligen (Nicht-)raucher- und Kaffeepausen konnten wir uns gegenseitig unser Leid klagen, was in den frustrierenden Phasen meiner Promotion ein sehr wichtiges Ventil war. Deine gelegentlichen Tourette-Anfälle, die immer so lieblich über unseren Korridor schallten, werde ich wohl sehr vermissen. In den letzten Monaten hatte außerdem Johannes Görlitz oft ein offenes Ohr für mich. Ich danke dir sehr für dein Verständnis und offenkundiges Interesse. Unserem [un-(?)]freiwilligen IT-Guru Philipp Fuchs danke ich letztlich für sein Angebot schokoladiger Nervennahrung, ohne welche ich wohl Unsummen in Nutellamuffins aus dem iCoffee investiert hätte.

Äußerst wichtig für das reibungslose Gelingen meines Vorhabens waren natürlich auch die Akteure hinter den Kulissen: Elke Huschens, nicht nur Dreh- und Angelpunkt in allen organisatorischen Belangen, hat es immer verstanden mit ihrem schier unglaublichen Frohsinn die Stimmung der Arbeitsgruppe nach oben zu treiben. Ohne dein Zutun, liebe Elke, würden wir alle doch sehr kopfflos durch die Gegend rennen. Ebenfalls unabdingbar war die vorzügliche Arbeit der Mechanik- sowie der Elektronikwerkstatt. Lediglich dank eurer Hilfe wurden meine Aufbauten so präzise, robust und überhaupt funktionsfähig, wie sie es sind.

In meinem nunmehr sechs Jahre überschreitenden hiesigen Aufenthalt habe ich viele Leute kommen und/oder gehen gesehen, die ich leider nicht alle mit einer persönlichen Widmung würdigen kann. Ihr alle habt wesentlich zu unserem guten Arbeitsklima beigetragen und ich wünsche jedem einzelnen Erfolg und Glück in den kommenden Jahren.

Der überwiegende Teil meiner experimentellen Ergebnisse ist aus unserer ergiebigen und bereits mehrere Doktorandengenerationen überspannenden Zusammenarbeit mit den Quantenpunktspektroskopen der Universität Stuttgart erwachsen. Ich möchte Prof. Dr. Peter Michler für die Übersicht über unsere gemeinsamen Projekte danken. Besonderer Dank gilt auch Jan Kettler, Jonas Weber und Simone Portalupi für die grenzenlose Fachkompetenz im Labor, die vielen Erklärungen zur Physik der Quantenpunkte, die zahllosen Kick-erpartien, welche die Nachtschichten deutlich erträglicher machten, sowie das Bekanntmachen mit dem vorzüglichen Leberkäsweck (LKW) des Nahkaufs der Uni Stuttgart.

Einen nicht zu vernachlässigenden Beitrag zu meiner Promotion hat ebenfalls die nahezu ununterbrochene Versorgung mit Kaffee geleistet. Besonders hervorzuheben sind hier die Dienste unseres immer treuen PHILIPS EP5310/10 Kaffeefullautomat in schwarz. Sein hoher Kaffeedurchsatz und seine vielseitige Verwendbarkeit gepaart mit niedrigem Reinigungs- und Wartungsaufwand machten den Konsum des schwarzen Goldes zu einem besonderen Genuss. Gedenken möchte ich aber auch der gefallen Kaffemaschinen der letzten Jahre, die im Dienste der Physik viel zu früh ihre Funktionalität verloren. Euer Opfer bleibt unvergessen.

Auch außerhalb der Universität gibt es viele Menschen, die ich nicht uner-

wähnt lassen möchte. Allem voran sind das meine Kollegen von Belgarien: Martin (Ulath), Alexander (Bob) und der Wim (die Keule). Ganz gleich ob im Proberaum, bei Auftritten, Geburtstagen, Grillevents, Filme- oder Spieleabenden, im XoX, JWD oder Musiktheater, bei Quartestern, Festival- oder McDonalds-Besuchen – ihr wart immer präsent und meine Erinnerungen an unsere gemeinsame Zeit werden mir auf ewig heilig sein.

Ich danke auch meiner Familie: meiner Mutter Viola, die mich zu einem empathischen Menschen erzogen hat, der stets seine Umwelt kritisch hinterfragt (obwohl man mich zugegeben sehr leicht an der Nase herum führen kann). Meinem Vater Eckhard, mit dem ich viele Werte und definitiv meinen schwarzen Humor teile. Und auf jeden Fall meinem Bruder Christopher, dessen Denken und Handeln ähnlicher und gleichzeitig unterschiedlicher von meinem nicht sein könnte. Vieles von dem, was mich definiert, ist in irgendeiner Weise auf deinen Einfluss zurück zu führen. Vergiss nie, dass du ein unglaublich wertvoller Mensch bist. Ich hab dich lieb!

Almost seven years ago, I was moreover welcomed to a new “secondary” family, for which I am incredibly grateful. Never have I met such warm, kind-hearted, and selfless people. Without the slightest sign of doubt you trusted me to take care of your daughter, sister, and aunt Mina. Batool, Amir, Fariba, Elham, Azar, Mahtab, Shahram, Ali, and Mana... and since (not that much) recently also the newest members Ashida and Anita – all of you have become very dear to me.

Last, but definitely not least, möchte ich meiner Frau Mina meinen Dank aussprechen. In den letzten Jahren haben wir alle Höhen und Tiefen, die mit der Promotion einher kamen, gemeinsam durchlebt. Diese Zeit wird auch auf immer mit unserer Entwicklung als Lebenspartner, beste Freunde und Eheleute verbunden sein. Ich danke dir für deine Geduld und dein Verständnis, welches du selbst dann für mich hattest, wenn ich auch von Zeit zu Zeit mal grummelig war, um es vorsichtig zu formulieren. Ich danke dir ebenfalls für die zahlreichen kleineren Dinge, mit denen wir unseren gemeinsamen Alltag gestaltet haben: all die “Mexican Wrap & Chimichanga”-Restaurantbesuche, Netflixabende, zweistündigen Whirlpoolbelagerungen, sowie endlosen Koch- und Backsessions haben mich in den letzten Jahren die Sorgen außen herum zumindest für einige Zeit effektiv vergessen lassen. Meine liebe Mina, ich bin sehr gespannt auf die Zukunft, die uns in den nächsten Jahren erwarten wird.

Man mag es kaum glauben, damit bin ich auch schon am Ende. Es bleibt mir nur noch mich zu verabschieden mit einem finalen...

So long, and thanks for all the fish.

— Douglas Adams,
“The Hitchhiker’s Guide to the Galaxy”